ASME
SETTING THE STANDARD
1880 — 2005

Transactions of the ASME, Journal of Heat Transfer (ISSN 0022-1481) is published monthly by The American Society of Mechanical Engineers, Three Park Avenue, New York, NY 10016. Periodicals postage paid at New York, NY and additional mailing offices. POSTMASTER: Send address changes to Transactions of the ASME, Journal of Heat Transfer, c/o THE AMERICAN SOCIETY OF MECHANICAL ENGINEERS, 22 Law Drive, Box 2300, Fairfield, NJ 07007-2300. **CHANGES OF ADDRESS** must be received at Society headquarters seven weeks before they are to be effective. Please send old label and new address.
 INDEXED by Applied Mechanics Reviews and Engineering Information, Inc. Canadian Goods & Services Tax Registration #126148048.

Journal of Heat Transfer

Published Monthly by ASME

VOLUME 127 • NUMBER 1 • JANUARY 2005

(**Contents continued on inside back cover**)

This journal is printed on acid-free paper, which exceeds the ANSI Z39.48-1992 specification for permanence of paper and library materials. ♾™
♻ 85% recycled content, including 10% post-consumer fibers.

Journal of Heat Transfer **Volume 127, Number 1** **JANUARY 2005**

TECHNOLOGY REVIEWS

The ASME Journal of Heat Transfer is abstracted and indexed in the following:

Applied Science and Technology Index, Chemical Abstracts, Chemical Engineering and Biotechnology Abstracts (Electronic equivalent of Process and Chemical Engineering), Civil Engineering Abstracts, Compendex (The electronic equivalent of Engineering Index), Corrosion Abstracts, Current Contents, E & P Health, Safety, and Environment, Ei EncompassLit, Engineered Materials Abstracts, Engineering Index, Enviroline (The electronic equivalent of Environment Abstracts), Environment Abstracts, Environmental Engineering Abstracts, Environmental Science and Pollution Management, Fluidex, Fuel and Energy Abstracts, Index to Scientific Reviews, INSPEC, International Building Services Abstracts, Mechanical & Transportation Engineering Abstracts, Mechanical Engineering Abstracts, METADEX (The electronic equivalent of Metals Abstracts and Alloys Index), Petroleum Abstracts, Process and Chemical Engineering, Referativnyi Zhurnal, Science Citation Index, SciSearch (The electronic equivalent of Science Citation Index), Theoretical Chemical Engineering

Journal of Heat Transfer

Foreword

In honor of Richard Chu, a symposium on ''Thermal Management of Electronic Systems'' was held at the ASME IMECE in Washington D.C., in November 2003, where over 45 papers were presented. This special issue of the *ASME Journal of Heat Transfer* is a compilation of papers selected from that symposium and is a token of appreciation for Richard Chu's sustained contributions to electronics cooling and thermal management of electronic systems.

Richard Chu began his professional career at IBM in 1960 as a thermal engineer. During these early years he worked on the development of the IBM System/360. His 1965 invention of a multilevel air-liquid hybrid cooling design was pivotal to IBM's successful introduction of its System/360 Model 91, the world's highest performance computer system at the time. The introduction of this hybrid cooling system marked the beginning of the water-cooling era, which lasted through the years of bipolar technolgy. In 1966 he became a manager with the assignment of establishing and leading a heat transfer technology group to develop new and improved cooling technologies.

Throughout his career, Dick has been a prolific technical innovator as demonstrated by his impressive record of inventions. During his career he has received 38 IBM invention awards for over 100 patents and has authored over 150 patent disclosure publications. As one of the inventors of the cooling scheme for the IBM Thermal Conduction Module (TCM), he received an IBM Outstanding Innovation Award and a Corporate Award. This high thermal conduction technology, coupled with his modular cold plate cooling system idea, constituted the primary cooling design for IBM's large computer systems for over 15 years following their implementation in 1980. Variations of this water-cooling concept were adapted by each of the major worldwide computer mainframe manufacturers during this time period.

He also received an IBM Outstanding Innovation Award for a heat sink design and water-cooled cold plate development. The importance of his many contributions to IBM through his creativity, thermal expertise, and technical leadership led to his appointment as an IBM Fellow in 1983, the company's highest technical honor. He is still contributing in this capacity today with a small group dedicated to exploring cooling technology for future computers. In 1996, Dick initiated a study for the feasibility of using lower temperature cooling to enhance CMOS performance. He co-invented a dual-channel evaporator cold-plate enabling modular refrigeration cooling (MRC) with redundancy and concurrent maintenance. This MRC cooling concept has been used on all of IBM's CMOS-based high performance computers since 1997.

In addition to providing ongoing leadership in electronics cooling and thermal management, Dick has been looking ahead to the need for new generations of thermal engineers. He chaired the National Electronic Manufacturing Initiative (NEMI) technical working group in 2000 and 2002 to produce a thermal management roadmap chapter for the NEMI Technology Roadmap. Dick is also widely known through his active participation in both ASME and IEEE sponsored conferences, presenting papers and often serving as a keynote speaker. He is a co-author of one of the earliest books on electronic cooling entitled *Heat Transfer in Microelectronic Equipment*, and in 2002, he co-authored a second book entitled *Thermal Management of Microelectronic Equipment* published by ASME Press.

The importance of Richard Chu's contributions are widely recognized and further attested to by a number of awards and honors he has received, including the ASME Heat Transfer Memorial Award, the InterPACK Achievement Award, and the Semi-Therm Significant Contributor Award. He was the first recipient of the Itherm Memorial Award, and is a member and past president of the IBM Academy of Technology. He is a Fellow of ASME, American Association for the Advancement of Science and a member of the National Academy of Engineering. He also received honorary doctorate degrees from Purdue University and the American University of the Caribbean.

Richard Chu has been an inspiration to the electronics cooling and packaging community through his pioneering research contributions and his invention achievements. This special issue of the *ASME Journal of Heat Tranfer* honors Dick's outstanding leadership, contributions, and service.

Cristina Amon
Raymond J. Lane Distinguished Professor of Mechanical Engineering,
Director, Institute for Complex Engineered Systems (ICES),
Carnegie Mellon University,
Pittsburgh, PA 15213

Dereje Agonafer
Professor Mechanical and Aerospace Engineering Department,
Director, Electronics, MEMS & Nanoelectronics Systems Packaging Center,
University of Texas at Arlington,
Arlington, TX 76019

Next Generation Devices for Electronic Cooling With Heat Rejection to Air

Ralph L. Webb
e-mail: rlwebb@psu.edu
Penn State University,
University Park, PA 16802

Conventional technology to cool desktop computers and servers is that of the "direct heat removal" heat sink, which consists of a heat sink/fan mounted on the CPU. Although this is a very cost effective solution, it is nearing its end of life. This is because future higher power CPUs will require a lower R-value than can be provided by this technology, within current size and fan limits. This paper discusses new technology that uses "indirect heat removal" technology, which involves use of a single or two-phase working fluid to transfer heat from the hot source to an ambient heat sink. This technology will support greater heat rejection than is possible with the "direct heat removal" method. Further, it will allow use of higher performance air-cooled ambient heat sinks than are possible with the "direct heat removal" heat sink. A concern of the indirect heat removal technology is the possibility that it may be orientation sensitive. This paper identifies preferred options and discusses the degree to which they are (or not) orientation sensitive. It should be possible to attain an R-value of 0.12 K/W at the balance point on the fan curve.
[DOI: 10.1115/1.1800512]

Introduction

The most popular device used for first generation desktop computer cooling is the ''active'' heat sink. The currently used version consists of a small aluminum heat sink on which a small fan (e.g., 60 mm diameter) is mounted. This has been found adequate to remove up to approximately 75 W. The device has evolved since it was first used with the Pentium processor. The major changes have been in the physical size of the heat sink and fan, and in use of a copper ''heat spreader'' to spread the heat from the ever decreasing CPU size. As a result of smaller CPU size and increased power, the heat flux at the CPU has significantly increased. This has resulted in great improvements of thermal interface material (TIM).

As CPU power increases and die size decreases, it appears that limits will exist on the possible power dissipation of CPU mounted heat sinks. The factors that will limit the possible heat dissipation are the heat sink plan area and height, and the fan size, speed, and allowable noise. When this limit is reached, it will be necessary to identify a new concept for heat removal.

We believe it is appropriate to introduce a new terminology for heat removal concepts. Rather than using terms, such as ''active'' heat sink, we propose to introduce the following definitions:

1. Direct Heat Removal (DirHR) for an ambient heat sink that is directly attached to the hot source.
2. Indirect Heat Removal (IndHR) for an ambient heat sink that is remote from the hot source, and uses a ''working fluid'' to transport heat from the hot source to the heat sink.

The term ''ambient heat sink'' (AmbHS) is defined to mean the final heat rejection device that rejects heat to the ambient, via air or water-cooling. Use of IndHR establishes the need for a second heat sink located at the hot source. This will be called the ''hot source heat sink'' (HS-HS). For several years, notebook computers have used a heat pipe to accomplish indirect heat removal.

This paper will deal only with heat rejection to ambient air. Thus, we will define Direct Heat Removal (DirHR) devices with air-cooling as 1^{st} generation devices. Indirect Heat Removal (IndHR) devices with air-cooling are defined as 2^{nd} generation devices. Although water-cooling may be considered as an option for ambient heat removal, it is unlikely that IndHR devices will be used with heat rejection to ambient water. Future very high heat rejection systems, such as servers, will likely use evaporative cooling of air (e.g., a closed circuit cooling tower).

A key advantage of DirHR with air-cooling is that the device is orientation insensitive. The importance of this advantage has been taken for granted until recent work on high power 2^{nd} generation devices. A variety of 2^{nd} generation devices have been proposed for future generation desktop computers and servers, which are the key focus of this paper. One concern of some of the devices under current consideration is their orientation sensitivity. Designers of heat pipe systems for notebook computers are already aware of the orientation sensitivity of heat pipes. A device that is sensitive to orientation may not be as desirable as one that is orientation insensitive. Hence, this concern will be addressed in our discussion of 2^{nd} generation IndHR devices.

Component Thermal Resistances

The heat transfer rate is typically defined in terms of the driving temperature difference between the hot surface (T_{hot}) and the inlet air temperature ($T_{air,in}$). For a heat dissipation of q (Watts), the total thermal resistance is

$$R_{tot} = \frac{T_{hot} - T_{air,in}}{q}$$

For a DirHR device, the R_{tot} typically consists of three basic components in series—interface (R_{int}), spreading (R_{sp}), and the heat sink (R_{amb}). The thermal resistance associated with the ambient heat sink is called R_{amb} and is a convection resistance. If an IndHR the heat sink is located remote from the hot source, a ''working fluid'' must be used to transfer the heat from the hot surface to the convection heat sink. Possible means of heat transport are:

1. A heat pipe, which is typically used in notebook computer
2. Convection via a single-phase or two-phase fluid.

Use of a working fluid in the IndHR device will involve additional convection thermal resistances. Consider for example the

Contributed by the Heat Transfer Division for publication in the JOURNAL OF HEAT TRANSFER. Manuscript received by the Heat Transfer Division April 12, 2004; revision received July 6, 2004. Assoc. Editor: C. Amon.

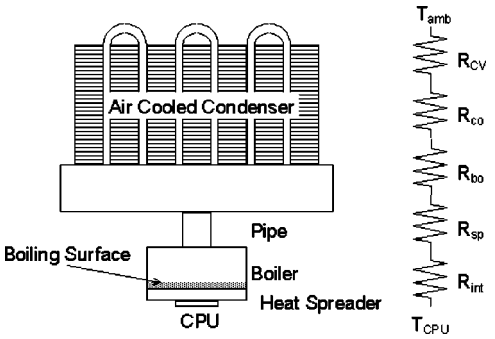

Fig. 1 Schematic of remotely located thermosyphon heat rejection device

device illustrated in Fig. 1, which boils a fluid at the hot source and condenses it at the ambient heat sink. The associated thermal resistances of the indirect system are

1. $R_{H,cv}$ that is the convection resistance at the hot source.
2. R_{transp}, which is the thermal resistance, associated with transporting the working fluid to the ambient heat sink.
3. $R_{C,cv}$, which is the convection resistance, associated with transferring heat from the working fluid to the ambient heat sink.

The sum of these three additional thermal resistances is defined as R_{ind} and is the additional resistance introduced by use of a working fluid with an IndHR device.

Notebook computers may use a heat pipe to transfer heat from the hot surface to the heat sink. The heat pipe has the same three additional thermal resistances. Thus, the thermal resistance associated with pressure drop of the vapor between the boiler and the condenser is R_{transp}. The working fluids used in an IndHR devices may be gases, single-phase liquids, and two-phase fluids. Specific devices that may be used to remove heat at the hot source ($R_{H,cv}$) and transfer it to the ambient heat sink, where $R_{C,cv}$ exists will be addressed in a later section.

Limits on Direct Heat Removal With Air-Cooling (DirHR)

It is important to define probable limits (Watts heat rejection) that may be attained by DirHR devices. It is expected that DirHR will be used as long as possible, because of their low cost. For the same Watts heat rejection, 2nd generation IndHR are expected to cost more than DirHR devices.

Figure 2 illustrates a DirHR air-cooled heat sink that is designed to directly attach to the central processor unit (CPU) of a desktop computer. The plan area of computer heat sinks is limited by the space allocated on the circuit board. Further limitations exist in the height of the fan-heat sink combination. The mounted fan provides air flow though the finned array, as shown in Fig. 2. The air flow through the heat sink may be either ''impinging'' flow or ''duct flow.'' The Fig. 2 heat sink must operate at the balance point on the fan curve. Because of the design geometry constraints, it is probable that the air flow frontal area will be fixed (for a given flow orientation). For a given heat sink/fan combination it is important to determine whether higher performance will be obtained by duct flow or impinging flow. This question was studied by Saini and Webb [1,2] for plain fins. They fixed the plan area at 60 mm$\times$60 mm and the total heat sink/fan height at 50 mm. They performed analysis to determine the optimum fin pitch and fin thickness for each flow geometry using a 60 mm$\times$60 mm fan operating at 4700 rpm. They found that the minimum R_{cv} will occur for the highest allowable fin height. They also extended the analysis to consider increased air flow rate and a larger heat sink size 80 mm$\times$80 mm.

Fig. 2 Air cooled heat sink with fan

Based on the analysis of Saini and Webb [1], it appears that impinging flow with plain fins will yield the lowest possible R_{amb}. And, it appears that the 0.15 K/W may be a practical limit for R_{cv}, within current design limitations. Setting values for R_{int} and R_{sp} allows one to predict the limiting heat dissipation. Assuming the hot source is 16 mm square and $R_{\text{int}}=0.0157$ K-in^2/W the interface resistance is 0.04 K/W. With 80$\times$60 mm base area case and 4.0 mm thick copper heat spreader, the $R_{sp}=0.142$ K/W for impinging flow. Substituting these values in Eq. (1) gives $R_{\text{tot}}=0.336$ K/W. Using $T_{\text{hot}}=70°$C and $T_{\text{amb}}=35°$C, one would predict the limiting heat dissipation to be 104 W. Thus, it appears that the DirHR devices will be limited to heat rejection values close to 100 W.

Clearly, the highest performance for any heat sink geometry will be attained if all of the air flow from the fan passes through the heat sink. Any design factors that allow airflow to bypass the heat sink fins will reduce the heat sink performance.

2nd Generation IndHR Devices for Heat Removal at Hot Source

Figure 3 shows a tree of various indirect concepts that may be used to remove heat at the hot source surface. The 1st generation DirHR method has limited heat rejection capability. The 2nd generation IndHR methods are expected to provide greater heat removal capability and are of specific interest here. The heat removed from the hot source surface by a working fluid is transferred to the remote ambient air-cooled heat sink. Excluding gases, the working fluid may be a single-phase liquid, or a two-phase fluid. A key concern is whether the methods are orientation sensitive or insensitive. Figure 3 is annotated to indicate whether the concepts are expected to be orientation sensitive or insensitive. The concepts are separated into the basic categories ''single-phase'' and ''two-phase,'' which refers to the working fluid. Discussion of the ambient heat sink used to cool the working fluid will be discussed later.

Single-Phase Fluids. This concept uses a pump to force a single-phase fluid through multiple parallel micro-channels at the hot source. The fluid must be sub-cooled and it must be pressurized to remain sub-cooled. Liquids are expected to provide higher heat transfer performance than gases. The heated single-phase liquid must be cooled in the ambient heat-exchanger. The heated liquid will be cooled in micro channels in the ambient heat ex-

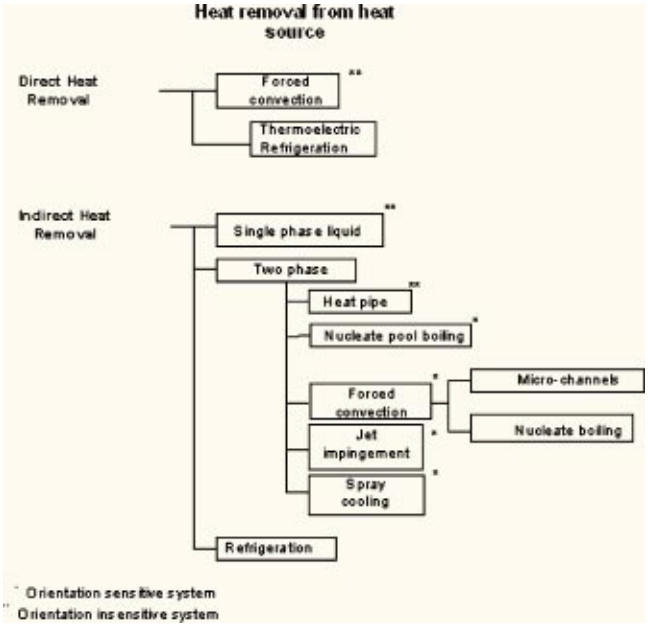

Fig. 3 Tree of methods of removing heat from hot source surface

changer. Because the system operates under forced convection, it is orientation insensitive. More discussion of this concept is discussed in a later section.

Two-Phase Fluids. Higher performance is expected by using a two-phase working fluid than is possible with a single-phase liquid. For two-phase heat removal at the hot source, the working fluid must be condensed at the ambient air-cooled heat sink. If the working fluid is circulated by a pump, the system will be orientation insensitive. However, a passive system will be orientation sensitive. If the condensate is returned to the hot source by gravity, the device will be orientation sensitive. In this case, the boiler must be located at a lower elevation than the condenser. Pool boiling systems, which do not use a pump, are orientation sensitive. Heat pipes have height limits to their orientation sensitivity. Jet impingement devices may or may not be orientation sensitive at the hot surface, but how the condensate is returned to the pump sump will determine their orientation sensitivity. These several concepts are discussed below.

Several factors will affect the choice of an acceptable working fluid. Material compatibility prevents use of aluminum with water. However, copper or brass are compatible with water. Flammability concerns will tend to prevent use of propane, or iso-butane. Table 1 shows some possible candidate fluids. Environmental concerns eliminate fluids having ''ozone depletion potential'' (ODP). Recently introduced concerns include the ''Global Warming Potential'' (GWP). Note that FC-72 has very high GWP. Although HFE-7100/7200 have significantly lower GWP than R-134A, they also have significantly lower heat transfer coefficients for the same operating conditions.

Heat Pipe. The heat pipe is a well known concept. It has limited orientation sensitivity.

Nucleate Boiling. Much work has been done on development of high performance nucleate boiling surfaces. Among this is work on boiling of refrigerants, as discussed in Chap. 11 of Webb [3]. An excellent choice is the sintered, porous boiling surface, which was used by Webb and Yamauchi [4] for their thermosyphon device. If water is used, the boiling surface must especially configured to boil water at very low system pressure. Chien and Chang [5] provide design recommendations and test results on copper porous boiling surfaces for $T_{sat}=70°C$. Figure 4 shows how the boiling coefficient is influenced by particle size.

To compare the nucleate boiling performance of different working fluids, we have estimated the pool boiling heat transfer coefficient (h) for saturated boiling at 70°C on a plain surface using the Cooper [6] correlation. Water has the highest boiling coefficient, followed by R-134A. The boiling coefficient of HFE-7200 is much less than that of R-134A. If water is used as the working fluid, copper components are required. Water cannot be used in aluminum, because it causes pin-hole corrosion. Water is the most environmentally acceptable working fluid. Although water is an environmentally acceptable fluid, a principal concern is the problem that may result from freezing. An ethylene glycol-water mixture would be acceptable to protect from freezing.

Forced Convection. In forced convection vaporization, there are ''forced convection'' and ''nucleate boiling'' components. If vaporization occurs in micro-channels, it is probable that the nucleate boiling component will be small compared to the forced convection component. However, if a high performance enhanced nucleate boiling surface is used (e.g., [5]), the process will be nucleate boiling dominated. It is important that the exit vapor quality be controlled to prevent dryout.

Spray Cooling. Thin film evaporation produced by droplet spray cooling has been shown to provide higher heat transfer coefficients, and higher critical heat flux (CHF) than provided by nucleate boiling. In this approach, one uses a pump and atomizing nozzles to spray fine droplets on the hot surface, where they evaporate as a thin film. The vapor must be condensed in an attached condenser. The system pressure is established by the condensing temperature. The condenser may be either air or water cooled, depending on the system requirements. Typically, a higher mass flow rate is sprayed on the surface than is evaporated. This will allow attainment of a higher CHF. Because only part of the liquid flow rate is evaporated, the remaining liquid must either gravity drain to a sump for recirculation by the pump, or it must be entrained and carried to the condenser. Although use of a subcooled liquid will increase the CHF, the fluid will be only slightly subcooled in practical heat rejection systems having a condenser. Although the primary heat transfer mechanism is evaporation of the thin liquid film at the liquid-vapor surface, some nucleation can also occur at the surface.

Discussion of Advanced Heat Removal Concepts

Jet Impingement/Spray Cooling Devices. For two-phase applications, jet impingement and spray cooling both involve spray-

Table 1 Properties and operating conditions of candidate working fluids

Refrigerant	M	λ @ 1 atm (kg/kJ)	P_{cr} (MPa)	P (MPa) (Temp= 70°C)	Fig. of Merit ($\times 10^{-9}$)	GWP
R-134a	102	178.0	4.06	2.162	8.37	1300
FC-72		88.47			6.80	
HFE-7100	250		2.23	0.127	4.49	
HFE-7200	264	125.61	2.07	0.1		90
Water	18.02	2445.0	22.12	0.031162	203	0

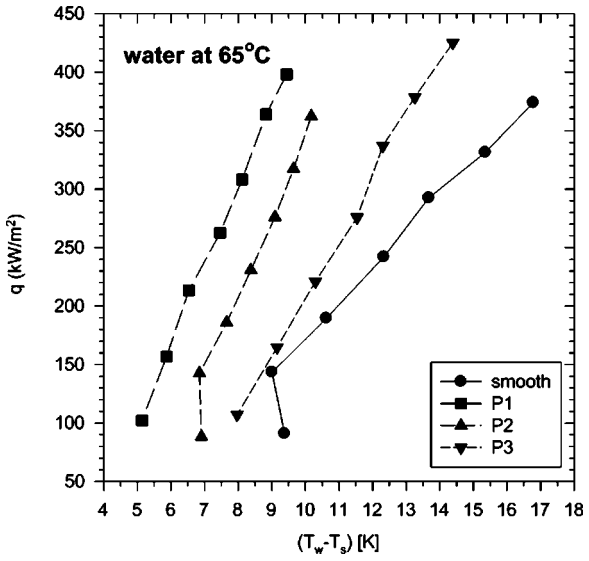

Fig. 4 Boiling performance of water at T_{sat}=65°C on 0.5 mm thick porous boiling surfaces. P-1 (100-200 μm), P-2 (50-100 μm), P-3 (30-50 μm), from Chien and Chang [5].

ing a liquid on the hot surface, where spreads as a thin film and is evaporated. However, spray cooling specifically means that the liquid impinges on the surface as small droplets. Most high performance work has involved spray cooling.

Work has been done for single nozzles, or plates having closely spaced nozzles of very small diameter. It is very important to have a uniform spray distribution over the heated surface area, or nonuniform surface temperature can result. Results have been reported by Pais et al. [7], Marcos et al. [8], and Xia [9] for water. If the working fluid is water, the evaporation will occur at very low absolute pressure for a hot surface temperature in the range of 70°C. Figure 5 shows two design concepts that have been tested with water. Figure 5(*a*) illustrates the single nozzle concept used by Marcos et al. [8] to cool a 1.0 cm^2 heat source. Figure 5(*b*) shows the Xia et al. [9] multiple nozzle design with atomization assisted by a vibrating plate driven by a piezo-electric actuator. The outlet nozzles were approximately 100 μm diameter with 160–240 μm nozzle pitch. When the piezo-electric plate vibration reaches a certain frequency (in the vicinity of 5.0 kHz), the micro liquid streams are broken into micro-drops.

Figure 6 shows the performance measured by Xia et al. [9] for water boiling on a 1.0 cm^2 electrically heated flat plate. The data were taken for 1.6 m/s jet velocity and 8.0 mm spacing between the hot surface and the nozzle plate. The different nozzle diameters and pitches (A, B, C, D) made little difference, except at the lowest heat fluxes. This figure shows that heat fluxes as high as 900 W/cm^2 can be supported. The ''Temperature Rise'' on the abscissa is the surface temperature above the saturation temperature. Thus, at 400 W/cm^2 heat flux, the boiling coefficient is approximately 16.6 W/cm^2-K, or 166 kW/m^2-K. Comparing this with the nucleate boiling data of Chien and Chang [5] for a porous surface, we see that the boiling coefficient on the porous surface at 400 W/cm^2 is significantly lower (4.2 W/cm^2-K). Hence, jet impingement provides much higher heat transfer coefficients than were measured for nucleate boiling of water on a porous surface. Further, jet impingement provides a much higher CHF. It is possible that a heat spreader will not be required for jet impingement, because of the high heat transfer coefficient. At 400 W/cm^2, the thermal resistance at the 1.0 cm^2 hot surface is 0.06 K/W.

Although the atomized spray on the hot surface is insensitive to orientation, the spray rate is several times higher than the evaporation rate, so a liquid sump must exist from which the excess

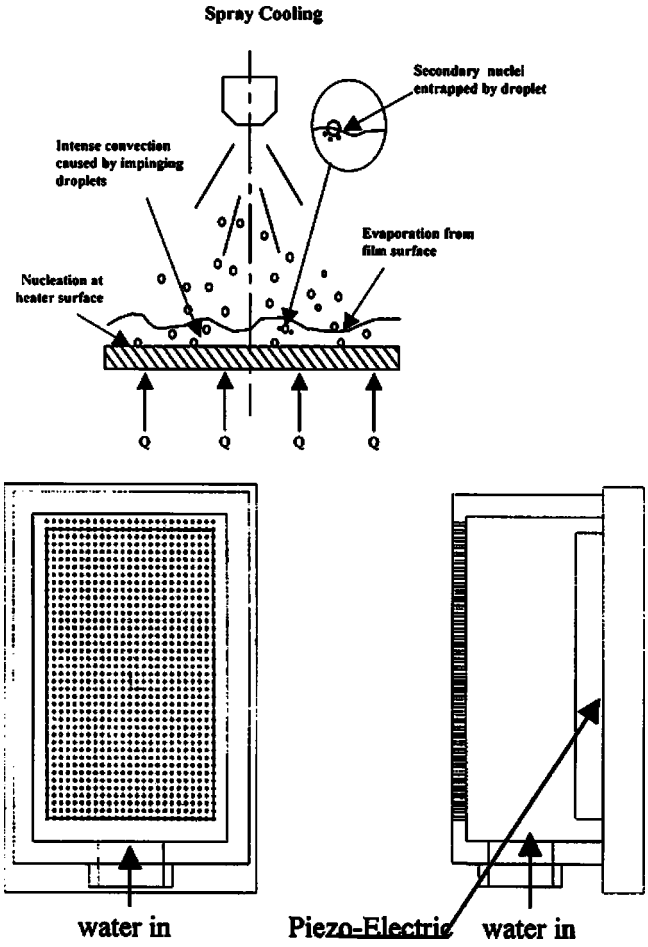

Fig. 5 Spray cooling concepts: (*a*) Single nozzle used by Marcos et al. [8], and (*b*) Multiple nozzle with piezo-electric vibrator sued by Xia [9].

liquid is pumped. The excess liquid will be drained by gravity, to the lowest point, at which the pump suction line is located. If total orientation insensitivity is desired, it will be necessary to have a design that allows the pump suction line to automatically relocate to the lowest point in the system. Such concepts are possible that allow the pump suction line to automatically locate via gravity force to the lowest point in the system.

The previous works addressed jet impingement on smooth, flat surfaces. Murthy et al. [10] investigated the benefits of using closely pitched micro-jets on a three-dimensional structured surface with HFE-7200. They show that the thin film can wet a three-dimensional shape, which was intended lead to higher heat flux (based on projected base surface area) at a given wall superheat. However, this was found to be effective only in the subcooled region. They also experimented with different nozzle orifice shapes. Data taken at the highest heat flux (30 W/cm^2) show a heat transfer coefficient of 1.2 W/cm^2-K, which is quite low compared to the values for jet impingement) or by Chien and Chang [5], who measured 3.75 W/cm^2-K for nucleate boiling on a sintered surface (Fig. 5) at the same heat flux.

Heffington et al. [11] used a piezo-electric transducer to vibrate a plate at about 2.5 kHz, which produces a shower of small diameter drops on the boiling surface. A multi-hole orifice plate (1.6 mm diameter holes) just above the driver assists in forming the small drops. These drops impinge on the hot surface and evaporate as a thin film. This concept is similar to that of Xia [9], although the nozzle diameter used by Xia was much smaller (approximately 100 μm). The concept is called ''vibration-induced

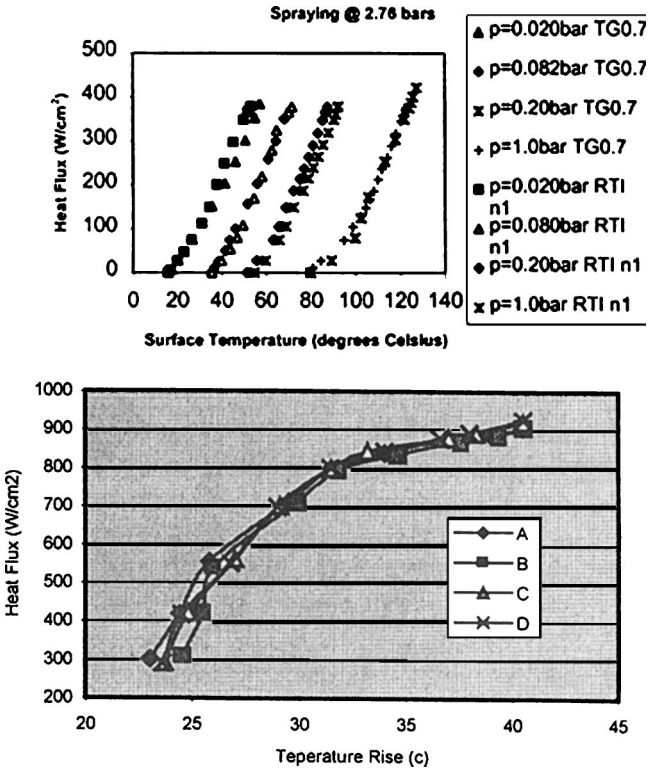

Fig. 6 Boiling heat flux versus superheat for four different micro-nozzle plates, from Xia [9].

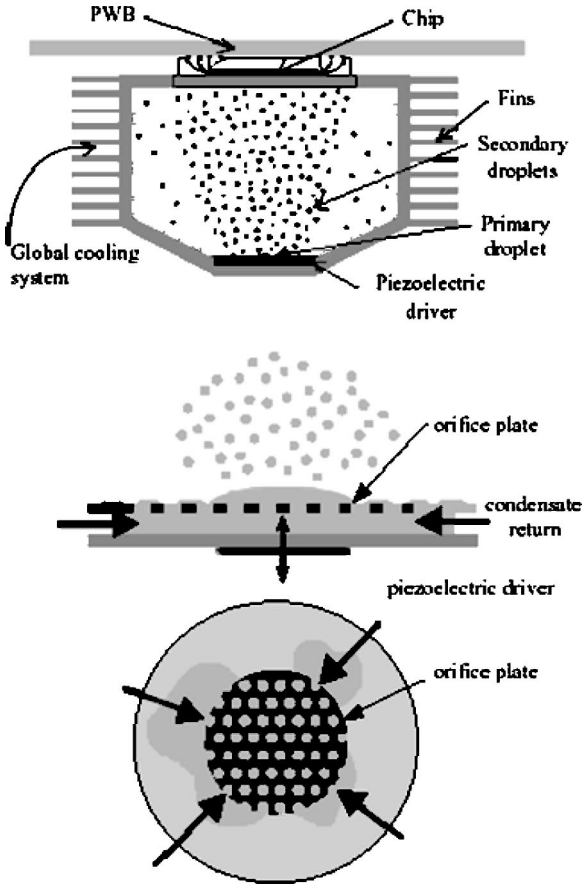

Fig. 7 Vibration induced droplet atomization (VIDA) boiling device. (*a*) Cross-section schematic with air cooling fins on outer cylinder walls, and (*b*) Illustration of droplets formed at multiple orifice plate. From Heffington [11].

droplet atomization'' (VIDA), and is illustrated in Fig. 7. The vapor can be taken to a remote condenser, or can condense on the side walls of the cell, if the outside of the cell is cooled by convection. Tests were performed using water at 100°C, and at lower temperatures. Their measured CHF was 109 W/cm^2 for 100°C heater temperature. They do not provide data that allows calculation of the boiling coefficient. As tested by Heffington et al. [11], the hot surface must be above the driver to allow the overspray to gravity drain to the driver. Another concern is the significant noise generated by the piezoelectric transducer.

It is noted that all none of the devices discussed in this section used forced convection vaporization. Thus, in all, the vapor was condensed in a reflux condenser, which makes them orientation sensitive. It is probable that these concepts could be adapted to a forced convection concept.

Single-Phase Micro-Channel Cooling. Realistic applications would use laminar, rather than turbulent, liquid flow in micro-channels. The very small hydraulic diameter would require very high fluid velocity to obtain turbulent conditions. Further, the pressure drop of turbulent flow would be extremely high, which would require high pump cost.

Two-Phase Micro-Channel Cooling. Use of two-phase heat transfer will significantly reduce the required flow rate and pumping power, compared to liquid flow. An example of two-phase micro-channel cooling is that of Koo et al. [12]. Their concept used 25 parallel micro-channels machined in a silicon substrate and is illustrated in Fig. 8. They proposed to use an electro-kinetic pump to force subcooled water through the micro-channels, where vaporization occurs. Koo et al. have provided predicted results (supported by single-channel tests) for a 25 mm square heat sink having either 150 or 200 μm channel depth. Figure 8 shows the thermal conductance (G in W/K) as a function of channel width (or number of channels). The conductance (G) is defined either in terms of the average surface temperature (G_{avg}) or the maximum surface temperature (G_{max}). Although Fig. 8 shows that the best performance is provided by the smallest channel size, large pressure drop exists for channels below 100 μm wide. For 150 μm deep and 100 μm wide channels (125 channels in the heat sink), the thermal conductance is $G_{avg}=4.1$ W/K. Converted to thermal resistance, the result is 0.039 K-cm^2/W. This thermal resistance is approximately equal to that of the water boiling surface of Webb and Yamauchi [4]. Note that the stated performance data are based on predictions and single-channel data. Koo et al. [12] performed single-channel boiling tests in a 50 μm$\times$70 μm$\times$20 mm long and compared their predictions with the single-channel data. The data and predictions agreed reasonably well.

Jiang et al. [13] constructed and tested a multi-micro-channel heat sink similar to the concept of Koo et al. [12]. They used 40

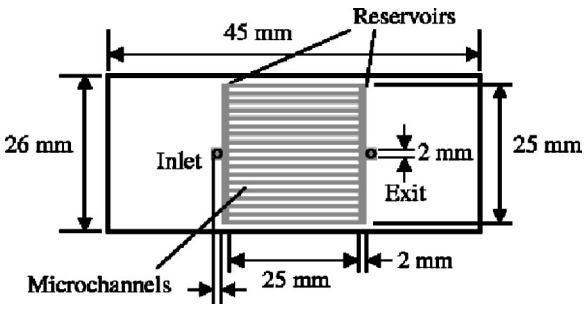

Fig. 8 Schematic of a microchannel heat sink from Koo et al. [12].

Table 2 Air-cooled ambient heat sink concepts for indirect heat removal

Design Option	Liquid Return	Liquid (or Two-Phase) Side	Air-Side
1	Forced conv.	Micro-Channels	Flat plate with heat spreader and air fins
2	Forced conv.	Round tubes with Serpentine circuit	Plate fins
3	Gravity	Flat tubes with parallel circuiting	Serpentine fins
4	Forced conv.	Flat tubes with serpentine circuiting	Serpentine fins

parallel channels and 100 μm square etched in a $20\times29\times0.5$ mm thick silicon wafer with water as the working fluid. This device was able to reject only 30 W before flow instabilities occurred, which resulted in large temperature excursions. The R-value of the heat sink was 0.25 K/W (or 1.5 K-cm^2/W). Compared to the predictions of Koo et al. [12] for 100 μm$\times$150 μm size channels, the experimental performance is far below that based on the Koo et al. analysis. It is possible that flow maldistribution in the 40 channel heat sink may be responsible for the poor performance.

Another etched silicon wafer water-cooled heat sink is described by Perret et al. [14]. Water flowed in a 20 mm square wafer having 230 μm wide rectangular micro-channels. For 0.5 l/min water flow rate and 100 W heat input, the measured thermal resistance was quite high-approximately 0.85 K-cm^2/W. The performance of the Perret et al. micro-channel heat sink is considerably better than that of Jiang et al. [13]. Note that the micro-channel concept requires use of a high-pressure micro-pump. The pump adds considerably to the cooling system cost. However, the system will be orientation insensitive. If the micro-channel concept were used in a refrigerated server application, use of a high-pressure micro-pump would not be required.

Most studies of two-phase micro-channel flow have typically shown instabilities and uneven temperature distribution on the hot surface. Examples of these are Hestroni et al. [15] and Zhang et al. [16]. It is possible that the flow instabilities are, in part, caused by flow mal-distribution in the parallel channels. Flow from the pump is discharged into a manifold, which feeds the parallel flow channels. It is very difficult to achieve uniform flow distribution in the micro-channels. If some channels have less flow than others, local regions of overheating will exist. However, two-phase flow instability can also occur in single-channels. Considerable work has been done on design of manifold flow distributors for single-phase flow. Webb [17] discusses manifold design and presents numerical simulations that show the degree of flow non-uniformity that may exist for various manifold designs.

For two-phase applications, it is not practical to design for complete evaporation. This is because dryout will occur before 100 percent vapor quality is attained, resulting in significant surface overheating. In a practical system, flow instabilities and uneven heating cannot exist. More work is needed to define the conditions that affect the dryout condition, the possibility of avoiding flow instabilities, and manifold design needed to insure uniform flow distribution.

Enhanced Two-Phase Forced Convection Cooling. This envisions that a high performance nucleate boiling enhancement will be used for the boiling surface. Then, the process will be nucleate boiling dominated. This concept differs from the enhanced nucleate pool boiling concept in that the condenser may also use forced convection condensation, so the entire system will be insensitive to orientation.

Remote Heat-Exchangers for IndHr

The remote heat-exchanger is the final heat sink, at which heat is rejected from the system. On earth, this will involve sensible heat rejection to air and water. However, it is possible to have ''air-cooling with evaporative assist.'' In this system, a water film is sprayed on the cooling surface and is evaporated into the air stream. This is called an evaporative condenser, or evaporative fluid cooler, depending on whether the working fluid is a vapor that is condensed or a liquid that is cooled. When working in air-borne or space applications, one may also consider rejecting heat to an expendable fluid that is evaporated, or by radiation to space. These are beyond the scope of the present paper.

Designers of electronic cooling systems have been speculating for some time about when the limits to air-cooling will reached, forcing use of water-cooled systems. Use of air-cooling is preferred, and it is desired to use this concept as long as possible. The present paper seeks to address ''high-power'' applications. This is an ambiguous term. However, for the present purposes, we will envision heat rejection levels in the range of 100–300 W per electronic chip. If the system contains multiple, ''high-power'' electronic chips (e.g., a server), the system total heat rejection will be significantly higher. The author believes that power dissipation requirements in the 100–300 W are within the domain of air cooling. However, it is necessary to consider design technology different from the DirHR devices that have been commonly used in the past. The IndHR is ideal for use of such advanced air-cooling technology.

More design freedom is possible for an IndHR ambient heat exchanger than is possible for the DirHR type. For example, it is possible to locate the IndHR ambient heat exchanger in the back wall of the computer case and supply the air flow via a dedicated fan. This will insure that all of the air flow from the fan passes through the ambient heat sink. Very little work has been reported for high performance ambient heat sinks. Table 2 lists four design options for the air –cooled ambient heat-exchanger. It is assumed that heat is transferred from a two-phase condensing vapor (or a liquid) to air. The means of liquid return to the boiler is listed as ''forced convection'' or ''gravity return.'' The ''forced convection'' concepts, which use one pump, are insensitive to orientation.

Option 1 assumes the two-phase (or single-phase) fluid flows in a flat plate containing parallel micro-channels, such as shown Figure 9. It would probably be necessary to use an air-cooled heat sink of a design similar to that used in the current DirHR systems. To achieve heat rejection goals of 100–300 W, one would a heat sink having quite large plan area. This would require spreading the heat over a large area. Such a design is not believed to be a practical approach to the present goal.

Option 2 would use a ''finned tube'' air-cooled heat exchanger, such as used for condensers in small residential air-conditioning. The tubes are joined by return bends to form ''serpentine'' refrigerant circuiting. The preferred tube diameter would be chosen to meet capacity requirements and may be in the range of 6–9 mm diameter. The design would also be applicable to the condenser section of a heat pipe.

Option 3 uses a design typical of that in automotive refrigerant condensers. Figure 9 illustrates the air-cooled condenser design concept. This concept uses flat tubes (16 mm air flow depth) that provide little obstruction to the air flow. It provides higher air heat transfer coefficients and lower air pressure drop than that of Option 2. If all of the tubes are in parallel, the liquid return to the boiler would be gravity dominated, and device would be orientation sensitive.

Option 4 is the same as Option 3, except that the tube-side has

Fig. 9 Air-cooled thermo-syphon and tube cross-section (16 mm tube depth) from Webb and Yamauchi [4]

serpentine circuiting. This will make the liquid return forced convection dominant and the device will be orientation insensitive. One would use flat tubes having small internal passages yielding very small hydraulic diameter.

A prototype of the Option 3 concept was built and tested by Webb and Yamauchi [4] for use with their thermo-syphon IndHR. This prototype is shown in Fig. 9 and was designed to reject 100 W. The flat tubes of the aluminum design (see cross-section photo in Figure 9) uses flat tubes of 3×16 mm cross-section and having internal membranes that permits high internal fluid pressure. The air-side fins have high performance louver fins. The use of flat tubes yields air pressure drop considerably below that of typical 9.5 mm diameter round tubes used in residential air-cooled refrigerant condensers. It is important that a dedicated fan supply air to this heat-exchanger, and that all of the air from the fan passes through the heat-exchanger. A typical fin height is approximately 8.0 mm and a small louver pitch (e.g., 1.0 mm) is used to obtain high air-side heat transfer coefficients. The heat-exchanger may be made either of aluminum or copper. Figure 9 shows aluminum and copper heat exchangers made by Webb and Yamauchi [4]. Joining of the tubes, headers, and fins is done by brazing. The preferred design will have a high air-side heat transfer coefficient and the smallest possible friction factor, which will result in high air flow rate at the fan/heat-exchanger balance point. Copper fins offer performance advantages over aluminum fins, because the high thermal conductivity copper fins may be made thinner (e.g., 25 μm) and will yield high air flow rate at the balance point.

Figure 10 compares the heat transfer and pressure drop performance of the Figure 9(a) aluminum flat tube design (21.5 fins/in, 16 mm deep) with that of a round tube heat exchanger (9.5 mm tube diameter and plain fins) designed to give the same air-side thermal performance. The equal thermal performance round tube design has 2-rows, is 44.0 mm deep, and has 15.7 fins/in). The flat tube/louver fin heat exchanger performance was predicted using the correlation of Webb et al. [18], and the round tube design was predicted by the Chang and Wang [19] correlation. Both heat exchangers have the same finned frontal are ($75\text{ mm}\times54\text{ mm}$). The air-side heat transfer performance is defined by $\eta hA/A_{fr}$, where η is the fin efficiency, and A_{fr} is the heat exchanger frontal area. For the same $\eta hA/A_{fr}$ as the flat tube design the round tube design has 100% higher air pressure drop than that of the flat tube design. Also, the air flow depth of the round tube design is 1.75 times greater.

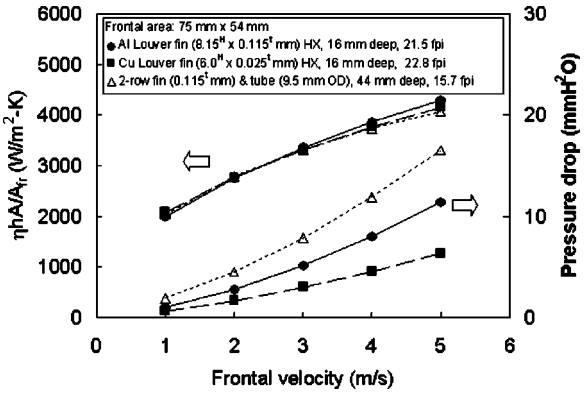

Fig. 10 Air-cooled thermo-syphon and tube cross-section (16 mm tube depth) from Webb and Yamauchi [4]

As previously stated, the Fig. 9(b) heat exchanger is made of copper construction for use with water working fluid. The thickness of copper fins is only 25 μm versus 115 μm for aluminum fins. For the same $\eta hA/A_{fr}$, Fig. 10 shows that the flat tube pressure drop of the copper heat exchanger is 36% lower than that of the aluminum flat tube heat exchanger. For 2.0 m/s air frontal velocity and $97\times70\text{ mm}^2$ frontal area, the air-side R-value of the copper heat exchanger is 0.05 K/W.

Condensing Surfaces. Vapor condenses in the tubes of the air-cooled heat exchanger. Surface tension force may be used to enhance the condensation coefficient. This technology uses small micro-grooves to remove condensate from the fin tips and is well developed within the refrigeration industry. The extruded aluminum tube used in the Fig. 9(a) heat-exchanger has 0.2 mm high microfins. If the tube is made of copper or brass, one may use a brazed, corrugated insert. Condensate will be pulled into the corners, which thins the condensate film on the flat surfaces. The author has work in progress to make a flat copper tube having microfins, which is similar to the Fig. 9(a) aluminum tube.

Design for Multiple Heat Sources. If multiple heat sources exist, as in a server, it is possible to design the remote air-cooled heat exchanger so that the vapor generated at each heat source is routed to one ambient air-cooled heat exchanger for heat rejection. The vapor from each boiler is routed to one air-cooled condenser. Fig. 11 is a schematic of the concept for two CPUs system. To ensure proper return of the working fluid to each boiler, the air-cooled heat condenser is divided into multiple zones—one for each boiler. This is done using a separator disk in the headers to create a partitioned condenser.

System Performance for the IndHr System

Consider the IndHr system designed to use water as the working fluid with jet impingement cooling at the hot surface operating at a heat flux of 200 W/cm^2 on a 1.0 cm^2 surface area. The vapor generated from this 200 W heat load is condensed in an air-cooled ambient heat exchanger of the Figure 9 design having 6800 mm^2 frontal are (82 mm square). The total thermal resistance is composed of the boiling resistance at the hot source ($R_{H,cv}$), the condensing resistance ($R_{C,\text{cond}}$ and the air-side convection resistance ($R_{C,cv}$). At $q''=200$ W/cm^2, Figure 6 indicates $R_{H,cv}=0.10$ K/W. Based on the tests of Webb and Yamauchi (2002), the $R_{C,\text{cond}}\cong0.03$ K/W, and $R_{C,cv}=0.05$ K/W. The sum of these thermal resistances is 0.18 K/W. Note that a heat spreader is not required for jet impingement. System installation would also involve a spreading resistance (R_{sp}), which may be as low as 0.015 K/W.

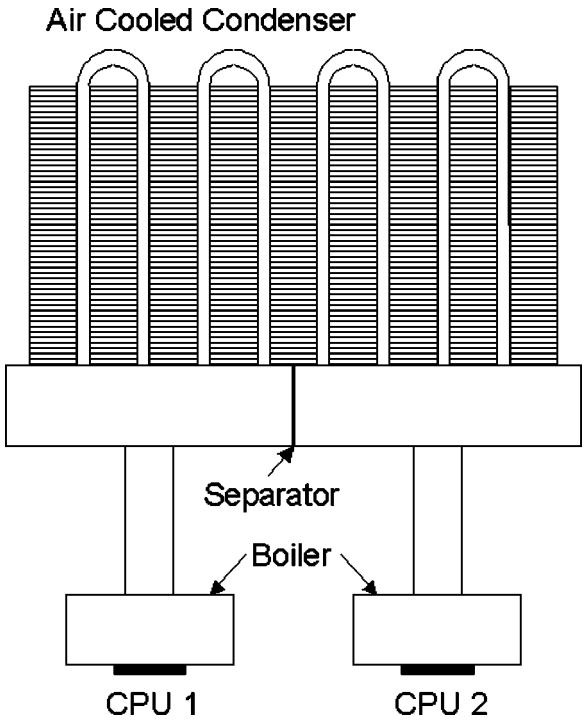

Fig. 11 A schematic of a high performance IndHR ambient heat exchanger for a two CPU system from Webb and Yamauchi [4]

Conclusions

1. Direct heat removal devices typically used for desktop computers are expected to be limited to approximately 100 W heat rejection.
2. Heat removal for more than 100 W will require new technology. An indirect heat removal concept using a working fluid will likely meet the higher heat rejection requirements. The working fluid may be either single or two-phase. All of these concepts, except a thermo-syphon will require use of a pump.
3. The need for orientation insensitivity will likely dictate the working fluid system design of choice.
4. Several boiling concepts are available for heat removal from the hot source. The highest performance and highest heat flux will be provided by pump actuated spray cooling.
5. Although considerable work has been done on jet impingement and spray cooling concepts, none of the prototype systems are orientation insensitive. It should be possible to adapt the concept to orientation insensitive forced convection circulation.
6. Hot source heat removal by two-phase flow in microchannels is yet to be established as a viable system, because of uneven heat removal at the hot source.
7. The indirect heat removal system will require a high performance ambient heat exchanger using a dedicated fan. Little work has been done to identify such concepts. Webb and Yamauchi (2002) have described a high performance indirect ambient heat exchanger that uses a two-phase working fluid.

Nomenclature

A = total heat transfer surface area, m^2
A_{fr} = frontal heat exchanger area, m^2
G = conductance, W/K
G_{avg} = conductance based on the average surface temperature, W/K
G_{max} = conductance based on the maximum surface temperature, W/K
h = heat transfer coefficient, W/m^2-K
q = heat dissipation or thermal power, W
q'' = heat flux, W/m^2-K
p = pressure, Pa
p_c = critical pressure, Pa
p_r = p/p_{cr}
R_{bo} = boiling thermal resistance, K/W
R_{co} = condensing thermal resistance, K/W
$R_{H,cv}$ = convection thermal resistance, K/W
R_{int} = interface thermal resistance, K/W
R_{sp} = spreading thermal resistance, K/W
R_{tot} = total thermal resistance, K/W
R_{transp} = thermal resistance to transport working fluid to the ambient heat sink.
$T_{air,in}$ = inlet air temperature, °C
T_{hot} = hot source surface temperature, °C
T_{sat} = saturation temperature, °C
T_w = surface temperature, °C
η = fin efficiency
Δp = pressure drop, mm-H_2O

References

[1] Saini, M., and Webb, R. L., 2002, "Heat Rejection Limits of Air Cooled Plane Fin Heat for Computer Cooling," *Proc. ITherm 2002, 8th Intersociety Conf. On Thermal and Thermomechanical Phenomena in Electronic Systems*, May 30-Jun 1, San Diego, CA, pp. 1–8.

[2] Saini, M., and Webb, R. L., 2002, "Validation of Models for Air Cooled Plane Fin Heat Sinks Used in Computer Cooling," *Proc. ITherm 2002, 8th Intersociety Conf. On Thermal and Thermomechanical Phenomena in Electronic Systems*, May 30-Jun 1, San Diego, CA, pp. 243–250.

[3] Webb, R. L., 1994. *Principles of Enhanced Heat Transfer*, John Wiley & Sons, New York.

[4] Webb, R. L., and Yamauchi, S., 2002. "Remote Heat Sink Concept for High Power Heat Rejection," in *THERMES 2002, Thermal Challenges in Next Generation Electronic Systems*; eds. Y. Joshi and S. Garimella, Millpress, Rotterdam, pp. 201–210, 2002 (Also published in IEEE Trans. Components and Materials Packaging, Vol. 25, pp. 608–614, 2002).

[5] Chien, L.-H., and Chang, C.-C., 2002. "Experimental Study of Evaporation Resistances on Porous Surfaces in Flat Heat Pipes," *Proc. ITherm 2002, 8th Intersociety Conf. On Thermal and Thermomechanical Phenomena in Electronic Systems*, May 30-Jun 1, San Diego, CA, pp. 236–242.

[6] Cooper, M. G., 1984, "Saturation Nucleate, Pool Boiling—A Simple Correlation," Int. J. Heat Mass Transfer, **23**, pp. 73–87.

[7] Pais, M. R., Chow, L. C., and Mahefkey, E. T., 1992, "Surface Roughness and its Effects on the Heat Transfer Mechanism in Spray Cooling," ASME J. Heat Transfer, **114**, pp. 211–219.

[8] Marcos, A., Chow, L. C., Du, J., Lei, S., Rini, D. P., and Lindauer, J. J., 2002, "Spray Cooling at Low System Pressure," *18th IEEE SEMI-THERM Symposium*, pp. 169–175.

[9] Xia, Chunlin, 2002, "Spray/Jet Cooling for Heat Flux High to 1 kW/cm^2," *18th IEEE SEMI-THERM Symposium*, pp. 159–163.

[10] Murthy, J. Y., Amon, C. H., Gabriel, K., Kumta, P., and Yao, S. C., 2001, "MEMS-Based Thermal Management of Electronics Using Spray Impingement," *Proc. of IPACK'01*, July 8–13, 2001, Kauai, Hawaii, Paper IPACK2001-15567.

[11] Heffington, S. N., 2001, "Vibration-Induced Droplet Atomization Heat Transfer Cell for Cooling of Microelectronic Components," *Proc. of IPACK'01*, Paper IPACK2001-15596.

[12] Koo, J. M., Jiang, L., Zhang, L., Zhou, P., Banerjee, S. S., Kenny, T. W., Santiago, J. G., and Goodson, K. E., 2000, "Modeling of Two-Phase Microchannel Heat Sinks for VLSI Chips," *Proc. of the 14th Annual IEEE International MEMS-01 conference*, Interlaken, Switzerland, pp. 422–426.

[13] Jiang, L., Koo, J. M., Zeng, S., Mikkelsen, J. C., Zhang, L., Zhou, P., Santiago, J. G., Kenny, T. W., Goodson, K. E., Maveety, J. G., and Tran, Q. A., 2001, "Two-Phase Microchannel Heat Sinks for an Electrokinetic VLSI Chip Cooling System," *Proc. of the 17th IEEE SEMI-THERM Symposium*, March 20-22, 2001, San Jose, CA, pp. 153–157.

[14] Perret, C., Boussey, J., Schaeffer, C., and Coyaud, M., 2000, "Analytic Modeling, Optimization, and Realization of Cooling Devices in Silicon Technology," IEEE Transactions on Components and Packaging Technologies, **23**(4), pp. 665–672.

[15] Hestroni, G., Mosyak, A., Segal, Z., and Zisking, G., 2002, "A Uniform Heat Sink for Cooling of Electronic Devices," Int. J. Heat Mass Transfer, **45**, pp. 3275–3286.

[16] Zhang, L., Wang, E., Koo, J., Jiang, L., Goodson, K., Santiago, J., and Kenny, T., 2002, ''Enhanced Nucleate Boiling in Microchannels,'' *Proc. 15th Int'l. Conf. on Micro Electro Mechanical Systems MEMS 2002*, Las Vegas, NV, pp 89–92.
[17] Webb, R. L., 2003, ''Effect of Manifold Design on Flow Distribution in Parallel Micro-Channels,'' Paper 35251, IPack '03, Maui, HI, July 2003.
[18] Webb, R. L., Chang, Y., and Wang, C., 1995. ''Heat Transfer and Friction Correlations for the Louver Fin Geometry,'' *1995 Vehicle Thermal Management Systems Conference Proceedings*, SAE, pp. 533–541.
[19] Chang, Y.-J., and Wang, C.-C., 1997, ''A Generalized Heat Transfer Correlation for Louver Fin Geometry,'' Int. J. Heat Mass Transfer, **40**, pp, 533–544.

Thermal Design of an Airborne Computer Chassis With Air-Cooled, Cast Pin Fin Coldwalls

Donald C. Price
Life Fellow, ASME
Principal Fellow,
Raytheon Co.,
McKinney, Texas, 75071
e-mail: dprice@raytheon.com

B. Elliott Short, Jr.
Mem., ASME
Senior Principal Mechanical Engineer,
Raytheon Co.,
McKinney, Texas, 75071
e-mail: eshort@raytheon.com

This paper documents the thermal design process required to provide effective thermal management for an airborne computer, consisting of 24 modules (two P/S modules and 22 PWB modules), which are edge-cooled to two cast, pin fin coldwalls. The computer chassis is mounted in an electronics pod mounted underneath the centerline of an aircraft. The pod consists of several electronics bays and a self-contained, air-cycle, environmental control system (ECS). The computer chassis is mounted in the forward bay, and the ECS is mounted in the rear bay of the electronics pod. The ECS is an air-cycle refrigeration system, which operates on captured ram air directed by an inlet/diffuser to an expansion turbine. This turbine produces low-pressure, chilled air, which is then directed through an air-to-liquid, load heat exchanger to produce chilled liquid. The chilled liquid is piped through small liquid lines to the forward bay of the pod, where the air-cooled computer chassis is located. The chilled liquid is converted back to chilled air in an air-to-liquid heat exchanger. The chilled air is supplied to the forward bay volume and is drawn through the computer chassis coldwalls by a fan integral to the computer chassis. The temperature of the chilled air, produced in this manner, becomes a strong function of the altitude and flight speed of the aircraft, because of the effect of these two parameters on the ram air mass flow rate and temperature at the inlet to the expansion turbine. The mass flow of the air used to cool the chassis is also a variable, because the density of the air is a function of the flight altitude and the fan has altitude-dependent operating characteristics. This fan provides the flow of air through the chassis. Emphasis is placed in the design process on the effect of the operating characteristics of the fan at altitude and the determination of the system performance curve associated with the pin fin coldwalls. This performance curve is controlled by the pressure drop characteristics of the pin fin coldwalls, which are a function of the Fanning f-factor and Colburn j-factor characteristics of the cast pin fin design. Design examples are used to demonstrate the design process.
[DOI: 10.1115/1.1839583]

Introduction

All electronic systems create an electronic power dissipation, which must be properly managed if the electronics are to operate at acceptable temperatures. For airborne electronic systems, the most direct approach to thermal management would be to use chilled air or chilled liquid provided by the aircraft. In cases of new aircraft designs, the electronic dissipations of all of the electronic systems to be used on the aircraft are contemplated during the design of the aircraft environmental control system (ECS). For electronic systems added to an existing aircraft, there often is insufficient space available in the avionics bays, and the electronic systems must be placed in a supplemental volume called an electronics pod, which is suspended from the aircraft wing or fuselage by pylons. This pod creates the space necessary to house the electronics. Most often the aircraft cannot provide any chilled air or chilled liquid to the pod. In addition, the aircraft cannot provide enough electrical power to operate the additional electronics or support a vapor-cycle ECS thermal management system within the pod. This means that the pod thermal management must be self-sustaining, and if active cooling is required, the pod must provide the method and the means. In this application, the pod has a dedicated ECS mounted within the pod volume. This ECS operates as an air-cycle refrigeration system. In addition to the electronic power dissipation within the pod, the external ambient environment may be extremely adverse. For electronic equipment, which is often air-cooled, the wide variance of flight altitudes results in variable air densities, which can become quite low at the higher altitudes. For electronic systems operating at altitudes up 13.7 km (45 kft), the low air density will result in an extremely low mass flow rate, particularly if the air flow is generated by a fan.

Manuscript received April 30, 2004; revision received August 13, 2004. Review conducted by: C. Amon.

Description of Airborne Pod

The electronics pod is shown in Fig. 1. Bay #1 of the pod is at the forward end and houses the communications antenna covered by a radome. Bay #2, which contains several electronics chassis, is shown immediately behind bay #1. A closer view of bay #2, containing several electronic boxes, is shown in Fig. 2, and includes an air-cooled computer. Bay #3 is located in the center of the pod. Bay #4 contains some additional electronics and bay #5 is devoted to the air-cycle ECS, which provides chilled air and chilled liquid through the use of ram air collected by an external ram air inlet. A diffuser is added to the inlet to reduce the speed of the air prior to entrance to the first ECS HX. Figure 3 shows the ram air inlet/diffuser mounted in this bay.

Pod Thermal Management Concept

Many of the electronic boxes selected for use in bay #2 were designed to be air-cooled with self-contained supply fans. This included the computer, which is the focus of this paper. Several of the chassis were new designs and were designed for cooling by

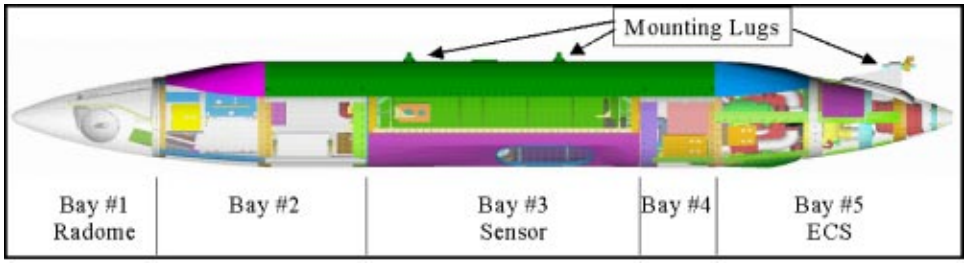

Fig. 1 Full length side view of electronics pod indicating five different bays

chilled liquid. It was therefore decided that an ECS would be designed to provide chilled air for bay #3 and the air-cooled equipment in bay #2. The only way to provide the chilled air in bay #2 would be to transport chilled liquid from bay #5 to bay #2 by small liquid lines through the strong back (structural support section of the pod) to the liquid-cooled electronics and a liquid-to-air HX in bay #2. This HX converted the chilled liquid to chilled air within bay #2. Figure 4 shows the location of the liquid-to-air HX, which produces chilled air for bay #2. A single fan pushes air from the starboard side of the pod through the HX to the port side of the pod. Once the chilled air produced by the HX is on the port side of the pod, it is pushed through the four air-cooled chassis (#7 through #10) using fans, integral to the air-cooled boxes. Bays #1 and #2 are separated by a bulkhead, which has a supply and return duct consisting of holes in the bulkhead on either side of the pod. There is also a flow barrier separating the port and starboard sides of the pod.

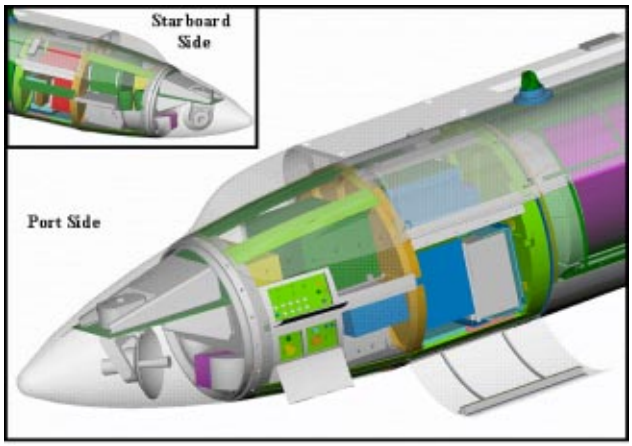

Fig. 2 Isometric view of bays #1 and #2 from both the starboard side and port side of the pod showing location of antenna and electronic boxes

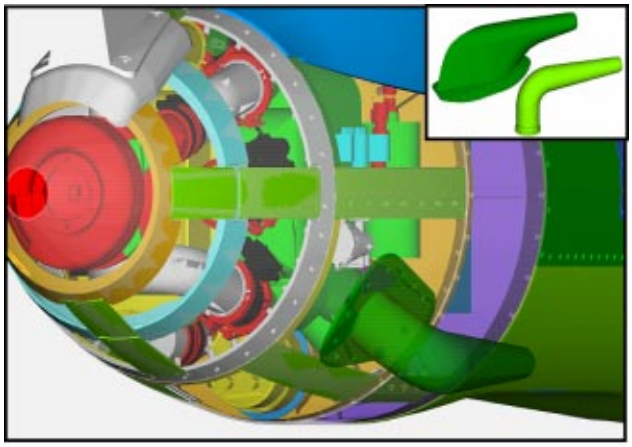

Fig. 3 Transparent skin, isometric view of bay #5 showing ECS and ram air inlet with diffuser

Thermal Design Environments

The external environmental temperatures listed in Table 1 are used to develop the external aerodynamic heating along the surface of the pod, which must be added to the power dissipation of the electronics. The external environment also controls the stagnation temperature of the air at altitude, which is the temperature of the air ingested by the ram air inlet. The temperature of the air supplied to the pod ECS HXs and expansion turbine and the HX located in bay #2 indirectly controls the temperature of the air at the inlet to each of the air-cooled electronic chassis in bay #2.

Cooling-Air Temperature Requirements

For the direct, air-cooled equipment housed in bays #1 and #2, Table 2 will be used as the guide for an acceptable local ambient environment.

Performance of ECS

The operation and performance of the ECS for the electronic pod has been previously determined. Internal ambient air temperatures were developed for a variety of flight altitudes, flight speeds, ambient environments, and ECS operating modes. It was demonstrated that the cooling-air supply temperatures to the electronic boxes were as good as, or lower than, the temperatures given in Table 2. The designs of the electronic boxes, which normally involve the design of the coldwalls, the prediction of the PWB edge temperatures, and the thermal design of the PWBs were not included. The focus of this paper is the thermal design of one of the electronic boxes (a computer subsequently described in later sections of this paper), where it will be assumed that the cooling-air supply temperatures were equal to the values shown in Table 2.

Table 1 External ambient air temperatures as a function of attitude

Altitude		External Ambient
(km)	(kft)	(°C)
1.0	3.28	40.0
1.5	5.0	34.8
2.0	6.5	30.0
3.0	10.0	23.2
4.0	13.1	17.0
4.6	15.0	13.8
6.0	19.7	6.0
6.1	20.0	5.5
8.0	26.2	−5.0
9.1	30.0	−9.6
10.0	32.8	−13.0

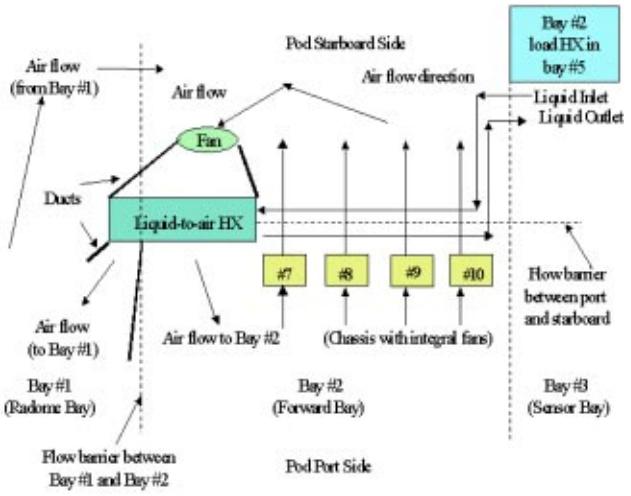

Fig. 4 Schematic showing thermal management concept for air-cooled electronics located in bays #1 and #2

Fig. 5 Photograph of air-cooled computer chassis

Description of Computer Chassis

The thermal design of a computer located in bay #2 of the electronics pod is discussed in this section. The computer chassis slides into the pod through a door on the port side of the pod as shown in Fig. 2. A photo of the computer chassis is shown in Fig. 5. An exploded view of that chassis is shown in Fig. 6. In the exploded view, slots for the 24 modules (two P/S modules and 22 PWB modules) may be seen. These electronic boards are edge-cooled to two cast, pin fin coldwalls on the top and bottom of the chassis. The boards are inserted into their respective slots and plugged into a back plane, which is also visible.

The inlet plenum and integral fan are shown on the right end of the chassis, and the cooling air is drawn through the two coldwalls from left (front) to right (back), thereby passing from the port side (cold side) to the starboard side (hot side) of the pod. The PWBs may be inserted and removed from the port side of the pod where the access door is located. This removal and reinsertion may be accomplished without removing the chassis from the pod. This means that the PWB card edges are aligned with the flow direction of the air in the coldwalls. The coldwalls are integral to the chassis and are constructed of cast aluminum. A casting was specified for cost-reduction considerations in a production environment. The alternative for the design was a vacuum-braze construction using coldwalls of the plate-fin type. For the cast aluminum coldwalls, pin fins were considered to be the most suitable.

Table 2 Maximum allowable ambient air temperatures for airborne, air-cooled, electronics

Altitude km (kft)	Maximum allowable cooling air supply temperature °C(°F)
0.00(0.0)	55.0(131.0)
0.06(0.2)	55.0(131.0)
0.61(2.0)	55.0(131.0)
1.52(5.0)	54.0(129.2)
3.05(10.0)	53.0(127.4)
4.57(15.0)	51.0(123.8)
6.09(20.0)	48.0(118.4)
9.15(30.0)	41.0(105.8)
9.75(32.0)	38.0(100.4)
10.67(35.0)	36.0(96.8)
11.28(37.0)	35.0(95.0)
12.19(40.0)	31.0(87.8)
12.80(42.0)	29.0(84.2)
13.72(45.0)	26.0(78.8)

The configuration of the pin fins is described in Fig. 7. In order to design the pin fin coldwalls for this chassis, experimental correlations were developed for the Fanning *f*-factor and Colburn *j*-factor, as a function of Reynolds number, for a range of pin heights and streamwise and transverse pin spacing using air as the fluid. The development of these correlations is described in detail

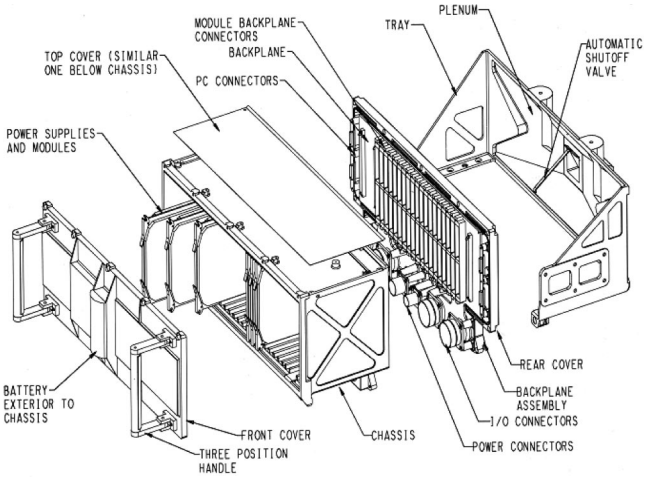

Fig. 6 Exploded view of air-cooled computer chassis showing inlet air plenum, PWB card guides, and pin fin coldwalls

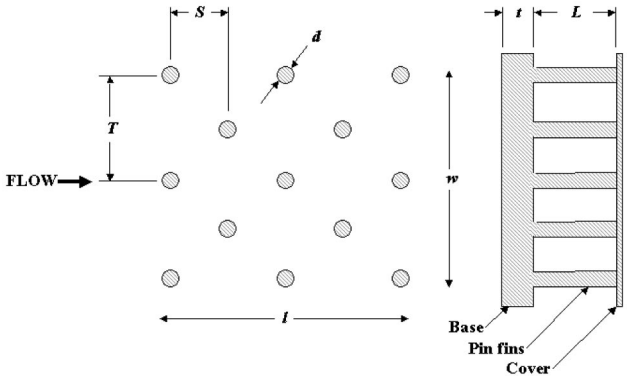

Fig. 7 Drawing of pin fin coldwall configuration indicating pin height and pin spacings

Table 3 PWB power dissipations for PWBs mounted in card guide slots in computer chassis

PWB card slot no.	Power dissipation (W)
1	9.3
2a	31.4
2b	30.0
3	13.7
4	5.7
5	5.7
6	19.1
7	14.2
8	14.5
9	13.3
10	13.3
11	13.3
12	5.7
13	5.7
14	13.3
15	13.3
16	13.3
17	24.4
18	14.5
19	14.5
20	14.2
21	19.1
22	5.7
23a	32.5
23b	31.3
24	9.3
Total	400.3

in Short, Raad, and Price [1,2]. The range of validity for these correlations is given as:

S/d	T/d	L/d	$\mathrm{Re}_{d,\min}$	$\mathrm{Re}_{d,\max}$
1.8–3.2	2.0–6.4	1.9–7.2	175–1100	1600–4500

For $\mathrm{Re}_d<1000$, the resulting correlations for friction factor and Colburn j-factor are given by Eqs. (1) and (2):

$$f=35.1(S/d)^{-1.3}(T/d)^{-0.78}(L/d)^{-0.55}\,\mathrm{Re}_d^{-0.65}, \quad \{\sigma=\pm 0.076\} \tag{1}$$

$$j=0.760(S/d)^{0.16}(T/d)^{0.20}(L/d)^{-0.11}\,\mathrm{Re}_d^{-0.67}, \quad \{\sigma=\pm 0.101\} \tag{2}$$

For $\mathrm{Re}_d>1000$, the correlations are given by Eqs. (3) and (4):

$$f=0.221(S/d)^{-1.4}(T/d)^{-0.54}(L/d)^{0.056}\,\mathrm{Re}_d^{-0.080}, \quad \{\sigma=\pm 0.090\} \tag{3}$$

$$j=0.419(S/d)^{0.077}(T/d)^{0.20}(L/d)^{-0.30}\,\mathrm{Re}_d^{-0.55}, \quad \{\sigma=\pm 0.105\} \tag{4}$$

Several detailed design examples of pin fin coldwalls, using these correlations, are documented in detail in Short, Price, and Raad [3,4].

Design of Computer Chassis

A thermal model of the chassis, which included all of the dimensions, materials, and conduction paths, was created using a numerical modeler. This modeler has capabilities similar to commercial numerical modelers, such as MSC.Patran [5] and Maya TMG Thermal [6]. The power dissipations of the 24 modules in the computer chassis were determined and are shown in Table 3.

The computer chassis required an integral fan to draw the air through the coldwalls from the port side to the starboard side of the pod. With the knowledge that a pin fin coldwall design would result in large pressure drops at the flow rates that would be required, several fans were evaluated for suitable pressure drop characteristics as a function of mass flow rate. A fan, Airscrew Howden Model No. 75-MA1-574 [7], was selected for this application, because of a high-static-pressure/high-volume-flow characteristic curve. The fan diameter was 95 mm (3.75 in.) and the length of the fan was 120.0 mm (4.72 in.). The fan requires 200 V, 3Φ, and 400 Hz electrical power.

The fan characteristic performance curve, provided by the manufacturer, was plotted as the static pressure (p) developed by the fan as a function of mass flow rate. The mass flow rates were measured at conditions of 101.35 kPa (14.7 psia) and 15°C (59°F), where the density of air is 0.001237 g/cm^3 (0.0772 lbm/ft^3). These are STP conditions, so that the ratio of the actual air density to the air density at STP (σ) is equal to unity. The volume flow rate (Q) at STP conditions was calculated using

$$Q=\dot{m}/\rho \tag{5}$$

This calculated volume flow rate was than used to calculate the mass flow rate at the sea level pressure of 101.35 kPa (14.7 psia) at the temperature of 55°C (131°F), the sea level operating temperature for this military environment, by using the relationship

$$\dot{m}_{\mathrm{SL}}=[\sigma_{\mathrm{SL}}][\rho_0 Q_{\mathrm{const}}] \tag{6}$$

For the sea level condition, the density of air is 0.001089 g/cm^3 (0.068 lbm/ft^3) and the value of the density ratio σ is 0.881.

Since the volume flow rate is constant over altitude for this fan, the mass flow rates at other altitudes and temperatures may be calculated using appropriate values of σ for that altitude and temperature as given in Table 4.

In order to create a new fan performance curve for the higher altitude conditions, the static pressure developed by the fan at STP conditions must also be multiplied by the appropriate value of σ for the higher altitudes, according to procedures outlined in Gebert [8]. The performance curves for this fan, created for six altitudes from sea level operating conditions to operating conditions at 13.72 km (45 kft), are shown in Fig. 8. The fan performance curves show that the static pressure developed by the fan is a maximum at a mass flow rate of zero. As the load on the fan (mass flow rate) increases, the static pressure developed by the fan decreases to zero at the maximum flow rate.

Using the pin fin correlations, a system response curve was developed through analysis of the two pin fin coldwall candidate designs. In each case, the flow length of the cold wall is 152.4 mm (6.0 in.) and the flow width is 406.4 mm (16.0 in.). The two candidate coldwall designs in this study are designated as core #1 and core #2. The dimensions of these candidate cores are shown in Table 5, which gives the pin length L, the pin diameter d, the streamwise spacing S, and the transverse spacing T, of the pins. core #1 and core #2 were selected as alternative designs with pin densities within normal casting limits.

The system response curves for these two coldwall designs were plotted as the static pressure drop through the system ($\sigma\Delta p$) as a function of the mass flow rate flowing through the system, and then the system response curves were superimposed on the altitude performance curves for the fan that had been selected.

This graphical representation is shown in Fig. 8. In order to obtain the actual mass flow rates developed by the fan-system combination, the operating point of the fan is determined at the intersection of the fan curve and the system curve. As may be seen in Fig. 8, this operating point varies with altitude indicating that the mass flow rate developed in the coldwall decreases with increasing altitude. The operating points for the fan are shown as a function of altitude in Table 4 for each of the coldwall cores.

As may be seen in Fig. 8, the system response curve for core #1 crosses the fan curves in the flat portion of the fan curve, where large changes in mass flow rate occur with small changes in static pressure, indicating that the fan efficiency in this region is not good. A better operating system would result if core #2 were used, since the intersection of the fan curve and the system curve is on the downslope of the fan curve. For this reason core #2 was selected for further evaluation.

Table 4 Fan operating points as a function of altitude for candidate coldwall cores #1 and #2

Coldwall core #1						
Altitude			Mass flow rate		$\sigma\Delta p$	
(km)	(kft)	σ ρ/ρ_0	(kg/s)	(lbm/min)	(kP a)	(inches H_2O)
0	0.0	0.881	0.0438	5.80	3.139	12.61
1.52	5.0	0.734	0.0431	5.70	3.035	12.19
4.57	15.0	0.503	0.0363	4.80	2.182	8.77
7.62	25.0	0.389	0.0280	3.70	1.321	5.31
10.67	35.0	0.279	0.0204	2.70	0.721	2.90
13.72	45.0	0.140	0.0136	1.80	0.423	1.70

Coldwall core #2						
Altitude			Mass flow rate		$\sigma\Delta p$	
(km)	(kft)	σ ρ/ρ_0	(kg/s)	(lbm/min)	(kPa)	(in. H_2O)
0	0.0	0.881	0.0885	11.70	1.790	7.19
1.52	5.0	0.734	0.0779	10.30	1.401	5.63
4.57	15.0	0.503	0.0567	7.50	0.762	3.06
7.62	25.0	0.389	0.0404	5.35	0.398	1.60
10.67	35.0	0.279	0.0272	3.60	0.185	0.75
13.72	45.0	0.140	0.0174	2.30	0.090	0.36

Each of the coldwall designs was evaluated using the pin fin performance correlations for the range of altitudes of interest. The inlet air temperature to the chassis at various altitudes, as indicated in Table 2, and the mass flow rates, developed from the fan operating points at the operating altitudes, as shown in Table 4, were used to calculate the exit air temperature from the coldwall and the heat transfer coefficients between the coldwall surface and the air.

Table 5 Dimensions of coldwall cores selected for analysis

Coldwall dimensions	Coldwall core designation	
	Core #1	Core #2
Coldwall flow width w (mm)	406.4	406.4
Coldwall flow length l (mm)	152.4	152.4
Longitudinal pin spacing S (mm)	3.810	6.350
Transverse pin spacing T (mm)	4.318	7.620
Pin length L (mm)	6.350	9.525
Pin diameter d (mm)	1.778	2.286
S/d ratio	2.14	2.78
T/d ratio	2.43	3.33
L/d ratio	3.57	4.17

A numerical thermal model was developed for the chassis, which is shown in Fig. 9. Notation on Fig. 9 indicates the location of the 24 electronic modules. These 24 modules consist of 22 PWBs and two P/S modules, which take two slots each (slots 2a, 2b, 23a, and 23b). For this numerical model, the PWB power dissipations from Table 3 were imposed as heat sources and the inlet air temperature and the heat transfer coefficients from the pin fin evaluations were used as boundary conditions to the model.

Evaluation of the chassis thermal model provides different results for each flight altitude (each mass flow rate). The results, shown in the temperature contour plot of Fig. 10, represent the chassis temperatures for a sea level flight altitude. There would be a similar model evaluation for each of the other five flight altitudes.

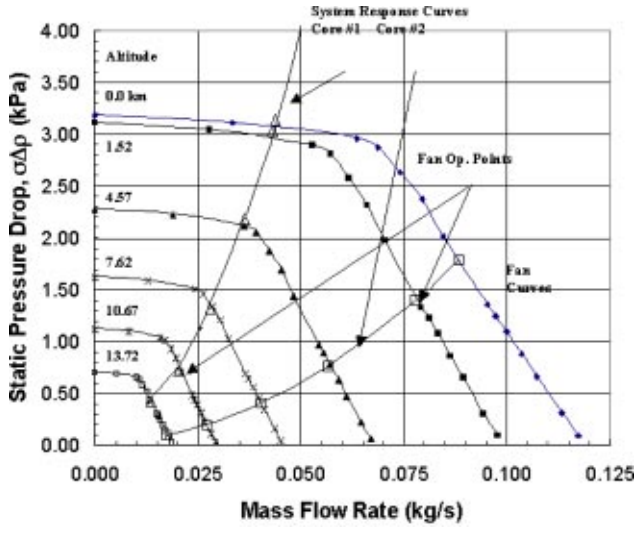

Fig. 8 System response curves for two candidate pin fin coldwall cores superimposed on fan performance curves showing fan operating points as a function of altitude

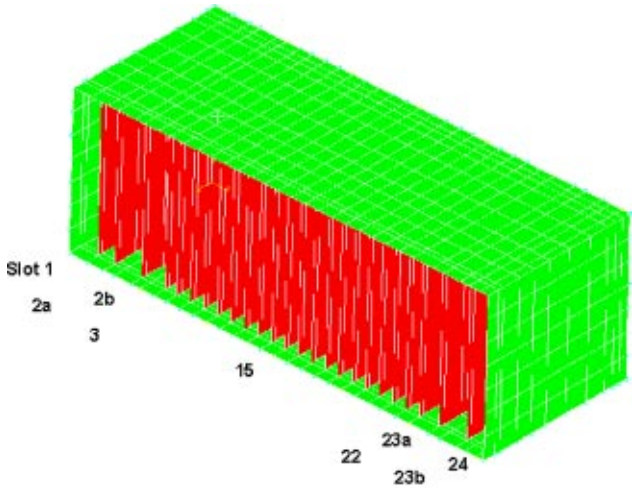

Fig. 9 Finite-element model of computer chassis including top and bottom coldwalls and PWB card slots

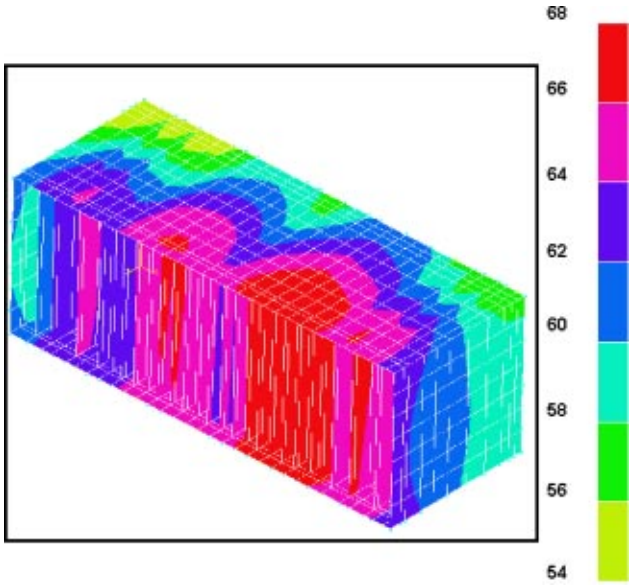

Fig. 10 Color contour plot of finite-element model of computer chassis using pin fin core #2 evaluated at sea level flight altitude

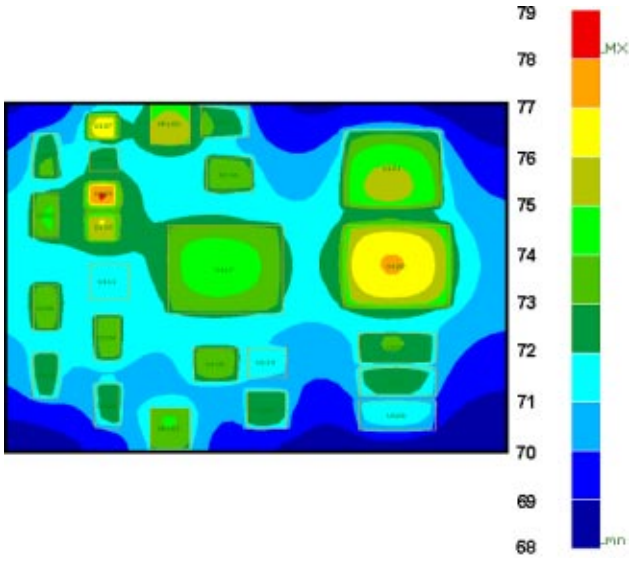

Fig. 11 Color contour plot of model of front side of typical PWB in computer chassis using pin fin coldwall #2 evaluated at sea level flight altitude

Using the evaluation results from the numerical model, the temperature distributions along the card edge for each PWB were established. As would be expected, these temperatures were not constant, as they would be in a chassis where the flow of air was perpendicular to the PWBs. Since the flow of air is parallel to the PWB card edge, a variable coldwall slot temperature resulted. Since the temperature of the PWB card edge will track these chassis slot temperatures, if the contact resistance at the interface is considered, the temperature boundary condition for the thermal model of the PWBs is a variable along the length of the board edge.

Thermal Model of a Typical PWB

In order to predict the junction temperatures of all of the electronic components on each of the 24 modules in the chassis, a numerical model was developed for each module. This numerical model was developed and evaluated using a modeler/solver with attributes similar to the commercial modeler, Harvard Thermal TAS [9]. The acronym TAS stands for Thermal Analysis Software and has a special module for the modeling and evaluation of PWBs.

The modules have dimensions of 152.4 mm (6.0 inches) by 152.4 mm (6.0 in.) and are 5.588 mm (0.220 in.) thick, being comprised of two FR-4 boards with a thickness of 1.524 mm (0.060 in.) bonded to a metal core with a thickness of 2.54 mm (0.100 in.). The metal core had a thermal conductivity of 0.1986 W/mm °C (5.0 W/in °C), which is greater than aluminum with a thermal conductivity of 0.1575 W/mm °C (4.0 W/in °C). The P/S modules consisted of two such boards mounted side by side and connected by flex cable.

With reference to Table 3, it may be seen that the P/S modules have large power dissipations on the order of 31 to 32 W, as would be expected. Of the other boards, most have power dissipations on the order of 13 to 14 W, except for the PWBs in slots #6, #17, and #21. All of these boards were modeled and evaluated and the component junction temperatures reported for reliability analysis. One PWB, located at slot #16, which experiences the highest chassis temperatures and thereby the highest PWB edge temperatures, has been selected as a typical PWB. This PWB has a power dissipation of 13.3 W. The thermal model of the PWB was evaluated for a chassis with coldwalls constructed with core #2 at a flight altitude of sea level. These results are shown in Fig. 11 for the front side of the board and Fig. 12 shows the results for the back side of the board. The minimum temperature of the board is 68°C and the maximum is about 79°C.

From this point, a bookkeeping procedure is used to predict the junction temperatures of each of the components on the boards. The procedure may be described as follows:

1. Using the board temperature shown in Fig. 11 and Fig. 12 for the sea level case, calculate the average temperature of the board under each component.
2. Develop junction-to-case thermal resistance information for each component, which is either supplied by the component vendor or developed by custom thermal models of components for which the vendor information is either not available or is suspected of being inaccurate.

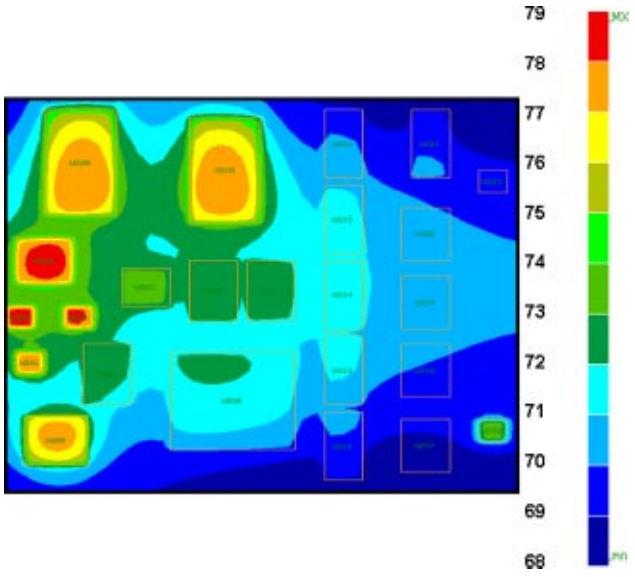

Fig. 12 Color contour plot of model of back side of typical PWB in computer chassis using pin fin coldwall #2 evaluated at sea level flight altitude

3. Compact thermal models, which have been developed for direct-air-cooled PWBs are of little value for conduction-cooled components on edge-cooled PWBs but could be employed if modified to eliminate the air-cooled resistances. The main advantage of compact thermal models lies in the reduction of the number of nodes and resistances necessary to characterize the components on the PWB for a thermal model.

4. Calculate the case-to-board thermal resistance with knowledge of the method used to mount the component to the board.

5. With these values, the junction temperature of each component may be calculated.

The next step is to consider the effect of altitude on the thermal performance of the electronic components. This requires consideration of the platform and the method of providing the cooling air. For an aircraft where the cooling air is provided by an aircraft ECS, the temperature and flow rate of the cooling air is matched to the power dissipation of the chassis in a way that insures that the exhaust temperature from the chassis is held constant. For this situation, experience will demonstrate that it is not necessary to evaluate the board temperatures at higher altitudes.

For electronic chassis that provide cooling air using a fan dedicated to the chassis, this is not the case. Since the fan provides a flow that is variable with altitude and the inlet temperature of the cooling air to the chassis is also variable, the PWB thermal models must be evaluated at the maximum flight altitude of 13.72 km (45 kft) to determine the effect of altitude on the junction temperatures. If the board temperatures are found to vary significantly, the bookkeeping calculations must be repeated.

These component junction temperatures are then supplied to reliability engineers who evaluate the effect of temperature on the PWB and system reliability.

Summary

In summary, the electronics pod hardware has been described, as well as the pod thermal management concept, which includes the generation of both air- and liquid-cooling loops through the application of a self-contained air-cycle ECS for the pod. The thermal environments are discussed, and the cooling-air temperature requirements are developed. The ECS performance is described with reference to earlier publications.

The computer chassis, the subject of this paper, is described in detail, with respect to the hardware and the thermal design of the pin fin coldwalls. The fan selection is discussed and the fan operating points are selected. The mass flow rates of air generated by the fan as a function of altitude are calculated and the pin fin coldwalls are evaluated for coldwall temperatures and airside heat transfer coefficients calculated. These parameters are used to develop a thermal model of the chassis and results for a contour plot of a typical PWB are presented.

Acknowledgments

The authors wish to acknowledge the collaborative efforts of John Schroeder, Raytheon Space and Airborne Systems in El Segundo, California, the engineering staff of Raytheon Technical Services Company in Indianapolis, Indiana, and the engineering staff of Honeywell in Yoevil, England. Without the efforts of this team of engineers, the thermal design of this electronics pod would not have been successful.

Nomenclature

Abbreviations:

ECS = environmental control system
HX = heat exchanger
Hz = frequency (cycles per second)
IR = infrared
P/S = power supply
PWB = printed wiring board
STP = standard temperature and pressure

Variables:

d = pin base diameter, [m]
f = Fanning friction factor based on d, where $f=d\Delta p/2\rho V_{\max}^2 l$
j = Colburn j-factor=St $\mathrm{Pr}^{2/3}$
l = coldwall flow length, [m]
$\dot{m}$ = mass flow rate, [kg/s]
p = static pressure, [kPa]
Δp = pressure drop, [kPa]
t = wall thickness (of heated wall), [m]
w = coldwall width, [m]
L = pin length, [m]
Q = air volume flow rate, [m^3/s]
Re_d = Reynolds number based on d, Eq. (11)
$\mathrm{Re}_{\mathrm{trn}}$ = transition Reynolds number
S = streamwise pin row-to-row distance, [m]
T = transverse pin center-to-center distance, [m]
V = voltage

Pin fin configuration parameters:

L/d = dimensionless pin length
S/d = streamwise direction dimensionless pin spacing
T/d = transverse direction dimensionless pin spacing

Notation:

c-c = center-to-center distance

Greek symbols:

ρ = air density, [kg/m^3]
σ = standard deviation
σ = ρ/ρ_0, ratio of the density of air at altitude to the density of air at STP
Φ = electrical phase

References

[1] Short, Jr., B. E., Raad, P. E., and Price, D. C., 2002, ''Performance of Pin Fin Cast Aluminum Coldwalls: Part 1—Friction Factor Correlations,'' J. Thermophys. Heat Transfer, **16**, No. 3, pp. 389–396.
[2] Short, Jr., B. E., Raad, P. E., and Price, D. C., 2002, ''Performance of Pin Fin Cast Aluminum Coldwalls: Part 2—Friction Factor Correlations,'' J. Thermophys. Heat Transfer, **16**, No. 3, pp. 397–403.
[3] Short, B. E., Jr., Price, D. C., and Raad, P. E., 2003, ''Design of Cast Pin Fin Coldwalls for Air-Cooled Electronic Systems,'' Paper No. InterPACK2003-35004, *Proceedings of InterPACK'03*, ASME *International Electronic Packaging Technical Conference and Exhibition*, Maui, Hawaii, 6–11 July, 2003.
[4] Short, Jr., B. E., Price, D. C., and Raad, P. E., 2004, ''Design of Cast Pin Fin Coldwalls for Air-Cooled Electronic Systems,'' ASME J. Electron. Packag., **126**, pp. 67–73.
[5] MSC.Patran, MSC Software Corporation, 2 MacArthur Place, Santa Ana, CA, 92707, USA, 714-540-8900, http://mscsoftware.com
[6] Maya TMG-Thermal, Maya Heat Transfer Technologies Ltd., 4999 St. Catherine St. West, Suite 400, Montreal, Quebec, Canada, H3Z 1T3, 514-369-5706, http://www.mayahtt.com
[7] Howden Group Limited, Old Govan Road, Renfrew, Renfrewshire, PA4 8XJ, United Kingdom, Telephone: +44 141 885 7300, http://www.howden.com
[8] Gebert, G. G., ''How Altitude Affects Forced Air Cooling Requirements of Electronic Equipment,'' AMETEK Rotron, Mil-Aero Products, 9 Hasbrouck Lane, Woodstock, NY 12498, http://rotron.com/
[9] Harvard Thermal TAS Version 7.0 (Thermal Analysis System) and Harvard Thermal TASPCB (Printed Circuit Board Modeler/Solver), Harvard Thermal Inc., Harvard, MA, 20002, http://www.harvardthermal.com/

A Multi-Grid Based Multi-Scale Thermal Analysis Approach for Combined Mixed Convection, Conduction, and Radiation Due to Discrete Heating

Lan Tang
e-mail: lantang@andrew.cmu.edu
Carnegie Mellon University,
Pittsburgh, PA 15213

Yogendra K. Joshi
e-mail: Yogendra.Joshi@me.GaTech.edu
The George W. Woodruff School of Mechanical Engineering,
Georgia Institute of Technology,
Atlanta, GA 30332

A multi-grid embedded multi-scale approach is presented for conjugate heat transfer analysis of systems with a wide range of length scales of interest. The multi-scale analysis involves a sequential two-step "zoom-in" approach to resolve both the large length scales associated with the system enclosure, and the smaller length scales associated with fine spatial structures of discrete heat sources contained within. With this approach, computation time is shortened significantly, compared to conventional single-step computational fluid dynamics/computational heat transfer (CFD/CHT) modeling, with a very fine mesh. Performance of the two-step multi-scale approach is further enhanced by integrating the multi-grid technique in the CFD/CHT solver. Implementation of the enhanced approach is demonstrated for thermal analysis of an array of substrate mounted discrete heat sources cooled by mixed and forced convection, with accompanying experiments performed for validation and for the assessment of the importance of mixed convection. It is found that the multi-grid embedded multi-scale thermal analysis reduces simulation run time by 90% compared to the multi-grid integrated single step solution. The computed temperatures were in good agreement with measurements, with maximum deviation of 8%.
[DOI: 10.1115/1.1852495]

1 Introduction

Multi-mode or conjugate heat transfer problems are commonly encountered in the design of electronic systems, in which air is used as the coolant to carry away heat dissipated from active digital, analog, radio frequency, and optical devices, while conducting their mission of computation, signal transmission, signal processing, routing, switching, amplification, storage, etc. Such problems were solved for many years in an uncoupled manner, with solution of the heat conduction equations in multiple media, such as the printed wiring board (PWB) and attached heat generating components, obtained with specified convective heat transfer coefficient boundary conditions. Commonly used heat transfer coefficient correlations for PWBs include those by Aung [1], Miyatake and Fujii [2], Bar-Cohen and Rosehsnow [3,4], Wirtz and Stutzman [5], Wills [6], Landis and Elenbaas [7], and Moffat and Ortega [8]. Many of these correlations explore the influence of parameters such as geometry, temperature differential, and flow conditions, on heat transfer.

Since flow fields near the surfaces of the electronic and optical devices attached to PWB substrate in many modern applications are quite different from the conditions that these correlations were based on, there is a significant need to develop computational procedures that can easily bring in system enclosure level influences on these computations. System level CFD/CHT simulations have been conducted by solving the governing equations of continuity, momentum, and energy equations simultaneously, on a discretized mesh. The multiplicity of length scales, ranging from the heat generating silicon chip with dimensions in the 10^{-3} m scale, to system enclosure boundaries with dimension in the 1 m scale range, make the simultaneous resolution of all geometrical details expensive, and often unrealistic. Complex geometries and large variations in thermo-physical properties of packaging materials add to the numerical computation convergence difficulties.

Several strategies have been introduced to handle these issues. Among the most popular ones, faster solvers have been implemented in several commercial packages. Among this category are the approaches of block correction (Braaten and Patankar [9], Kelkar [10]), and multi-grid (Brandt [11], Vanka [12], Sathyamurthy and Patankar [13], Heindel et al. [14]). Another strategy is creation of simplified, reduced, or compact models of components and heat sinks (Linton and Agonafer [15], Ewes [16], Rosten et al. [17], Adams et al. [18], Tang and Joshi [19], etc.), with small scale details lumped together and transparent to the simulation. Use of isotropic or anisotropic representations of multilayer PWB, containing electrically and thermally conducting copper traces and signal/thermal vias (Azar and Graebner [20], Nelson [21]), is usually necessary for such simulations. The net effect of these measures is a much less dense mesh and reduced computational time, at the expense of coarser resolution of component thermal details. If thermal details at component level are of interest, a follow-on modeling at the smaller length scales associated with the PWB and the components is sometimes conducted. Very little research has been conducted to address how to interface the enclosure level modeling results with component/board level modeling in a systematic manner.

The multi-scale analysis approach demonstrated in this study synthesizes system and component level analyses, taking full advantage of the merits of both. First, system level analysis is performed, with simplified component, heat sink, and PWB models. At this level of simulation, a multi-grid method is implemented to improve the computational efficiency. Next, local thermal information, in forms of convective heat transfer coefficients, heat fluxes, solid surface temperatures, are extracted. Lastly, component level analysis is carried out with thermal information obtained in the second step as boundary conditions. The advantages of this multi-scale analysis approach are shortened computation

Manuscript received April 19, 2004; revision received September 12, 2004. Review conducted by: C. Amon.

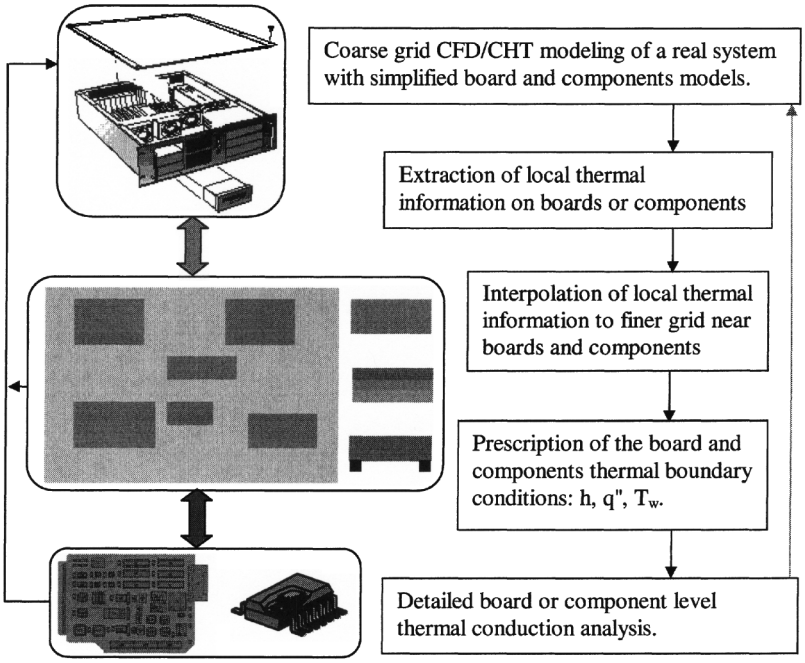

Fig. 1 Multi-scale thermal modeling: bridging the gap between system and board/component modeling

cycles, resulting from simplified component models and the multi-grid solution method, and improved accuracy of the solution at the detailed component level through the use of real boundary conditions. The methodology requires input from experiments to assess the importance of mixed convection effects that influences effective PWB thermal conductivity evaluation in multi-mode simulations.

2 Outline of Multi-Scale Thermal Analysis Approach

The overall approach utilized is shown in Fig. 1. First, a global model or system level model is developed on a coarse grid, with components (chip packages), PWBs, heat sinks, and other significant parts simulated as simplified blocks of effective thermal properties representing lumped values. Thus, flow blockage effects around large discrete heat sources and heat sinks are retained. In order to avoid excessive computational time and memory space consumption, fine structural details, such as copper traces on PWB, individual component to PWB interconnects, and individual fins of heat sinks, are not explicitly modeled at this stage.

Thermal information from the global model, including board and component surface temperatures, local heat transfer coefficients, reference temperatures, and heat fluxes, are extracted. The extracted thermal information is then interpolated on a finer grid and mapped to PWB and component level analyses as boundary conditions. In the local analysis, since only conduction in solid regions is tackled, a much finer grid can be deployed to resolve fine structures. With suitably derived boundary conditions from the global system level modeling and appropriate structure details, chip or junction temperature and temperature gradients are predicted with high resolution and accuracy.

As seen in Fig. 1, results from the component level local analysis may be fed back to the system level global analysis for a more refined analysis. This may be needed when mismatch between the results from experimental measurements and thermal analysis is observed, or physically unreasonable temperature predictions at system or component level are encountered. Under these circumstances, possible remedies are:

1. Refinement of grid for system level modeling
2. Use of alternative simplified package, PWB, and heat sink models
3. Trying different boundary condition inputs for component level modeling
4. Refinement of thermo-physical properties used

3 Experimental Measurements

The experimental facility (Fig. 2) consists of a low speed wind tunnel, an epoxy fiberglass (FR-4) test board carrying nine plastic-quad-flat-pack (PQFP) thermal test packages, and a computer controlled data acquisition system. The low speed wind tunnel had a transparent test section 30.5 cm wide, 30.5 cm high, and 90.2 cm long. The test board was placed on a layer of styrofoam with thickness of 2.54 cm on the bottom wall of wind tunnel test section. Figure 3 depicts the relevant geometric details.

3.1 Experiment Setup Details. Each of the nine electronic components was of outer dimensions of 15.7 mm by 15.7 mm by 2.1 mm and was attached to the test board with 88 peripheral leads (22 along each side). Each of these components contained a heat generating silicon chip with dimensions 7.8 mm by 7.8 mm by 0.5 mm thick, mounted on a copper alloy lead frame (Fig. 4). The silicon chip was encapsulated within epoxy and contained a diffused resistive heater to dissipate power. A string of five serially connected diodes located at the center was used to measure the temperature sensitive forward voltage. The diodes were calibrated by placing the un-powered test board in an air circulated environ-

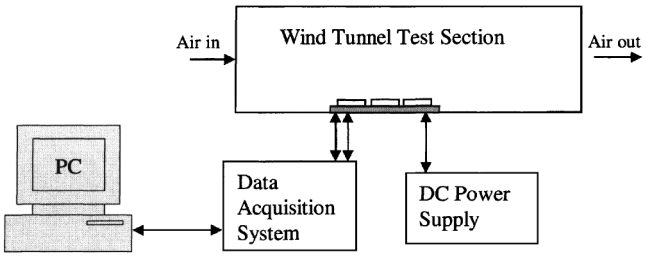

Fig. 2 Wind tunnel and the rest of the test facility

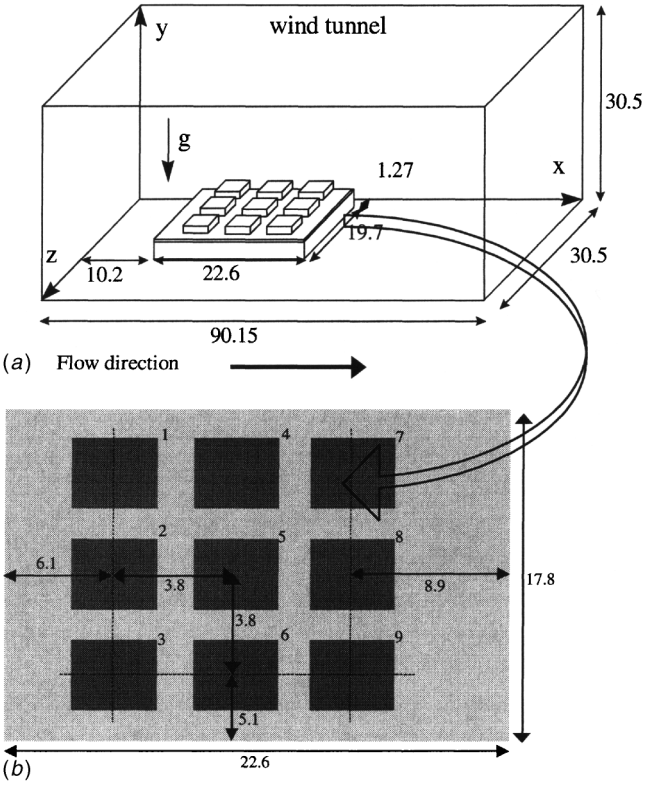

Fig. 3 (a) Computational domain for system level modeling (b) Test board with 9 PQFPs surface mounted and the block on lead model (all dimensions in cm)

mental chamber in the range of 30°C to 100°C. A quadratic curve fit was employed to compute chip (junction) temperature as a function of the diode voltage. The cumulative uncertainty in the silicon chip temperature determination was ±1.1% of the specified value.

Copper traces for electric current inputs and signal outputs radiate from the foot print of each component and terminated at one edge of the PWB. The electric current and signal wires were routed out through a brush-sealed slot in the side wall of the test section. These copper wires were next connected to an external data acquisition system and D.C. power supply (0–10 A, 0–20 V), respectively. Data collection was automated by running LabVIEW software on a personal computer.

Copper-Constantan (type-T) Thermocouples of 0.13 mm diameter were used. At the inlet of the test section, a thermocouple was suspended in the center *x-y* plane about 23 mm from the bottom to measure the inlet air temperature. At the center of the top surface of each component, a thermocouple was attached to measure case temperature. The thermocouple measurement uncertainty is estimated to be ±0.7°C at 100°C (0.8% of temperature difference between sensed and reference temperatures).

The wind tunnel is an Eiffel type and designed to operate up to 5.0 m/s. Due to space restriction, details on wind tunnel calibration and free stream velocity measurements are omitted, referring to Tang [22]. The uncertainty in the measurement of free stream velocity was estimated to be less than ±3% at 0.1 m/s and ±1% at 5.0 m/s.

In each test run, power was applied to the components, and the system was allowed to achieve steady state before data collection. Experiments were performed for imposed velocities of 0.253 m/s, 0.431 m/s, 0.514 m/s, 0.608 m/s, 0.697 m/s, 0.794 m/s, 0.992 m/s, 1.485 m/s, 2.004 m/s, 2.528 m/s, 3.051 m/s, and 3.571 m/s. The low and high end velocities were chosen to help develop flow regime maps to assess the importance of mixed convection. It is noted that no measurements of the velocities in the mixed convection flow were carried out, which would require a special calibration procedure. To maintain the junction temperature below 130°C, low to moderate power dissipation rates (Q=0.3, 0.5, 0.7, 1.0, 1.5 W) were used.

3.2 Experimental Flow Regime Map for Determination of PWB Effective Thermal Conductivity. The conductive heat spreading within the PWB was strongly affected by the externally imposed flow regime. A smaller heat spreading region around the package was involved for forced convection dominant flow, while more extensive spreading was found for mixed convection dominant flow. For fully heated surfaces, the average Nusselt number (Sparrow et al. [23]) is traditionally used with the ''5% deviation rule'' as the parameter to delineate the flow regimes of natural,

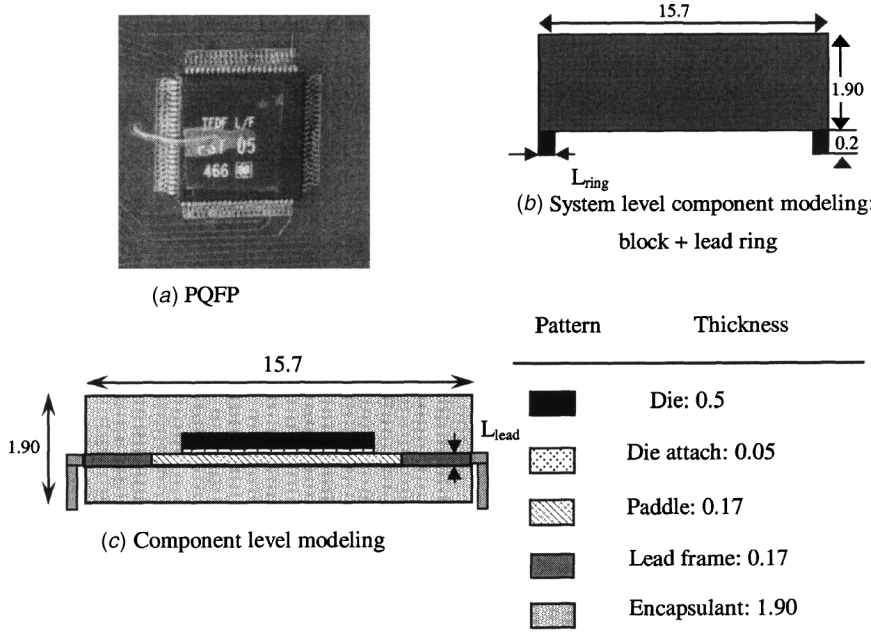

Fig. 4 PQFP and the detailed dimension for component level modeling (All dimensions in mm)

Table 1 Values of C_1, and C_2 for individual components

	C_1	C_2
P. #1	0.185	1.6
P. #2	0.2	1.6
P. #3	0.19	1.6
P. #4	0.19	1.45
P. #5	0.215	1.45
P. #6	0.205	1.45
P. #7	0.185	1.3
P. #8	0.22	1.3
P. #9	0.215	1.3

mixed and forced convection. For conjugate heat transfer problems involving discrete heat sources, the area over which the average Nusselt number applies is unclear. As an alternative, a ''modified 5% deviation rule'' (Choi and Kim [24]), using maximum component temperature as the reference parameter, has been used to delineate the mixed and forced flow regimes. Using this methodology, Sikka et al. [25] developed a flow regime map for a single PQFP mounted on a test PWB.

In the present study, flow regime maps for individual packages on the test board were developed using measured junction temperatures and the parameter Gr^*/Re^2. When $Gr^*/Re^2 \to \infty$, the flow is dominated by natural convection. In contrast, when $Gr^*/Re^2 \to 0$, the flow is dominated by forced convection. For both cases, asymptotic expressions were obtained from present experimental data. A correlation for non-dimensional temperatures applicable across these two extreme cases was obtained by following the asymptotic-matching procedure of Churchill and Usagi [26]:

$$\frac{\theta}{\mathrm{Re}^{-0.3}} = C_1 \left\{ 1 + \left[C_2 \left(\frac{\mathrm{Gr}^*}{\mathrm{Re}^2} \right)^{-0.16} \right]^{-n} \right\}^{-1/n} \tag{1}$$

The first term on the right of Eq. (1) is the asymptote for forced convection, and the second term is the asymptote for natural convection, and $n=6$ is determined to be the blending exponent. Values of C_1 and C_2 were tabulated in Table 1 for each package.

By using 5% departure from the forced asymptote as the delineation criterion, the transition from forced to mixed convection regime occurs at $Gr^*/Re^2=2$ for the multi-component PWB investigated in this study. This is a later transition compared to a PWB with single component (Sikka et al. [25]), where such transition occurred at $Gr^*/Re^2=0.2$.

4 Multi-Grid System Level Modeling

The computational domain employed for the illustration of the multi-scale approach is shown in Fig. 3. It includes the rectangular horizontal test section of a wind tunnel in which the populated test PWB is placed. A layer of styrofoam was used to separate the test board from the bottom wall of the wind tunnel. Modeling of the PWB was complicated due to its anisotropic thermal properties and nonuniformly distributed surface copper metallization, which was denser near the footprint of each package and sparser further away. Two different metallization area coverage values of 6% and 18%, representing the low and high bounds, were selected. Based on these values, and an average thermal conductivity of 0.43 W/mK for the PWB without metallization, effective thermal conductivity values of 1.0 and 2.0 W/mK were used for the system level (global) simulation. A block-on-lead-ring model (Fig. 4(b)) is adopted to represent components at the global level, while a more detailed model (Fig. 4(c)) is employed in local modeling. All the properties used are provided in Table 2. As indicated earlier, two effective thermal conductivity values for the PWB are employed, depending on the flow regime encountered, due to the nonuniformity of metallization and the difference in resulting board heat spreading effects.

Table 2 Thermophysical properties used for system and component level modeling

Material	Thermal conductivity (W/m-K)	Emissivity
Air	0.0263	—
PWB	1.0 (mixed convection)/ 2.0 (forced convection)	0.9
Compact block	30	0.9
Compact lead ring	18.7	—
Encapsulant	0.3	0.9
Die	148	—
Die attach	1.0	—
Paddle	260	—
Lead frame mixture	138.5	—

4.1 System Level Solution. Assuming three-dimensional, steady state, laminar conjugate heat transfer with no viscous dissipation and the Boussinesq approximation, the governing equations for system level modeling written in primitive variable form are:

continuity

$$\nabla \cdot \vec{V} = 0 \tag{2}$$

x-momentum

$$\rho \nabla \cdot (u\vec{V}) = -\frac{\partial P}{\partial x} + \mu \nabla^2 u \tag{3}$$

y-momentum

$$\rho \nabla \cdot (v\vec{V}) = -\frac{\partial P}{\partial y} + \mu \nabla^2 v + \rho g \beta (T - T_{ref}) \tag{4}$$

z-momentum

$$\rho \nabla \cdot (w\vec{V}) = -\frac{\partial P}{\partial z} + \mu \nabla^2 w \tag{5}$$

energy

for air

$$(\rho C_p) \nabla \cdot (T\vec{V}) = k \nabla^2 T \tag{6}$$

for solid

$$(\rho C_p)_s \nabla \cdot (T\vec{V}) = k_s \nabla^2 T + q''' \tag{7}$$

where q''' accounts for internal heat generation in the components $\dot{q}$, and/or surface radiation energy exchange q^r applicable to test package and PWB top surfaces in contact with air

$$q''' = \frac{q^r \Delta A}{\Delta V} + \dot{q} \quad \text{with} \quad q^r = \sigma \varepsilon (T_w^4 - T_{\mathrm{ref}}^4)$$

Boundary conditions at the channel walls:

Velocity $u=v=w=0$, at all the interior walls of the channel

$$u = U_{\mathrm{ref}} \quad \text{at } x=0; \quad \frac{\partial u}{\partial x} = \frac{\partial v}{\partial x} = \frac{\partial w}{\partial x} = 0 \quad \text{at } x=L$$

Temperature

$$x = L: \frac{\partial T}{\partial x} = 0;$$

All the other walls: $T = T_{\mathrm{ref}}$

The governing equations (2)–(7) are discretized using the control volume formulation of Patankar [27] on a staggered grid displacement. Tang and Joshi [28] have found SIMPLER to be less efficient than Symmetrically Coupled Gauss-Seidel (SCGS) method in handling pressure and velocity coupling, the performance of single-level grid deteriorating as the number of grid

Table 3 Grid refinement study results for heater-on-board geometry: with nominally uniform power input per component $Q_i = 1.0$ W, $U_{ref} = 0.99$ m/s

Grid Size	CPU Hrs	Qtop/Qtotal (%)			Average Heat Transfer Coefficient (w/m^{2}K)		
		#3	#5	#7	#3	#5	#7
56×26×52	13.21	31.6	32.4	33.5	26.2	24.2	26.0
56×30×54	21.27	31.6	32.2	33.2	26.1	23.9	25.2
60×32×56	23.21	31.9	32.3	33.6	26.0	23.2	24.9

points increases. The SCGS solution method was successfully employed [28] to simulate conjugate natural and forced convection from protruding heaters.

In the present study, a multi-grid SCGS (MG-SCGS) method is employed as the system level solver in-lieu of single grid SIMPLER. With this method, velocity and pressure are updated simultaneously on two-level grids. The equations are solved in the form of blocks consisting of momentum and continuity equations. With this modification, considerable saving in CPU time is realized. The use of the multi-grid method is necessitated by the large differences in thermophysical properties and grid aspect ratios within the solution domain, typical of electronics cooling applications.

The MG-SCGS procedure used in the present study involves modeling at two grid levels in the computational domain. The solution to the finer grid equations provides the solution to the original discretized governing equations. On the other hand, correction equations on coarser grids provide the corrections that are applied to the preceding finer grid equations. The solution was assumed converged when the maximum temperature and velocity (T, u, v, and w) changes during successive iterations were less than 1.0×10^{-5}. Also, at the time of convergence, overall mass and energy balances were maintained within 2% of the total mass flow into the system and total power dissipation by all the packages. The numerical modeling covered power dissipations from 0.5 W to 2.0 W per component, and inlet air velocity from 0.5 m/s to 1.5 m/s, including both mixed and forced convection regimes. Additional details are available in [22].

A partial grid refinement study was conducted by evaluating progressively finer nonuniform grid sizes of 56×26×52, 56×30×54, and 60×32×56. As the purpose of the global model was to predict flow and temperature fields and heat flow patterns, heat transfer coefficients and heat flow rates on selected surfaces were used to determine adequacy of the grid refinement. Selected results are shown in Table 3. A maximum difference of 1.0% in heat dissipation rate and 4.5% in average heat transfer coefficient was observed for the top walls of the selected components, when the mesh was refined from the coarsest to the finest. A 56×26×52 grid was determined sufficient for the system level modeling, as a compromise between computational effort and accuracy.

With MG-SCGS, in addition to the fine grid of 56×26×52 for generating the solution to the discretized governing equations, a coarser grid of 30×15×28 was used to generate correction factors to the solutions on the fine grids. As the results on fine grid gets close to a converged solution, the grid correction factors approaches zero. The interfaces of material discontinuity were represented as control volume surfaces. Solutions were considered as converged after the three criteria mentioned were met.

Figure 5 shows the sample system level temperature contours and velocity vectors through the center of the components on the second column for both mixed (Fig. 5(a) with $Gr/Re^2=3.3$) and forced (Fig. 5(b) with $Gr/Re^2=0.63$) convection. For both cases, recirculating cells were observed between the leading edge of the PWB and the first package. These cells compressed the isothermal temperature contour lines for the components in the leading row. In Fig. 5(a)-temperature contour, the rising plume indicated the significance of buoyancy effect. With larger inlet velocities (Fig. 5(b)), velocity and thermal boundary layers developed above the components. In general, with the selected level of grids and physical detail of components, important flow and temperature distribution features were captured.

4.2 Data Extraction and Interpolation. Results from global or system level computations must be mapped to components

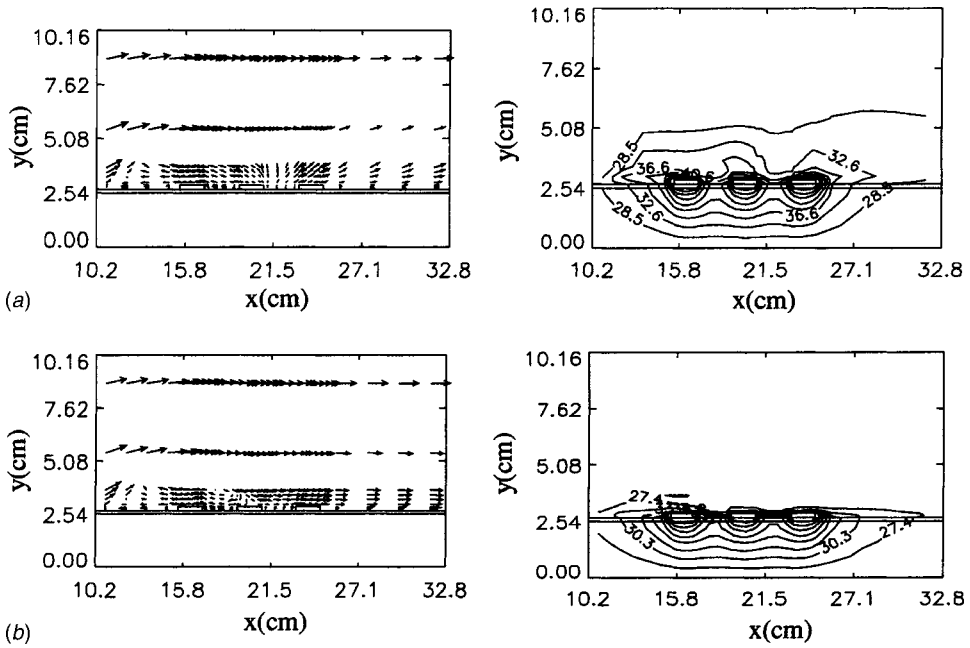

Fig. 5 Velocity vectors and temperature contours for $Q=0.5$ W, at $z=10.03$ cm: (a) $U=0.43$ m/s, $(\sqrt{u^2+v^2})_{max}=0.526$ m/s, $T_{max}=64.8°C$; and (b) $U=0.99$ m/s, $(\sqrt{u^2+v^2})_{max}=1.21$ m/s, $T_{max}=53.7°C$

as boundary conditions to integrate modeling at the two levels. Since different mesh resolution and component physical details were used for system and component levels, interpolation of thermal information from coarser grid ($5\times3\times5$ per component) system level to finer grid ($21\times17\times21$ per component) component level was next performed. In this study, surface convection boundary conditions (B.C.) were extracted from global simulations, and applied to the top surface of the component under study. The reference temperature used to calculate heat transfer coefficient was the inlet air temperature. A prescribed heat flux B.C. was extracted and applied at the other five surfaces of the components.

A block-on-lead-ring compact or reduced model of the component was utilized for global modeling, which required special consideration in mapping of extracted thermal information from the bottom surface of a component. With this model, the leads correctly conducted a large fraction of heat from the chip to the PWB, but through the bottom surface, instead of the side surfaces which ought to play a significant role due to the connecting leads. Thus, heat flux for the peripheral area of the bottom surface with lead ring attached was the net effect of the side and bottom surface. The following measures were followed to decompose this sum into the portions ascribed to the bottom and side surfaces:

i. When constructing the compact model at the system level, the width of the lead ring (L_{ring} in Fig. 4(b)) was set equal to the thickness of the lead (L_{lead} in Fig. 4(c)). As a result, the heat conduction area at the system level was kept the same as in the detailed model: $A_{lead}=A_{ring}$
ii. When extracting heat flux on the bottom wall of the component, the heat flux along the nodal points in the peripheral region of the bottom surface was decomposed into two parts, the lead part and the encapsulant epoxy part: $q''_{\text{ring}}=q''_{\text{lead}}+q''_{\text{epoxy}}$

The lead part was mapped to the lead frame on the side surfaces of the package, while the epoxy part remained with the bottom surface. Since leads are ubiquitous in the attachment of components to PWBs, the preceding formulation can be applied rather broadly.

5 Component Level Modeling

The boundary condition inputs obtained from the global analysis were convection coefficients for the top surface and heat fluxes for the other surfaces of the components. Convergence criteria on energy balance and relative change of temperature were 2% and 1.0×10^{-5}, respectively. The refined component model and dimensions of the PQFP are shown in Fig. 4(c). A silicon chip was placed at the center of the epoxy encapsulant. The chip (die) was bonded to the copper alloy paddle lead frame using a die attach epoxy. The 88 leads peripherally extending from the package could be modeled explicitly. However, this was not necessary since the amount of heat conducted from the root of leads was known from the previous section. As an alternative, heat flux q''_{leads} mapped from the lead ring was applied to the area of side surfaces as boundary condition.

5.1 Heat Flow Paths. Figure 6 shows heat flow paths for individual components. Three inlet velocities $U_{\text{ref}}=0.61$, 0.99, and 1.49 m/s were considered, corresponding to $\text{Gr}^*/\text{Re}^2=3.36$, 1.26, and 0.562 respectively. The first value corresponded to mixed convection, while the other two fell in the forced convection regime. For mixed convection regime, conduction heat spreading within the PWB is stronger, extending to regions with a less dense metallization, resulting in a lower effective bulk thermal conductivity of the PWB of 1.0 W/mK. For forced convection regime, heat spreading in the board is localized to regions close to the footprint of the component with denser metallization, leading to a higher effective bulk thermal conductivity of the PWB of 2.0 W/mK.

In Fig. 6(a), for mixed convection with $\text{Gr}^*/\text{Re}^2=3.36$, 12~14% of the total power was dissipated by radiation from the top surfaces of the packages. In the forced convection regime ($\text{Gr}^*/\text{Re}^2=1.26$,0.562), component temperatures decrease, and radiation becomes less significant, being 8–10% of the total heat input.

In Fig. 6(b), convection was stronger for the lowest velocity 0.61 m/s (mixed convection), resulting in 5% higher $Q_{\text{conv}}/Q_{\text{total}}$ compared to forced convection. This could be due to stronger heat spreading effect, or lower effective thermal conductivity of the PWB, and higher thermal resistance into the PWB, seen by each component. As the velocity increases to 0.99 m/s, the PWB heat spreading effect becomes weaker, while the effective thermal conductivity of the PWB increases, or thermal resistance between board and component gets smaller. Hence, more heat is conducted to the board, and less is dissipated directly from the top surfaces of components. When air velocity increases further to 1.49 m/s, the board heat spreading effect remains the same. With an increase in the average heat transfer coefficient, a slightly stronger convection effect was observed.

Figure 6(c) summarizes radiation and convection contributions from top surfaces of each component. Since radiation and convection effects of components are stronger in mixed convection regime, the fraction of total heat dissipated from the top surface of each component is higher than that for the two forced convection cases.

5.2 Variation of Chip or Junction Temperature With Gr^*/Re^2. Sikka et al. [25] carried out measurements for a single 4 mm thick, 28 mm×28 mm, 208-lead PQFP surface mounted on a PWB. The PWB was placed in the test section of a rotatable wind tunnel. Component 5 on the current PWB was selected to study the difference between cooling of single component and multiple components on board. Component 5 is at the center of the other 8 components, and is under the thermal wake of component 1, 2, and 3.

Compared to cooling of single component on a board, cooling of multiple components, in general, is deteriorated due to thermal interference between neighboring components. For multiple components, convection cooling of components in the rear rows suffers from heating of the air by components in the front row(s), conduction cooling through board also suffers from the thermal blanketing effect of the neighboring components.

As shown in Fig. 7, the above mentioned thermal interference effect is not significant in forced convection and high velocity end of the mixed convection regime. As the buoyancy force gets stronger, the thermal interference becomes significant and cooling of components in the rear rows gets worse, leading to higher temperature for component 5 compared to the single component case. Between $\text{Gr}^*/\text{Re}^2=0.1$ to 10, temperature variation with Gr^*/Re^2 for single component is more vigorous, as shown in Fig. 7. The slope for the data points of the single component studied by Sikka et al. [25] is steeper compared with that for the data points for the current study. This explains the earlier transition from forced to mixed convection for single component on board mentioned in section 4.1.

5.3 Junction Temperature Prediction for Different Power Levels. Figure 8 compares the junction temperatures predicted from the multi-scale analysis approach with experimental measurements. In Fig. 8(a), results for three power levels were presented, corresponding to mixed convection. The difference of chip junction-to-ambient temperature between experimental measurements and multi-scale analysis is within 7.7% for all the packages. With inlet velocity of 0.99 m/s, comparison was made for three power levels $Q_i=0.5$, 1.0, and 1.5 W per component, corresponding to $\text{Gr}^*/\text{Re}^2=0.63$, 1.26, and 1.89 respectively. For all three cases, the differences are within 6.4%, as shown in Fig. 8(b).

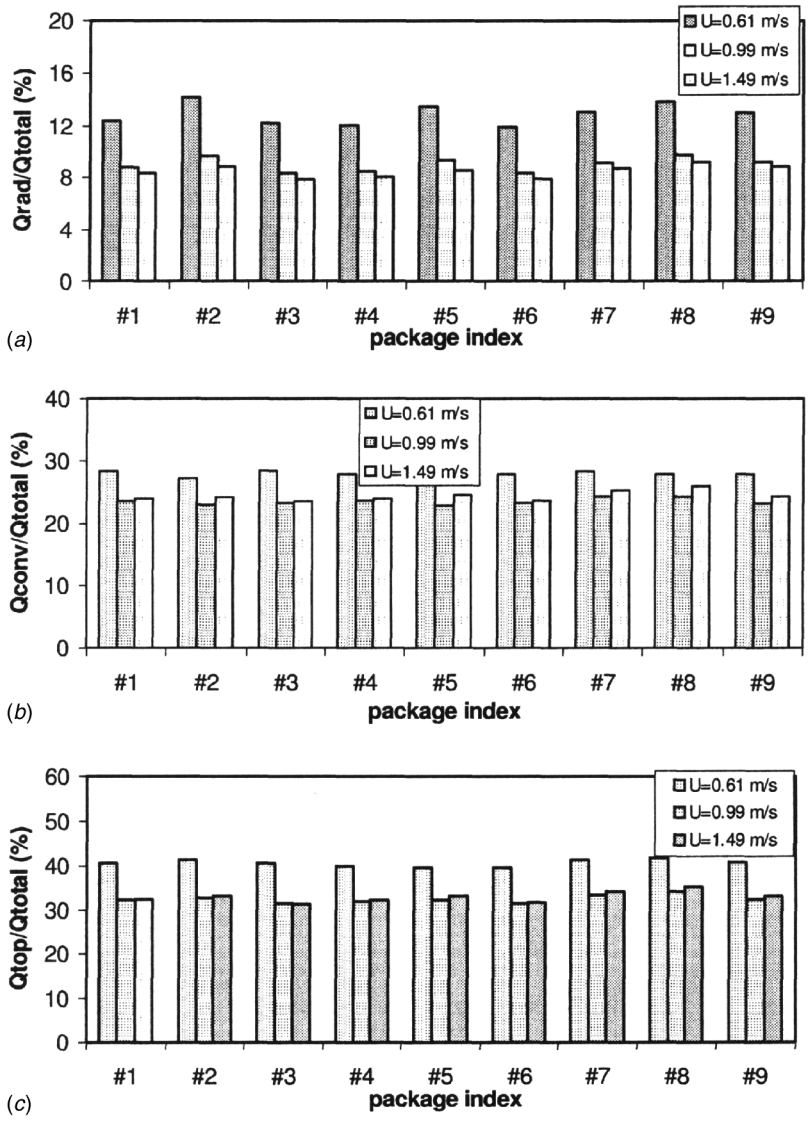

Fig. 6 Energy budget for nominal Q_i=1.0 W: (a) radiation effect, (b) convection effect, and (c) percentage of heat dissipation from package top surface

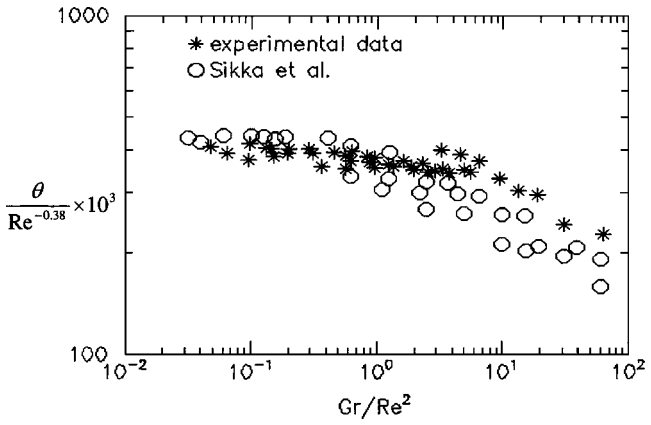

Fig. 7 Comparison of junction temperature between measured and published in literature for component 5

When inlet velocity increases to 1.49 m/s, with nominal power $Q_i = 1.0$, and 1.5 W, which corresponds to strong forced convection ($Gr^*/Re^2 = 0.562$, and 0.842), the differences are within 6.9%, as shown in Fig. 8(c).

5.4 Computational Time Savings. Evaluations of CPU time consumption were performed for nominally uniform power input per component of $Q_i = 1.0$ W and air velocity $U_{ref} = 0.99$ m/s. Both MG-SCGS and SIMPLER were employed as the solution methods at the system level. For the same configuration, with identical power inputs and air velocity mentioned above, when the 56×26×52 grid was used, SIMPLER took 153.5 CPU hours to get converged results, in contrast to only 11.76 CPU hours required by MG-SCGS. Similar results were obtained for other meshes and power and velocity inputs. Larger saving in CPU time may be expected when the mesh is further refined.

6 Conclusion

A multi-scale thermal analysis approach using a multi-grid numerical technique was presented for a combined conduction, mixed convection and radiation heat transfer application, charac-

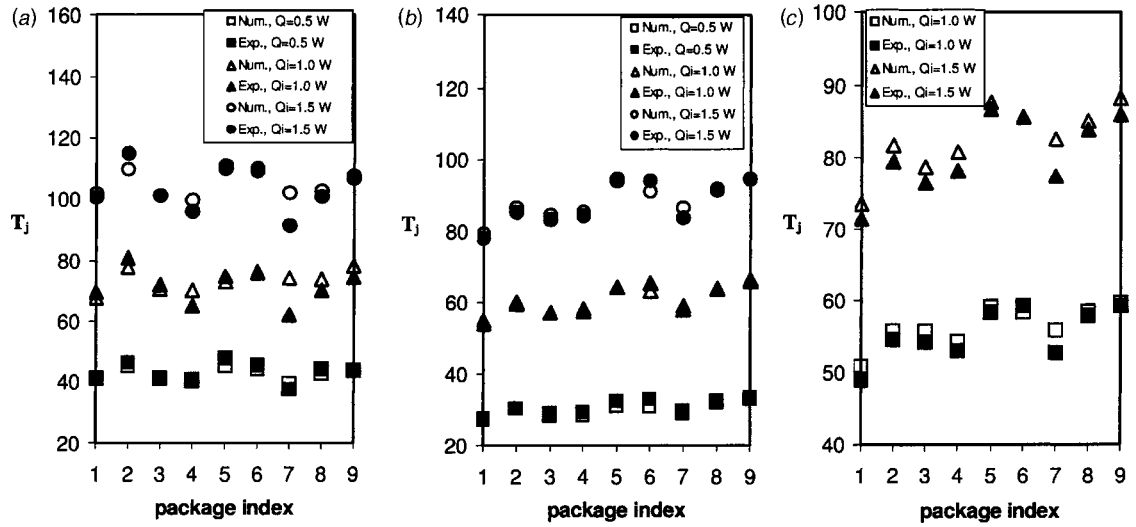

Fig. 8 Comparison of junction temperature from multi-scale thermal analysis with experimental measurement: (a) $U_{ref}=0.61$ (0.43 for $Q_i=0.5$ W) m/s; (b) $U_{ref}=0.99$ m/s; and (c) $U_{ref}=1.49$ m/s

teristic of electronics cooling. With this approach, good agreement between temperature predictions and experimental measurements, along with significant computational time saving were achieved. While the computing capabilities are continually increasing, the approach reported in this work will provide added benefits over such increased computational power. The following features were crucial to the success of the approach:

1. Adequate selection of reduced component and substrate model, and evaluation of effective component and board thermal conductivity.
2. Application of computationally efficient system level solver through integration of multi-grid with an efficient pressure and velocity coupling strategy, such as SCGS.
3. Integration of coarse system level analysis with detailed component level analysis, implemented as a systematic approach.

While the approach was demonstrated with good agreement for PQFP with peripheral leads, it can be easily extended to area array interconnect components, such as Ball Grid Array (BGA) packages, of which conduction through bottom solder balls and convection from top surface both played important heat transfer roles. The PWB in the current study was regarded as isotropic due to insignificant in-plane thermal conductivity variation, compared to cross-plan values. If conduction in the two directions are significantly different, the PWB should be modeled orthotropically.

Acknowledgment

The authors are thankful to Mr. Dave Blackburn (NIST) and Dan Rodkey (Delco) for providing the thermal test components.

Nomenclatures

C_1, C_2 = coefficient for natural and forced convection asymptotes
Cp = specific heat at constant pressure (J/Kg-K)
g = gravitational acceleration (m/s^2)
Gr* = Modified Grashof number $\mathrm{Gr}^*=g\beta QH^2/k\nu^2$
H = component length (m)
k = thermal conductivity (W/m-K)
n = blending exponent
p = pressure (N/m^2)
q^r = radiation heat flux (W/m^2)
q''' = volumetric heat generation rate (W/m^3)
Q = total power input (W)
Re = Reynolds number $\mathrm{Re}=U_{ref}H/\nu$
T = temperature (°C)
u, v, w = velocity components (m/s)
$\vec{V}$ = velocity vector
x, y, z = coordinate directions

Greek letters

α = thermal diffusivity (m^2/s)
β = coefficient of volumetric thermal expansion (1/K)
θ = non-dimensional temperature $\theta=\kappa_{air}H(T_j-T_{ref})/Q_i$
ε = Emissivity
μ = dynamic viscosity (Kg/s-m)
ν = kinematic viscosity (m^2/s)
σ = Stefan-Boltzmann constant, 5.67×10^{-8} W/m^2-K^4

Subscripts

air = properties for air
Ave = average value
c = case temperature
i = component index i=1~9
j = junction temperature
ref = temperature or velocity at the inlet of the channel
s = solid
w = wall

Special

ΔA = radiation surface area of the control volume block, m^2.
ΔV = volume of the control volume block, m^3.

References

[1] Aung, W., 1972, "Fully Developed Laminar Free Convection Between Vertical Plates Heated Asymetrically," Int. J. Heat Mass Transfer, **15**, pp. 1577–1580.
[2] Miyatake, O., and Fujii, T., 1974, "Natural Convection Heat Transfer Between Vertical Parallel Plates With Unequal Heat Fluxes," Heat Transfer-Jpn. Res., **3**(3), pp. 29–33.
[3] Bar Cohen, A., and Rohsenow, W. M., 1980, "Thermally Optimal Spacing of Vertical Natural Convection Cooled Parallel Plates," ASME J. Heat Transfer, **102**, pp. 221–227.
[4] Bar Cohen, A., and Rohsenow, W. M., 1984, "Thermal Spacing of Vertical, Natural Convection Cooled Parallel Plates," ASME J. Heat Transfer, **106**, pp. 116–123.
[5] Wirtz, R. A., and Stutzman, R. J., 1982, "Experiments on Free Convection Between Vertical Plates With Symmetric Heating," ASME J. Heat Transfer, **104**, pp. 501–507.
[6] Wills, M., 1983, "Thermal Analysis of Air-Cooled PCBs," Electronic Products, May, pp. 11–18.

[7] Landis, F., and Elenbaas, W., 1986, ''Heat Dissipation of Parallel Plates by Free Convection,'' ASME HTD-57, pp. 11–22.
[8] Moffat, R. J., and Ortega, A., 1988, ''Direct Air Cooling of Electronic Components,'' *Advances in Thermal Modeling of Electronic Components and Systems*, A Bar-Cohen and A. D. Kraus, eds., Hemisphere Publishing Corp., New York, NY.
[9] Braaten, M. E., and Patankar, S. V., 1989, ''A Block-Correction Subdomain Solution Procedure for Recirculating Flow Calculations,'' Numer. Heat Transfer, Part B, **15**, pp. 1–20.
[10] Kelkar, K. M., 1990, ''Iterative Method for the Numerical Prediction of Heat Transfer in Problems Involving Large Differences in Thermal Conductivities,'' Numer. Heat Transfer, Part B, **17**, pp. 113–128.
[11] Brandt, A., 1977, ''Multi-Level Adaptive Solutions to Boundary Valued Problems,'' Math. Comput., **31**, pp. 333–390.
[12] Vanka, S. P., 1986, ''Block-Implicit Multi-Grid Solution of Navier-Stokes Equations in Primitive Variables,'' J. Comput. Phys., **65**, pp. 38–158.
[13] Sathyamurthy, P. S., and Patankar, S. V., 1994, ''Block-Correction-Based Multi-Grid Method for Fluid Flow Problems,'' Numer. Heat Transfer, Part B, **25**, pp. 375–394.
[14] Heindel, T. J., Ramadhyani, S., and Incropera, F. P., 1996, ''Conjugate Natural Convection From an Array of Protruding Heat Sources,'' Numer. Heat Transfer, Part A, **29**, pp. 1–18.
[15] Linton, R. L., and Agonafer, D., 1994, ''Coarse and Detailed CFD Modeling of a Finned Heat Sink,'' *Proceedings of I-THERM IV*, InterSociety Conference on Thermal Phenomena in Electronic Systems, pp. 156–161.
[16] Ewes, I., 1995, ''Modeling of IC-Packages Based on Thermal Characteristics,'' EUROTHERM Seminar No. 45, Thermal Management of Electronic Systems, Delft Conference Proceedings, Leuven, Belgium.
[17] Rosten, H. I., Parry, J. D., Addison, J. S., Viswanath, R., Davies, M., and Fitzgerald, E., 1995, ''Development, Validation, and Application of a Thermal Model of a Plastic Quad Flat Pack,'' *Proceedings of 45th Electronic Components and Technology Conference*, pp. 1140–1151.
[18] Adams, V. H., Blackburn D. L., Joshi, Y., and Berning, D. W., 1997, ''Issues in Validating Package Compact Thermal Models for Natural Convection Cooled Electronic Systems,'' *Proceedings of the 13th IEEE SEMI-THERM Symposium*, Austin, TX.
[19] Tang, L., and Joshi, Y., 1999, ''Integrated Thermal Analysis of Natural Convection Air Cooled Electronic Enclosure,'' ASME J. Electron. Packag., **121**, pp. 108–115.
[20] Azar, K., and Graebner, J. E., 1997, ''Thermal Conductivity Measurements in Printed Wiring Boards,'' ASME J. Heat Transfer, **119**(3), pp. 401–405.
[21] Nelson, R., 2001, ''Wiring Statistics and Printed Wiring Board Thermal Conductivity,'' *Proceedings of SEMI-THERHM 2001*, p. 252.
[22] Tang, L., 1998, ''A Multi-Scale Conjugate Thermal Analysis Methodology for Convectively Cooled Electronic Enclosures,'' Ph.D. dissertation, Univ. of Maryland, College Park, MD.
[23] Sparrow, E. M., Eichhorn, R., and Gregg, J. L., 1959, ''Combined Forced and Free Convection in a Boundary Layer,'' Phys. Fluids, **2**, pp. 319–329.
[24] Choi, C. Y., and Kim, S. J., 1996, ''Conjugate Mixed Convection in a Channel: Modified Five Percent Deviation Rule,'' Int. J. Heat Mass Transfer, **39**(6), pp. 1223–1234.
[25] Sikka, K. K., Fisher, T. S., Torrance, K. E., and Lamb, C. R., 1997, ''Effects of Package Orientation and Mixed Convection on Heat Transfer From a PQFP,'' IEEE Trans. Compon., Packag. Manuf. Technol., Part A, **20**(2), pp. 152–159.
[26] Churchill, S. W., and Usagi, R., 1972, ''A General Expression for the Correlation of Rates of Transfer and Other Phenomena,'' AIChE J., **18**(6), pp. 1121–1128.
[27] Patankar, S. V., 1980, *Numerical Heat Transfer and Fluid Flow*, Hemisphere, New York.
[28] Tang, L., and Joshi, Y., 1999, ''Application of Block-Implicit Multi-Grid Approach to Three-Dimensional Heat Transfer Problems Involving Discrete Heating,'' Numer. Heat Transfer, Part A, **35**, pp. 717–734.

Ephraim M. Sparrow
Mechanical Engineering Department,
University of Minnesota,
Minneapolis, MN

John P. Abraham
e-mail address: jpabraham@stthomas.edu
School of Engineering,
University of St. Thomas,
St. Paul, MN

Paul W. Chevalier
Mechanical Engineering Department,
University of Minnesota,
Minneapolis, MN

A DOS-Enhanced Numerical Simulation of Heat Transfer and Fluid Flow Through an Array of Offset Fins With Conjugate Heating in the Bounding Solid

The method of Design of Simulation (DOS) was used to guide and enhance a numerical simulation of fluid flow and heat transfer through offset-fin arrays which form the interior geometry of a cold plate. The basic problem involved 11 independent parameters. This prohibitive parametric burden was lessened by the creative use of nondimensionalization that was brought to fruition by a special transformation of the boundary conditions. Subsequent to the reduction of the number of parameters, the DOS method was employed to limit the number of simulation runs while maintaining an accurate representation of the parameter space. The DOS method also provided excellent correlations of both the dimensionless heat transfer and pressure drop results. The results were evaluated with respect to the Colburn Analogy for heat and momentum transfer. It was found that the offseting of the fins created a larger increase in the friction factor than that which was realized for the dimensionless heat transfer coefficient. [DOI: 10.1115/1.1800531]

Introduction

The use of cold plates as a means for cooling electronic equipment is a well-established technology. However, in response to the ever-increasing heat loads that must be dealt with, the geometric complexity of cold plates has increased markedly in recent years. For example, in a very recent application involving the cooling of magnetrons for radar applications, a cold-plate configuration has been proposed in which the passages for the coolant consist of five highly distinctive geometries in series, each with its own particular complexity. Although, in principle, experiments can be undertaken for specific cold-plate geometries, this approach is not cost-effective during a development process in which optimal geometrical passage configurations are being sought [1–10].

To facilitate an evaluation of the characteristics of various candidate cold-plate geometries, effective use may be made of numerical simulations. Although this approach is, in principle, well suited for the identification of optimal configurations, it, too, has potential operational drawbacks. For instance, an appraisal of the number of independent parameters which describe the geometrical and operating conditions may well reveal a dozen or more. As a consequence, a more efficient approach that goes beyond mere numerical simulation must be employed.

In the present investigation, where a highly complex, three-dimensional flow passage is to be considered, there are a total of 11 independent geometrical and operating parameters. This prohibitive parametric load has to be reduced to a more reasonable set before simulation can be considered. Two techniques were employed to diminish the number of parametric inputs. One of these is skillful use of nondimensionalization. The other technique is akin to the well-established method used in experimental work to extract the maximum amount of information from the minimum number of data runs. That technique is commonly known as ''Design of Experiments'' (DOE) [11]. In what follows, the method to be used here for the selection of simulation runs will be denoted as ''Design of Simulations'' (DOS).

Contributed by the Heat Transfer Division for publication in the JOURNAL OF HEAT TRANSFER. Manuscript received by the Heat Transfer Division April 12, 2004; revision received July 10, 2004. Assoc. Editor: C. Amon.

The specific cold-plate configuration to be considered here is an array of offset fins contained between two large cover plates. The array is made up of a large number of rows such that it is expected that sufficiently far downstream from the array inlet, a periodic flow pattern will develop. This type of flow pattern is called periodically fully developed by Patankar, Sparrow, and Liu [12]. There is, however, a hydrodynamic development region which must be dealt with in the numerical simulation. With regard to heat transfer, it is expected that there will also exist a thermally developed regime in which the heat transfer coefficient for each module of the array becomes a constant. Here again, there is a region immediately downstream of the inlet in which the temperature field develops.

The goals of the research encompass both heat transfer and pressure drop. From the standpoint of engineering practice, emphasis will be placed on identifying those geometrical and operating parameters which have the greatest impact on the aforementioned results. The identification of the relative importance of the parameters will be enabled by the DOS method. In addition to the identification of the importance of the various parameters, the DOS method will provide quantitative algebraic relationships for the dimensionless heat transfer coefficient (the Stanton number) and the dimensionless pressure gradient (friction factor). The determination of Stanton numbers and friction numbers enables the evaluation of the Colburn Analogy (a modification of the Reynolds Analogy). The nature of the flow field development will be exhibited by means of contour diagrams.

The numerical simulations were performed by means of ANSYS FLOTRAN software. This is a finite-element-based program that is one of the suite of programs of the ANSYS package.

Minimization of Parametric Inputs. From an examination of the governing differential equations and boundary conditions, 11 parameters were identified. These included (a) physical dimensions: interfin spacing, fin length, fin thickness, and fin height; (b) boundary conditions: surface heat flux, fluid inlet temperature, and inlet fluid velocity; and (c) thermophysical properties: fin conductivity, fluid conductivity, fluid specific heat, and fluid density. The first task of the analysis is to reduce the number of parametric

inputs to a manageable value. Two methods will be used to accomplish this goal. These tasks will be set forth in the order in which they were employed.

Nondimensionalization of the Governing Equations. The starting point of the nondimensionalization is the governing conservation equations and the appropriate boundary conditions. The nondimensionalization proceeds rather smoothly for the governing equations, but special care has to be taken when the boundary conditions are made dimensionless. Since the problem is three dimensional, there are five governing equations: three momentum conservation equations, the energy equation, and the mass conservation equation. Since the nondimensionalization of the momentum equations is similar for all three, it is necessary for present purposes to work with only one of them. For concreteness, the *x*-direction momentum equation will be considered. For laminar, constant property fluid flow, the *x*-momentum equation is:

$$\rho\left(u\frac{\partial u}{\partial x}+v\frac{\partial u}{\partial y}+w\frac{\partial u}{\partial z}\right)=-\frac{\partial p}{\partial x}+\mu\left(\frac{\partial^2 u}{\partial x^2}+\frac{\partial^2 u}{\partial y^2}+\frac{\partial^2 u}{\partial z^2}\right) \quad (1)$$

The relevant energy and mass conservation equations are

$$\rho c_p\left(u\frac{\partial t}{\partial x}+v\frac{\partial t}{\partial y}+w\frac{\partial t}{\partial z}\right)=k_{\text{fluid}}\left(\frac{\partial^2 t}{\partial x^2}+\frac{\partial^2 t}{\partial y^2}+\frac{\partial^2 t}{\partial z^2}\right) \quad (2)$$

$$\frac{\partial u}{\partial x}+\frac{\partial v}{\partial y}+\frac{\partial w}{\partial z}=0 \quad (3)$$

The next step is to select reference quantities to serve as the basis for the nondimensionalization. Natural reference quantities include (a) the mean velocity of the flow $\bar{U}$ and (b) one of the characteristic dimensions of the system. The chosen reference dimension is the width ω of a flow passage in the fin array. For the temperature *t*, it is appropriate both to shift the datum and to scale the magnitude. With regard to scaling the magnitude of the dimensionless temperature, cognizance has to be taken of the nature of the thermal boundary conditions. For the present problem, the thermal boundary conditions are a given inlet temperature ($t=t_0$) for the fluid flow and uniform heat flux q_{surf} at the bounding walls of the cold plate. When these conditions are taken into account, it is natural to use t_0 as the datum and the reference temperature as $q_{\text{surf}}\omega/k_{\text{fluid}}$. By the use of these reference quantities, the dimensions, coordinates, velocities, and temperature emerge in dimensionless form as

$$\tau=T/\omega, \quad \lambda=L/\omega, \quad \eta=H/\omega \quad (4)$$

$$X=x/\omega, \quad Y=y/\omega, \quad Z=z/\omega \quad (5)$$

$$U=u/\bar{U}, \quad V=v/\bar{U}, \quad W=w/\bar{U} \quad (6)$$

$$\Theta=\frac{t-t_0}{(q_{\text{surf}}\omega/k_{\text{fluid}})} \quad (7)$$

In these equations, the quantities *T*, *L*, *H*, and ω represent the dimensions of the offset fin array. To provide perspective for these quantities, it is useful to make reference to Fig. 1. The figure is a schematic diagram of a representative subsection of the array. In this figure, the fins are portrayed as the darker-shaded regions and are further identified by a callout. The space between the fins is the region of fluid flow. Further inspection of the figure shows that there are two degrees of periodicity. In the flow direction, the geometry repeats with a period of $2L$ while in the transverse direction, the periodic length is $\omega+T$.

Also indicated in the figure is the thermal boundary condition that has been imposed on the upper cover plate of the array. Although not shown in the diagram, the lower cover plate of the array is also a surface of uniform heat flux of the same magnitude as that of the upper cover plate. Consequently, there is a plane of thermal symmetry situated midway between the upper and lower cover plates. This plane of symmetry also corresponds to a plane

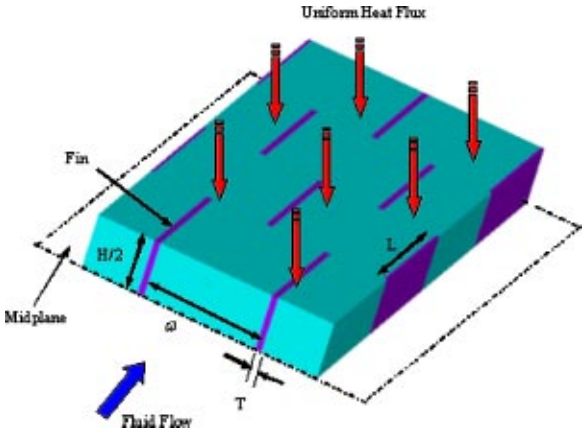

Fig. 1 Schematic diagram of a representative subsection of the offset fin array

of symmetry for fluid flow. This symmetry plane has been designated as the midplane and is indicated as such in the figure. Further inspection of the figure indicates that *L* is the length of an individual fin in the flow direction, ω is the transverse inter-fin spacing, *T* is the thickness of the material from which the fins are made, and *H* is the total channel height between the cover plates.

Attention may be redirected to the nondimensionalization process. It still remains to make the pressure into a dimensionless quantity, and the suitable reference quantity is $\rho\bar{U}^2$, so that

$$P=\frac{P}{\rho\bar{U}^2} \quad (8)$$

When the dimensionless variables and parameters defined in Eqs. (4)–(8) are inserted into the conservation equations, Eqs. (1)–(3), additional dimensionless groups emerge. They are,

$$\text{Re}=\frac{\rho\omega\bar{U}}{\mu}$$

$$\text{Pe}=\frac{\rho c_P\omega\bar{U}}{k_{\text{fluid}}}=\text{Re}\cdot\text{Pr} \quad (9)$$

$$\text{Pr}=\frac{c_P\mu}{k_{\text{fluid}}}$$

With these, Eqs. (1)–(3) become

$$U\frac{\partial U}{\partial X}+V\frac{\partial U}{\partial Y}+W\frac{\partial U}{\partial Z}=-\frac{\partial P}{\partial X}+\frac{1}{\text{Re}}\left(\frac{\partial^2 U}{\partial X^2}+\frac{\partial^2 U}{\partial Y^2}+\frac{\partial^2 U}{\partial Z^2}\right) \quad (10)$$

$$U\frac{\partial\Theta}{\partial X}+V\frac{\partial\Theta}{\partial Y}+W\frac{\partial\Theta}{\partial Z}=\frac{1}{\text{Pe}}\left(\frac{\partial^2\Theta}{\partial X^2}+\frac{\partial^2\Theta}{\partial Y^2}+\frac{\partial^2\Theta}{\partial Z^2}\right) \quad (11)$$

$$\frac{\partial U}{\partial X}+\frac{\partial V}{\partial Y}+\frac{\partial W}{\partial Z}=0 \quad (12)$$

When these equations are to be modeled in FLOTRAN, note must be taken that the software is configured to work with dimensional quantities. In fact, the software works with Eqs. (1)–(3). To facilitate using the software as written, it is appropriate to introduce values of density, specific heat, viscosity, and thermal conductivity which brings congruence between Eqs. (1)–(3) and Eqs. (10)–(12). A comparison of these equations yields

$$\rho=1, \quad c_p=1,$$
$$\mu=1/\text{Re}, \quad k_{\text{fluid}}=1/\text{Pe} \quad (13)$$

These nondimensional thermophysical properties are, of course, different from the actual thermophysical properties. They will be termed pseudo properties. To make this distinction, a superscript ($'$) is appended to each of the pseudo properties so that

$$\rho' = 1, \quad c_p' = 1, \qquad \mu' = 1/\mathrm{Re}, \quad k'_{\mathrm{fluid}} = 1/\mathrm{Pe} \tag{14}$$

Nondimensionalization and Transformation of the Boundary Conditions. The nondimensionalization of the governing differential equations is now complete. Next, consideration will be given to the boundary conditions and the continuity conditions at internal solid-fluid interfaces. It is convenient to deal first with the continuity conditions. The continuity of temperature is automatically satisfied by the nature of the computer program. On the other hand, for heat flux continuity,

$$\left(k\frac{\partial T}{\partial n}\right)_{\mathrm{fluid}} = \left(k\frac{\partial T}{\partial n}\right)_{\mathrm{solid}} \tag{15}$$

where n represents the normal to the interface in question. The insertion of the dimensionless parameters and variables leads to

$$\left(k\frac{\partial \Theta}{\partial N}\right)_{\mathrm{fluid}} = \left(k\frac{\partial \Theta}{\partial N}\right)_{\mathrm{solid}} \tag{16}$$

where $N = n/\omega$. As was set forth in connection with Eq. (14), the computer program was operated with pseudo properties in lieu of the actual thermophysical properties. Therefore, as far as the software is concerned, the value of k_{fluid} is $k'_{\mathrm{fluid}} = 1/\mathrm{Pe}$. Correspondingly, the operational value of k_{solid} must also be a pseudo property k'_{solid}. Therefore, from Eq. (16), it is seen that to preserve heat flux continuity at a solid-fluid interface

$$\frac{k'_{\mathrm{solid}}}{k'_{\mathrm{fluid}}} = \frac{k_{\mathrm{solid}}}{k_{\mathrm{fluid}}} \tag{17}$$

which leads to

$$k'_{\mathrm{solid}} = \frac{1}{\mathrm{Pe}}\left(\frac{k_{\mathrm{solid}}}{k_{\mathrm{fluid}}}\right) \tag{18}$$

The value of the pseudo conductivity k'_{solid} given in Eq. (18) was used as an input to the software.

The heat flux condition on the cover plates will now be assessed. In applying the given heat flux boundary condition, it is noted that the thicknesses of the respective cover plates were set at a very small value (infinitesimally thin) in order to avoid the occurrence of an additional parameter. A physical consequence of this assumption is that there is no spreading of heat in the plane of a cover plate. Another consequence is that the applied heat flux is imposed directly on the flowing fluid or the base of a fin.

For the case in which the heat flux is applied directly to the flowing fluid, the application of the given heat flux boundary condition yields

$$q_{\mathrm{surf}} = k_{\mathrm{fluid}}(\partial T/\partial n)_{\mathrm{fluid}} \tag{19}$$

in which n is the outward normal on the top cover plate. When the nondimensional variables and parameters are introduced into this equation, there follows:

$$(\partial \Theta/\partial N)_{\mathrm{fluid}} = 1 \tag{20}$$

Although this equation is correct, it does not provide information that is acceptable for the software. In fact, the software requires the input of a value of the heat flux itself rather than the temperature gradient. When the software is operated using the dimensionless temperature gradient $\partial\Theta/\partial N$ and the pseudoproperty k'_{fluid}, the heat flux boundary condition at the cover plate becomes

$$q'_{\mathrm{surf}} = k'_{\mathrm{fluid}}(\partial \Theta/\partial N)_{\mathrm{fluid}} \tag{21}$$

The derivative is given by Eq. (20), and k'_{fluid} is expressed by Eq. (14), so that

$$q'_{\mathrm{surf}} = 1/\mathrm{Pe} \tag{22}$$

For the case in which the heat flux is applied to the portion of the cover plate which mates with a fin,

$$q_{\mathrm{surf}} = \left(k\frac{\partial T}{\partial n}\right)_{\mathrm{solid}} \tag{23}$$

When this equation is transformed into the variables of the analysis, it is found that

$$q'_{\mathrm{surf}} = 1/\mathrm{Pe} \tag{24}$$

From the foregoing development, it is seen that the heat flux to be provided to the FLOTRAN software is 1/Pe.

For the temperature problem, it remains to specify the boundary conditions at the inlet and at a location far downstream from the inlet. Since $t = t_0$ at the inlet, then, Eq. (7) gives

$$\Theta_{\mathrm{inlet}} = 0 \tag{25}$$

Far downstream from the inlet, the standard outflow boundary conditions are imposed.

$$\partial \Theta/\partial X = 0 \tag{26}$$

Attention will now be turned to the boundary conditions for the velocity problem. The software automatically enforces the no-slip condition at all solid-fluid interfaces, and this condition continues in force for the dimensionless velocities. At the inlet to the array, the streamwise velocity in dimensionless form becomes

$$U = 1 \tag{27}$$

and the other velocity components are zero. At a far downstream location, the standard outflow boundary conditions were applied.

It is appropriate to assess what has thus far been accomplished in the task of parameter reduction. At this stage of the task, there remain six dimensionless parameters: Re, Pe, $k_{\mathrm{solid}}/k_{\mathrm{fluid}}$, τ (fin thickness), λ (fin length), and η (fin height). In the forthcoming numerical calculations, specific consideration will be given to air as the coolant fluid. This selection fixes Pr and, thereby, eliminates Pe ($=\mathrm{Re}\,\mathrm{Pr}$) as a separate parameter. In addition, in view of current practice, the fin height parameter η was set equal to 1.0. Therefore, at this stage of the analysis, the numerical simulations require the specification of four parameters.

Design of Simulations (DOS). To initiate the implementation of the DOS approach, the first step is to select high and low values of the four parameters. This selection provides eight numerical values which may be identified as $\mathrm{Re}_{\mathrm{hi}}$, $\mathrm{Re}_{\mathrm{lo}}$, τ_{hi}, ... By making use of the selected values, a table is formed which will be used as the basis of the simulation runs. As can be seen from Table 1, 16 cases have been synthesized using permutations and combinations of the aforementioned hi and lo values of the parameters.

Execution of the Simulations

The FLOTRAN finite-element software was utilized to perform the numerical simulations. This program is one of the suite of programs of the ANSYS package. The simulations were run using approximately 15,000 elements, and each of the 16 cases required approximately 200 iterations to achieve convergence. The elements chosen to span the solution domain were strictly quadrilateral. From the menu of available solvers, the SIMPLEF pressure-velocity coupling was selected, which is an enhanced version of the well-established SIMPLE velocity-pressure coupling technique. For the solution of the simultaneous equations which are inherent in the simulation, the following solvers were selected, on the basis of advice provided in the ANSYS operation manual: (a)

Table 1 DOS parameter list

Case	Re	k_{solid}/k_{fluid}	τ	λ
1	100 (lo)	646 (lo)	0.05 (lo)	1.0 (lo)
2	2000 (hi)	646	0.05	1.0
3	100	6460 (hi)	0.05	1.0
4	2000	6460	0.05	1.0
5	100	646	0.10 (hi)	1.0
6	2000	646	0.10	1.0
7	100	6460	0.10	1.0
8	2000	6460	0.10	2.0 (hi)
9	100	646	0.05	2.0
10	2000	646	0.05	2.0
11	100	6460	0.05	2.0
12	2000	6460	0.05	2.0
13	100	646	0.10	2.0
14	2000	646	0.10	2.0
15	100	6460	0.10	2.0
16	2000	6460	0.10	2.0

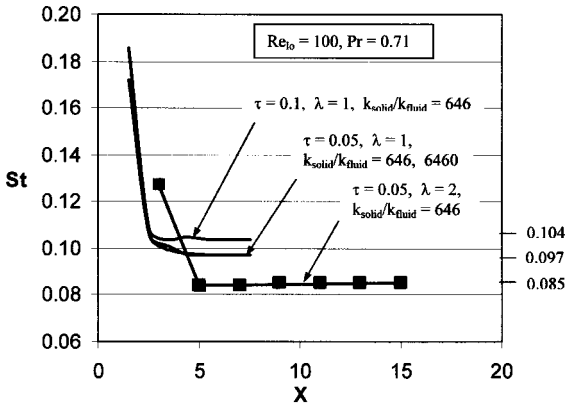

Fig. 2 Per-module Stanton numbers for $Re_{lo}=100$

for the velocity field, the TriDiagonal Matrix Algorithm (TDMA); (b) for the pressure field, the Preconditioned Conjugate Gradient Technique; and (c) for the temperature, the Preconditioned Generalized Minimum Residual Method.

Since the solution domain is, in principle, doubly infinite, steps were taken to reduce it to manageable size while maintaining all of the essential physical features of the fin array. Since the geometry forces the attainment of periodically fully developed flow in the streamwise direction, it was only necessary to extend the solution domain through the hydrodynamic entrance region. The thermal boundary conditions also are conducive to the attainment of a thermally developed situation, so that, once again, the thermal entrance region was all that had to be traversed. The transverse width of the solution domain was bounded by the use of symmetry lines. Advantage was also taken of the existence of the symmetry plan midway between the upper and lower coverplates (see Fig. 1 where the midplane is identified).

Results and Discussion

The presentation of the results will include four different foci that, in the order of appearance, are (1) quantitative heat transfer and pressure drop results, (2) Colburn Analogy connecting heat transfer and pressure drop, (3) correlation of the results by means of the DOS method, and (4) flow-field and pressure-field contour diagrams.

Quantitative Heat Transfer Results. The results of greatest interest include the heat transfer and pressure drop characteristics of the offset fin array. For both the heat transfer and the pressure drop, results will be presented for the entrance region values, the periodically fully developed values, and the length of the entrance region. The presentation begins with a graphical depiction of local heat transfer and pressure distributions. For the case of heat transfer, the presented results are for a module-averaged heat transfer coefficient $\bar{h}$ which, in dimensionless form, is represented by the per-module Stanton number, $St=\bar{h}/(\rho c_p U)$. The numerical results for the Stanton number are presented in Figs. 2 and 3.

The streamwise distribution of the per-module Stanton number for the low Reynolds number Re_{lo} are set forth in Fig. 2 for various parametric values of the dimensions and conductivity ratio. As can be seen from the figure, the Stanton number decreases sharply through the thermal entrance region and achieves a fully developed value. In particular, the fully developed state is attained at $x/\omega \approx 3-4$ for the cases depicted in the figure. This result is surprisingly close to what would be predicted from laminar, pipe-flow theory, which gives the thermal entrance length as approximately 0.05 Re Pr. For instance, for Re=100 and Pr=0.71, the pipe-flow entrance length would be approximately 3.5 diameters!

Perspective on the magnitude of the Stanton numbers can be obtained by considering fully developed, laminar heat transfer in a square duct for which the fully developed Nusselt number is 3.6. The square duct is chosen for a comparison case because the present offset-fin geometry has a cross-sectional shape which is square (fin height=interfin spacing). From the definition of the Stanton number, St=Nu/Pe, the fully developed Stanton number for the square duct is 3.6/71=0.051. This value is to be compared with the fully developed Stanton numbers that are indicated at the right-hand margin of Fig. 2. Those values are substantially higher than 0.051, which is for fully developed duct flow. This difference is fully accounted when consideration is given to the differences between the cases being compared. Of greatest significance is the fact that in the fully developed regime for the offset fins, new boundary layers are periodically initiated at the beginning of each module. The boundary layer development is responsible for the enhanced heat transfer coefficients.

As a final discussion item with respect to Fig. 2, the physical basis of the vertical arrangement of the curves will now be addressed. The effect of fin thermal conductivity is clearly of no importance. The fin-thickness effect is slight but is not totally negligible as witnessed by the spread between the two uppermost curves in the figure. Of somewhat greater significance, but still not of major importance, is the effect of fin length. The greater fin length enables a thicker boundary layer to grow in the streamwise direction and, as a consequence, the per-module heat transfer coefficient must decrease.

Results similar to those of Fig. 2, but for $Re_{hi}=2000$, are presented in Fig. 3. Inspection of Fig. 3 and comparison with Fig. 2 reveals a significant difference in the values of the Stanton number as witnessed by the differing ordinate scales. Most of the difference between the two sets of Stanton numbers is actually

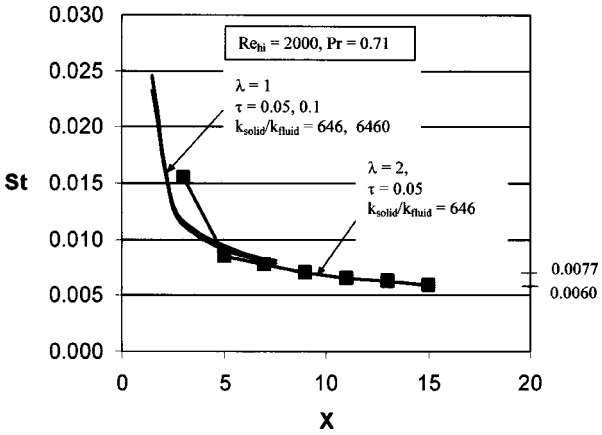

Fig. 3 Per-module Stanton numbers for $Re_{hi}=2000$

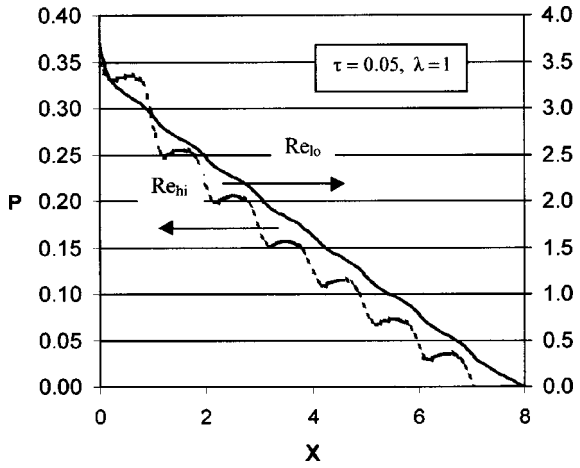

Fig. 4 Variation of the dimensionless pressure with streamwise position along the midplane of the array, τ=0.05, λ=1

inherent in the definition of the quantity itself. This is readily seen by noting that the heat transfer coefficient in the Stanton number is divided by the mean velocity. Since the higher Reynolds number corresponds to a higher velocity, it is reasonable that smaller Stanton numbers correspond to higher Reynolds numbers. In this regard, it is also of interest to compare the fully developed Stanton numbers of Fig. 3 with those of laminar flow in a square duct in which Re=2000 and Pr=0.71. By making use of the fully developed, square-duct Nusselt number of 3.6, the corresponding Stanton number follows as 0.0025. As expected from the discussion in the penultimate paragraph, this value is considerably lower than the fully developed values indicated at the right-hand margin of Fig. 3. The other trends in Fig. 3 are similar to those already discussed in connection with Fig. 2.

Quantitative Pressure Drop Results. The pressure drop results will be presented from two points of view. One of these will display the actual streamwise pressure variations, and the other will be focused on friction factors. Figures 4 and 5 have been prepared to display the pressure variations as a function of streamwise position in the array.

The effect of Reynolds number on the streamwise pressure variation is exhibited in Fig. 4. The most noteworthy characteristic displayed in the figure is the periodic nature of the pressure distribution. This behavior is most strongly in evidence for Re_{hi}. In assessing the more evident periodic nature of the pressure variation for Re_{hi} relative to that for Re_{lo}, it is relevant to take account of the two contributions that give rise to pressure drop. For a low-Reynolds-number flow, the major contributor to pressure drop is fluid-surface viscous interaction while separation-related pressure drops are minimal. On the other hand, at high Reynolds numbers, both of these mechanisms are major contributors. Downstream of separated regions, there is a region of pressure recovery. Such pressure recovery is in evidence for the Re_{hi} case appearing in Fig. 4. On the other hand, in the absence of separated regions, there is no recovery mechanism, and friction causes a continuous decrease of the pressure.

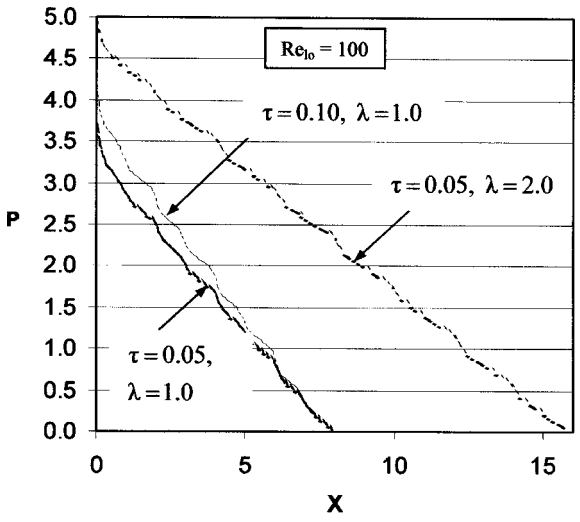

Fig. 5 Variation of the dimensionless pressure with streamwise position along the midplane of the array, Re_{lo}=100

The next figure showing pressure distributions is concerned with the effect of various geometric parameters for a fixed value of $Re_{lo}=100$. This information is conveyed by Fig. 5. The figure contains three curves, each of which corresponds to a particular geometry. Since all of the results exhibited in the figure correspond to Re_{lo}, there is little evidence of the pressure recovery that has already been discussed in connection with Fig. 4. Further inspection of Fig. 5 reveals that the effect of fin thickness is moderate, with only a slightly higher pressure drop for the dimensionless fin thickness $\tau=0.10$ compared with that for $\tau=0.05$. The $\lambda=2.0$ case corresponds to a fin which is of double streamwise length relative to the $\lambda=1.0$ case. For the former, the pressure drop per fin is larger, but not twice as large as the pressure drop per fin for the latter. On the other hand, the pressure drop per unit length of the array is smaller for the $\lambda=2.0$ case.

An alternative characterization of the pressure drop results can be made via the well-known friction factor. The friction factor is defined in what appears to be the conventional manner as

$$f=\frac{(-dp/dx)\omega}{(1/2)\rho\overline{U}^2}=2\frac{dP}{dX} \tag{28}$$

However, the evaluation of dP/dX has to be carried out keeping in mind the geometric periodicity. With this in mind, geometrically identical points separated by a streamwise distance L were selected and the pressures at these points were differenced, thereby providing the numerical value of dP/dX. This operation was performed for a succession of points in the streamwise direction, and the corresponding friction factors were evaluated.

Tabulation of the Quantitative Results. A listing of the fully developed Stanton numbers and friction factors is made in Table 2. The table is laid out with the case number on the left-hand margin and the adjacent St and f columns representing the results of the numerical simulations. Some of the Stanton numbers appearing in the table have already been exhibited in Figs. 2 and 3 along the right-hand margins. The friction factor listing in the table conveys new results. To provide perspective for the friction factor results, it may be noted that the friction factor for fully developed, laminar flow in a square duct is given by $f=57/\mathrm{Re}$. For Re=100, this gives $f=0.57$. This numerical value may be compared to the f values for cases 1, 3, . . . ,15 that appear in Table 2. It is interesting to observe that for those tabulated cases corresponding to long fins, the agreement between the fully developed duct flow and the offset fin array is quite satisfactory. On the other hand, for those cases characterized by shorter fins, the tabulated friction factors are substantially larger than 0.57. This behavior reflects the more frequent re-initiation of the boundary layer when the fins are short. A similar discussion may be made for the results of the higher Reynolds numbers.

Stanton Number—Friction Factor Correlation. Over the years, there have been many attempts to correlate heat transfer and friction results with a view to diminishing the need to separately measure these two quantities. The earliest work produced the well-known Reynolds Analogy ($f/2=\mathrm{St}$). This relationship was limited to fluids whose Prandtl number is approximately 1.0.

Table 2 Tabulation of fully developed St and *f* values

Case	St	*f*	Colburn Factor	Predicted St (32)	Predicted St (33)	Predicted St (34)	Predicted *f* (35)	Predicted *f* (36)	Predicted *f* (37)
1	0.096	0.86	5.63	0.098	0.098	0.096	0.92	0.92	0.86
2	0.0078	0.080	6.44	0.0078	0.0078	0.0077	0.086	0.088	0.080
3	0.097	0.86	5.57	0.098	0.098	0.096	0.92	0.92	0.86
4	0.0070	0.080	7.18	0.0078	0.0078	0.0077	0.086	0.088	0.080
5	0.10	0.98	6.16	0.098	0.098	0.10	0.92	0.92	0.98
6	0.0084	0.094	7.03	0.0078	0.0078	0.0079	0.086	0.088	0.094
7	0.10	0.98	6.16	0.098	0.098	0.10	0.92	0.92	0.98
8	0.0080	0.094	7.38	0.0078	0.0078	0.0079	0.086	0.088	0.094
9	0.085	0.58	4.29	0.087	0.087	0.085	0.63	0.64	0.58
10	0.0060	0.052	5.45	0.0056	0.0057	0.0056	0.057	0.058	0.052
11	0.085	0.58	4.29	0.087	0.087	0.085	0.63	0.64	0.58
12	0.0057	0.052	5.73	0.0056	0.0057	0.0056	0.057	0.058	0.052
13	0.088	0.68	4.86	0.087	0.087	0.089	0.63	0.64	0.68
14	0.0050	0.064	8.04	0.0056	0.0057	0.0058	0.057	0.058	0.064
15	0.091	0.68	4.70	0.087	0.087	0.089	0.63	0.64	0.68
16	0.0060	0.064	6.70	0.0056	0.0057	0.0058	0.057	0.058	0.064

Colburn [13] is credited with generalizing the Reynolds Analogy to make it applicable to fluids having Prandtl numbers different from 1.0, with the result $f/2 = \mathrm{St}\,\mathrm{Pr}^{2/3}$. The latter is often referred to as the Colburn Analogy.

The present results for St and *f* will be examined with regard to their adherence to the Colburn Analogy. For this purpose, it is convenient to define

$$\text{Colburn Factor} = (f/2)/(\mathrm{St}\cdot\mathrm{Pr}^{2/3}) \tag{29}$$

The Colburn factor was evaluated for the friction factors and Stanton numbers that were determined from the numerical simulations, and these values are listed in Table 2. The table reveals that the Colburn factor for the present results is well above 1.0, thereby indicating that the friction factor is notably larger than the Stanton number for the investigated geometries. This finding may be regarded as a failure of the Colburn Analogy. On the other hand, the analogy was developed for simple flows where flow separation is non-existent. Notwithstanding this, by selecting a representative value of the Colburn factor (for example, 6), it is possible to estimate a value of the friction factor provided the Stanton number is known, or vice versa.

Correlation of the St and *f* Using the DOS Method. From the statistical theory that underlies the DOS method, it is straightforward to develop correlations of the form

$$\mathrm{St} = a_0 + a_1 A + a_2 B \ldots + b_1 AB + b_2 AC \ldots \tag{30}$$

where a_i are numerical coefficients and $A, B, \ldots$ represent the independent parameters. A similar form can be used for the friction factor. Alternatively, a curve fit of the form

$$1/\mathrm{St} = c_0 + c_1 A + c_2 B \ldots + d_1 AB + d_2 AC \ldots \tag{31}$$

can be constructed, and similarly for the friction factor. Support for the latter form can be obtained by observing that the Stanton number and the friction factor vary inversely with the Reynolds number and the fin length, both of which appear on the right-hand side of Eq. (31).

In the software that is used to process the DOS method, there is a focus on the relative importance of the various parameters with regard to their influence on the results. From the numerical information provided by this portion of the software, it was found that two of the four parameters, conductivity ratio and the dimensionless fin thickness had virtually no effect on the results. This is a major finding. On the other hand, the Reynolds number exerted a major influence upon the results, with the dimensionless fin length being of lesser importance.

In order to explore the sensitivity of the Stanton numbers predicted by the DOS correlation equations, several forms of the correlations were examined. These are

$$1/\mathrm{St} = 5.131 + 0.03762\,\mathrm{Re} - 1.191\lambda + 0.02480(\mathrm{Re}\cdot\lambda) \tag{32}$$

$$\mathrm{St} = 0.1144 - 5.228\times10^{-5}\,\mathrm{Re} - 0.01147\lambda + 4.671\times10^{-6}(\mathrm{Re}\cdot\lambda) \tag{33}$$

$$\mathrm{St} = 0.1082 - 4.930\times10^{-5}\,\mathrm{Re} + 0.0840\tau - 0.01147\lambda - 3.974 \times10^{-5}(\mathrm{Re}\cdot\tau) + 4.671\times10^{-6}(\mathrm{Re}\cdot\lambda) \tag{34}$$

A comparison of the values of the Stanton numbers obtained from evaluating Eqs. (32)–(34) with the results directly obtained from the simulations is presented in Table 2. A careful inspection of the table indicates that for the majority of the cases (10 of the 16 cases) the agreement between the predictions of the fitted equations and the directly computed results is excellent, within a few percent. For the other cases, the deviations are generally within 10 percent. This level of agreement is regarded as a triumph of the DOS method in that it is able to provide excellent predictions based on a remarkably small number of direct simulations. A deeper examination of the table suggests that there is not a great difference in the accuracy of the different algebraic fits; however, strictly speaking, the best fit is provided by Eq. (34).

The friction factor results were also post-processed by the DOS method, yielding algebraic correlations. The correlation equations contain different numbers of terms in accordance with a consideration of the importance of the various parameters.

$$1/f = 0.3161 + 2.70\times10^{-3}\,\mathrm{Re} + 0.224\lambda + 2.817\times10^{-3}(\mathrm{Re}\,\lambda) \tag{35}$$

$$f = 1.268 - 5.758\times10^{-4}\,\mathrm{Re} - 0.3037\lambda + 1.374\times10^{-4}(\mathrm{Re}\,\lambda) \tag{36}$$

$$f = 1.095 - 4.992\times10^{-4}\,\mathrm{Re} + 2.302\tau - 0.3037\lambda - 1.021 \times10^{-3}(\mathrm{Re}\,\tau) + 1.374\times10^{-4}(\mathrm{Re}\,\lambda) \tag{37}$$

A test of the accuracy of these equations is set forth in Table 2. The table shows that there is a considerable difference in the efficacy of the various fitted equations. In particular, Eq. (37) provides a perfect representation of the results obtained from the direct numerical simulations, whereas the other two representations are of lesser accuracy. It is, therefore, recommended that Eq. (37) be used for any further predictions of the friction factor.

Qualitative Depiction of the Velocity Field. To illustrate the attainment of the periodic, fully developed flow field, a computer-generated contour diagram is presented in Fig. 6 for $\mathrm{Re}_{lo} = 100$. The figure includes eight offset-fin modules. The velocity magnitude is represented by the various shades of gray which are keyed to the scale beneath the contour diagram. Careful study reveals that the attainment of the periodically fully developed regime is

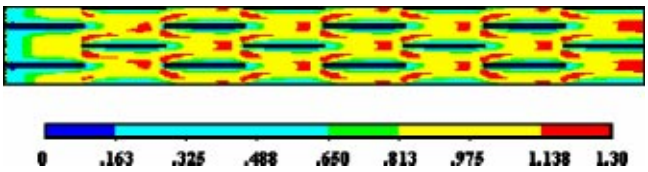

Fig. 6 Illustration of the velocity field corresponding to $Re_{lo}=100$. The attainment of the periodic regime occurs after the second module.

achieved after the second module. This rapid development is related to the low Reynolds number of the flow. At higher Reynolds numbers, the development length is somewhat larger.

Concluding Remarks

The practical problem of fluid flow and heat transfer in an offset-fin array which comprises the internal geometry of a cold plate has been solved by making use of direct numerical simulation in conjunction with methods of parameter minimization. The parameter minimization was accomplished by the use of two techniques. One of these makes use of nondimensionalized variables and parameters. Critical to this approach is the proper treatment of the boundary conditions. Once the reduction of the parameters had been accomplished, a second method, Design of Simulations (DOS), was employed to minimize the number of inputs needed to obtain an accurate representation of the parameter space. Although the original problem definition encompassed 11 parameters, only 16 simulation runs were required to provide the required information. Furthermore, the DOS method furnished algebraic correlations of the results obtained from the direct simulations so that the entire parameter space was fully covered. Another dividend of the DOS method was the identification of the importance of the various geometric and operating parameters.

The entire slate of results included Stanton numbers (dimensionless heat transfer coefficients), friction factors, and the development length for periodic and fully developed flow and heat transfer. The results enabled an assessment of the analogy between heat transfer and friction as embodied in the Colburn Analogy. This examination demonstrated that the complexity of the flow field gave rise to considerably larger friction factors than would have been predicted by the Analogy.

The algebraic format, Eqs. (32)–(37), facilitates various types of optimization studies. For instance, an algebraic form may be found for the pumping power as a function of the operating parameters of the problem. Such an algebraic representation would facilitate the use of a criterion such as constant pumping power.

Acknowledgments

The authors acknowledge with appreciation, the advice of Professor Perry Parendo of the University of St. Thomas concerning the DOS method. The support of H. Birali Runesha of the Supercomputing Institute for Digital Simulation & Advanced Computation at the University of Minnesota is gratefully acknowledged.

Nomenclature

c_p = specific heat of fluid
$\underline{f}$ = friction factor
h = per-module heat transfer coefficient
k = thermal conductivity
n = dimensional coordinate normal to a surface
N = dimensionless coordinate normal to solid-fluid interface, $=n/\omega$
p = pressure
P = nondimensional pressure, $=p/\rho\overline{U}^2$
Pe = Peclet number, $=\rho c_P \omega \overline{U}/k_{\text{fluid}}=\text{Re}\cdot\text{Pr}$
Pr = Prandtl number, $=c_P\mu/k_{\text{fluid}}$
Re = Reynolds number, $=\rho\omega\overline{U}/\mu$
q_{surf} = surface heat flux
St = per-module Stanton number, $=\overline{h}/(\rho c_p \overline{U})$
t = temperature
t_0 = fluid inlet temperature
T, L, H = fin thickness, fin length, and fin height
u, v, w = velocity components in the x, y, and z-directions
U, V, W = nondimensional velocity components in the x, y, and z-directions, $=u/\overline{U},\ v/\overline{U},\ w/\overline{U}$
$\overline{U}$ = average velocity
x, y, z = dimensional coordinates
X, Y, Z = nondimensional coordinates, $=x/\omega,\ y/\omega,\ z/\omega$

Greek Symbols

ρ = density
Θ = nondimensional temperature, $=t-t_0/(q_{\text{surf}}\omega/k_{\text{fluid}})$
τ, λ, η = nondimensional fin thickness, fin length, and fin height, $(\tau=T/\omega,\ \lambda=L/\omega,\ \eta=H/\omega)$
μ = viscosity
ω = channel width

Superscripts

$'$ = nondimensional thermophysical properties

References

[1] Wieting, A., 1975, "Empirical Correlations for Heat Transfer and Flow Friction Characteristics of Rectangular Offset Fin Heat Exchangers," ASME J. Heat Transfer, **97**, pp. 488–490.
[2] Kays, W. M., and London, A. L., 1984, *Compact Heat Exchangers*, 3rd ed., McGraw-Hill, New York.
[3] Hatada, T., and Senshu, T., 1984, "Experimental Study on Heat Transfer Characteristics of Convex Louver Fins for Air Conditioning Heat Exchangers," ASME Paper 84-HT-74.
[4] Joshi, H. M., and Webb, R. L., 1987, "Prediction of Heat Transfer and Friction in the Offset Strip Fin Array," Int. J. Heat Mass Transfer, **30**, pp. 69–84.
[5] Kurosaki, T., Kashiwagi, T., Kobayashi, T., Uzuhashi, H., and Tang, S.-C., 1988, "Experimental Study on Heat Transfer From Parallel Louvered Fins by Laser Holographic Interferometry," Exp. Therm. Fluid Sci., **1**, pp. 59–67.
[6] Manglik, R. M., and Bergles, A. E., 1990, "The Thermal-Hydraulic Design of the Rectangular Offset-Strip-Fin Compact Heat Exchanger," in *Compact Heat Exchangers*, R. K. Shah, A. D. Kraus, and D. Metzger, eds., Hemisphere Publishing Corp., Washington, D.C., pp. 123–150.
[7] Usami, H., 1991, "Pressure Drop Characteristics of Offset Strip Fin Surfaces," *Proceedings of the 1991 ASME/JSME Joint Thermal Engineering Conference*, **4**, J. R. Lloyd and Y. Kurosaki, eds., ASME, New York, pp. 425–432.
[8] Majumdar et al., 1992, "Heat and Momentum Transport in Oscillatory Viscous Flows," ASME J. Heat Transfer, **114**, pp. 866–875.
[9] Majumdar et al., 1997, "Oscillatory Momentum Transport Mechanisms in a Transitional Complex Geometry Flow," ASME J. Fluids Eng., **119**, pp. 29–35.
[10] Amon et al., 1992, "Numerical and Experimental Studies of Self-Sustained Oscillatory Flows in Communicating Channels," Int. J. Heat Mass Transfer, **35**, pp. 3115–3129.
[11] Montgomery, D. C., 2000, *Design and Analysis of Experiments*, 5th ed., John Wiley & Sons, New York.
[12] Patankar, S. V., Sparrow, E. M., and Liu, C. H., 1977, "Fully Developed Flow and Heat Transfer in Ducts Having Streamwise-Periodic Variations of Cross-Sectional Area," ASME J. Heat Transfer, **99**, pp. 180–186.
[13] Colburn, A. P., 1933, "A Method of Correlating Forced Convection Heat Transfer Data and a Comparison With Fluid Friction," Trans. AIChE **29**, pp. 174–210.

Coupled Field Analyses in MEMS With Finite Element Analysis

Ravi Chandra Sikakollu

Lemmy Meekisho
Department of Mechanical Engineering,
Portland State University,
Portland, OR

Andres LaRosa
Physics Department,
Portland State University,
Portland, OR

This paper deals with the design and analysis of a horizontal thermal actuator common in MEMS applications using Finite Element Analysis; with the objective of exploring means to improve its sensitivity. The influence of variables like voltage and the dimensions of the cold arm of the actuator unit were examined by comprehensive, coupled thermal-stress analyses. Simulation results from this study showed that the sensitivity of the actuator increases with the applied voltage as well as the width of the cold arm of the thermal actuator. An important observation made from this study is that the size and thermal boundary conditions at the fixed end of the actuator primarily control the stroke and the operating temperature of the actuator for a given potential difference between cold and hot arms. The coupled field analyses also provided a design tool for maximizing the service voltage and dimensional variables without compromising the thermal or structural integrity of the actuator. [DOI: 10.1115/1.1804204]

Introduction

The great potential of Micro Electro Mechanical Systems (MEMS) lies in the ability to produce mechanical motion at the microscale. Such devices are typically low power and fast, taking advantage of microscale phenomena such as strong electrostatic forces and rapid thermal response. MEMS-based sensors and actuators have been progressively accepted, developed and commercialized. MEMS technologies have shown significant prospect and applications in many fields of science and engineering including, applications in optics, transportation, aerospace, robotics, chemical analysis systems, biotechnologies, medical engineering and microscopy using scanning micro probes [1], etc. The wireless industry has shown significant vested interest in MEMS because of the potential that RF systems may play in developing powerful and sophisticated components, with significantly reduced footprint sizes. At the same time, the performance can be greatly increased by reducing signal delay time and noise effects through the applications of on-chip assembly of components. These key advantages and promising applications of MEMS-based RF components have become a noticeable driving force for many MEMS designers [2].

MEMS devices have seen very rapid growth in the recent past because their manufacturing process is closely tied to the advances in the manufacture of microelectronics, specifically, the integration of mechanical elements and electronics on a common silicon wafer using microfabrication technologies [3]. The electronics can be fabricated by an integrated circuit (IC) process sequence and the mechanical elements constructed by micromachining methods that are compatible with the IC fabrication process. The sensors and actuators are made of mechanical elements, and signal processing and control units are built by using electronics components. The whole system can thus be integrated on a single chip without any extra assembly process. The motivation for integrating the whole system on a single chip is miniaturization and parallel processing which leads to inexpensive fabrication in large quantities. It also has the ability to make devices with functions that cannot be achieved with traditional manufacturing technologies. In the early of 1990s, MEMS emerged from the development of IC fabrication processes, in which sensors, actuators and control functions are co-fabricated on silicon.

To date, Computer Aided Design (CAD) software packages are still quite time consuming and not powerful enough to adequately address all the actual factors that affect the operation of MEMS devices at one time. The commercial code Coventorware was used to design and analyze the thermal actuator presented in this paper. The complexity of MEMS components is also a big issue for MEMS designers. Typical MEMS devices, even simple ones, manipulate electrical, thermal and mechanical energy. This requires that the MEMS designer understands and finds ways to control complex interactions between these microscale domains. Secondly, from a fabrication perspective, the cost element for a state-of-the-art silicon foundry is often prohibitive for most MEMS device developers. MEMS packaging impacts the performance of MEMS devices enough to become one of the most fundamental problems in MEMS research. Due to their diversity, each new MEMS device almost by necessity requires a totally new and specific packaging method [4].

Thermal microactuators are compact and can provide high output forces. Bimorph-like thermal actuators are composite structures made of two or more layers of materials with different coefficients of thermal expansion [5]. A different category of thermal actuators comprises single material structures whose behavior is controlled largely by the shape and dimensions of the structure, and is the subject of this paper; see Fig. 1. The application of a voltage difference between the arms of the actuator results in nonuniform thermal expansion because of the geometric parameter details of the actuator. Actuators made of a single material (such as the one reported here), have been known to produce higher deformations than bimetallic strips constrained similarly and subjected to the same voltage difference [5]. The thin arm of the microactuator has a higher electrical resistance than the wide arm, therefore it gets heated more than the wider arm and consequently elongates farther than the wider arm. Thermal actuators produce forces of the order of 1 mN at significantly low voltages in the range of 5–10 V; compared to electrostatic actuators of comparable size, which produce output forces of the order of 1 μN at voltage of in the range of a 100 V [5–8]. The mode of operation of the thermal actuator is elongation in the axial direction due to thermal expansion resulting in significant motion in the lateral direction, as illustrated in Fig. 2.

Modeling and Analysis Considerations

The design of the thermal actuator is shown in Fig. 1 with corresponding dimensional details in Table 1 and material property data in Table 2.

The principle of operation of the actuator is that the supplied voltage generates joule heating in both arms of the actuator and the flexure link. The narrow arm has higher thermal resistance

Contributed by the Heat Transfer Division for publication in the JOURNAL OF HEAT TRANSFER. Manuscript received by the Heat Transfer Division April 13, 2004; revision received July 6, 2004. Associate Editor: C. Amon.

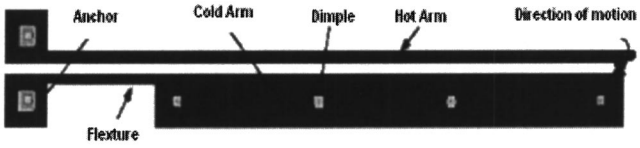

Fig. 1 Design of the thermal actuator

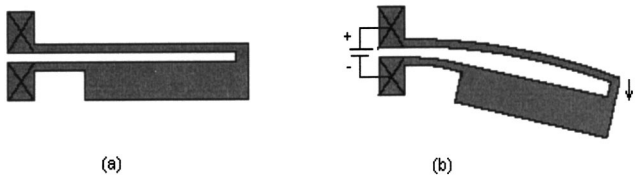

Fig. 2 Schematic of the thermal actuator before and after actuation

than the larger arm. As well, the narrow arm will have less self-restraint (bulk) than the larger arm. As a result of the joule heating, the narrower arm (the hot arm) will heat up more and deflect farther than the larger arm (the cold arm). The objective of this study was to explore the sensitivity of the actuator as a result of variations in input voltage and width of the cold arm. Temperature fields were computed for the actuator, and were used to compute thermal strains from the coefficient of thermal expansion, which were coupled with mechanical restraints to compute the displacements and stresses.

The Thermal Problem and Boundary Conditions. The electric potential used for the FEA engine of Coventorware software was determined from the geometric details and the thermo physical properties of polysilicon, the actuator material. Four dimples were used for the standard actuator dimensions, Fig. 1; and five dimples were used for wider cold arms, Fig. 3. From a physical perspective, the dimples serve the function of reinforcing the cold arm, hence assist in its structural integrity to avoid excessive deflection under its own bulk, and after elongating from the joule heating. For finite element analysis, the temperature of the anchor points and the dimples in the cold arm of the actuator were prescribed at 300 K. They thus served as the sink for the joule heating generated by the voltage source and satisfied the necessary boundary conditions for the thermal problem.

The Mechanical Problem and Boundary Conditions. The left hand side ends (Fig. 1) of the actuator were firmly constrained. The thermal history from the preceding heat transfer analysis phase was used as data to compute thermal strains at all locations in the actuator. Given the geometry, thermal strains and boundary conditions, the response of the actuator emulated the behavior of a cantilever beam with maximum deflections at the free end, and maximum average stresses at the anchored end.

Analysis of Actuator With Variable Widths of the Cold Arm. The narrow arm of the actuator was deemed not a good candidate in seeking improvement in the sensitivity of the actuator since its dimensions were close to the limits of its manufacturability, and had just enough self-restraint to withstand the thermally induced deformation without mechanical damage. Therefore, the alternative approach to try to improve the sensitivity of the actuator was to increase the width of cold arm in the *Y*-direction, as shown in Fig. 3. With this approach it was possible to increase the surface area for cooling while decreasing current density to reduce the joule heating effects.

The procedure used was to scale the original width dimension of the cold arm. The width of the actuator was scaled using four scaling factors; while keeping the length and the thickness constant. Figure 3 shows the scaling origin point of the scaling direction for the cold arm.

Table 1 Dimensions of the actuator

Component	Dimension (μm)
Length of hot arm	240
Length of cold arm	200
Length of flexure	40
Width of gap	2
Thickness of Polysilicon	2

Table 2 Thermal, mechanical and electrical properties of the thermal actuator

Property	Values
Elastic Modulus	1.65E+05 MPa
Density	2.30E−01 kg/$\mu\cdot$m^3
Thermal Expansion	3.5E−06 1/K
Thermal conductivity	5.0E+07 pW/μm·K
Electrical conductivity	7.0E+10 pA

Table 3 Maximum temperature variation with voltage

Voltage (v)	Temperature (K)
0	300
0.5	326
1.0	406
1.5	538
2.0	724
2.5	962
3.0	1254

Results

Thermal Response of Actuator From Voltage Variations. It was observed that the temperature of the actuator increased with voltage. This observation was consistent with expectation, in the sense that joule heating increases with applied voltage. In all cases the temperature distribution was such that for the hot arm, the anchored end had the prescribed temperatures of 300 K, and the temperature increased to maximum values at the free tip as shown

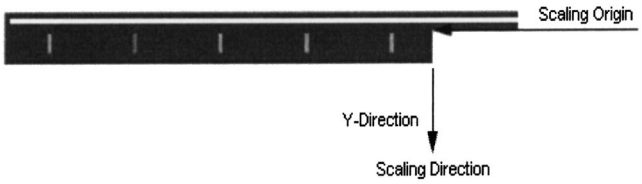

Fig. 3 Scaling of the cold arm of the actuator

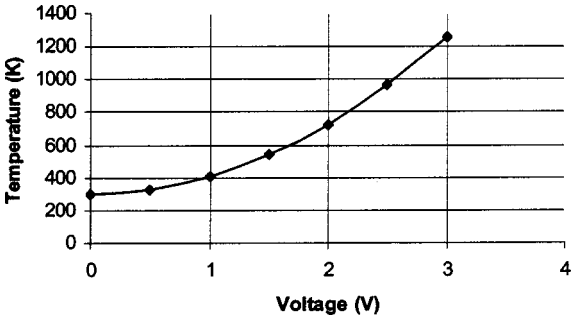

Fig. 4 Temperature variation with voltage

in Table 3. The cold arm on the other hand exhibited the prescribed temperature of 300 K at the anchored end and in the neighborhood of the dimple location with higher temperatures towards the free end. In all cases the highest temperatures in the cold arm were considerably lower than temperatures recorded for the hot arm. The maximum temperatures at the free tip of the hot arm with corresponding voltages are summarized in Table 3 and the raw data is plotted in Fig. 4.

Structural Response From Voltage Variations. It was found that the maximum displacements of the free tip of the hot arm increased with voltage as summarized in Table 4 and plotted in Fig. 5. This was also consistent with expectation since maximum temperatures were recorded at the free tip of the hot arm.

Maximum stress levels were observed near the fixed end of the actuator, and near the free tip. Sample results of maximum von Mises stress values are summarized in Table 5 and plotted in Fig. 6.

Thermal and Structural Response From Variations in the Cold Arm Width. Results of the sensitivity analysis with respect to variations of the cold arm of the actuator are summarized in Table 6, Fig. 7, and Fig. 8. It can be seen that increasing the

Table 4 Tip displacement versus voltage

Voltage (V)	Displacement (μm)
0	0
0.5	0.49
1.0	1.949
1.5	4.325
2.0	7.413
2.5	10.8
3.0	14.1

Table 5 Maximum von Mises stresses as a function of voltage

Voltage (V)	Maximum von Mises Stress (Pa)
0	0
0.5	26.19
1.0	66.54
3	502.64

Table 6 Results of sensitivity analysis from variations of the cold arm width

Scale Factor	Temperature (K)	Displacement (μm)
0.5	1149	12.4
1.0	1254	14.14
1.5	1302	14.85
2.0	1328	15.25

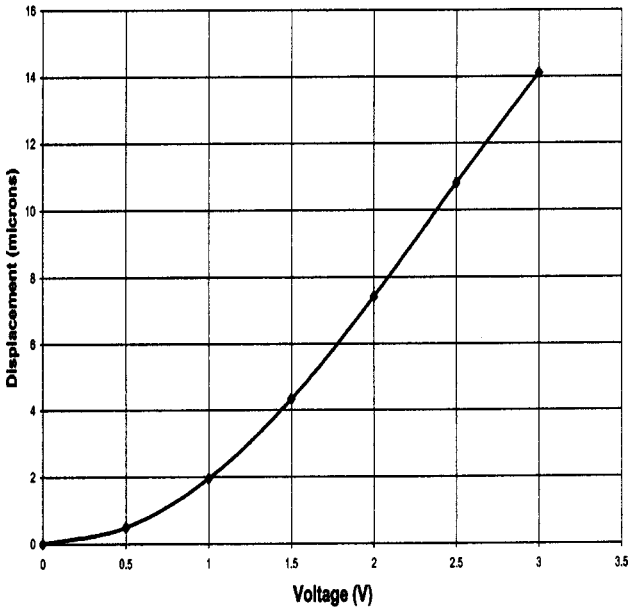

Fig. 5 Tip displacement versus voltage

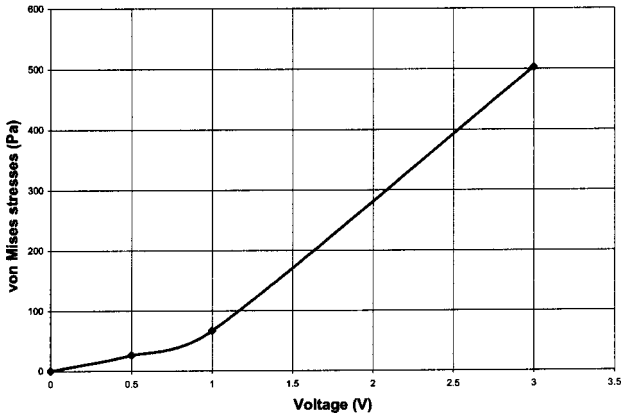

Fig. 6 Values of von Mises stresses versus voltage

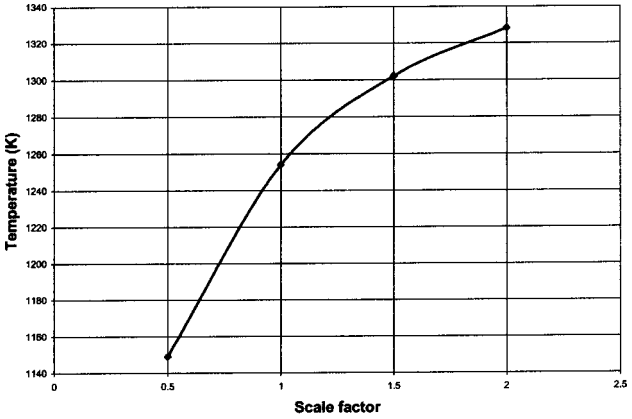

Fig. 7 Tip temperature versus scale factor

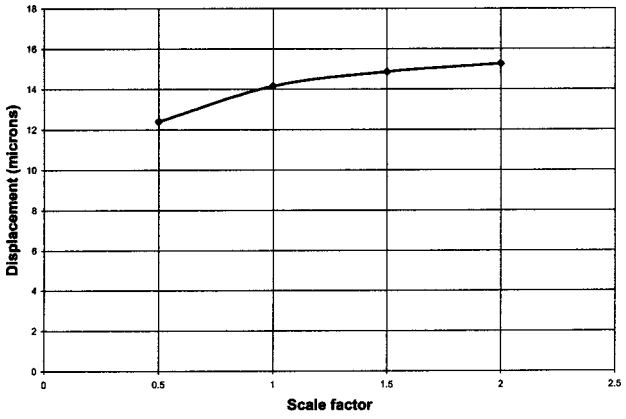

Fig. 8 Tip displacement versus scale factor

width of the cold arm increased both the temperature and the maximum tip displacement. Improvement in the sensitivity of the actuator from variations of the width of the cold arm was far less dramatic than sensitivity improvements from voltage variations. This is quite evident when Fig. 5 and Fig. 8 are compared side by side. For this reason, detailed stress analysis of the actuator as a function cold arm width was not conducted since it was deemed not critical.

Conclusions

This study was successful in advancing the understanding of working principles of horizontal thermal actuators in MEMS. Finite Element Analysis was used to simulate the response of a thermal actuator under variable input voltages, and geometric parameters. Voltage variation resulted in better sensitivity of the actuator, with displacements and temperatures that varied in proportion to the joule heating rates. Increasing the width of the cold arm had minimal sensitivity improvement due to the added bulk of the actuator. Further thermal-stress analysis was conducted using the finite element method. In this study, thermally induced strains as well as the cantilever-type structural boundary conditions of the actuator were applied to compute the stress fields in the actuator. The safe limits of the actuator can be determined by keeping track of stress levels as the voltage and actuator dimensions are changed. An important outcome of this study is its value as a potential design tool for the safe limits of operation of the actuator.

References

[1] Hsu, T. R., 2002, *MEMS & Microsystems Designs and Manufacture*, McGraw-Hill.
[2] Rebeiz, G. M., 2003, *RF MEMS: Theory, Design and Technology*, John Wiley.
[3] Madou, M., 2002, *Fundamentals of Microfabrication, the Science of Miniaturization*, CRC Press.
[4] Hak, G. E., 2002, *The MEMS Handbook*, CRC Press.
[5] Nguyen, T. C. H., Tang, W. C., and Howe, R. T., 1989, ''Laterally Driven Polysilicon Resonant Microstructures,'' Sens. Actuators, **A20**, pp. 25–32.
[6] Sentura, S. D., Mehregany, M., Nagarkar, P., and Lang, J. H., 1990, ''Operation of Microfabricated Harmonic and Ordinary Side-Drive Motors,'' *Proc. IEEE MEMS*, pp. 1–8.
[7] Fujita, H., 1997, ''A Decade of MEMS and its Future,'' *Micro Electro Mechanical Systems*, MEMS '97, Proceedings, IEEE, Tenth Annual International Workshop, pp. 1–7.
[8] Que, L., Park, J. S., and Giachandani, Y. B., 1999, ''Bent Beam Electro-Thermal Actuators for High Force Application,'' *Proc. MEMS '99.*

A Comparative Study of Cooling of High Power Density Electronics Using Sprays and Microjets

Matteo Fabbri

Shanjuan Jiang

Vijay K. Dhir
e-mail: vdhir@seas.ucla.edu

Mechanical and Aerospace Engineering Department,
Henry Samueli School of Engineering and Applied Science,
University of California Los Angeles,
420 Westwood Plaza, Los Angeles, CA 90095

Direct cooling by means of jets and sprays has been considered as a solution to the problem of cooling of high power density electronic devices. Although both methods are capable of very high heat removal rates no criterion exists that helps one decide as to which one is preferable, when designing a cooling system for electronic applications. In this work, the results of an investigation of the performances of sprays and arrays of micro jets are reported. Experiments have been conducted using HAGO nozzles and orifice plates to create droplet sprays and arrays of micro jets, respectively. The liquid jets had diameters ranging from 69 to 250 μm and the pitches between the jets were 1, 2, and 3 mm. The test fluid was deionized water and the jet Reynolds number ranged between 43 and 3813. A comparison of heat transfer and pressure drop results obtained employing both sprays and jets has been carried out. The microjet arrays proved superior to the sprays since they required less pumping power per unit of power removed. A cooling module employing impinging jets was tested. Such a module would require three primary components: an orifice plate for forming jets or a nozzle to form the spray; a container to hold the nozzle, the heat source and the cooling liquid, which also serves as a heat exchanger to the ambient; and a pump which recirculates the coolant. A fan could be used to improve the heat transfer to the ambient, and it would allow the use of a smaller container. An impinging jets cooling module has been designed and tested. Heat fluxes as high as 300 W/cm^2 at 80°C surface temperature could be removed using a system which includes a 4×6 array of microjets of water of 140 μm diameter impinging on a diode 5.0×8.7 mm^2. [DOI: 10.1115/1.1804205]

Introduction

As the chip fabrication technology keeps improving, smaller and more powerful components are introduced in the market. The traditional air cooling techniques are proving to be inadequate in removing the high heat fluxes generated by these new microchips and new ways are being sought to cool the components. Hence, active cooling methods are now being seriously considered, particularly those that can provide high heat transfer rates.

Liquid droplet sprays and jet impingement cooling have been widely used in the metal manufacturing industry and have been shown capable of high heat removal rates. Researchers have investigated the possibility of applying such techniques to the cooling of electronic components. In this study the ultimate goal was to develop a close loop system where the liquid is sprayed directly on the back surface of the microchip thereby removing the heat. The liquid is then collected and cooled down in a small heat exchanger, and finally is recirculated with a pump.

The droplet sprays can have the form of a mist, and impinge on the surface with a random pattern or they can be formed by one or more streams of droplets which impinge upon the surface with a fixed pattern. If the frequency of the streams is high enough, the droplets merge forming continuous liquid jets. After hitting the surface, the liquid droplets spread and, if the spreading area is small enough a continuous thin liquid film covering the surface is formed. If the wall superheat is high, a thin vapor layer can be present underneath the droplets or the thin liquid film. The heat transfer process is transient and it involves liquid and vapor convection, thin film evaporation, and air convection. The areas not covered by the film dry out.

When continuous liquid jets are employed, the liquid film covering the surface is continuous and the heat is removed mainly by convection. Evaporation from the thin film may occur at high heat fluxes or low flow rates.

The physics governing the heat removal process by droplet sprays is very complex and still is not completely understood, and few theoretical models are available in the literature. Hence, it has turned out to be easier to investigate the various aspects of the problem by performing experimental work. Several studies have been conducted in the past on sprays, but most of them deal with the boiling regime, which was not considered in the present work. Air driven sprays obtained using atomizer nozzles are not considered in this study either because they would be impractical to use in a closed system for electronic cooling.

Literature Review. Because it is associated with high heat removal rates, jet impingement cooling has been the cooling technique of choice for many industrial applications, such as cooling of metal sheet or high power lasers. Many studies have been conducted in recent years to investigate the heat transfer occurring during the impingement process. Most of the attention has been on single phase heat transfer, but several studies have also been carried out in the boiling regime as well. In this work only free surface circular jets are considered (liquid jets injected into a gaseous environment). Submerged liquid jets yield slightly higher heat transfer rates than free surface jets but are subject to higher pressure drops. On the other hand, gaseous jets do not yield high heat transfer rates. Both submerged liquid jets and gaseous jets are not considered in this study.

Webb and Ma [1] and [2–19] published a thorough review of the experimental and theoretical studies on single-phase jet impingement heat transfer. In their study most of the experimental data were obtained in the turbulent regime but the modeling was only performed for the laminar regime. An important conclusion

Contributed by the Heat Transfer Division for publication in the JOURNAL OF HEAT TRANSFER. Manuscript received by the Heat Transfer Division May 12, 2004; revision received July 24, 2004. Associate Editor: C. Amon.

was that the heat transfer under a free surface liquid jet decreases rapidly as one moves away from the stagnation point towards the periphery.

Elison and Webb [2] presented the results of an experimental study where they investigated the heat transfer associated with a single water jet. Three nozzles, with diameters of 0.584, 0.315, and 0.246 mm were tested. These nozzles were long enough to allow for a fully developed velocity profile under any circumstances. They found that in the laminar regime the Nusselt number (Nu) varied as $\mathrm{Re}_{d_n}^{0.8}$, where $\mathrm{Re}_{d_n}=\rho V d_n/\mu$ is the jet Reynolds number, whereas previous studies had shown that $\mathrm{Nu}\propto\mathrm{Re}_{\mathrm{dn}}^{0.5}$. They thought that this difference was caused by surface tension effects at the nozzle exit, which increased the actual jet diameter.

Multiple jets impinging on a heater surface can improve the spatial uniformity of the heat transfer coefficient on the surface. Jiji and Dagan [3] carried out an experimental study of multiple single-phase free surface jets impinging on an array of microelectronic heat sources. In their experiments, square jet arrays of 1, 4, and 9 jets impinged on a square heat source 12.7×12.7 mm^2 in area. FC77 was the test liquid used. They noticed that the surface temperature became more uniform as the distance between the jets was decreased. They also did not find any changes in the heat transfer as the ratio of the nozzle to heater distance (z) and the jets' diameter (d_n) varied between 3 and 15. The area averaged Nusselt number ($\overline{\mathrm{Nu}}$) was correlated as

$$\overline{\mathrm{Nu}_L}=3.84\,\mathrm{Re}_{d_n}^{1/2}\,\mathrm{Pr}^{1/3}\left(0.08\frac{L}{d_n}N+1\right) \tag{1}$$

where L is the heater length and N is the number of jets.

This correlation was developed based on the following parameters: jet pitch to diameter ratios (s/d_n) of 5.08 and 10.16, two jets diameters, 0.5 and 1.0 mm, jet velocities between 2.2 and 14.5 m/s, and Re_{dn} between 2800 and 12,600. They had only two data points with water as the test liquid (single jet of 1 mm diameter, $\mathrm{Re}_{dn}=10{,}000$ and 20,000). They concluded that, for flow rates less than 20 ml/s and a heater area of 1.61 cm^2, the thermal resistance was of the order of 1 K/W when the coolant was FC77, and of the order of 0.1 K/W when the coolant was water. Using the correlation they developed, they predicted that for FC77 it was possible to remove approximately 100 W/cm^2 with an array of nine jets of 0.3 mm in diameter at a flow rate of 10 ml/s, when the temperature difference between the jet and the impinged surface was 60°C.

Pan and Webb [4] investigated the local heat transfer under two different array configurations of water jets: a 3×3 inline array and a seven jet staggered array. They found that the stagnation Nu was independent of the interjet spacing, but depended on the nozzle to plate spacing. The local heat transfer for the two different arrays was not found to differ substantially; only minor differences were noted in the radial flow region between the jets. They also noted that at $z/d_n=2$ the central jet was submerged, while at $z/d_n=5$ it was a free surface jet. They correlated the average heat transfer coefficient as

$$\overline{\mathrm{Nu}_{d_n}}=0.225\,\mathrm{Re}_{d_n}^{2/3}\,\mathrm{Pr}^{1/3}e^{-0.095(s/d_n)} \tag{2}$$

This correlation is valid for the following range of parameters: $2\leqslant s/d_n\leqslant8$, $2\leqslant z/d_n\leqslant5$, and $5000\leqslant\mathrm{Re}_{dn}\leqslant20{,}000$. The jet diameters used in these tests were 1, 2, and 3 mm, respectively.

If only the data for higher z/d_n values (only free jets) were considered then Pan and Webb [4] reported a better fit of their experimental data using the expression,

$$\overline{\mathrm{Nu}}=0.129\,\mathrm{Re}_{d_n}^{0.71}\,\mathrm{Pr}^{0.4}\exp\left(-0.1\frac{s}{d_n}\right) \tag{3}$$

Womac et al. [5] experimentally investigated two different jet array configurations (2×2 and 3×3 jets). They used water and FC77 to cover a range of Prandtl numbers between 7 and 24. Two jet diameters of 0.513 and 1.02 mm were employed, and two pitches of 5.08 and 10.16 mm were tested. The Reynolds numbers covered both the laminar and the turbulent regimes, ranging from 500 to 20,000. The range of the other significant parameters was $4.98\leqslant s/d_n\leqslant19.8$ and $9.9\leqslant z/d_n\leqslant20$. The heat transfer was unaffected by changes in z/d_n within the range tested, but an increase was detected when for a given flowrate the jet velocity was increased. However, a substantial reduction in the heat transfer was found to occur when lowering the liquid flowrate for very low flowrates. They claimed that this behavior was caused by the bulk heating of the fluid (i.e., the thermal boundary layer reaches the free surface of the liquid film).

Using the results of an earlier work on single jets [6], they used an area weighted method to account for the differences in heat transfer in the stagnation and in the radial flow regions to correlate the data. The resultingcorrelation was given as,

$$\overline{\mathrm{Nu}_L}=\left[0.516\,\mathrm{Re}_{d_i}^{0.5}\left(\frac{L}{d_i}\right)A_r+0.344\,\mathrm{Re}_{L*}^{0.579}\left(\frac{L}{L*}\right)(1-A_r)\right]\mathrm{Pr}^{0.4} \tag{4}$$

where $A_r=N\pi d_i^2/4L^2$, $V_i=(V_n^2+2gz)^{0.5}$, $d_i=(V_n d_n^2/V_i)^{0.5}$, L is the heater length, and L^* is an estimate of the average distance associated with radial flow in the wall jet regions of the heater and is given by $L^*=(\sqrt{2}+1)s-2d_i/4$.

Yonehara and Ito [7] carried out an analytical study of the heat transfer under a square array of impinging free surface liquid jets on an isothermal surface. The resulting correlation was given as

$$\overline{\mathrm{Nu}}=2.38\,\mathrm{Re}_{dn}^{2/3}\,\mathrm{Pr}^{1/3}(s/d_n)^{(-4/3)} \tag{5}$$

They also performed experiments to validate their model. They found good agreement between the experimental data and the analytical results for $\mathrm{Re}_{dn}/(s/d_n)^2\geqslant5$. The tests were conducted for the following range of parameters: $13.8\leqslant s/d_n\leqslant330$, $7100\leqslant\mathrm{Re}_{dn}\leqslant48{,}000$.

Another study involving arrays of jets was carried out by Oliphant et al. [8], in which the performance of sprays and arrays of liquid jets were compared. They utilized arrays of 4 and 7 jets of deionized water impinging on top of a 1.9 cm diameter aluminum cylinder. A cartridge heater was placed in the aluminum cylinder and 6 thermocouples were used to measure the temperatures under the wetted surface. The surface heat flux, surface temperature, and heat losses were calculated from the measured temperature profile. Two jet diameters were used: 1 and 1.59 mm. The jet Reynolds numbers investigated in the study ranged between 3150 and 11,300 (41.8–178.46 kg/m^2 s). The jets were spaced such that each covered an equal fraction of the total heat transfer area.

In order to produce the spray, the orifice plate, used to generate the jets, was substituted with a full-cone, air-assisted atomizer (Delavan Airo Type B). Mass fluxes between 1 and 30 kg/m^2 s were investigated. The manufacturer's specified mean Sauter diameter for the droplets was 50 μm. Plotting the heat transfer coefficient as a function of the mass flux, they concluded that both spray and jets have heat transfer coefficients of the same order of magnitude, but the spray required a lower mass flux. They also stated that if the data for the spray are extrapolated to the same mass flux range as that of the jets, ''the spray impingement is significantly more effective than the liquid jet arrays''. However, no particular effort was made towards investigating or understanding the effect of the parameters which affect the heat transfer under liquid jet arrays.

The jet diameters used in the study by Oliphant et al. [8] can be considered large for electronic cooling applications and so can the mass fluxes utilized to generate the jets. Also, the conclusions reached in [8] are limited to the particular case studied. In fact it is not fair to conclude that sprays are better than jets in a general way, unless the performance of optimal configurations for both sprays and jets are compared with each other.

Jiang [9] performed a few experiments using circular arrays of free surface water jets having very small diameters, 50, 100, and

Table 1 Range of parameters for the experimental work of Ghodbane et al. [2] and Holman et al. [3]

Variable	Range [2]	Range [3]	Units
$\dot{V}$	5–126	6.3–56.8	ml/s
d_n (max free passage)	0.63–2.38	0.635–1.27	mm
z	180–350	184.2–193.7	mm
v_{br}	5.4–28	11.4–28.5	m/s
d_d	210–980	96–343	μm
T_w	20–90	20–80	°C
T_{liq}	5–10	4–10	°C
q	0.12–50	0.28–25.2	W/cm^2
$We=\rho_{liq}v_{br}^2 d_d/\mu_{liq}$	2200–13,750	2400–11,775	
$Re=\rho_{liq}v_{br}d_d/\mu_{liq}$	2557–61,878	4875–12,850	
Pr	7.5–10.5	6.0–10.7	

150 μm. The interjet spacing used was 1, 2, and 3 mm. The Reynolds numbers varied from 410 to 4740, and were much lower than those investigated by other researchers. Another unique feature of her experiments was that the mass fraction of air in the environment surrounding the jets was controlled. Experiments were conducted both at very low air partial pressures, 2 to 4 kPa, and also at partial pressures close to 101 kPa. The total system pressure was maintained at 101 kPa. The experiments revealed a surprising increase in the single-phase heat transfer coefficient as the air content of the ambient was reduced. This is most probably due to an increase in the evaporation rate from the liquid film on the heater. Unfortunately the data collected was limited.

Recently Fabbri, Jiang and Dhir [10] have studied the heat transfer occurring under arrays of impinging jets with diameters between 69 and 250 μm. They were able to remove heat fluxes as high as 250 W/cm^2 at relatively low surface temperatures using deionized water as the coolant. They didn't limit their investigation to water but also used FC40 in order to cover a broader range of Prandtl numbers. Based on the experimental data, a correlation that predicted all the data within ± 25 percent was obtained as

$$\overline{\mathrm{Nu}} = 0.043\,\mathrm{Re}_{d_n}^{0.78}\,\mathrm{Pr}^{0.48}\exp\left(-0.069\,\frac{s}{d_n}\right) \tag{6}$$

The range of parameters of validity of Eq. (6) was $43 \leqslant \mathrm{Re}_{d_n} \leqslant 3813$, $2.6 \leqslant \mathrm{Pr} \leqslant 84$, and $4 \leqslant s/d_n \leqslant 26.2$. Nu predicted by Eq. (6) were quite different from those predicted from the correlations of Womac et al. [5], Pan and Webb [4], Yonehara and Ito [7].

Bonacina et al. [11] presented a study in which they developed a one-dimensional conduction model for multi drop evaporation. They compared the predictions from the model to the experimental results they obtained using water droplets impinging on an aluminum surface, at low wall superheats. The average droplet size was approximately 400 μm and the impinging velocity was between 1 and 2 m/s. They used cameras (both still and video) to obtain information about the fraction of the heater area covered by the droplets. The highest heat transfer coefficient achieved in the experiments was 150 kW/m^2 K, and the maximum heat flux was 220 W/cm^2. The experimental data matched well with their prediction.

Ghodbane and Holman [12] and Holman and Kendall [13] studied spray cooling on constant heat flux vertical surfaces. They tested full-cone circular and square hydraulic nozzles with Freon-113 as test liquid. Two square heat transfer surfaces were studied (7.62×7.62 cm^2 and 15.24×15.24 cm^2) and from that they concluded that the heat transfer is independent of the impinged area as long as the spray is uniform. They also found that the heat transfer increases almost linearly with the droplet mass flux, and that a high degree of subcooling causes higher superheat for the onset of nucleate boiling and CHF. They correlated all the data obtained in [12] and [13] by the expression

$$\frac{qz}{\mu_{liq}h_{fg}} = 9.5\mathrm{We}^{0.6}\left(\frac{c_{p\_liq}(T_w - T_{liq})}{h_{fg}}\right)^{1.5} \tag{7}$$

where We is the droplet Weber number and it was defined as

$$\mathrm{We} = \rho_{liq}v_{br}^2 d_d \sigma^{-1} \tag{8}$$

and v_{br} is the droplet breakup velocity given by

$$v_{br} = (v_1^2 + 2\Delta P/\rho_{liq} - 12\sigma/\rho_{liq}d_d)^{0.5} \tag{9}$$

They opted to calculate the droplet mean Sauter diameter according to the correlation developed by Bonacina et al. [14], since it had the best agreement with the nozzle manufacturer's specifications. That equation was given as

$$d_d = \frac{9.5d_n}{\Delta P^{0.37}\sin(0.5\beta)} \tag{10}$$

In Eq. (10) all properties except for h_{fg} were evaluated at the mean film temperature. The range of parameters for their experiments is given in Table 1.

Cho and Ponzel [15] experimentally investigated spray cooling of a heated solid surface using subcooled and saturated water. They tested three full-cone nozzles having orifice diameters of 0.51, 0.61, and 0.76 mm, respectively. The distance between the nozzle and the 50 mm diameter copper heated surface was 30 mm. Three liquid flowrates were tested (8.7, 5.4, and 3.7 ml/s). From the analysis of their data, Cho and Ponzel concluded that the droplet size was important only when evaporation occurred on the liquid film deposited on the impinged surface. Even though most of the data showed that the liquid flow rate had negligible effect on the heat transfer in single-phase, for the case of the 0.51 mm diameter nozzle, where a flowrate of 1.8 ml/s was also tested, the heat transfer improved as the flowrate increased. They correlated the single-phase heat transfer data as a function of Reynolds and Prandtl number as

$$\overline{\mathrm{Nu}} = 2.531\,\mathrm{Re}^{0.667}\,\mathrm{Pr}^{0.309} \tag{11}$$

where

$$\mathrm{Re} = \rho_{liq}\dot{V}/A_H d_d/\mu_{liq} \quad \text{and} \quad \overline{\mathrm{Nu}} = h d_d/k_{liq}$$

They used the empirical formula developed by Mudawar et al. [16] given in Eq. (12) to calculate the droplet diameter. The fluid properties were evaluated at the mean film temperature.

$$d_d = 3.67 d_n[\mathrm{We}_{d_n}^{0.5}\,\mathrm{Re}_{d_n}]^{-0.259} \tag{12}$$

It is not unreasonable to consider deionized water as a coolant for electronic applications, provided the components are electrically insulated from the fluid. Shaw et al. [18] successfully provided electrical insulation by applying, through a vapor phase process, a 25 μm thick coating of Parylene to the exposed surfaces of a commercial 3-phase IGBT power module. The power

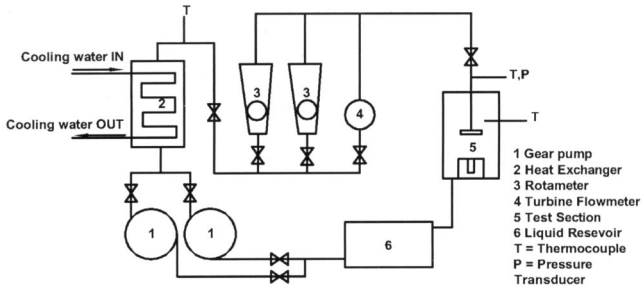

Fig. 1 Schematic of the experimental setup

Table 2 Details of the orifice plate

s mm	d_n exit μm	STD μm	d_n inlet μm	STD μm	Thickness mm
1	69.3	1.5	94.3	2.9	0.51
2	76.4	3.3	139.5	6.3	0.51
3	122.6	6.0	69.2	4.5	0.63
1	118.7	4.7	136.8	9.7	0.51
2	113.8	3.9	167.5	6.3	0.51
3	116.3	5.4	184.8	6.3	0.51
1	182.1	8.3	263.8	10.0	0.51
2	178.5	5.8	228	9.6	0.51
3	173.6	5.1	263	8.7	0.51
1	250	n.a.	n.a.	n.a.	0.51

module, which was part of a 15-hp variable-speed AC motor drive system was then directly cooled with deionized water jets. No electrical leakage was detected even though the power module operated with high standoff voltages of about 325 VAC.

The purpose of this study is first to compare the heat transfer performance of liquid droplet sprays and micro jet arrays in a range of parameters suitable for electronic cooling applications, and to find out under what conditions one is better than the other. Experiments have been carried out with both sprays and arrays of micro jets in the single-phase regime. Secondly, to demonstrate the capabilities of a cooling module based on impinging microjets. A prototype with a diode as heat source has been built and tested.

Experiments

Experimental Apparatus

Microjets Setup. In order to carry out a comparison between the performances of jets and sprays some of the results obtained from an experimental investigation by Fabbri et al. [10] are used together with the experimental results of tests performed on the same experimental set up using a HAGO nozzle to generate droplet sprays.

An experimental rig was designed and built to test ten different arrays of jets. Figure 1 shows a schematic of the experimental setup. The coolant is circulated with two variable speed gear pumps, installed in parallel. Two rotameters and a turbine flowmeter were installed in parallel to measure the flow rate of the liquid being sprayed. The accuracy of these flow meters is ± 3 percent. Before entering the flowmeters, the coolant passed through a heat exchanger, where it was cooled down to the specified spray temperature. The liquid was then pushed through a 0.5 mm thick stainless steel orifice plate to form the jets. The holes in the plate were laser drilled and were arranged in a circular pattern giving a radial and circumferential pitch of 1 mm for 397 jets, 2 for 127 jets and 3 for 61 jets.

Unfortunately, the laser drilling process was not very accurate when dealing with such small dimensions. Visual inspection of the orifice plates under a microscope showed that the holes in the plate were slightly tapered and not exactly circular. Based on photographs of the orifice plates, taken using a camera attached to the microscope, the size of the holes were determined. These values are listed in Table 2. Measurement of the diameters on both sides of the plate confirms that the holes are tapered. The taper also varies from hole to hole.

The orifice plate was attached with screws to a stainless steel adapter, which was in turn connected to the flowmeters with a pipe. The pipe passed through a flange positioned on top of the heat transfer surface. The pipe could be moved in the vertical direction so that the distance between the orifice plate and the heat transfer surface could be adjusted to the desired value. The liquid pressure was measured before the stainless steel adapter using an Omega PX202-300AV absolute pressure transducer (0–2.07 MPa), which had been factory calibrated and that had an accuracy of 0.25 percent and a zero balance within 1 percent of full scale.

The jets impinged on a 19.3 mm diameter top surface of a copper cylinder, which represented the backside of an electronic microchip. The copper cylinder was enclosed in a Teflon jacket that provided thermal insulation. The cylinder had a larger cylindrical base (76.2 mm in diameter and 16.5 mm in length), which contained six 750 W cartridge heaters. The power to the heaters was controlled with a variac. Four K-type thermocouples, soldered at different axial locations (5 mm apart starting from 1.8 mm below the top surface) along the central axis of the cylinder were used to measure the temperature profile. The heat flux and the temperature of the heat transfer surface were calculated from the measured temperature profile.

Figure 2 shows a schematic of the test chamber. The Teflon jacket—copper block assembly was mounted on a stainless steel plate. The sprayed liquid was drained back to reservoir installed below the test section. Thermocouples to measure the liquid temperature were installed both upstream of the flow meters and downstream of the orifice plate. Another thermocouple was used to measure the ambient temperature. All the data were recorded using two IOTech 16-bit data acquisition boards.

It is important to note that the outer one or two rings of jets, depending on the pitch used, did not directly hit the copper surface but instead impinged on the surrounding Teflon surface. Thus, the actual number of jets impinging directly on the copper surface was 37, 61, and 271 for 1, 2, and 3 mm pitch, respectively.

Spray Setup. The experimental rig used for the testing of droplets spray is the same as the one used for the microjets, but instead of orifice plates a HAGO nozzle was installed above the copper heat transfer surface. Originally designed for use with home power spray humidifiers, this nozzle produces the finest possible atomization with direct water pressure operation. The minimum operating pressure is 274.8 kPa gage pressure but increasingly finer droplets result from higher operating pressures. Each nozzle is individually spray tested for flow rate, spray angle, and spray quality. The standard spray angle is 70 deg.

The extremely fine atomization achieved by the Type B nozzle has resulted in it being used extensively in applications where fine atomization and precise flow rates are required such as evaporative cooling, humidification, moisture addition and misting. The

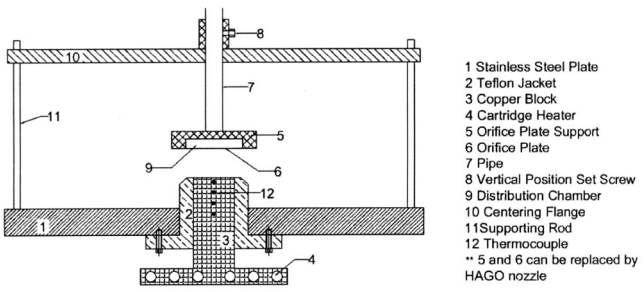

Fig. 2 Details of the test section

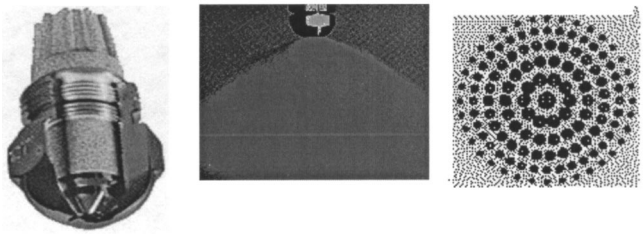

Fig. 3 HAGO nozzle and spray details

"DFN" type nozzle is designed for low flow rates (18.9 ml/min to 63 ml/min). It employs two sintered bronze filters, which give more surface filtration. The specific type of the nozzle used in this study is "DFN" B100. Figure 3 shows a picture of the nozzle, of the spray cone, and of the droplets pattern on the impinged surface. The mean Sauter diameter of droplets for the DFN-B100 nozzle at 274.8 kPa gage pressure is 44 μm according to the manufacturer. The orifice diameter of the spray nozzle is 356 μm.

Cooling Module. An impinging jets based cooling module requires three primary components: an orifice plate for forming jets; a containment vessel to hold the nozzle, the heat source and the cooling liquid, which also serves as a heat exchanger to the ambient; and a pump which recirculates the coolant. A fan could be used to improve the heat transfer to the ambient, and that would also allow the use of a smaller container. From a thermal management point of view, the heat is first transferred from the heat source (the electronic component), to the sprayed liquid. This causes part of the liquid to evaporate. Heat is transferred from the hot liquid and vapor to the ambient by conduction through the container's walls. Details of a cooling module based on this idea are discussed below.

The cooling module, shown in Fig. 4, consists of an aluminum box with internal dimensions of 50×50×65 mm and wall thickness of 3.175 mm. At the bottom, the box is closed with a 3.175 mm thick stainless steel plate. A 6.25 mm thick aluminum flange, welded to the box walls, provides the interface for the bottom plate and the space for an o-ring.

Inside the container, a stainless steel orifice plate is installed on a support located above the heat source, as shown in Fig. 5. The heat source consists of a diode used in current controlled mode to avoid high voltages. The diode is mounted on a Direct Bond Copper (DBC) substrate layer, which is in turn glued on top of a G10 insulating base (not shown in Fig. 5). The diode is 8.68×4.97 mm in size. The electrical connections are provided by means of two copper rods, 3.175 mm in diameter. Four threaded rods hold both

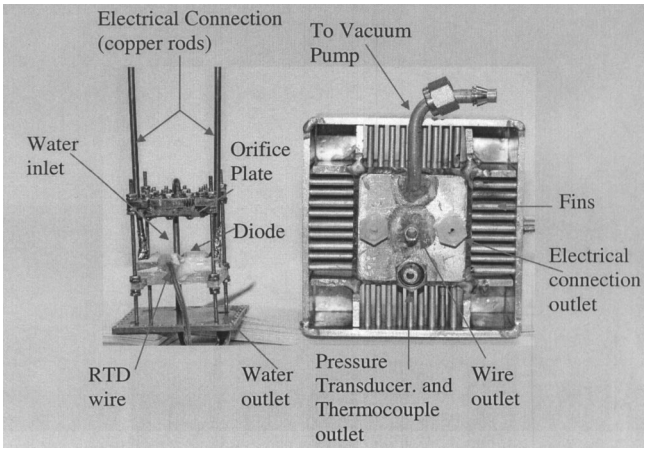

Fig. 4 Cooling module

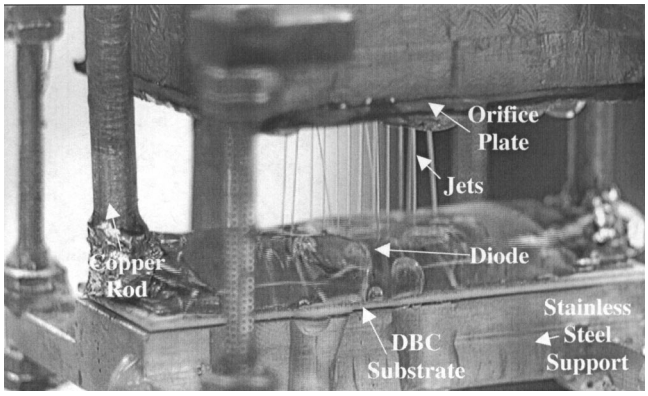

Fig. 5 Details of the diode and the jets

the diode and the orifice plate assembly together and allow adjustment of the relative distance between the diode and the orifice plate. The threaded rods are screwed into the stainless steel plate, which forms the bottom of the box.

The orifice plate, 0.5 mm thick, has 24 holes (140 μm in diameter), distributed on a square array pattern with 2 mm spacing. Details of the orifice plate are given below. A 3.175 mm OD stainless steel tube connects the orifice plate to the outlet of the pump. The loop is closed with a 6.25 mm OD stainless steel tube connecting the bottom plate to the pump inlet. Aluminum pin fins, 20 mm long and 3.175 mm in diameter, are installed on the outside of the container in a 45 deg staggered pattern with both pitches equal to 10.16 mm. The fin tips are inserted into holes drilled into four aluminum plates, which are welded at the corners and form an external shroud. A small DC fan is mounted at the bottom which pushes ambient air over the fins. The air is forced only over the fins, since the gaps in the corners between the external shroud and the fin array were blocked off. Figure 6 shows a schematic of the experimental apparatus.

K-type thermocouples are used to measure the air temperature at the inlet and outlet of the fin array, the inlet water temperature, and the temperature of the environment in the chamber. Two RTD's are used to measure the temperatures on the top of the diode and on the back of the DBC, as shown in Fig. 7.

An absolute pressure transducer is also installed to measure the pressure in the chamber. An outlet for the RTD's connecting wires and the electrical connections is provided on the top of the box. To check the liquid level inside the box a short piece of Tygon tubing is installed on the outside between the top and the bottom of the box.

Two pressure taps are present on one of the external plates and are connected to a differential pressure transducer, which measures the pressure drop across the fins. A variable speed gear pump is used to pump the liquid through the pipes and the orifice

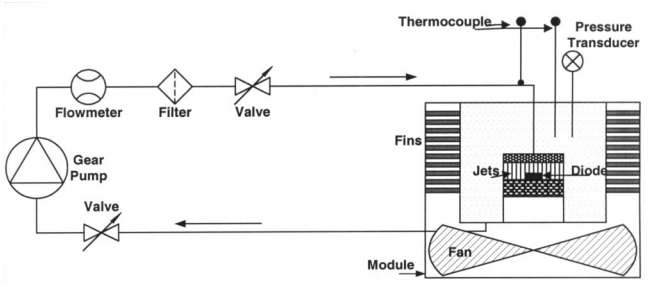

Fig. 6 Cooling module set up

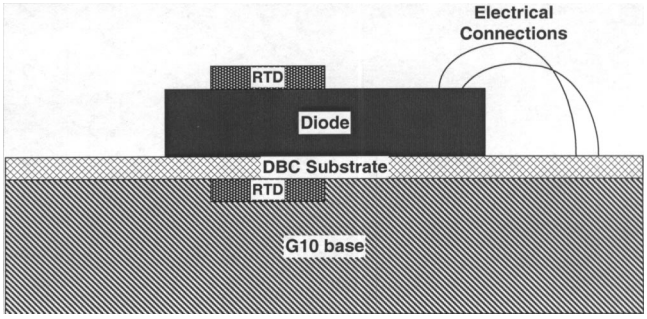

Fig. 7 Schematic of the RTDs placement

plate. The liquid flow rate is measured using a rotameter. The overall dimensions of the whole module, including the fan, are 100×100×130 mm.

Experimental Procedure

Microjets and Spray Experiments. The thermocouples were calibrated prior to installation, by submerging them in an ice bath and in boiling water, and comparing the readings with those provided by a high accuracy mercury thermometer (±0.1°C). Prior to running the experiments, the copper surface was polished using a 600 grit sandpaper and then a copper polishing solution, which resulted in a smooth and shiny surface. Thereafter, in order to guarantee the same surface condition throughout the duration of the experiment, the surface was oxidized in air for five hours at 320°C. The contact angle for a water droplet placed on the oxidized copper surface was measured to be 44°.

After the pumps were started, and the liquid flow rate set to the desired value, the cartridge heaters were energized. Once all the parameters reached steady state, the values were recorded for 100 s at a sampling rate of 1 Hz. The data acquisition system allowed real time monitoring of all the parameters in both digital and graphical form so that it was possible to assess when steady state had been reached. Thereafter, the power to the copper block was increased and a new set of data recorded. The experiment was stopped when either the surface temperature was above the boiling point or when the temperature at the base of the copper block rose above 350°C, which could damage the Teflon jacket and the electrical wires.

Cooling Module Experiments. Before the experiment was started, the thermocouples were calibrated by submerging them in a pool of boiling water and in an ice bath, whose temperatures were measured with a mercury thermometer with an accuracy of ±0.1°C. The absolute pressure reading from a pressure transducer (accuracy ±325 Pa) was used to determine the saturation temperature of water and this was then compared with the value given by the thermometer submerged in a pool of boiling water. The two values were found to be within ±0.1°C.

The module was first charged with 40.8 ml of deionized water at room temperature. Subsequently the pump was started and the flow rate was set to the desired value. Thereafter, the internal pressure of the chamber was reduced by means of a vacuum pump. At steady-state chamber conditions, the vapor partial pressure was calculated, using steam tables, assuming the temperature measured in the chamber is equal to the vapor saturation temperature at the computed vapor partial pressure. Thereafter, power was supplied to the diode and the data were recorded.

Assuming that the relative humidity inside the chamber is equal to 100 percent, the air partial pressure can be calculated using Dalton's law, as the difference between the total pressure and the vapor partial pressure. The thermocouples, RTDs and chamber pressure readings were recorded with a 16-bit Strawberry Tree data acquisition system. The voltages supplied to the diode, the fan and the differential pressure transducer readings were recorded using a Fluke multimeter. The current through the diode was read directly from the power supply and the current through the fan was measured using a Fluke multimeter.

Once steady state was reached, either the power supplied to the diode or the fan speed was varied. Due to the fact that thermocouples could not be used to measure the diode's temperatures and that the RTD's contact area was not negligible compared to the total area of the diode, a preliminary series of runs was performed. In those tests, for each diode—DBC assembly was tested, with one RTD attached on top of the diode and one on the back of the DBC layer. This was done to determine the thermal resistance across the diode. The relationship between the temperatures on the front and back sides of the diode was found to be linear. While conducting the experiments reported in this work, the top RTD was removed to expose the whole top surface of the diode to the jets.

The very small air flowrates, produced by the Flight II 80 DC fan (Comair-Rotron, 80×80×25 mm in size) could not be measured directly. To determine the flowrate, the relationship between the fan voltage and the pressure drop across the fins was first established. Thereafter, air from a compressor, at a known flow rate measured with a Dwyer rotameter, was blown over the fins and the pressure drop was measured again. Finally, the relationship between airflow rate and fan voltage was established.

The minimum and maximum uncertainties for the data are as follows:

- Power ±4.2 percent at 130 W and ±8.1 percent at 20 W
- Heat flux ±4.2 percent and ±8.1 percent
- Temperature ±0.1°C
- Thermal resistances ±4.2 percent and ±8.7 percent
- Heat transfer coefficient ±4.2 percent and ±8.6 percent

The minimum values occurred when the power was the highest and consequently the temperature differences between the chip surface and the chamber and between the chamber and the ambient air were also close to their highest values. On the other hand, the maximum uncertainty occurred when the power level was low, and the temperature differences were also low. In such situations, the uncertainty on the individual measurements had a greater impact on the calculated quantities.

Data Reduction

Microjets and Sprays Experiments. For each data set recorded, the heat flux at the heat transfer surface is given by the slope of the temperature profile obtained from the four thermocouples embedded in the copper block. The same temperature profile, which was mostly linear, allowed the temperature at the heat transfer surface to be calculated (by extrapolation).

The average heat transfer coefficient, Nusselt number, and Reynolds number were also calculated as

$$\overline{h} = \frac{q}{T_w - T_{\text{liq}}} \tag{13}$$

$$\overline{\text{Nu}} = \frac{\overline{h} d_n}{k_{\text{film}}} \tag{14}$$

$$\text{Re}_{d_n} = \frac{\rho_{\text{film}} v_{\text{jets}} d_n}{\mu_{\text{film}}} \tag{15}$$

All the physical properties are evaluated at the mean film temperature, T_{film}. The pumping power is given by the product of the volumetric flowrate and the pressure drop across either the orifice plate or the HAGO nozzle. It can be expressed as

$$Q_{\text{pumping}} = \dot{V} \Delta P_{\text{jets/nozzle}} \tag{16}$$

Repeatability of the data was verified by randomly repeating some of the cases already tested. The minimum and maximum

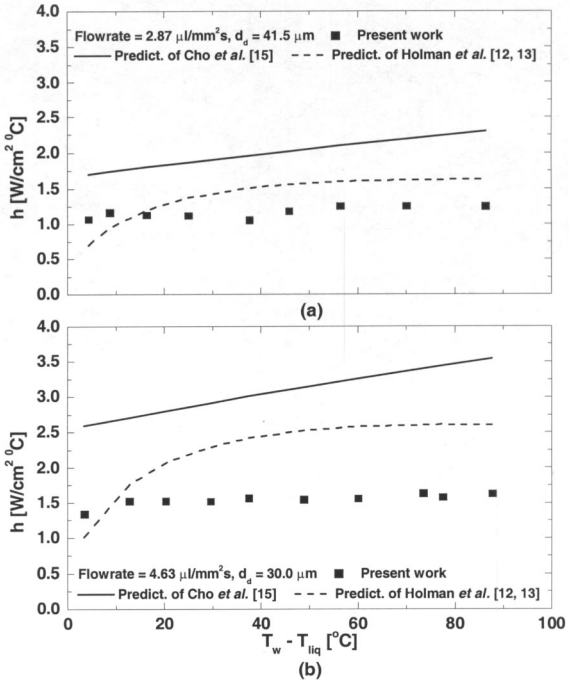

Fig. 8 Comparison of spray data for two flowrates (a) 50.56 ml/min [2.87 μl/mm^2 s] and (b) 81.56 ml/min [4.63 μl/mm^2 s], with the predictions of Holman et al. [12,13] and Cho et al. [15]

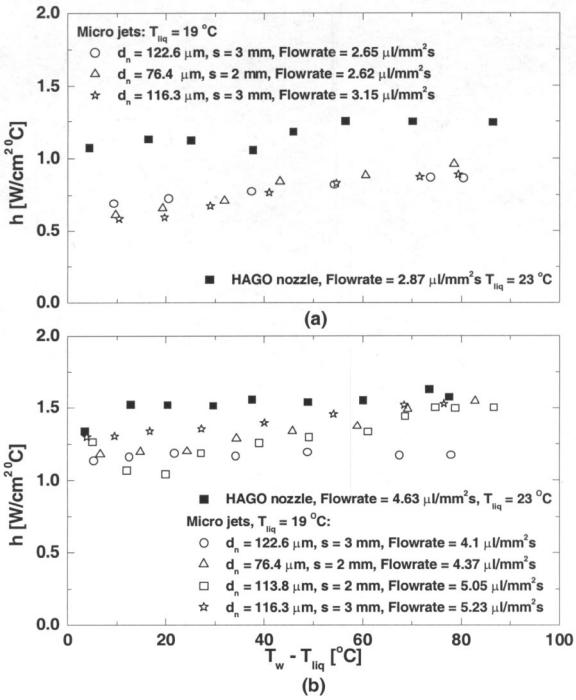

Fig. 9 Comparison between spray and micro jets performance for two flowrates (a) 50.56 ml/min [2.87 μl/mm^2 s] and (b) 81.56 ml/min [4.63 μl/mm^2 s]

uncertainties of the main parameters, which was calculated according to the procedure outlined by Kline and McClintock [17], as follows:

- Temperature ± 0.1°C
- Heat flux ± 2.7 percent and ± 28.9 percent
- Heat transfer coefficient ± 2.9 percent and ± 29.6 percent
- Nusselt number ± 6.7 percent and ± 33.0 percent
- Reynolds number ± 7.2 percent and ± 22.7 percent
- Pumping power ± 0.5 percent and ± 26.0 percent

The uncertainty of ± 28.9 percent in the heat flux occurred when the heat flux was only 1.75 W/cm^2 and it was caused by the small temperature gradient in the copper block.

Results and Discussion

Microjets and Sprays Experiments. Many different criteria can be used to evaluate the cooling performance of different systems. In this study, the heat transfer performance of droplet sprays and arrays of micro jets are evaluated by comparing results for test cases having either the same water flow rate or same heat transfer rate or same amount of power spent for the heat removal process. A suitable parameter used in this evaluation is the ratio between the power removed from the copper surface (which represents an electronic device), and the power necessary for accomplishing this task. The power consumed for the cooling process corresponds to the pumping power necessary to push the liquid through the HAGO nozzle or the orifice plate. The losses through pipes and fittings are not included. It is this parasitic power which can be of concern in some applications.

The water flowrates tested using the HAGO nozzle were 50.56 ml/min (2.87 μl/mm^2 s) and 81.56 ml/min (4.63 μl/mm^2 s), corresponding to the minimum working pressure for the HAGO nozzle and the maximum flowrate attainable by the pump, respectively. The major drawback of the HAGO nozzle is the high flow coefficient, which causes the pressure drop to increase rapidly with increasing flowrate. At a flowrate of 2.87 μl/mm^2 s the pressure drop is 283 kPa, whereas at a flowrate of 4.63 μl/mm^2 s it becomes 843 kPa.

In Figs. 8(a) and (b) the heat transfer coefficients obtained in the experiments (further details are available in the work of Jiang [9]) with the HAGO nozzle are compared to those predicted from Eqs. (7) and (11). The experimental data obtained in this study shows the heat transfer coefficient to be independent of the wall to liquid temperature difference. It can be seen the experimental data are overpredicted by both correlations. The differences can probably be attributed to the fact that the droplet size generated with the HAGO nozzle (smaller than 44 μm) is different than that in the experiments of Ghodbane et al. [12], Holman et al. [13] (between 210–980 μm), and Cho et al. [15]. The We_{d_d} for the results of this work is between 317 and 1080 and it is out of the range for which Eq. (7) was originally developed.

The area-averaged heat transfer coefficients obtained using the HAGO nozzle are shown in Fig. 9. Figures 9(a) and (b) along with those obtained using micro jets for similar values of liquid flowrate (or mass flux, since the water temperatures for sprays and jets tests are only few degrees apart and the heater area is the same for both cases). The flowrate accounts only for those jets directly impinging on the heated area, which had a diameter of 19.2 mm. Figure 9(a) shows that at a liquid flowrate of about 2.87 μl/mm^2 s, the spray performs better than the micro jets, while a liquid flowrate of about 4.63 μl/mm^2 s (Fig. 9(b)), the droplets and the micro jets have almost the same heat transfer rate. The heat transfer coefficient is found to be independent of $T_w - T_{\mathrm{liq}}$ for the droplets spray and to increase weakly with $T_w - T_{\mathrm{liq}}$ for the microjet arrays. In both cases the ratio of pumping power to power removed for the droplet spray is much higher than for most of the jet arrays (Figs. 10(a,b)).

Referring to Figs. 10(a) and (b), it can be seen that for the spray the ratio of power consumed to power removed is higher than that for most jet configurations. For the microjets arrays it can also be inferred that the pumping power is less for higher flow rate and larger jet diameters than for small high velocity jets. A similar conclusion can also be drawn by comparing the heat transfer coefficients on a constant pumping power basis. As Fig. 11 illustrates, most of the micro jets configurations outperform the sprays.

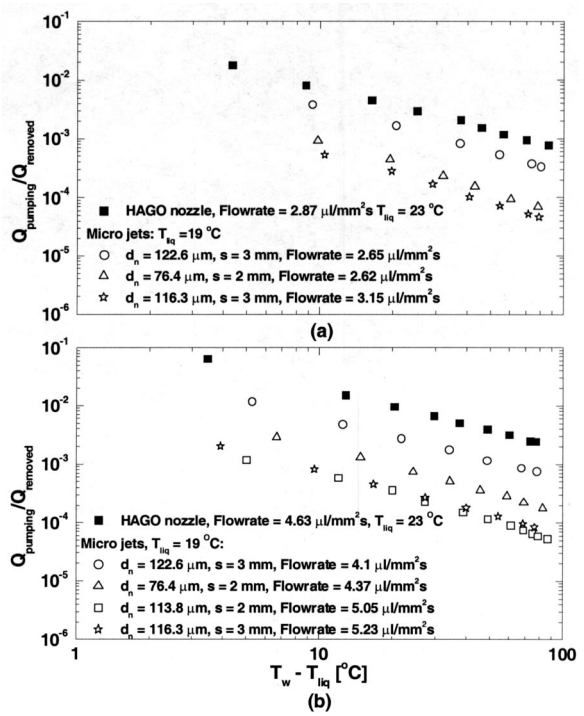

Fig. 10 Comparison of process efficiency between spray and micro jets for two flowrates (a) 50.56 ml/min [2.87 μl/mm^2 s] and (b) 81.56 ml/min [4.63 μl/mm^2 s]

Micro jets of 173.6 μm diameter spaced 3 mm apart yield a heat transfer rate almost three times higher than a spray for the same $T_w - T_{\text{liq}}$ and using the same pumping power.

The data obtained by Oliphant et al. [8] for spray and jets are plotted together with the present data in Fig. 12. It can be seen that the two different types of sprays have similar heat transfer coefficients with a small edge in favor of the HAGO nozzle. On the other hand, the highly populated micro jet arrays used in this study are preferable than the arrays with few large jets, because they require a much lower flowrate to obtain the same heat transfer rates. Better performance is obtained with microjets because of the presence of a thinner liquid film and of the presence of many more stagnation points on the heater surface. The microjet configuration considered here is near optimal [10].

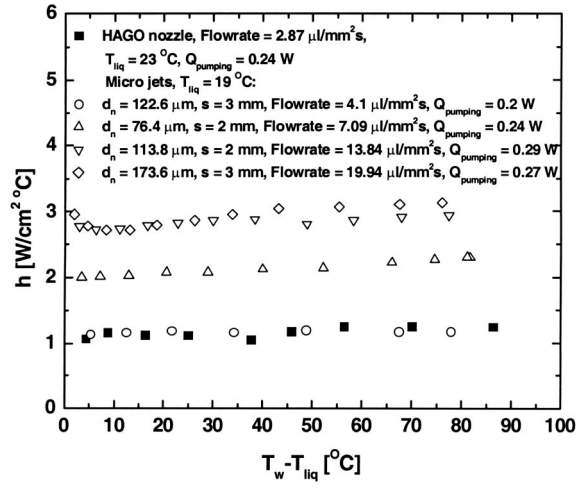

Fig. 11 Comparison between spray and micro jets performance for the same pumping power

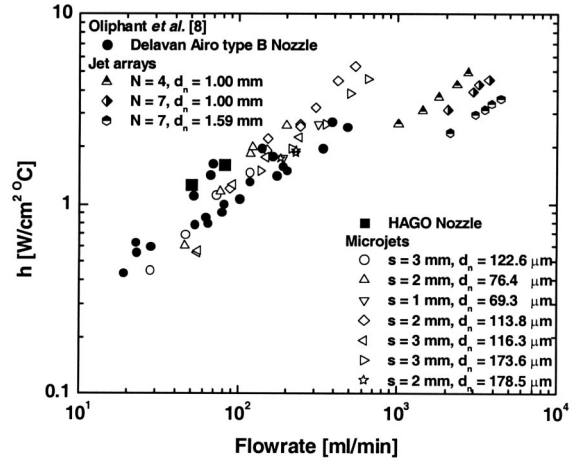

Fig. 12 Comparison of the present data with the results by Oliphant et al. [8]

In general, the pressure drop through an atomizer nozzle depends on the mechanism through which droplets are formed. Although there may exist other nozzle designs for which the pressure losses are lower at the flowrates considered in the present work than those produced by the HAGO nozzle, the results presented in this work are limited to HAGO nozzle.

The sprays represent a transient process whereas the jets provide steady state cooling. The physics of the sprays is much more complex. For higher flowrates and denser sprays, the heat transfer rates with sprays are expected to approach the heat transfer rates for jets. As such, the additional power consumed in creating droplets does not provide any benefit.

Cooling Module. Because microjets were found to perform better than the sprays, microjets were implemented in a self contained cooling module. All the tests were conducted keeping the jet velocity approximately constant at 4.5 m/s. Figure 13 shows the heat flux at the diode surface as a function of the temperature difference between the top surface of the diode (T_w) and the sprayed liquid (T_{jets}). Single phase heat transfer prevailed for the curves described by the solid symbols, while boiling was the dominant mode of heat transfer for those represented by the open

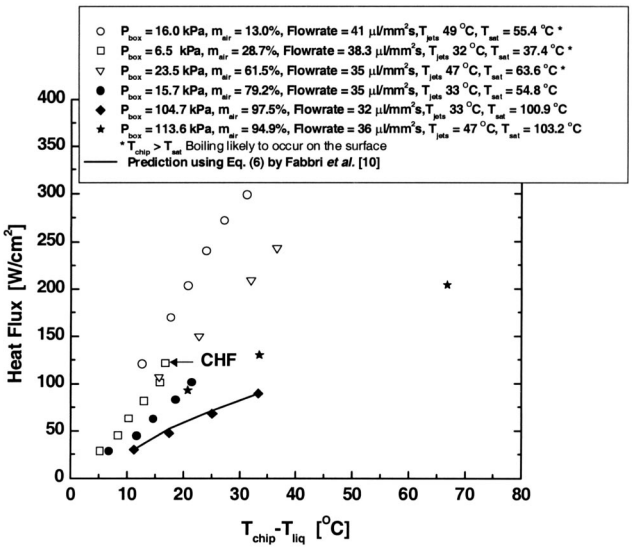

Fig. 13 Cooling module test results (4×6 array of jets, $d_n = 140$ μm, $s = 2$ mm): heat flux as a function of $T_{\text{chip}} - T_{\text{liq}}$

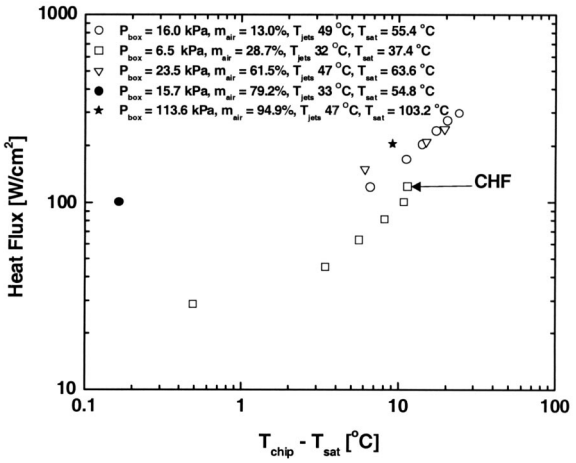

Fig. 14 Heat flux as a function of wall superheat

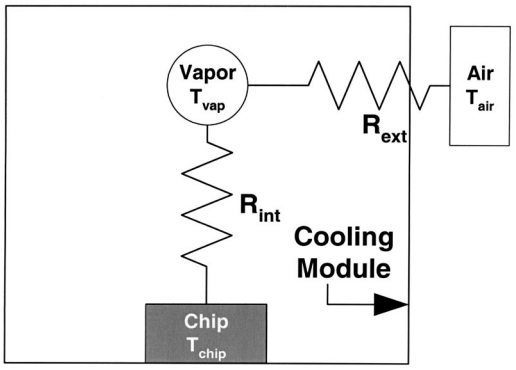

Fig. 15 Equivalent thermal circuit for the cooling module

symbols. Although in this work single phase heat transfer has been investigated, the module tests with jets have been conducted over both the single and two phase regimes in order to explore the full potential of the implementation of the concept in cooling of a device. No comparison was carried out between the performance of droplet sprays and microjet arrays in the boiling regime or when evaporation played a significant role.

In Fig. 13, the highest heat fluxes that could be achieved were limited by the high current flow through the diode, as in the 16 kPa data set, or by the fan speed reaching a maximum, as for the 104 kPa, or by critical heat flux (CHF) conditions, as in the 6.5 kPa case. Furthermore, the prediction for the $m_{\text{air}}=97.5$*percent* obtained using Eq. (6) by Fabbri et al. [10] is also plotted in Fig. 13. Good agreement is seen between the prediction and the data for 97.5 percent mass fraction of noncondensable gas. The mass fraction of air was obtained from

$$m_{\text{air}}=\frac{P_{\text{air}}/P_{\text{box}}M_{\text{air}}}{P_{\text{air}}/P_{\text{box}}M_{\text{air}}+(P_{\text{box}}-P_{\text{air}})/P_{\text{box}}M_{\text{water}}} \tag{17}$$

where P_{air} and P_{box} are the air partial pressure and the total pressure in the chamber, respectively, and M_{air} and M_{water} are the molecular weights of air and water, respectively.

The advantageous effect of reducing the pressure in the chamber is clearly illustrated in Fig. 13. Lowering the system pressure lowered the boiling inception point. For the same $T_w=80°\text{C}$ and $T_{\text{jets}}=47°\text{C}$, the heat flux increased from 130 W/cm^2, achieved with single-phase heat transfer, to 300 W/cm^2, obtained with boiling, when the pressure was reduced from 114 to 16 kPa. This can be seen by comparing the curves represented by the open circles and solid stars, in Fig. 13.

Figure 14 shows the heat flux as a function of the wall superheat. It can be seen that, when fully developed boiling occurs on the chip surface, all the curves collapse into one. The total pressure is the key parameter in this case. The last point ($q=122.2$ W/cm^2, $T_w-T_{\text{jets}}=16.7°\text{C}$) of the 6.5 kPa curve represents the critical heat flux. A 5 percent increase in the jet velocity and a vapor to liquid density ratio of 2.4 times higher than the $4.5\cdot10^{-5}$ value at 6.5 kPa, is attributed for critical heat flux exceeding at 300 W/cm^2 for the 16 kPa pressure.

Referring to Fig. 15, two main thermal resistances, an internal and an external, were defined as

$$R_{\text{int}}=\frac{T_w-T_{\text{vap}}}{Q} \tag{18}$$

and

$$R_{\text{ext}}=\frac{T_{\text{vap}}-T_{\text{air}}}{Q} \tag{19}$$

The external resistance was found to be unaffected by the presence of air inside the module, and depended only on the air flowrate indicating that the air side resistance dominated the condensation resistance on the inner wall of the box (Fig. 16). The internal resistance did not account the sensible heat stored in the liquid which flowed from the chip to the bottom of the module from where it was drained and recirculated. The data available is insufficient to draw any conclusions on R_{int}.

Another important aspect that must be considered is the ratio of the power consumed (used for cooling the diode and operating the fan) to the power removed from the chip. The pumping power varied between 3.8–5.1 W, while the fan power varied from 0 to 2.2 W. Although the flowrate was kept constant during each run, slightly different values of flowrates were used and the pumping power for each of them was also different.

From Fig. 17, it can be seen that spray cooling becomes more effective as the heat removed from the diode increases. This means that it is not convenient to employ this cooling technique if the power to be removed and the heat flux are low. For the most efficient case, the ratio of the total power spent to the power removed was around 4.4 percent. However this value is still a very conservative value since in several cases the power input to the chip was limited by restriction imposed by the current rather than the critical heat flux.

The values of the ratio of the power consumed to the power removed obtained from the cooling module tests are substantially

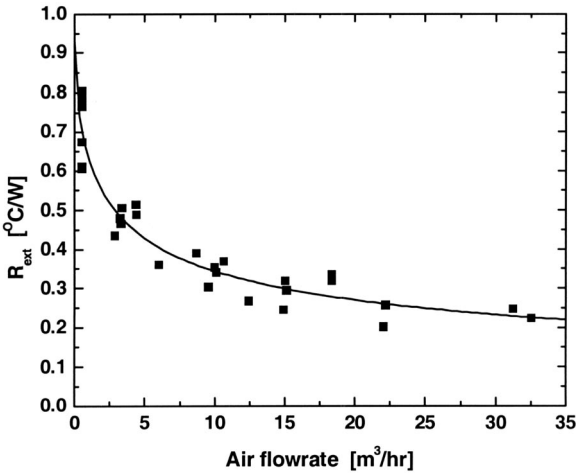

Fig. 16 Cooling module test results: external resistance versus air flowrate

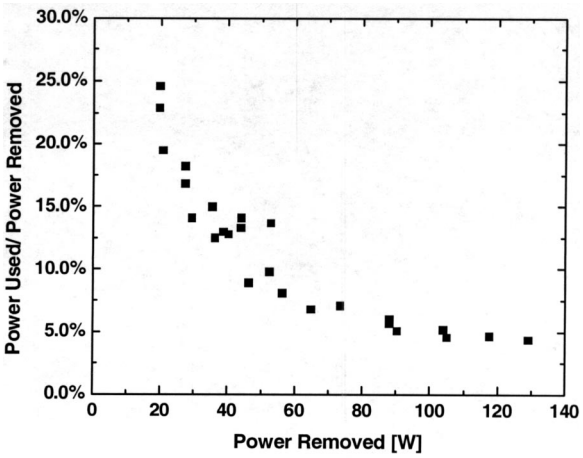

Fig. 17 Cooling module test results

higher than those shown for the orifice plates. There are several reasons for this. Because some of the jets did not impinge on the diode since the area covered by the jet array was larger than that of the diode, part of the water did not remove any heat, while still being pumped. The flowrates listed in Fig. 10 were given only by jets impinging on the target surface. Also, the results in Fig. 10 do not include fan losses, efficiencies of both the pump and the fan, and the losses in the piping and fittings of the flow loop for the liquid.

Summary

1. The single phase heat transfer rates using droplets sprays and arrays of micro jets have been compared. It is found that at a flowrate of 2.87 μl/mm^2 s the spray has a higher heat transfer rate than any jet configuration, while at a higher flowrate of 4.63 μl/mm^2 s jet arrays can perform as well as the spray.

2. The micro jets arrays are usually associated with lower energy consumption rate than the spray generated by the HAGO nozzle for the same flow rate. For equal pumping power and $T_w - T_{liq} = 76°C$, the jets can remove heat fluxes as high as 240 W/cm^2, while the spray can only handle 93 W/cm^2. It is possible that there may exist other nozzle designs that produce lower pressure losses than the HAGO nozzle at the flowrates considered, however the results presented in this work are limited to the HAGO nozzle.

3. The pressure drop for the HAGO nozzle quickly reaches values that are not practical. In practice, there is always a combination of jet diameter and jet spacing that yields the same heat transfer coefficient as that of the spray, but at a much lower energy cost.

4. The concept of using arrays of liquid micro-jets was successfully implemented. The module has proved capable of dissipating 129 W, with a heat flux of 300 W/cm^2 at a surface temperature of 80°C, which is a considerable achievement at the present time.

5. Reducing the system pressure had the effect of lowering the boiling inception temperature, thus allowing for higher heat removal rates at lower surface temperature.

6. The external resistance decreased with increasing air flowrate and was found to be unaffected by the mass fraction of air present in the module. The data were too limited to make any judgment on the internal resistance behavior with respect to the mass fraction of air. The lowest value for the ratio of power consumed to power removed was about 4 percent.

Acknowledgment

This work received support from DARPA within the HERETIC program.

Nomenclature

A = area [m^2]
c_p = specific heat [J/kg K]
d = jet or droplet diameter [m]
D = diameter
ΔP = pressure drop across the nozzle or the orifice plate [Pa]
h = heat transfer coefficient [W/m^2 K], $h = q/(T_w - T_{liq})$
h_{fg} = latent heat of vaporization [J/kg]
k = thermal conductivity [W/m K]
L = heater characteristic length [m]
L = thickness [m]
L^* = length of the radial flow region [m]
M = molecular weight [kg/k mole]
N = number of jets
Nu = Nusselt number $Nu = hd_n/k$
Pr = Prandtl number
q = heat flux [W/m^2]
Q = power [W]
Re = Reynolds number
s = pitch between the jets [m]
T = temperature [K]
v = velocity [m/s]
$\dot{V}$ = volumetric flowrate [m^3/s]
We = Weber number
z = nozzle to heater distance [m]

Greek Symbols

α = thermal diffusivity [m^2/s]
β = standard spray angle [deg]
μ = dynamic viscosity [kg/ms]
ν = kinematic viscosity [m^2/s]
ρ = density [kg/m^3]
σ = surface tension [N/m]

Subscripts

air = air or noncondensable gas
br = breakup
chip = surface of the chip
d = droplet
H = heater
i = at the impinging point
jets = jets
liq = sprayed liquid
n = at nozzle or orifice plate exit
plate = of the orifice plate
w = wall or surface

References

[1] Webb, B. W., and Ma, C. F., 1995, "Single-Phase Liquid Jet Impingement," Adv. Heat Transfer, **26**, pp. 105–217.
[2] Elison, B., and Webb, B. W., 1994, "Local Heat Transfer to Impinging Liquid Jets in the Initially Laminar, Transitional, and Turbulent Regimes," Int. J. Heat Mass Transfer, **37**(8), pp. 1207–1216.
[3] Jiji, L. J., and Dagan, Z., 1987, "Experimental Investigation of Single-Phase Multijet Impingement Cooling of an Array of Microelectronic Heat Sources," *Proceedings of the International Symposium on Cooling Technology for Electronic Equipment*, W. Aung, ed., Hemisphere Publishing Corporation, Washington, D.C., pp. 333–351.
[4] Pan, Y., and Webb, B. W., 1995, "Heat Transfer Characteristics of Arrays of Free-Surface Liquid Jets," ASME J. Heat Transfer, **117**, pp. 878–883.
[5] Womac, D. J., Incropera, F. P., and Ramadhyani, S., 1994, "Correlating Equations for Impingement Cooling of Small Heat Sources With Multiple Circular Liquid Jets," ASME J. Heat Transfer, **116**, pp. 482–486.
[6] Womac, D. J., Ramadhyani, S., and Incropera, F. P., 1993, "Correlating Equations for Impingement Cooling of Small Heat Sources With Single Circular Liquid Jets," ASME J. Heat Transfer, **115**, pp. 106–115.
[7] Yonehara, N., and Ito, I., 1982, "Cooling Characteristics of Impinging Mul-

tiple Water Jets on a Horizontal Plane,'' *Technol. Rep. Kansai University*, **24**, pp. 267–281.
[8] Oliphant, K., Webb, B. W., and McQuay, M. Q., 1998, ''An Experimental Comparison of Liquid Jet Array and Spray Impingement Cooling in the Non-Boiling Regime,'' Exp. Therm. Fluid Sci., **18**, pp. 1–10.
[9] Jiang, S., 2002, ''Heat Removal Using Microjet Arrays and Microdroplets in Open and Closed Systems for Electronic Cooling,'' Ph.D. Dissertation, University of California, Los Angeles, CA.
[10] Fabbri, M., Jiang, S., and Dhir, V. K., 2004, ''Optimized Heat Transfer for High Power Electronic Cooling Under Arrays of Microjets,'' submitted to the ASME J. Heat Transfer, accepted for publication.
[11] Bonacina, C., Del Giudice, S., and Comini, G., 1979, ''Dropwise Evaporation,'' ASME J. Heat Transfer, **101**, pp. 441–446.
[12] Ghodbane, M., and Holman, J. P., 1991, ''Experimental Study of Spray Cooling With Freon-113,'' Int. J. Heat Mass Transfer, **34**(4,5), pp. 1163–1174.
[13] Holman, J. P., and Kendall, C. M., 1993, ''Extended Studies of Spray Cooling With Freon-113,'' Int. J. Heat Mass Transfer, **36**(8), pp. 2239–2241.
[14] Bonacina, C., Del Giudice, S., and Comini, G., 1975, ''Evaporation of Atomized Liquids on Hot Surfaces,'' Lett. Heat Mass Transfer, **2**(5), pp. 401–406.
[15] Cho, C., and Ponzel, R., 1997, ''Experimental Study on the Spray Cooling of a Heated Solid Surface,'' *Proceedings of the ASME Fluids Engineering Division*, **244**, pp. 265–272.
[16] Estes, K. A., and Mudawar, I., 1995, ''Correlation of Sauter Mean Diameter and Critical Heat Flux for Spray Cooling of Small Surfaces,'' Int. J. Heat Mass Transfer, **38**(16), pp. 2985–2996.
[17] Kline, S. J., and McClintock, F. A., 1953, ''Describing Uncertainties in Single-Sample Experiments,'' Mech. Eng. (Am. Soc. Mech. Eng.), January, pp. 3–12.
[18] Shaw, M. C., Waldrop, J. R., Chandrasekaran, S., Kagalwala, B., Jing, X., Brown, E. R., Dhir, V. K., and Fabbri, M., 2002, ''Enhanced Thermal Management by Direct Water Spray of High-Voltage, High Power Devices in a Three Phase, 18-hp AC Motor Drive Demonstration,'' *Proceedings of the 8th Intersociety Conference on Thermal and Thermomechanical phenomena in Electronic Systems*, San Diego, CA, pp. 1007–1014.
[19] Mills, A. F., 1995, *Heat and Mass Transfer*, McGraw-Hill, Boston, MA.

Jae-Mo Koo
e-mail: jaemokoo@stanford.edu
Mechanical Engineering Department,
Stanford University,
Stanford, CA 94305

Sungjun Im
Materials Science and Engineering Department,
Stanford University,
Stanford, CA 94305

Linan Jiang

Kenneth E. Goodson

Mechanical Engineering Department,
Stanford University,
Stanford, CA 94305

Integrated Microchannel Cooling for Three-Dimensional Electronic Circuit Architectures

The semiconductor community is developing three-dimensional circuits that integrate logic, memory, optoelectronic and radio-frequency devices, and microelectromechanical systems. These three-dimensional (3D) circuits pose important challenges for thermal management due to the increasing heat load per unit surface area. This paper theoretically studies 3D circuit cooling by means of an integrated microchannel network. Predictions are based on thermal models solving one-dimensional conservation equations for boiling convection along microchannels, and are consistent with past data obtained from straight channels. The model is combined within a thermal resistance network to predict temperature distributions in logic and memory. The calculations indicate that a layer of integrated microchannel cooling can remove heat densities up to 135 W/cm^2 within a 3D architecture with a maximum circuit temperature of 85°C. The cooling strategy described in this paper will enable 3D circuits to include greater numbers of active levels while exposing external surface area for functional signal transmission.
[DOI: 10.1115/1.1839582]

Introduction

Three-dimensional (3D) circuit architectures enable the integration of logic with memory, RF devices, optoelectronic devices, and microelectromechanical systems on a single chip. These 3D circuits offer reduced communication delay between modules (e.g., between logic and memory), reduced interconnect length, and even improved reliability [1,2]. However, 3D circuits pose thermal management challenges due to the significant increase in total power generated per unit available surface area for cooling. Furthermore, the power generated per unit volume within a 3D circuit can vary significantly, yielding large junction temperature nonuniformities that can impair the collective operation of the circuit [2]. Another problem is that the increased functionality of the circuit demands greater surface area for input and output of electrical, optical, RF, and other types of signals, which further reduces the surface area available for heat removal. While the semiconductor research community is actively studying the electrical performance and manufacturing methods of 3D circuits with as many as one hundred device layers [3], the introduction of a new cooling approach is a critical issue in its implementation.

The heat removal problem is particularly challenging for vertically integrated circuit (3D IC) technologies [1,2]. The first thermal analysis of 3D ICs addressed concerns regarding heating effects in 3D complementary metal-oxide-semiconductor and investigated the effects of the silicon thickness of the upper chip layers [4]. Previous thermal analysis was performed through device-level [4,5] or chip-level [5,6] modeling, showing that thermal packaging technologies with thermal resistance below 0.5 K/W will be necessary to obtain reasonable chip temperature in 3D ICs. It is also reported that metal thermal vias and Cu bonding layers in 3D integration could be helpful for heat removal in 3D ICs [5]. Figure 1 is a conceptual schematic of a hyperintegrated 3D IC combined with a contemporary flip chip package and heat sink technology. The device layers are vertically separated from each other by interlayer dielectrics, which are very poor thermal conductors with thermal conductivity below 0.3 W/mK for some low-*k* dielectrics [7]. The thermal management challenge can be exacerbated by higher power densities in 3D circuit architectures. While the chip area is reduced, heat generation power per unit surface area will increase. The very large thermal resistance established between the bottom layer and the ambient results in a high junction temperature on the chip.

While there has been much previous research on advanced microprocessor cooling approaches, previous studies have been focused on traditional two-dimensional circuits with a single layer of active circuits. A broad variety of micromachined heat sink technologies include microjet impingement cooling devices [8], capillary loops with microscale evaporators [9], and microchannel heat sinks [10]. Pumped liquid cooling has been implemented in commercial laptop and desktop computers, in many cases exploring novel electrokinetic and electrohydrodynamic pumps [10,11]. These devices have made substantial improvements in the thermal resistance between the chip and the ambient temperature with values approaching as low as 0.1 K/W, and continued research in this field is expected to lead to cooling of 3D circuits as well. However, past work does not address the fundamental thermal management problems faced by designers of 3D circuits, specifically the limited surface area available for cooling and the large vertical thermal resistance between the bottom device layer and the cooling technology.

Figure 2 shows a schematic of the solution strategy proposed in this research, a 3D circuit with multiple layers of integrated microchannels. Heat generated by the device layers can be removed

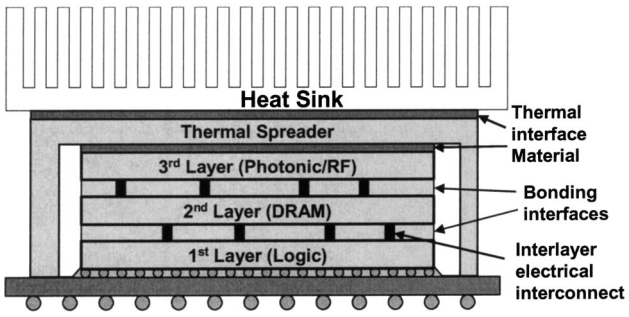

Fig. 1 Three-dimensional circuit architecture connected to a conventional heat removal device

Contributed by the Heat Transfer Division for publication in the JOURNAL OF HEAT TRANSFER. Manuscript received April 23, 2004; revision received September 11, 2004. Associate Editor: C. Amon.

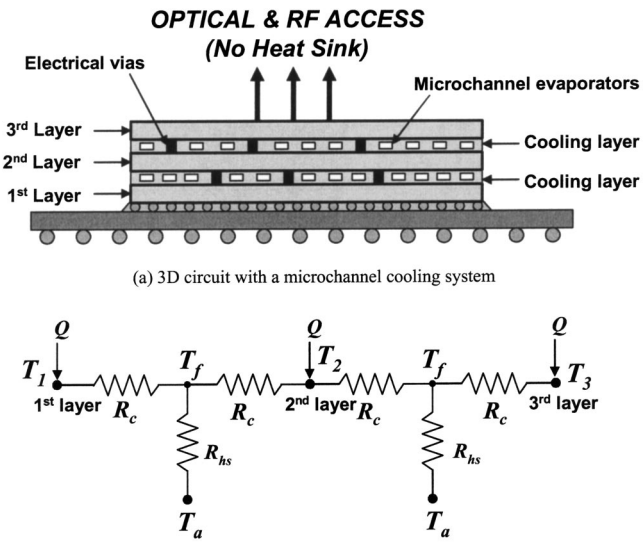

Fig. 2 Conceptual schematic of a microchannel cooling network for a 3D circuit and the thermal circuit model. (*a*) 3D circuit with a microchannel cooling system. (*b*) Thermal circuit for microchannel cooling.

locally to adjacent microchannel layers with low thermal resistance, and the number of device layers can be scaled indefinitely as long as sufficient cooling is provided for each layer. The top surface of the proposed 3D architecture is free and provides electronic and photonic access. Boiling convection cooling in microchannels is particularly promising because of the reduced fluid flow rates required for heat removal and the opportunities it provides for temperature regulation through fluid saturation pressure distribution [10,12]. An integrated microchannel network can achieve a reasonably low thermal resistance while utilizing fluid latent heat and minimizing pumping power. It also has unique attributes of small coolant inventory and fairly uniform temperature profile. Theory and experiments have characterized conduction, convection, and two-phase boiling regimes in microchannels and have shown that they can aggressively cool on-chip hotspots at a reasonable temperature while removing more than 100 W from the chip with a minimal heat sink volume (1 cm$\times$1 cm $\times$1 mm) and chip surface area (1 cm$\times$1 cm) [10,13].

The present work studies theoretically the potential of integrated microchannel cooling networks for removing local high heat generation rates from 3D circuit architectures. A conjugate conduction/convection heat transfer simulation approach solves the steady-state thermal resistance network of device layers and one-dimensional convection equations along the microchannels. It incorporates spatially varying heat transfer coefficients, fluid temperature profiles and pressure drop along the channels, and has been shown to be consistent with previous experimental data for pressure drop and temperature field along straight microchannels. This study examines the effect of hotspot locations on the junction temperature uniformity and the peak temperature. The simulated junction temperature field with the microchannel heat sink is compared with that using a conventional cooling system.

Three-Dimensional Circuit Fabrication Methods

Although this study focuses on the theoretical potential of microchannel cooling for enabling 3D circuits, a much larger challenge will be integrating the process steps for the microfluidic channels within the already demanding process flow required to make 3D circuits. The main goal of 3D circuit processing is creating additional semiconducting layers of silicon, germanium, gallium arsenide, or other materials on top of an existing device layer on a semiconducting substrate. There are several possible fabrication technologies to form these layers. The most promising near-term techniques are wafer bonding [14–17], silicon epitaxial growth [18–20], and recrystallization of polysilicon [21–24]. Figure 3 shows a schematic of 3D circuits illustrating two different fabrication schemes. The choice of a particular technology will depend on the requirements of the integrated circuit system, manufacturability, and process compatibility with current technology. There are a variety of methods available for forming microchannels within a three-dimensional circuit, including plasma

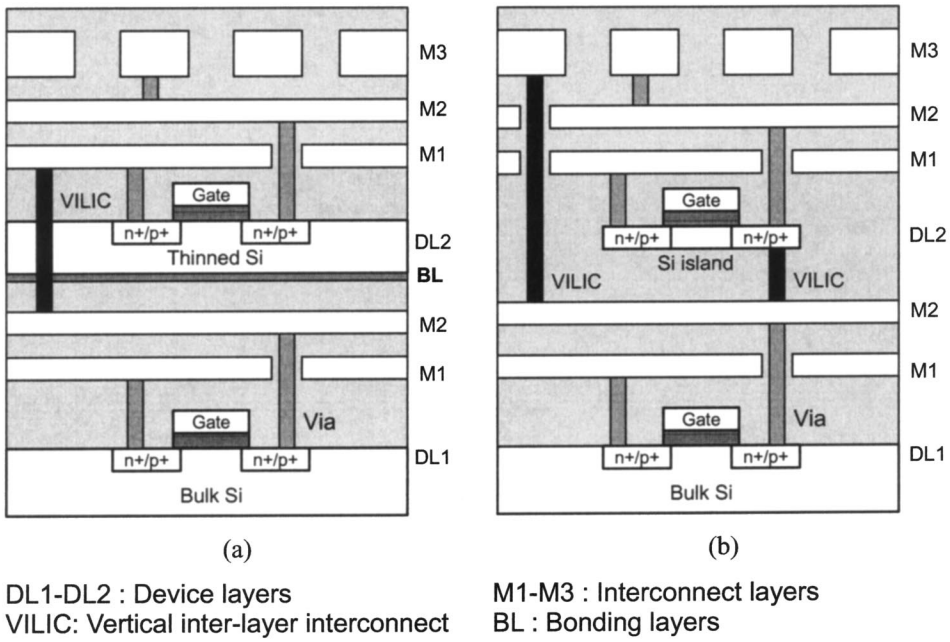

Fig. 3 Schematic of hierarchical 3D circuit structures fabricated by (*a*) wafer bonding, and (*b*) silicon epitaxial growth or recrystallization of polysilicon

etching prior to wafer bonding, sacrificial silicon channels, and even chemical etching. Furthermore, there has been much recent research on etching vertical channels through wafers for electrical connections, which can be leveraged to provide the vertical fluidic connections needed in this research.

Wafer bonding differs from other fabrication technologies due to the opportunity for independent processing of the wafers prior to bonding. Fully processed wafers are directly bonded using various techniques leading to the completely overlapped stacking of the chips. Wafer bonding can be achieved by using polyimide adhesive layers [14], Cu-Cu thermocompression method [15,17] and microbumps with liquid epoxy injection [16]. The wafer bonding process preserves electrical characteristics of each device layer and can be repeated without damaging existing circuits. The alignment tolerance of $\pm 1-2\ \mu$m [1,16] requires careful design of vertical interlayer interconnections.

Silicon epitaxial growth technique utilizes epitaxially grown single-crystal Si islands as device layers. Single-crystal Si islands are formed out of the open seed window by selective epitaxial growth, epitaxial lateral overgrowth, and chemical mechanical polishing of excess Si [18–20]. The major limitation of this technique is high process temperatures ($\sim 1000°$C), which results in significant degradation in the lower device layers especially with metallization layers. Although low-temperature epitaxial Si can be obtained using ultra-high-vacuum systems [25] and utilizing plasma [26], this process is not yet feasible for manufacturing.

Recrystallization of polysilicon [21–24] is another method for forming a second Si layer. This technique deposits polysilicon and induces recrystallization of the polysilicon film using intense laser or electron beams to enhance the performance of the thin-film transistors (TFTs). This technique requires high process temperatures during the melting of polysilicon layers. Beam-recrystallized polysilicon TFTs also exhibit low carrier mobility and unintentional impurity doping. Local crystallization, induced by patterned seeding of Ge [27] or by metal-induced lateral crystallization [28], can enhance TFT performance.

Previous Research on Two-Dimensional Microchannel Heat Sinks

There has been much past research on microchannel cooling in two-dimensional (2D) heat sinks, which forms the groundwork for the modeling study performed in the current study on a 3D microchannel network. Since Tuckerman and Pease [29] demonstrated that single-phase microchannel cooling can remove 790 W/cm^2, much of the subsequent research has focused on the physics and optimization of two-phase flow in microchannels. Perhaps the closest previous work to the current integrated 3D microchannel network is that of Wei and Joshi [30], who proposed stacked microchannels for cooling of microelectronic devices. A number of parallel microchannels are fabricated in the surface of a substrate and then each layer is bonded into a stacked heat sink which is attached to the chip. They proposed a simple thermal resistance network model and performed optimization to minimize the overall thermal resistance.

Past work indicates that the two-phase flow in microchannels exhibits different flow regimes and heat transfer characteristics compared to macroscale convective boiling [31]. Experimental investigation on boiling flow transition in microchannels showed no bubble generation in channels with hydraulic diameters ranging from 150 to 650 μm, although the heat transfer rate suggested that phase change occurred [32,33]. The authors called this phenomenon ''fictitious'' boiling and suggested that it was attributed to the condition $D_h < D_{crit}$, where D_{crit} is the critical diameter at which bubbles are stable considering surface forces and the pressure dependence of the saturation temperature. Bower and Mudawar [34,35] performed a thermal characterization of two-phase microchannel heat sinks with refrigerant as the working fluid and developed a homogeneous model for a two-phase pressure drop simulation. Predictions agreed well with experimental data for heat sinks with channel sizes from 510 μm to 2.54 mm. Stanley et al. [36] performed two-phase flow experiments in rectangular channels using inert gas–liquid water mixtures and proposed friction factor correlations for one-dimensional two-phase flow models. Based on available experimental observations, a gas–liquid two-phase flow regime map was proposed for a near-circular channel whose hydraulic diameter is less than 1 mm [37,38]. Recent experimental observations have shown that two-phase flow regimes in microchannels contain only the slug and annular flow regimes without bubbly flow patterns [13,31,39–45]. Peles et al. [39] proposed a one-dimensional flow model with flat evaporation front dividing the liquid and vapor into two distinct domains based on their experiments with 50 to 200 μm hydraulic diameter channels. Experiments were performed to investigate the flow patterns of two-phase flow in microchannels, to find the temperature distribution along the channels, and to study the effects of convection on chip instabilities [40,41]. They obtained nonuniform temperature distributions, with temperature increasing in single-phase regions and decreasing in two-phase regions. Qu et al. [42–44] performed measurements and predictions of saturated flow boiling heat transfer and pressure drop in a water-cooled copper microchannel heat sink with 21 parallel channels having a 231 μm$\times$713 μm cross section. They examined the conventional correlations for two-phase heat transfer coefficients and proposed a phenomenal annular flow model.

The problem of spatially varying heat flux from the microchannel walls has recently received attention. A homogeneous two-phase flow model has been developed to calculate the fluid pressure drop and junction wall temperature distributions [12,13,46,47]. A closed-loop cooling system was demonstrated utilizing microchannel heat sinks, which were designed using a homogeneous two-phase model [10]. Careful design is important to avoid dry-out and high junction temperatures for stable system operation. It was recommended that the heat sink be attached to the chip such that the hotspot is located near the exit of the channels to reduce the pressure drop along channels and thus leads to a decrease in the peak junction temperature [12,47]. While large thermal resistance of the single-phase region causes a high peak junction temperature, subchannels are incorporated to improve the heat sink performance [47].

Past work on two-phase microchannel cooling was focused on cooling of 2D circuits and on demonstration of a single- or multichannel system ignoring the effects of flow distributions in a channel network. Three-dimensional circuit cooling faces a conjugate heat transfer with 3D thermal conduction and boiling convection in microchannels. In a two-phase microchannel network, each channel experiences flow instability due to the random formation and growth of a void. The instability problem induced by the flow instability is more critical in microchannel cooling of 3D circuits, since more microchannel layers are coupled. These should be addressed to demonstrate an integrated microchannel cooling network for 3D circuits.

Modeling

Figure 4 shows a schematic of the microchannels implemented in a 3D circuit architecture within a coordinate system. It is assumed that the microchannels are distributed uniformly and fluid flows through each channel with the same liquid flow rate. The working fluid, water, flows in the z direction with a mass flow rate of $\dot{m}$. The junction heat generation rate q'' is assumed to vary only in the z direction. Using symmetry, a one-dimensional conjugate conduction/convection heat transfer analysis is applied to only one channel for each layer. The time- and space-averaged one-dimensional energy equations for the jth device layer and channel layer are

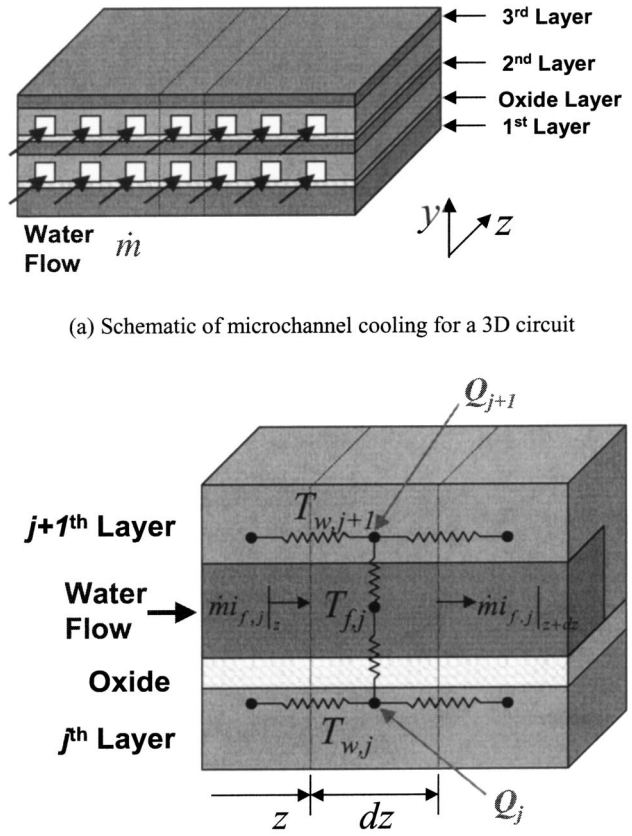

Fig. 4 Schematic of microchannels implemented in a 3D circuit and thermal modeling of microchannel cooling for a 3D circuit. Only one channel is analyzed in a cooling layer by geometric and thermal symmetries. Dotted lines indicate a control volume used in derivation of energy equations [Eqs. (1) and (2)]. (*a*) Schematic of microchannel cooling for a 3D circuit. (*b*) Thermal circuit of the *j*th microchannel.

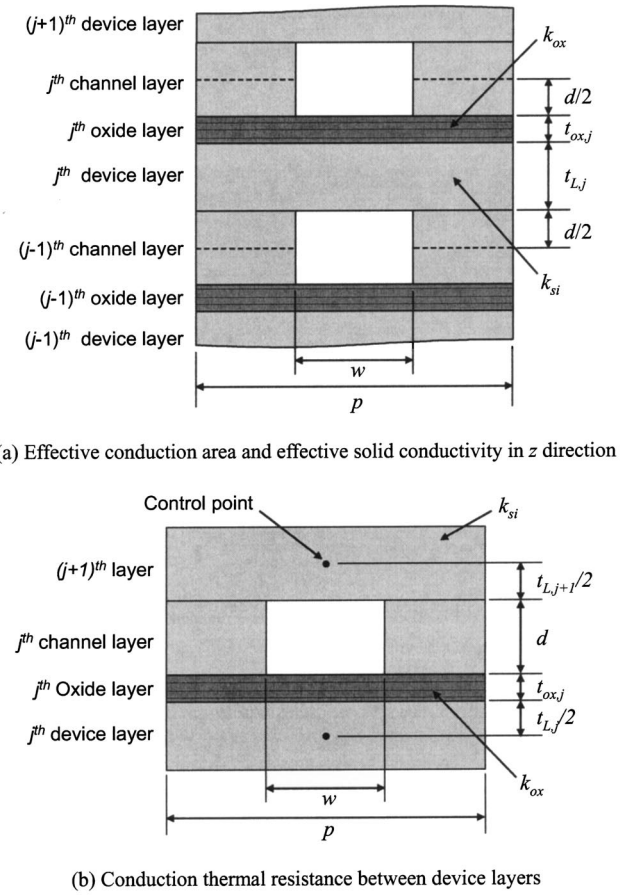

Fig. 5 Predictions for the effective thermal conductance and thermal resistance. (*a*) Effective conduction area and effective solid conductivity in the *z* direction. (*b*) Conduction thermal resistance between device layers.

Solid:

$$\frac{d}{dz}\left(k_{w,z,j}A_{w,j}\frac{dT_{w,j}}{dz}\right)=q''_j p+h_{conv,j}\eta_0(w+d)(T_{w,j}-T_{f,j-1})+h_{conv,j}\eta_0(w+d)(T_{w,j}-T_{f,j})+(T_{w,j}-T_{w,j+1})/R_{th,j}+(T_{w,j}-T_{w,j-1})/R_{th,j-1} \quad (1)$$

Fluid:

$$\dot{m}\frac{di_{f,j}}{dz}=h_{conv,j}\eta_0(w+d)(T_{w,j}-T_{f,j})+h_{conv,j}\eta_0(w+d)(T_{w,j+1}-T_{f,j}) \quad (2)$$

where $T_{w,j}$ and $T_{f,j}$ are the average local temperatures of the solid wall and the fluid, respectively. The subscript j indicates the property of the jth layer. The pitch of microchannels is denoted as p. The depth and width of the microchannel are represented as d and w, respectively. The forced convection coefficient for heat transfer between the solid wall and the working fluid is $h_{conv,j}$. In Eq. (2), diffusion terms are neglected since the Peclet number, defined as $\rho UD_h/\alpha$, is much greater than unity in this study. The fluid enthalpy per unit mass (i_f) is expressed in terms of local thermodynamic equilibrium fluid quality (x) which is the mass fraction of the vapor phase, using

$$i_f=(1-x)i_l+xi_v \quad (3)$$

where subscripts l and v represent liquid and vapor phase in a two-phase flow, respectively. The effective thermal conductivity of solid in the z direction is $k_{w,z,j}$ and $A_{w,j}$ is the effective solid cross-sectional area. From Fig. 5(*a*), effective conduction area in the z direction is obtained as

$$A_{w,1}=(t_{L,1}+t_{ox,1})p+d(p-w)/2, \quad (j=1)$$
$$A_{w,j}=(t_{L,j}+t_{ox,j})p+d(p-w), \quad (j=2\sim jmax-1)$$
$$A_{w,jmax}=(t_{L,jmax}+t_{ox,jmax})p+d(p-w)/2, \quad (j=jmax) \quad (4)$$

where $t_{L,j}$ and $t_{ox,j}$ are thicknesses of the jth layer and the jth oxide layer, respectively, and $jmax$ is the number of device layers. The corresponding effective solid thermal conductivity in the z direction is given as

$$k_{w,1}=\frac{(k_{si}t_{L,1}+k_{ox}t_{ox,1})p+k_{si}d(p-w)/2}{A_{w,1}}, \quad (j=1)$$
$$k_{w,j}=\frac{(k_{si}t_{L,j}+k_{ox}t_{ox,j})p+k_{si}d(p-w)}{A_{w,j}}, \quad (j=2\sim jmax-1)$$
$$k_{w,jmax}=\frac{(k_{si}t_{L,jmax}+k_{ox}t_{ox,jmax})p+k_{si}d(p-w)/2}{A_{w,jmax}}, \quad (j=jmax) \quad (5)$$

where k_{si} and k_{ox} are conductivities of silicon and oxide layers, respectively. In the present analysis, it is assumed that the thermal properties of solid are fixed at constant values. The conduction thermal resistance between control points on layers j and $j+1$, $R_{th,j}$, can be evaluated from Fig. 5(b) and is

$$R_{th,j}=\frac{t_{L,j+1}}{2k_{si}p}+\frac{d}{k_{si}(p-w)}+\frac{t_{ox,j}}{k_{ox}p}+\frac{t_{L,j}}{2k_{si}p} \tag{6}$$

The overall surface efficiency η_0 is employed to simplify the temperature variation in the y direction within the channel walls and is given by

$$\eta_0=1-\frac{d}{d+w}(1-\eta_f) \tag{7}$$

where η_f is the fin efficiency of the fin with insulated tip [48] assuming that the heat transfer coefficient is uniform along the periphery. The solid energy equation [Eq. (1)] accounts for heat conduction along the layer, heat transfer from solid to liquid, and heat transfer to the adjacent layers. The energy balance equation for fluid flow [Eq. (2)] indicates that convection heat transfer from the wall to fluid causes the change of fluid enthalpy. The analysis employs the thermal lumped capacitance assumption in the y direction for each infinitesimal control volume of the circuit layer, and assumes that the bulk silicon temperature is the same as the junction temperature. In the analysis of the two-phase flow, liquid and vapor phases are assumed to be in equilibrium at the fluid saturation temperature and pressure.

One of the important assumptions is that each microchannel has the same liquid flow rate. In multichannel heat sinks, the flow rate of each channel is determined by mass and momentum conservation equations and, in the steady state, requires equal pressure drop along a streamline from inlet to exit manifold for each individual channel [47]. In practical two-phase heat exchangers, the physics of bubble formation and pressure fluctuation can lead to spatial and temporal instabilities in the flow rate. The flow instabilities from one channel can cause oscillations to propagate in the surrounding channels by flow redistribution. This can lead to failure of the cooling system due to control problems and the change of local heat transfer characteristics. The design of inlet and exit manifolds is critical for uniform flow delivery in a 3D microchannel cooling network. One potential solution is for each microchannel layer to have its own manifold and an independent pump, which in turn would increase the design complexity dramatically. A far simpler approach would be to have inlet and exit manifolds for all channels in the network. However, it is difficult to simulate this geometry since there is limited knowledge about vertical fluid delivery coupled in series with a horizontal fluid delivery, in addition to further complications from boiling flow. The present work, however, ignores the variations in flowrate among channels and assumes the same flowrate to each channel in investigating the time- and space-averaged performance of the microchannel cooling for a 3D circuit.

To close the set of governing equations, complimentary relations are required for the convective heat transfer coefficients and the pressure drop. For a single-phase flow region, the heat transfer coefficient, $h_{conv,j}$, accounts for the effect of wall temperature variation in the axial direction [49]. This approach substitutes the fluid temperature in Eqs. (1) and (2) with the inlet fluid temperature, $T_{f,in}$. In evaluating the varying wall temperature effect, the present analysis uses the average temperature and average heat flux of adjacent layers as local wall temperature and local heat flux, respectively. For the two-phase flow, Kandlikar's correlation [50] is employed to calculate the heat transfer coefficient with the assumption of saturated boiling heat transfer and is given as

$$h_{conv}=h_l[C_1Co^{C_2}(25Fr)^{C_5}+C_3Bo^{C_4}F_k] \tag{8}$$

where h_l is the heat transfer coefficient for the liquid phase flowing alone. The factor F_k is a fluid-dependent parameter whose value for water is unity. The first term in the parenthesis accounts for the forced-convection effect on heat transfer and the second term represents the effect of nucleate boiling in regions with low fluid two-phase qualities. In applying this correlation for the present calculations, the forced-convective term is dominant over the nucleate boiling term, while it is assumed that they still capture the essential physics of the boiling process at the microscales. The constants C_1 to C_5 are determined from the value of Co as shown in Table 1. The dimensionless parameters are

Table 1 Constants in Kandlikar's correlation for horizontal channels [50]

Constant	Convective region ($Co<0.65$)	Nucleate boiling region ($Co>0.65$)
C_1	1.1360	0.6683
C_2	−0.9	−0.2
C_3	667.2	1058.0
C_4	0.7	0.7
C_5*	0.3	0.3

*$C_5=0$ with $Fr>0.04$.

$$Co=\left(\frac{1-x}{x}\right)^{0.8}\left(\frac{\rho_v}{\rho_l}\right)^{0.5} \tag{9}$$

$$Bo=\frac{q''}{m''i_{l_v}} \tag{10}$$

$$Fr=\frac{m''^2}{\rho_l^2 g D_h} \tag{11}$$

where ρ_v and ρ_l represent vapor and liquid densities in the saturation state, respectively. The heat of vaporization per unit mass is i_{l_v} and g is the acceleration due to gravity. Kandlikar's correlation was developed for two-phase horizontal or vertical flows in conventional size channels. Even though there is a controversy in applying the conventional two-phase heat transfer correlations to microchannel flows [37,43], some previous studies [10,12,13] supported Kandlikar's correlation in microchannel cooling and this study employs it as a correlation to predict two-phase heat transfer coefficients in microchannels. This correlation was developed for two-phase channel flows with Froude number (Fr) between 1.14 and 19.07. However, Fr of less than 1 is estimated in the present work. Future experimental work will more closely examine the accuracy of this correlation for flows with low Fr values. For simplicity, it is assumed that the two-phase flow is mixed well, and the convective heat transfer is independent of the wall and fluid temperature variations in the axial (z) direction. With these assumptions, the empirical correlation for the two-phase heat transfer coefficient is used without any adjustment from its original form.

For simplicity and efficiency in the calculation, the pressure drop is calculated using a homogeneous model, in which the liquid and gas flow velocities are identical, given by

$$-\left(\frac{dP_j}{dz}\right)=\frac{fm''^2}{2\rho_j D_h}+\frac{d}{dz}\left(\frac{m''^2}{\rho_j}\right) \tag{12}$$

where P_j and m'' represent the pressure and mass flux of fluid flow, respectively. The friction factor for the two-phase flow in a microchannel, f, is proposed by Stanley et al. [36] as

$$f=\frac{97}{Re}, \quad (Re<3000) \tag{13}$$

Equation (13) has been experimentally determined for values of the two-phase Reynolds number relevant for the current work. Although it was developed for the average shear stress along a channel, it is applied locally in the present analysis. The Reynolds number *Re*, evaluated using mean properties of two-phase flow, is written as

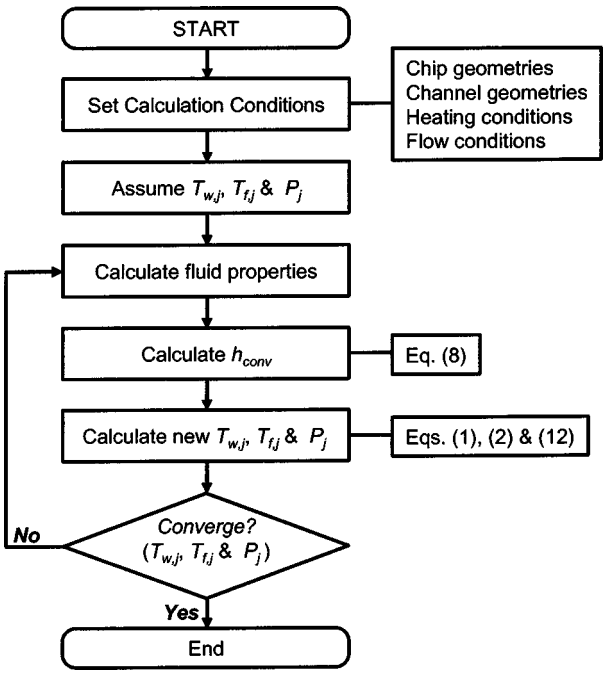

Fig. 6 Flowchart showing the calculation procedure used in this study

$$Re = \frac{\rho U D_h}{\mu} \tag{14}$$

where U is the mean velocity of the flow and D_h is the hydraulic diameter of the channel. For two-phase, the density ρ and dynamic viscosity μ of liquid–vapor mixture are evaluated using

$$\frac{1}{\rho} = \frac{(1-x)}{\rho_l} + \frac{x}{\rho_v} \tag{15}$$

$$\frac{1}{\mu} = \frac{(1-x)}{\mu_l} + \frac{x}{\mu_v} \tag{16}$$

The boundary conditions are adiabatic at both ends of the heat sink for the solid energy equation [Eq. (1)], which ignores conduction loss to the packaging of the microchannel heat sink. For fluid, Eqs. (2) and (12), the inlet fluid temperature and the exit pressure are given to close these equations. The present boundary conditions will overpredict the junction temperatures since they neglect heat loss to the packaging of the microchannel heat sink.

The numerical simulation solves the energy equations for one channel using the finite volume method [51]. Water properties are incorporated using thermodynamic property correlations accounting for their dependence on temperature and pressure [52]. Since this modeling includes strong temperature- and pressure-dependent properties of water, under-relaxation method is employed for convergence. The detailed algorithm is shown in Fig. 6. The number of the nonuniform grid network is 200. The mesh points were densely packed near the inlet. Convergence is declared when maximum relative variations in temperature and pressure between the successive iterations are less than 10^{-5} and when the energy balance has an error of less than 0.1% of the total applied heat. The effects of the grid density are carefully checked to ensure the reliability of the numerical solutions. The model was verified comparing to the experimental data using a 2D microchannel heat sink [10,13]. Good agreements establish confidence in applying this model to microchannels in a 3D circuit. To compare the performances between conventional and microchannel heat sinks, a 3D finite-element simulation is performed using ANSYS to evaluate the thermal performance of a conventional heat sink. For a conventional fin-array heat sink, shown in Fig. 1, the heat sink and thermal spreader are attached to the chip using a conventional thermal interface material. The thermal resistance of a fin heat sink is assumed to be 0.25 K/W and the thermal resistance of the thermal interface material is 0.2 cm^2K/W. The dimensions of a copper heat spreader are 28 mm$\times$28 mm$\times$1 mm. The chip is attached to the center of the spreader. ANSYS calculates the junction temperatures with a constant ambient temperature boundary condition at the top surface of the thermal spreader.

The elevated temperature and pressure may have an impact on the reliability of a 3D circuit. The temperature is, in itself, not an inherent problem in this cooling solution, since the aim of the technology is to reduce both temperature and temperature gradients. However, the high pressures experienced in the channels may induce strain fields in addition to piezoresistive phenomena that can influence the performance of the semiconductor devices. An approximation using beam theory can estimate the effects of pressure on the electrical resistivity of the circuit. The upper wall of the channel is approximated as a beam with fixed ends, with the pressure difference as an applied force. Assuming the pressure difference between the channels in adjacent layers to be 30 kPa, which is close to the maximum pressure gradient of the flow in this study, the maximum stress and strain are about 350 kPa and 3.5×10^{-6}, respectively. The corresponding maximum change in electrical resistance of the circuit is about 0.05%, based on piezoresistive coefficients for bulk silicon. A detailed assessment of this effect is beyond the scope of the present study, which focuses on the heat transfer features of the system. However, it is important to minimize the pressure drop to reduce the effect of temperature and pressure on reliability.

Results and Discussion

Analysis is performed to simulate 3D IC cooling performance with microchannels fabricated between two silicon layers using deep reactive ion etching and wafer bonding techniques [15,17]. Figure 7 illustrates four different 3D stack schemes for a given flow direction. To simulate nonuniform power distributions in practical 3D ICs, the device is divided into logic circuitry and memory, where 90% of the total power is dissipated from the logic and 10% from the memory [53]. This work assumes that the heat generation represents the power dissipation from the junctions and also from interconnect Joule heating. For case (a), the logic circuit occupies the whole device layer 1, while the memory is on the device layer 2. In the other cases, each layer is equally divided into memory and logic circuitry. For case (b), a high heat generation area is located near the inlet of the channels, while it is near the exit of channels for case (c). Case (d) has a combined thermal condition in which layer 1 has high heat flux and layer 2 has low heat dissipation near the inlet. The total circuit area is 4 cm^2, while the total power generation is 150 W.

Table 2 lists the microchannel geometries and simulation conditions. The conventional heat sink/spreader is assumed to be attached on the backside of device layer 1. It should be noted that the microchannel geometry is not optimized since the objective of this study is to identify the characteristics of 3D circuit cooling with microchannels. The channel geometry used in this study is from the past work [12] and gave an optimized performance for 2D chip cooling. The inlet liquid temperature is fixed at 70°C. The saturation temperature of water at atmospheric pressure, 100°C, is too high for very large scale integrated chips whose maximum operating temperature is below 90°C. The fluid absolute exit pressure is fixed at 0.3 bar, which yields a saturation temperature of about 70°C to simulate subatmospheric operation.

Figure 8 compares the thermal performance of the microchannels and conventional heat sinks and plots the predicted junction temperature distributions along the flow direction. In case (a), the heat generation from each layer is uniform and the junction temperature profile with conventional heat sink is symmetric. The microchannel cooling has distinct characteristics of a nonuniform

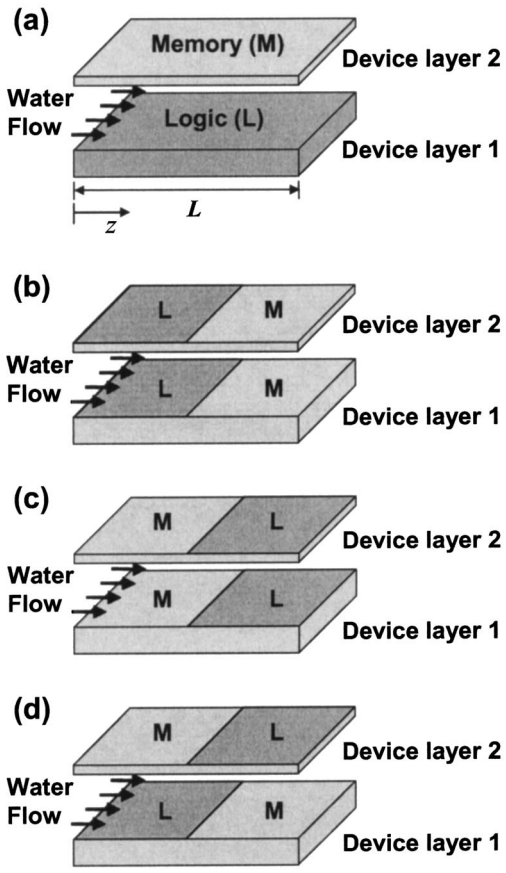

Fig. 7 Two-layer 3D circuit layouts for evaluating the performance of microchannel cooling. The areas occupied by memory and logic are the same and the logic disssipates 90% of the total power consumption [53].

Table 2 Parameters and geometries of a 3D circuit with a microchannel/conventional heat sink

3D circuit architecture	
Chip size	14.14 mm×14.14 mm
Power dissipation	150 W (Logic: 90%, Memory: 10%)
Device layer 1	
Silicon layer thickness	500 μm
Oxide layer thickness	10 μm
Device layer 2	
Silicon layer thickness	20 μm
Oxide layer thickness	10 μm
Microchannels	
Channel layer thickness	400 μm
Number of channels	18
Channel geometry	700 μm (width)×300 μm (depth)
Liquid water flow rate	15 ml/min
Inlet fluid temperature	70°C
Exit fluid pressure	0.3 bar
Conventional fin heat sink with a copper spreader	
Heat sink thermal resistance	0.25 K/W
Thermal interface material	1×10^{-5} m^2 K/W
Copper spreader size	28 mm×28 mm×1 mm

temperature distribution, even under a uniform heating condition. The temperature increases along the channel in the liquid phase region due to sensible heating, and decreases in the two-phase region due to decrease of the fluid saturation pressure along the channel. The junction temperature has its peak at the onsite of boiling point due to the dramatic change in convective heat transfer coefficient from a liquid-phase region to a two-phase region. The temperature difference between layers is greatly reduced by more than 10°C using microchannels because of the small thermal resistance of direct heat removal from layers.

In cases of (b) and (c), identical junction temperature distributions are presented for conventional fin heat sinks. Using microchannels, however, the temperature distribution is quite different, because of the convection nature of flow direction dependence. In both cases, the conventional heat sink presents highly nonuniform junction temperatures of about 25 and 45°C differences for layer 1 and layer 2, respectively, due to the concentrated heat flux. With microchannels, if more heat is applied to the upstream region, boiling occurs earlier resulting in increased pressure drop in the channel. Thus case (c) has a lower pressure drop, lower average junction temperature, and more uniform temperature field than case (b). In case (c), water is gradually heated up in the upstream region, where lower power dissipation is located, and downstream water boils and absorbs heat from the higher power region with low thermal resistance. Since the length of the two-phase region in case (c) is shorter than that in case (b), the overall junction temperature is lower due to a smaller pressure drop. An interesting result for case (c) is that the junction temperature distribution is quite uniform even with highly nonuniform power dissipation, which is one of the powerful merits of the two-phase microchannel cooling.

In case (d), the microchannel heat sink has almost the same pressure drop (26.3 kPa) as in case (a). In both cases, the flow has an identical wall heat rate from the silicon wall to the fluid and the channel fluid temperature profiles are almost identical. The junction temperature is determined by the heat flux and convective thermal resistance from the wall to the fluid. Layer 1 has a high temperature hump near the inlet due to high heat flux and low convective heat transfer coefficient in the single-phase region. The highest temperature in layer 2 is lower than that in layer 1, because of the convective nature of the flow direction dependence and high two-phase convective heat transfer. Except for the temperature hump of layer 1, the overall temperature profile with a microchannel heat sink is more uniform than that using the conventional fin heat sink. In all cases with conventional cooling, the temperature of layer 2 is always higher than that of layer 1 due to larger thermal resistance to the environment.

Concluding Remarks

The present work has theoretically explored the potential of a microchannel network for cooling of 3D circuits. The results indicate that the optimal thermal configuration when using microchannels is to manage the higher power dissipation near the outlet regions since this minimizes the pressure drop of the two-phase flow near the highest heat flux regions and thereby results in a decrease of the local wall temperature. Measurements are needed to confirm this prediction, in particular for the case of a strong spatial variation in the heat flux between regions on the chip. With the peak heat flux of 68 W/cm^2 per active layer, the microchannels keep the predicted maximum junction temperature as low as 85°C. A two-phase microchannel cooling network can achieve a more uniform junction temperature field within a layer and less temperature difference between layers, compared with conventional cooling technology. The maximum junction temperature gradient in a device layer with microchannel cooling in the proposed configuration is as low as 55°C/cm with a maximum junction temperature difference of 13°C, while a conventional cooling system yields 300°C/cm and 45°C. The maximum local tempera-

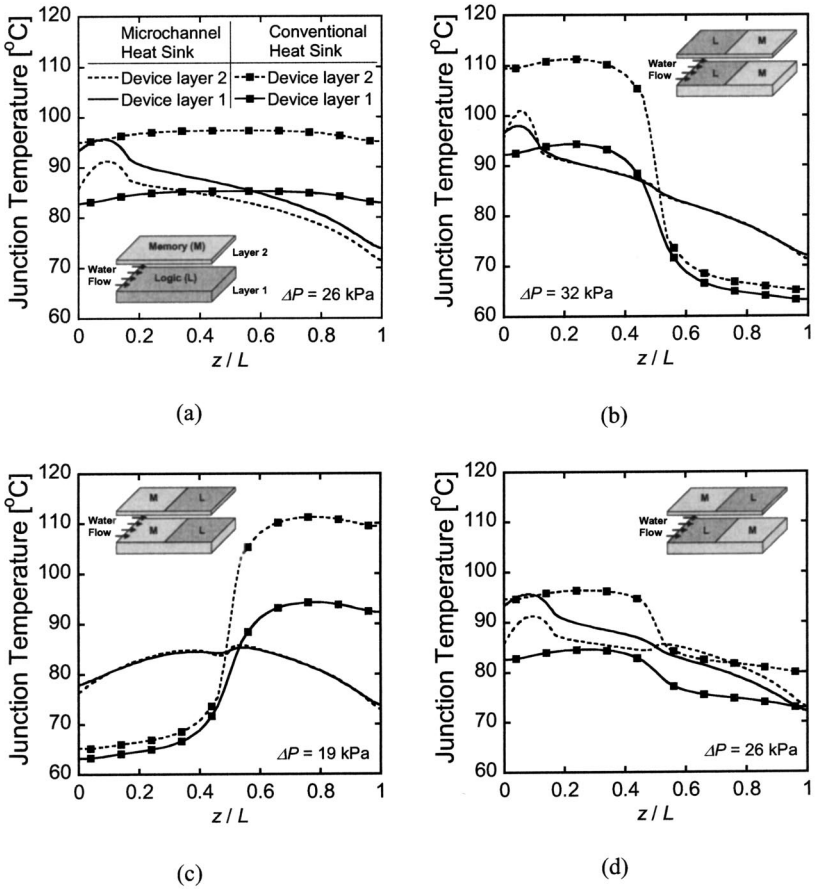

Fig. 8 Comparison of junction temperatures in a two-layer stacked circuit for the cases of an integrated microchannel heat sink and a conventional heat sink. The total flow rate of the liquid water is 15 ml/min and the mass flux is 1.36 $\times 10^{-5}$ kg/s.

ture difference between adjacent device layers is greatly reduced from 15°C by conventional heat sinks to 1.5°C when utilizing microchannels. With two device layers, the liquid flow rate per layer is 7.5 ml/min, and the pumping power, which is the product of pressure drop and the liquid volumetric flow rate at the inlet temperature, is 0.045 W. Generally, when N device layers are involved, the required water flow rate is $15(N-1)/N$ ml/min and the corresponding hydrodynamic pumping power is $0.09(N-1)/N$ W.

Experimental data on boiling convection in 3D microchannel networks are needed to verify the predictions in the current work. Critical is flow delivery to a 3D channel network as well as the potential for severe flow instabilities caused by bubble generation. The design of inlet and exit manifolds is one of the key challenges for the demonstration of a practical 3D circuit cooling system. Further experimental and theoretical work is required to find a relation for two-phase convective heat transfer coefficient. A 3D conjugate conduction/convection simulation is required to calculate the wall temperature under conditions of 3D nonuniform heat generation. Another challenge to be addressed in future work will be the optimization of the microchannel geometries and operating conditions with restriction from the circuit. The present study has illustrated the potential of a 3D microchannel cooling network for removing heat from stacked 3D circuits.

Acknowledgments

The authors appreciate financial support from MARCO Grant No. B-12-D00-S5-4, DARPA/Air Force Contract No. F33615-99-C-1442, and DARPA/Navy Contract No. N66001-04-1-8916.

Nomenclature

A = area, m^2
A_w = solid cross sectional area, m^2
Bo = boiling number
C_1, C_2, C_3, C_4, C_5 = constants in Kandlikar's correlations
Co = convection number
D_h = hydraulic diameter, m
F_k = fluid-dependent parameter in Kandlikar's correlation
Fr = Froude number
L = channel length, m
N = number of device layers
P = pressure, kPa
Q = applied heat, W
R_c = thermal resistance due to convection, mK/W
R_{hs} = thermal resistance due to heat sink system, mK/W
R_{th} = thermal resistance, mK/W
Re = Reynolds number ($=\rho U D_h/\mu$)
T = temperature, °C
U = mean flow velocity, m/s
d = channel depth, m
f = friction factor
g = gravitational constant, m/s^2
h_{conv} = convective heat transfer coefficient, W/m^{2}K

h_l = heat transfer coefficient for the liquid phase flowing alone, W/m^{2}K
i = enthalpy, J/kg
i_{lv} = latent heat, J/kg
k = thermal conductivity, W/mK
$\dot{m}$ = mass flow rate, kg/s
m'' = mass flux, kg/m^2 s
p = channel pitch, m
q'' = heat flux, W/m^2
t = thickness, m
w = channel width, m
x = thermodynamic equilibrium quality
y, z = coordinates, m

Greek symbols

α = thermal diffusivity, m^2/s
Δ = difference
η_0 = overall surface efficiency
η_f = fin efficiency of the fin with an insulated tip
ρ = fluid density, kg/m^3
μ = dynamic viscosity, kg/sm

Subscripts

L = device layer
a = ambient
f = fluid
hs = heat sink system
in = inlet
j = layer index
$jmax$ = number of device layers
l = liquid
ox = oxide layer
si = silicon
v = vapor
w = silicon wall

References

[1] Souri, S. J., Banerjee, K., Mehrotra, A., and Saraswat, K. C., 2000, ''Multiple Si Layer ICs: Motivation, Performance Analysis, and Design Implications,'' *Proc. 37th ACM Design Automation Conference*, Los Angeles, CA, pp. 213–220.

[2] Banerjee, K., Souri, S. J., Kapur, P., and Saraswat, K. C., 2001, ''3-D ICs: A Novel Chip Design for Improving Deep-Submicron Interconnect Performance and Systems-on-Chip Integration,'' Proc. IEEE, **89**(5), pp. 602–633.

[3] DARPA MTO CFP, Section 1: BAA 03-25 3D Integrated Circuits Proposer Information (http://www.darpa.mil/mto/solicitations/BAA03-25/S/Section1.html).

[4] Kleiner, M. B., Kuhn, S. A., Ramm, P., and Weber, W., 1995, ''Thermal Analysis of Vertically Integrated Circuits,'' *Tech. Dig.—Int. Electron Devices Meet.*, pp. 487–490.

[5] Rahman, A., and Reif, R., 2001, ''Thermal Analysis of Three-Dimensional (3-D) Integrated Circuits (ICs),'' *Proc. IITC*, pp. 157–159.

[6] Im, S., and Banerjee, K., 2000, ''Full Chip Thermal Analysis of Planar (2-D) and Vertically Integrated (3-D) High Performance ICs,'' *Tech. Dig.—Int. Electron Devices Meet.*, pp. 727–730.

[7] Hu, C., Morgen, M., Ho, P. S., Jain, A., Gill, W. N., Plawsky, J. L., and Wayne, Jr., P. C., 2000, ''Thermal Conductivity Study of Porous Low-k Dielectric Materials,'' Appl. Phys. Lett., **77**(1), pp. 145–147.

[8] Leland, J. E., Ponnappan, R., and Klasing, K. S., 2002, ''Experimental Investigation of an Air Microjet Array Impingement Cooling Device,'' J. Thermophys. Heat Transfer, **16**(2), pp. 187–192.

[9] Pal, A., Joshi, Y. K., Beitelmal, M. H., Patel, C. D., and Wenger, T. M., 2002, ''Design and Performance Evaluation of a Compact Thermosyphon,'' IEEE Trans. Compon., Packaging Tech., **25**(4), pp. 601–607.

[10] Jiang, L., Mikkelsen, J., Koo, J., Huber, D., Yao, S., Zhang, L., Zhou, P., Maveety, J. G., Prasher, R., Santiago, J. G., Kenny, T. W., and Goodson, K. E., 2002, ''Closed-Loop Electroosmotic Microchannel Cooling System for VLSI Circuits,'' IEEE Trans. Components Packaging Tech., **25**(3), pp. 347–355.

[11] Nguyen, N. T., Huang, X. Y., and Chuan, T. K., 2002, ''MEMS-Micropumps: A Review,'' J. Fluids Eng., **124**(2), pp. 384–392.

[12] Koo, J., Jiang, L., Bari, A., Zhang, L., Wang, E., Kenny, T. W., Santiago, J. G., and Goodson, K. E., 2002, ''Convective Boiling in Microchannel Heat Sinks with Spatially-Varying Heat Generation,'' *Proc. ITherm*, San Diego, CA, pp. 341–346.

[13] Zhang, L., Koo, J., Jiang, L., Asheghi, M., Goodson, K. E., Santiago, J. G., and Kenny, T. W., 2002, ''Measurements and Modeling of Two-phase Flow in Microchannels with Nearly-Constant Heat Flux Boundary Conditions,'' J. Microelectromech. Syst., **11**, pp. 12–19.

[14] Ramm, P. et al., 1997, ''Three Dimensional Metallization for Vertically Integrated Circuits,'' Microelectron. Eng., **37/38**, pp. 39–47.

[15] Fan, A., Rahman, A., and Reif, R., 1999, ''Copper Wafer Bonding,'' Electrochem. Solid-State Lett., **2**(10), pp. 534–536.

[16] Lee, K. W., Nakamura, T., Ono, T., Yamada, Y., Mizukusa, T., Hashimoto, H., Park, K. T., Kurino, H., and Koyanagi, M., 2000, ''Three-Dimensional Shared Memory Fabricated Using Wafer Stacking Technology,'' *Tech. Dig.—Int. Electron Devices Meet.*, pp. 165–168.

[17] Reif, R., Fan, A., Chen, K., and Das, S., 2002, ''Fabrication Technologies for Three-Dimensional Integrated Circuits,'' *Proc. ISQED*, pp. 33–37.

[18] Zingg, R. P., Friedrich, J. A., Neudeck, G. W., and Hofflinger, B., 1990, ''Three-Dimensional Stacked MOS Transistors by Locallized Epitaxial Overgrowth,'' IEEE Trans. Electron Devices, **37**(6), pp. 1452–1461.

[19] Neudeck, G. W., Pae, S., Denton, J. P., and Su, T., 1999, ''Multiple Layers of Silicon-on-Insulator for Nanostructure Devices,'' J. Vac. Sci. Technol., **17**(3), pp. 994–998.

[20] Pae, S., Su, T., Denton, J. P., and Neudeck, G. W., 1999, ''Multiple Layers of Silicon-on-Insulator Islands Fabrication by Selective Epitaxial Growth,'' IEEE Electron Device Lett., **20**(5), pp. 194–196.

[21] Kawamura, S., Sasaki, N., Iwai, T., Nakano, M., and Takagi, M., 1983, ''Three-Dimensional CMOS IC's Fabricated by Using Beam Recrystallization,'' IEEE Electron Device Lett., **4**(10), pp. 366–368.

[22] Sugahara, K., Nishimura, T., Kusunoki, S., Akasaka, Y., and Nakata, H., 1986, ''SOI/SOI/Bulk-Si Triple Level Structure for Three-Dimensional Devices,'' IEEE Electron Device Lett., **7**(3), pp. 193–195.

[23] Knio, T., Oyama, K., Hayashi, Y., and Morimoto, M., 1989, ''Three Dimensional ICs, Having Four Stacked Active Device Layers,'' *Tech. Dig.—Int. Electron Devices Meet.*, pp. 837–840.

[24] Kohno, A., Sameshima, T., Sano, N., Sekiya, M., and Hara, M., 1995, ''High Performance poly-Si TFTs Fabricated Using Pulsed Laser Annealing and Remote Plasma CVD with Low Temperature Processing,'' IEEE Trans. Electron Devices, **42**(2), pp. 251–257.

[25] Meyerson, B. S., Ganin, E., Smith, D. A., and Nguyen, T. N., 1986, ''Low Temperature Si Epitaxy by Hot Wall Ultrahigh Vacuum/Low Pressure Chemical Vapor Deposition Techniques: Surface Optimization,'' J. Electrochem. Soc., **133**, pp. 1232–1235.

[26] Donahue, T. J., and Reif, R., 1985, ''Silicon Epitaxy at 650–800°C using Low-Pressure Chemical Vapor Deposition Both With and Without Plasma Enhancement,'' J. Appl. Phys., **57**, pp. 2757–2765.

[27] Subramanian, V., and Saraswat, K. C., 1998, ''High-Performance Germanium-Seeded Laterally Crystallized TFT's for Vertical Device Integration,'' IEEE Trans. Electron Devices, **45**(9), pp. 1934–1939.

[28] Lee, S-W., and Joo, K-K., 1983, ''Low Temperature Poly-Si Thin Film Transistor Fabrication by Metal-Induced Lateral Crystallization,'' IEEE Electron Device Lett., **17**(4), pp. 160–162.

[29] Tuckerman, D. B., and Pease, R. F. W., 1981, ''High-Performance Heat Sinking for VLSI,'' IEEE Electron Device Lett., **2**(5), pp. 126–129.

[30] Wei, X., and Joshi, Y., 2002, ''Optimization Study of Stacked Micro-Channel Heat Sinks for Micro-Electronic Cooling,'' *Proc. ITherm*, San Diego, CA, pp. 441–448.

[31] Kandlikar, S. G., 2003, ''Heat Transfer Mechanisms During Flow Boiling In Microchannels,'' *Proc. 1st Int. Conference on Micro/Minichannels*, Rochester, NY, ICMM2003-1005.

[32] Peng, X. F., Hu, H. Y., and Wang, B. X., 1998, ''Boiling Nucleation During Liquid Flow in Microchannels,'' Int. J. Heat Mass Transfer, **41**(1), pp. 101–106.

[33] Peng, X. F., Tian, Y., and Lee, D. J., 2002, ''Arguments on Microscale Boiling Dynamics,'' Microscale Thermophys. Eng., **6**(1), pp. 75–83.

[34] Bowers, M. B., and Mudawar, I., 1994, ''Two-Phase Electronic Cooling Using Mini-Channel and Micro-Channel Heat Sinks: Part 1–Design Criteria and Heat Diffusion Constraints,'' ASME J. Electron. Packag., **116**, pp. 290–297.

[35] Bowers, M. B., and Mudawar, I., 1994, ''Two-Phase Electronic Cooling Using Mini-Channel and Micro-Channel Heat Sinks: Part 2–Flow Rate and Pressure Drop Constraints,'' ASME J. Electron. Packag., **116**, pp. 298–305.

[36] Stanley, R. S., Barron, R. F., and Ameel, T. A., 1997, ''Two-Phase Flow in Microchannels,'' DSC-Vol. 62/HTD-Vol. 34 MEMS, ASME, pp. 143–152.

[37] Triplett, K. A., Ghiaasiaan, S. M., Abdel-Khalik, S. I., and Sadowski, D. L., 1999, ''Gas-Liquid Two-Phase Flow in Microchannels, Parts I & II,'' Int. J. Multiphase Flow, **25**, pp. 377–410.

[38] Akbar, M. K., Plummer, D. A., and Ghiaasiaan, S. M., 2003, ''On Gas-Liquid Two-Phase Flow Regimes in Microchannels,'' Int. J. Multiphase Flow, **29**, pp. 855–865.

[39] Peles, Y. P., Yarin, L. P., and Hetsroni, G., 2001, ''Steady and Unsteady Flow in a Heated Capillary,'' Int. J. Multiphase Flow, **27**(4), pp. 577–598.

[40] Hetsroni, G., Mosyak, A., and Segal, Z., 2001, ''Nonuniform Temperature Distribution in Electronic Devices Cooled by Flow in Parallel Microchannels,'' IEEE Trans. Components Packaging Tech., **23**(1), pp. 16–23.

[41] Yarin, L. P., Ekelchik, L. A., and Hetsroni, G., 2002, ''Two-Phase Laminar Flow in a Heated Microchannels,'' Int. J. Multiphase Flow, **28**(10), pp. 1589–1616.

[42] Qu, W., and Mudawar, I., 2003, ''Measurement and Prediction of Pressure Drop in Two-Phase Micro-Channel Heat Sinks,'' Int. J. Heat Mass Transfer, **46**, pp. 2737–2753.

[43] Qu, W., and Mudawar, I., 2003, ''Flow Boiling Heat Transfer in Two-Phase Micro-Channel Heat Sinks–I. Experimental Investigation and Assessment of

Correlation Methods,'' Int. J. Heat Mass Transfer, **46**, pp. 2755–2771.
[44] Qu, W., and Mudawar, I., 2003, ''Flow Boiling Heat Transfer in Two-Phase Micro-Channel Heat Sinks–II. Annular Two-Phase Flow Model,'' Int. J. Heat Mass Transfer, **46**, pp. 2773–2784.
[45] Lee, M., Wong, Y. Y., Wong, M., and Zohar, Y., 2003, ''Size and Shape Effects on Two-Phase Flow Patterns in Microchannel Forced Convection Boiling,'' J. Micromech. Microeng., **13**, pp. 155–164.
[46] Koo, J., Jiang, L., Zhang, L., Zhou, P., Banerjee, S. S., Kenny, T. W., Santiago, J. G., and Goodson, K. E., 2001, ''Modeling of Two-phase Microchannel Heat Sinks for VLSI Chips,'' *Proc. Int. MEMS Workshop*, Interlaken, Switzerland, pp. 422–426.
[47] Koo, J., Im, S., Cho, E., Prasher, R. S., Wang, E., Jiang, L., Bari, A., Campion, D., Fogg, D., Kim, M., Kenny, T. W., Santiago, J. G., and Goodson, K. E., 2002, ''VLSI Hotspot Cooling Using Two-Phase Microchannel Convection,'' *ASME Proc. IMECE*, New Orleans, LA, IMECE2002-39585.
[48] Incropera, F. P., and DeWitt, D. P., 1996, *Fundamentals of Heat and Mass Transfer*, 4th ed., John Wiley, New York.
[49] Kays, W. M., and Crawford, M. E., 1993, *Convective Heat and Mass Transfer*, 3rd ed., McGraw-Hill, New York.
[50] Kandlikar, S. G., 1990, ''A General Correlation for Saturated Two-Phase Flow Boiling Heat Transfer Inside Horizontal and Vertical Tubes,'' ASME J. Heat Transfer, **112**, pp. 219–228.
[51] Patankar, S. V., 1980, *Numerical Heat Transfer and Fluid Flow*, McGraw-Hill, New York.
[52] Harr, L., Gallagher, J. S., and Kell, G. S., 1984, *NBS/NRC Steam Tables*, Hemisphere, Washington.
[53] Chiang, T.-Y., Souri, S. J., Chui, C. O., and Saraswat, K., 2001, ''Thermal Analysis of Heterogeneous 3-D ICs with Various Integration Scenarios,'' Tech. Dig.—Int. Electron Devices Meet., pp. 681–684.

C. Bower

A. Ortega
e-mail: ortega@u.arizona.edu

P. Skandakumaran

Department of Aerospace and Mechanical Engineering,
The University of Arizona,
Tucson, AZ 85721

R. Vaidyanathan

T. Phillips

Advanced Ceramics Research, Inc.,
3292 E. Hemisphere Loop,
Tucson, AZ 85706-5013

Heat Transfer in Water-Cooled Silicon Carbide Milli-Channel Heat Sinks for High Power Electronic Applications

Heat transfer and fluid flow in a novel class of silicon carbide water-cooled milli-channel heat sinks were investigated. The heat sinks were manufactured using an extrusion freeform fabrication (EFF) rapid prototyping technology and a water-soluble polymer material. Rectangular heat exchangers with 3.2 cm×2.2 cm planform area and varying thickness, porosity, number of channels, and channel diameter were fabricated and tested. The perchannel Reynolds number places the friction coefficients in the developing to developed hydrodynamic regime, and showed excellent agreement with laminar theory. The overall heat transfer coefficients compared favorably with the theory for a single channel row but not for multiple rows. [DOI: 10.1115/1.1852494]

Keywords: Milli-Channel, Liquid Cooling, SiC, IGBT Cooling, Extrusion Freeform Fabrication

Introduction

With the trend towards increasing levels of integration in the IC industry, heat-sinking technologies with a higher level of performance are required to meet the elevated power dissipation requirements in electronic devices. With air as a working fluid, it is increasingly difficult to design cost-effective heat sinks that can reject over 100 W/cm^2 [1]. To this end, compact microchannel structures implementing higher conductivity fluids such as water have received renewed attention as a possible cooling alternative. Single row microchannels etched directly into the backs of silicon wafers were first shown to be effective by Tuckerman and Pease [2] in which a maximum of 790 W/cm^2 was rejected with a rise in water temperature of 71°C. While the cost of manufacturing microfabricated heat sinks currently prohibits application in production level electronics, the study showed that microchannel structures are well suited to the task of cooling electronic devices.

Following the pioneering work of Tuckerman and Pease, considerable research has been conducted on microchannel heat sinks. Much of this research has focused on single rows of thin, deep channels, commonly analyzed with the fin approach [3]. The fin approach has more recently found application in analysis of foam structures [4] and other low aspect ratio structures. The accuracy of the fin approach is limited by several simplifying assumptions, including fluid temperature uniformity in the direction perpendicular to the fluid flow, one-dimensional heat transfer in the fins, and constant heat transfer coefficient. Thus, the range of accuracy of the fin approach in modeling microchannel heat sinks is restricted [5].

More recently, the reduction of relevant dimensions in classical flow structures found in microchannel heat exchangers has shown that they are amenable to investigation using a porous media approach. In a single equation porous media model, the fluid and solid properties and geometry are no longer considered separately, but are considered to have combined, effective thermal properties. In a two-equation model, the volume averaged equations for the fluid and solid phases are connected by a heat transfer coefficient. Koh and Colony [6] and Kim et al. [7,8] have approached the problem using either one or two equation models. This approach is well suited to channels with low aspect ratios such as foams or multiple rows of small straight channels.

To a large extent, research into micro- and milli-scale heat exchangers have been centered around heat sinks fabricated from a highly thermally conductive solid, such as copper or silicon, with rows of small channels fabricated into the surfaces by precision machining or chemical etching. High solid conductivity is particularly important in multiple row structures, as the amount of heat removed by any given row can be large. A highly conductive medium increases heat conduction into subsequent layers where it can be transferred to the fluid flow. This provides an advantage to multiple row heat sinks. In single-phase conditions, single row heat sinks exhibit large stream-wise increase in the water temperature due to high heat fluxes. This promotes a stream-wise increase in the temperature of the dissipating device [9]. This temperature increase is detrimental to temperature-sensitive devices such as microprocessors, which must operate below specified temperatures, and contributes to stresses arising from the thermal expansion coefficient (TEC) mismatch. Vafai and Zhu [10] showed that a two-layer counterflowing microchannel structure reduced the stream-wise temperature rise along the device surface, compared to that of the one-layered heat sink.

This paper presents results of an initial experimental study of the single phase heat transfer and pressure drop characteristics of compact, single and multi-row silicon carbide heat exchangers manufactured by an extrusion freeform fabrication method. This method allows the fabrication of heat sinks from non-traditional materials containing optimal number of rows, hole diameter, porosity, and other properties. The SiC implemented in this study has a bulk thermal conductivity of approximately 15 W/m·C. While not an ideal conductor, SiC has a thermal expansion coefficient (TEC) closely matched to that of silicon, allowing the exchanger to be more easily integrated directly into the packaging solution. The favorable TEC characteristic of these exchangers, when paired with the ease of manufacturing multiple row structures, has opened the door towards the development of integrated liquid cooled thermal solutions for high heat flux electronics.

Manuscript received May 25, 2004; revision received September 1, 2004. Review conducted by: C. Amon.

Fabrication

The current milli-channel SiC heat exchangers were fabricated by Advanced Ceramics, Inc., using an extrusion freeform fabrication method (EFF) [11]. The SiC substrate was fabricated by co-extruding multiple layers of a composite filament, where each filament consisted of an inner core of water-soluble polymer blend surrounded by an outer shell of SiC. The polymer core was removed during thermal processing, yielding high-surface-area microscale channels to accommodate the flow of a cooling fluid. EFF permits the fabrication of geometrically complex, three-dimensional structures directly from CAD designs. Rapid prototyping allows the fabrication of multi-row structures that do not have to be individually laminated.

Experiments

Test Samples and Instrumentation. Tests were performed on six SiC samples, each measuring approximately 3.2 cm×2.2 cm in planform area with varying thickness, *H*, number of channels, *N*, channel diameter, *d*, and number of channel rows. In addition, a copper validation sample with a single row of six two-millimeter diameter holes was fabricated for comparison. Figure 1 illustrates the nomenclature used in describing the test samples. Figure 2 shows photographs of representative SiC samples and the copper validation sample. The properties of the samples tested are shown in Table 1 where Sample 7 is the copper sample. The average diameter of the channels in each SiC sample was determined by photographing both inlet and exit faces of the samples, expanding the image, and measuring the total cross-sectional area of the channel openings. The average area for each channel was determined as the total channel area divided by number of channels, and the average effective per channel diameter, *d*, was determined assuming each channel had a circular cross-sectional area. Each of the samples was manifolded with 0.5-inch-thick G-10, a low-conductivity (0.288 W/m·C) glass/epoxy composite, allowing the sample to be flowed while minimizing heat lost through conduction. Pressure taps with a 0.08-cm ID were inserted 2 to 3 mm upstream and downstream of the exchanger inlet and exit respectively. Measurement of hydrodynamic pressure drop across a sample was performed by means of simple U-tube manometer. Figure 3 illustrates the sample with a manifold as configured for the heat transfer and pressure drop measurements. Type-K, 36-gauge, thermocouples were inserted in the flow allowing direct measurement of the mixed mean temperature approximately 2 cm from the heat exchanger entry and exit.

Water flow was delivered to the heat sink via a Neslab RTE 7 constant-temperature recirculator capable of absorbing 500 Watts at 20°C. Downstream of the recirculator outlet, flow metering was achieved with a bank of valved, correlated rotometers, with ranges from 1 to 1000 mL/min. From the flow meters, water flowed into the inlet of the milli-channel sample. The fluid exiting the heat sink was collected at the outlet manifold and returned to the recirculator reservoir at ambient pressure to be chilled for recirculation.

Heat Delivery and Measurement. Heat was supplied symmetrically via a matched set of copper metering bars measuring 6.35 cm × 6.35 cm in cross section at the ''head,'' which tapers to 2.54 cm × 2.54 cm in cross section at its contact with the sample. The bars contacted the heat exchanger external surfaces through a matching opening in the G-10 manifold. Three Incoloy cartridge heaters, each capable of developing 500 watts at 120 AC volts, were embedded in the ''head'' of each bar. Each set of heaters was driven via pulse width modulation of a standard 120-volt AC signal by a Fugi PXR-4 temperature controller and solid-state-relay combination. A series of five, 36-gauge, type-K thermocouples were embedded in the meter bar at 0.25-inch intervals beginning at 0.125 inch from the contact surface. Heat flow was determined by measurement of the temperature gradient along the meter bar, and using the one-dimensional conduction law:

$$q = A_m k_m \Delta T / \Delta x \tag{1}$$

In all instances the temperature gradient was seen to be linear in the meter bar, validating the use of the one-dimensional conduction equation. A high-conductivity interface compound was applied to all contact surfaces to ensure evenly distributed thermal contact while allowing for the placement of three additional 36-gauge, type-K thermocouples on the sample surface to estimate surface temperature. The heated end of the metering bars were attached to a precision platen die set and actuated by a pneumatic ram. All thermocouples were terminated in an isothermal zone box and temperatures were measured with a Fluke Hydra 2620-A data acquisition unit.

A typical test was conducted as follows: After insertion of a sample between metering bars, a 200-psi load was applied to ensure proper contact of surface thermocouples and to minimize

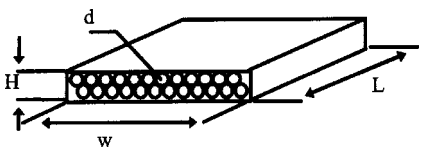

Fig. 1 Schematic of a representative sample

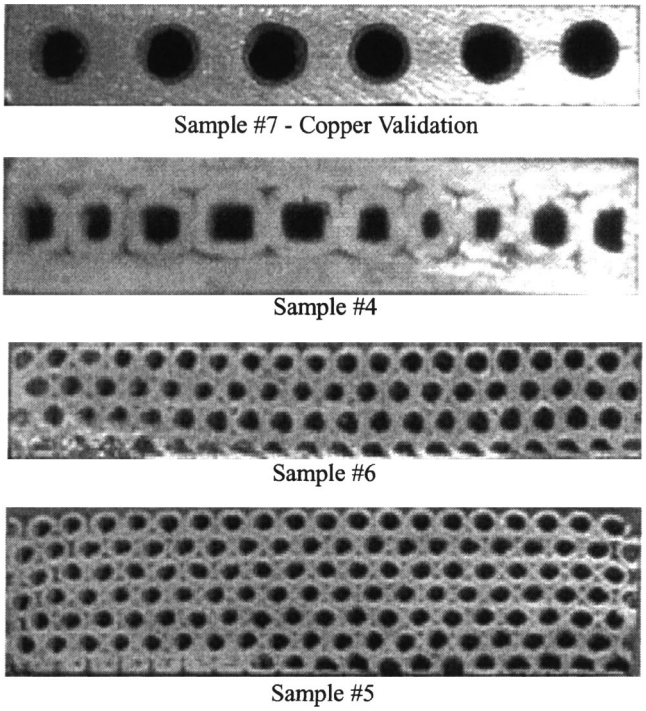

Fig. 2 Photographs of samples

Table 1 Geometric characteristics of tested samples

Sample ID	L×w×H $m \cdot 10^{-3}$	d $m \cdot 10^{-6}$	No. of rows	N
1	33×22×11.2	1300	5	42
2	33×22×10.8	335	11	155
3	32×22×11.8	940	7	49
4	30×22×5	1150	1	10
5	33×22×5	510	7	126
6	33×22×2.8	510	4	76
7	32×25.4×3.8	2030	1	6

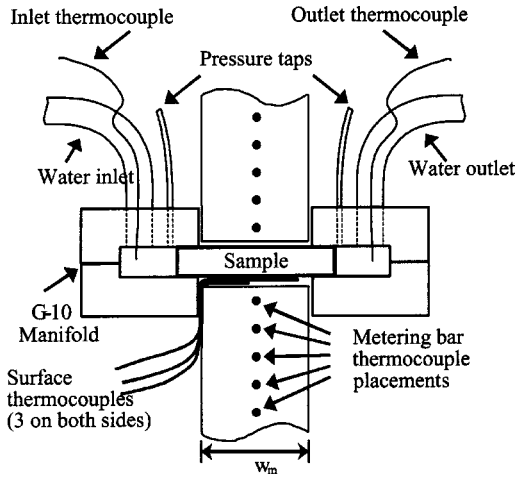

Fig. 3 Schematic of sample manifold and instrumentation

contact resistance. The flow loop was engaged at maximum flow rate, commonly 500 mL/min, and the heating was applied so as to establish a heater temperature of 90°C. The system was allowed to reach thermal equilibrium for a period of at least ten minutes or until surface temperatures changed by no more than 0.1°C in five minutes. Following collection of thermal and pressure data, the flow rate was systematically lowered and data acquisition was repeated.

Data Reduction

Thermal Characterization. The derived thermal metrics are stated in terms of either wet or base surface areas. A_{wet} is the total internal wetted area of all the channels

$$A_{\text{wet}} = \pi d w_m N \tag{2}$$

A_{base} is the total outer heated area:

$$A_{\text{base}} = 2 w w_m \tag{3}$$

where w is the width of the sample and w_m is the width of the metering bar, not the entire sample length, L. Note that all data presented are for heating on both outer surfaces of the sample. The overall heat transfer coefficient from the SiC to the water is calculated as shown by Incropera and DeWitt [12]

$$U = \frac{q}{A \Delta T_{s\text{-}w}} \tag{4}$$

where A can be either A_{wet} or A_{base}; $\Delta T_{s\text{-}w}$ is a log mean temperature difference between the external surface and fluid, defined as [12]

$$\Delta T_{s\text{-}w} = \frac{(T_s - T_{w,\text{in}}) - (T_s - T_{w,\text{out}})}{\ln \dfrac{T_s - T_{w,\text{in}}}{T_s - T_{w,\text{out}}}} = \frac{T_{w,\text{out}} - T_{w,\text{in}}}{\ln \dfrac{T_s - T_{w,\text{in}}}{T_s - T_{w,\text{out}}}} \tag{5}$$

The thermal resistance, R, is determined as

$$R = \frac{\Delta T_{s\text{-in}}}{q} \tag{6}$$

where q is the total heat supplied from the top surface, q_1, and bottom surface, q_2

$$q = q_1 + q_2 \tag{7}$$

and $\Delta T_{s\text{-in}} = T_s - T_{\text{in}}$, where T_s is the average surface temperature of the top and bottom surfaces.

During testing, it was observed that measurements of the outlet fluid temperature demonstrated significant temporal variation, attributed to incomplete mixing of the exiting fluid. It was therefore determined that the mixed outlet temperature could best be estimated indirectly by the use of the energy balance

$$q = \dot{m} c_p (T_{w,out} - T_{w,in}) + q_{\text{loss}} \tag{8}$$

A zero flow case was tested and losses were seen to be less than 2 Watts in all cases. Extraneous losses were therefore determined to be negligible when compared to the order of the heat throughput during tested flows.

Other non-dimensional numbers were defined as follows:

Reynolds Number

$$\text{Re}_d = \frac{\rho u d}{\mu} \tag{9}$$

Nusselt Numbers

$$\overline{\text{Nu}}_{\text{wet}} = \frac{U_{\text{wet}} d}{k_w}, \quad \overline{\text{Nu}}_{\text{base}} = \frac{U_{\text{base}} d}{k_w} \tag{10–11}$$

Prandtl Number

$$\text{Pr} = \frac{\mu c_p}{k_w} \tag{12}$$

Graetz Number

$$\text{Gz} = \frac{\text{Re}_d \, \text{Pr} d}{L} \tag{13}$$

The Nusselt number in a single channel was compared to the classical solution for the hydrodynamically developed but thermally developing case by Hausen [13]

$$\overline{\text{Nu}}_{\text{wet}} = 3.66 + \frac{0.0668(d/L)\text{Re}_d \, \text{Pr}}{1 + 0.04[(d/L)\text{Re}_d \, \text{Pr}]^{2/3}} \tag{14}$$

and to the combined entry length solution due to Sieder and Tate [14]

$$\overline{\text{Nu}}_{wet} = 1.86 \left(\frac{\text{Re}_d \, \text{Pr}}{L/d} \right)^{1/3} \left(\frac{\mu}{\mu_s} \right)^{.14} \tag{15}$$

Hydrodynamic Characterization. An important consideration in the development of cost effective heat exchangers is the pressure required to force a given flow rate. It is therefore desirable to be able to evaluate the pressure head loss based on physical characteristics of the heat sink alone. To this end, the SiC samples were tested and compared to expected pressure drop values as a function of mass flow rate. Pressure drop is best compared by expression in terms of the non-dimensional friction factor

$$f = \frac{2 \Delta P}{\rho u_m^2} \cdot \frac{d}{L} \tag{16}$$

where u_m is the average channel velocity. Since flow is laminar for all samples at all flow rates in this study, the present results can be compared to the classical solution for Moody friction factor in the developing flow regime for a circular duct as presented for example by Shah and London [15]

$$f = \frac{\dfrac{3.44}{(x^+)^{1/2}} + \dfrac{1.25/(4x^+) + 16 - 3.44/(x^+)^{1/2}}{1 + 0.00021(x^+)^{-2}}}{0.25 \, \text{Re}_d} \tag{17}$$

where x^+ is a nondimensional length

$$x^+ = \frac{L}{d \, \text{Re}_d} \tag{18}$$

This correlation converges to the classical solution of $f=64/\mathrm{Re}_d$ for the case where x^+ is large and the influence of the hydrodynamic entrance length diminishes.

Measurement Uncertainty. All temperature measurements were taken with type-K thermocouples terminated in an isothermal zone box with a true ice-point reference. Previous calibration and determination of zero and first order uncertainties lead to an overall uncertainty of ± 0.1°C. Uncertainty in the heat flow determination from Eq. (1) was estimated to be $\pm 5\%$ using the single sample uncertainty analysis proposed in [16]. The thermal conductivity of the copper bars was measured in a separate experiment by comparison to a NIST traceable carbon sample. The primary parameters contributing to the uncertainty in the hydrodynamic analysis were found to be uncertainty in volumetric flow rate, pressure drop, and average channel diameter. The supplier's estimated error in volumetric flow measurement was 2% of full scale, accounting for no more than 6% error in application. Absolute error in pressure measurements were assumed to be 3 mm H_2O, introducing large error estimates at lower mass flow rates, with values approaching 40%. Uncertainty in the determination of the average diameter proved to be the largest contributor at higher Reynolds numbers accounting for up to 4% deviation. Propagation of error using the root-sum square method [16], results in a maximum error for thermal measurements (R and Nu) of 5% and error in friction factor ranging from 6–40%.

Results and Discussion

Figure 4 shows the overall sample thermal resistance as a function of total volumetric flow rate collected on a high-performing, single-row SiC sample, compared to the copper validation sample. For reference, a line representing typical results from a high-performing air-impingement heat sink is also presented [17], but the air-cooled heat sink is heated only on one surface, whereas the present water-cooled heat sink is heated on both surfaces. At modest flow rates, both milli-channel sinks perform significantly better than their air counterparts with the copper and SiC heat sinks yielding thermal resistances of 0.2 C/W and 0.26 C/W, respectively, at a flow rate of 507 mL/min. It is interesting to note that despite its lower thermal conductivity, the SiC heat sink compares favorably with the copper heat sink at the same overall flow rate. To be sure, this is not a rigorous comparison, for example the per channel Reynolds number is different for the two cases. However, this comparison does offer preliminary evidence that the SiC heat sink thermal performance does not suffer greatly from the modest thermal conductivity of this formulation of SiC.

The thermal data from these single-row samples are validated in Fig. 5 by comparison with classical solutions for single tubes with a constant wall temperature. In this experiment, the surfaces were not held at a fixed temperature. A variation of 5°C at maximum was accounted for by averaging the thermocouple measurements taken along the sample surface. In the plot, data are seen to lie between the Nusselt number solutions for a fully developed hydrodynamic and thermally developing channel flow, and a combined entry length solution, both of which converge to the developed value of 3.66. Since the copper sample has larger holes than the SiC sample, it is expected that the copper sample will tend more to the combined solution, and the SiC to the thermally developing solution.

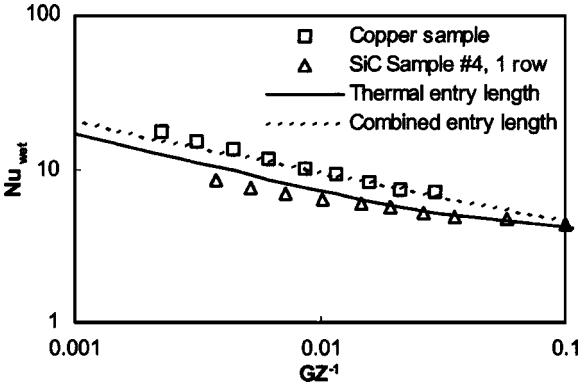

Fig. 5 Single-row samples compared to laminar heat transfer theory for a single isothermal circular channel

As additional rows are added to the heat exchanger, the presentation developed for Fig. 5 can be utilized to show that additional physics are in play. Figure 6 shows diminishing values for Nu_{wet} as the number of rows increase. Nu_{wet} compares well to theory for the case of a single row, implying that the wall temperature is nearly constant around the wetted-area and equal to the temperature measured at the outer surface area. When the number of rows increases, the temperature of the internal channels falls below the values measured on the outer surface. This results in an apparent reduction in Nu_{wet}. The diminished values of Nu_{wet} in Fig. 6 as the number of rows increase, affirms that the outer surface temperature and heat flux are not sufficient to describe the interior conditions. Furthermore, the reduction in Nu_{wet} does not imply that the overall performance is diminished in multiple row heat sinks, only that other formulations are necessary to describe their performance.

A common method for evaluation of heat sinks is the overall thermal resistance. A comparison of thermal resistance for samples of four and seven rows is shown in Fig. 7. These samples have identical geometrical parameters except for the number of rows. Here we see that the resistance drops for increase in mass flow rate and for an increase in number of rows, reflecting a corresponding reduction in device temperature. This effect can be

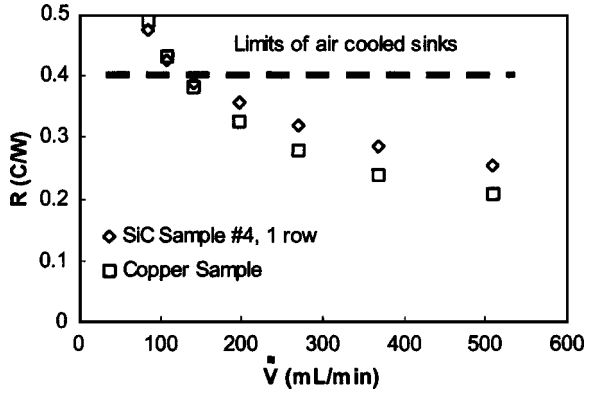

Fig. 4 Comparison of thermal resistance for SiC and copper heat exchangers and high-performance air sink

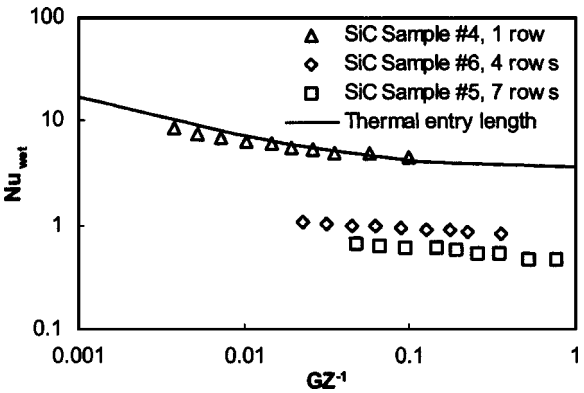

Fig. 6 Wetted Nusselt number dependence on number of rows

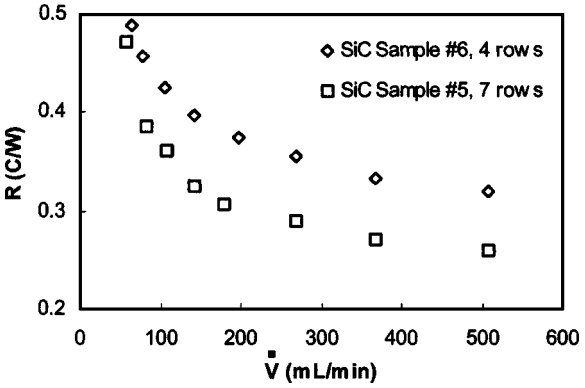

Fig. 7 Effect of increasing number of rows and flow rate on thermal resistance

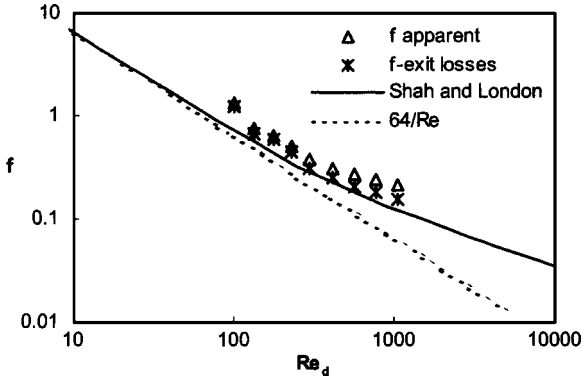

Fig. 10 Friction factor for the copper validation sample compared to theory

captured in a non-dimensional form by introducing an alternative definition of the Nusselt number, Nu_{base}, as formulated in Eq. (11). In this form, the base area is used to describe the overall heat transfer. Figure 8 compares Nu_{base} for samples with four rows and seven rows, and shows an increase in the Nu_{base} with an increase in the number of rows. Here it is seen that multiple rows allow heat to be conducted to subsequent interior rows. Due to the finite conductivity of the SiC samples, Nu_{base} will approach a limit where a further increase in the number of rows will no longer affect the overall thermal performance of the heat sink. It is anticipated that the increase in wetted channel area will not overcome the inability to conduct heat to the interior rows, and the drop in the per-channel mass flow rate. This is being investigated in a companion analytical study.

As important as thermodynamic performance in the selection of a viable compact heat exchanger, are the hydrodynamic characteristics. As seen in Fig. 9, the pressure drop from samples of similar cross sectional area depends on channel diameter, number of channels, and mass flow rate. Data reveal a well-behaved linear relationship between mass flow rate and pressure drop, an expected behavior in laminar flow conditions. Also, a reduction of channel diameter size from 1.3 mm to 0.34 mm, results in a nearly tenfold increase in pressure drop across the sample. Calculated friction factor data for the copper validation sample are shown in

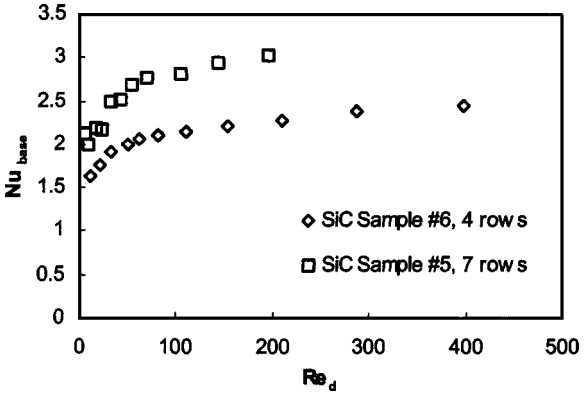

Fig. 8 Nusselt number based on base area for 4 and 7 row samples

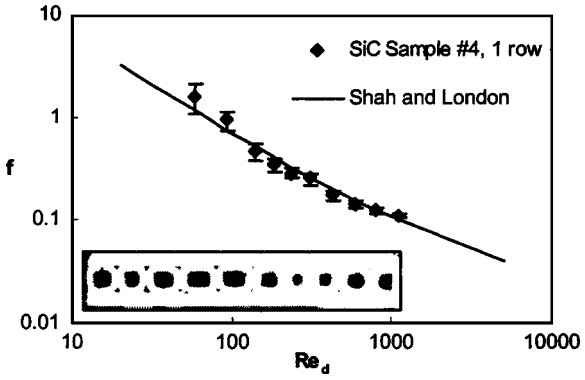

Fig. 11 Friction factor for a single-row SiC sample compared to theory

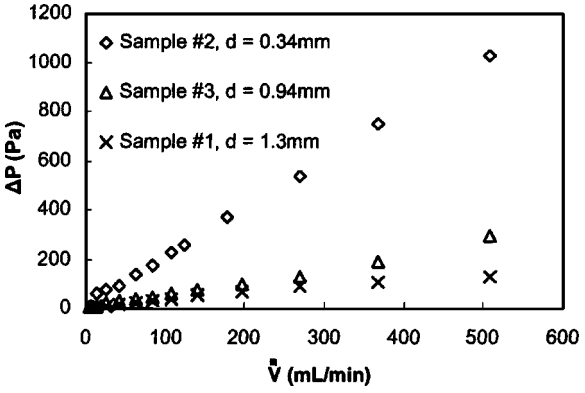

Fig. 9 Pressure drop as a function of mass flow and channel diameter for samples of similar cross-sectional area

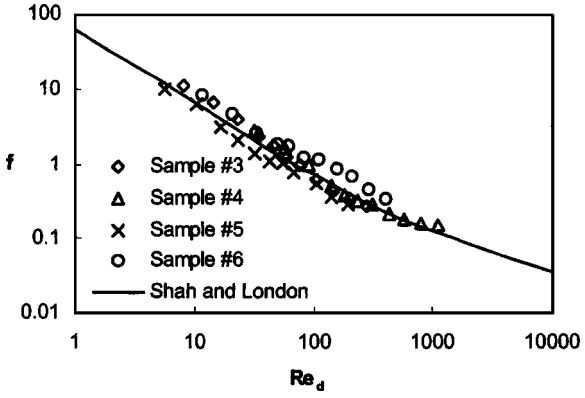

Fig. 12 Friction factors of several SiC samples compared to theory

Fig. 10, along with hydrodynamically developing friction factor theory. The copper sample contains a set of identically sized, smooth channels allowing for validation of the experimental setup for pressure drop measurement. The channels in the copper sample have a relatively small L/d ratio, making entrance and exit losses numerically significant. In Fig. 10, data for f are shown after subtracting inlet and exit pressure losses computed using a rounded entrance loss coefficient, and a contraction/expansion ratio of 0.1. As seen in the figure, these data compare favorably with the theory except at the lowest flow rates, where uncertainty was high.

The SiC samples exhibit departures from those idealized in the copper sample. Due to processing and sintering under high temperature and pressure, the SiC samples tested showed varying degrees of variation in channel size and shape. The results presented are for preliminary data and errors may be apparent from clogged channels, interface resistance, ''crushed'' holes, and variation in channel geometries. A view of the cross section of a typical sample and its measured friction factor data are shown in Fig. 11. It is evident that even with irregularity, the friction factors line up well with the laminar theory when using average effective channel diameter as the representative length scale. Figure 12 shows friction factor data for samples 3 through 6, again demonstrating good agreement with the laminar theory.

Conclusions

Although a relatively small set of samples were characterized, some definite conclusions can be stated as follows:

1. Liquid-cooled SiC heat sinks easily outperform air-cooled heat sinks and compare favorable with copper equivalents at similar overall flow rates.
2. Performance of single row SiC samples is not hindered by low thermal conductivity and can be predicted by theory developed for isothermal channels.
3. Thermal performance for multiple row samples cannot be conveniently captured by single channel, isothermal theory because the interior temperature differs from the easily measured external surface temperature.
4. Comparison of R and $\mathrm{Nu}_{\mathrm{base}}$, shows that multiple row samples are more effective than single row counterparts. It is anticipated that an optimum number of rows exists for a given geometry and sample thermal conductivity.
5. Hydrodynamic performance in the samples agrees with laminar theory and does not suffer from physical irregularities (size and shape variation) when the average effective per channel diameter is used as the relevant lengthscale.

Continuing Work

More refined second generation SiC samples are under investigation and an analytical model for multi-row milli-channel heat sinks is under development to allow full exploration of design optimization in such geometries. These results will be reported in future publications.

Acknowledgment

The research was performed under Army STTR contract no. DASG60-02-P-02-P-0280 monitored by Richard Rodgers.

Nomenclature

A = area (m^2)
c_p = specific heat of water (J/kg·C)
d = average or mean effective per channel diameter (m)
f = friction factor
Gz = Graetz number
H = sample thickness (m)
k_w = thermal conductivity (W/m·C)
L = sample length (m)
N = number of channels
$\overline{\mathrm{Nu}}$ = average Nusselt number
P = pressure (Pa)
Pr = Prandtl number
q = heat flow (W)
R = thermal resistance (C/W)
Re = Reynolds number
T = temperature (C)
u_m = mean channel velocity (m/s)
U = overall heat transfer coefficient ($\mathrm{W/m^2 \cdot C}$)
$\dot{V}$ = volumetric flow rate (mL/min)
w = sample width (m)
x = streamwise coordinate
x^+ = non-dimensional distance
y = normal coordinate

Greek

Δ = delta, change in property
μ = dynamic viscosity at mean temperature ($\mathrm{N \cdot s/m^2}$)
π = pi
ρ = fluid density ($\mathrm{kg/m^3}$)

Subscripts

1 = from top surface
2 = from bottom surface
base = based on contact area
d = based on mean effective diameter
h = based on sample height
in = inlet
m = meter bar
out = outlet
$o\text{-}i$ = outlet minus inlet
s = solid or surface, depending on context
$s\text{-}i$ = surface to inlet
$s\text{-}w$ = log mean, surface to wall
y = y direction, normal to flow
w = water
wet = based on wetted internal area

References

[1] Ortega, A., 2003, ''Air Cooling of Electronic Components: Review of Research Developments in the Period 1981–2001 and Their Impact on Our Understanding of Cooling Limits,'' Paper IMECE 2003-424122003.
[2] Tuckerman, D. B., and Pease, R. F. W., 1981, ''High-Performance Heat Sinking for VLSI,'' IEEE Electron Device Lett., **2**, pp. 126–129.
[3] Phillips, R. J., 1990, ''Micro-Channel Heat Sinks,'' in *Advances in Thermal Modelling of Electronic Components and Systems*, Vol. 2, A. Bar-Cohen and A. D. Kraus, eds., ASME, New York, Chap. 3.
[4] Lu, T. J., and Ashby, M. F., 1998, ''Heat Transfer in Open Celled Metal Foams,'' Acta Mater., **46**, pp. 3619–3635.
[5] Knight, R. W., Gooding, J. S., and Hall, D. J., 1991, ''Optimal Thermal Design of Forced Convection Heat Sinks—Analytical,'' ASME J. Electron. Packag., **113**, pp. 313–321.
[6] Koh, J. C. Y., and Colony, R., 1986, ''Heat Transfer of Microstructure for Integrated Circuits,'' Int. Commun. Heat Mass Transfer, **13**, pp. 89–98.
[7] Kim, S. J., Kim, D., and Lee, D. Y., 2000, ''On the Local Thermal Equilibrium in Microchannel Heat Sinks,'' Int. J. Heat Mass Transfer, **43**, pp. 1735–1748.
[8] Kim, S., and Kim, J. D., 1999, ''Forced Convection in Microstructure for Integrated Circuits,'' ASME J. Heat Transfer, **121**, pp. 635–645.
[9] Mudawar, I., 2000, ''Assessment of High Heat Flux Thermal Management Schemes,'' *Proceedings 7th IEEE InterSociety Conference on Thermal Phenomena in Electronic Systems* (ITHERM 2000), IEEE, Piscataway, NJ, Las Vegas, NV.
[10] Vafai, K., and Zhu, L., 1999, ''Analysis of Two-Layered Micro-Channel Heat Sink Concept in Electronic Cooling,'' Int. J. Heat Mass Transfer, **42**, pp. 2287–2297.

[11] Vaidyanathan, R., Walish, J., Lombardi, J. L., Calvert, P. D., Kasichainula, S., and Cooper, K., 2000, ''Extrusion Freeform Fabrication of Functional Ceramic Prototypes,'' J. Met., **52**(12), pp. 34–37.
[12] Incropera, F., and Dewitt, D., 2002, *Fundamentals of Heat and Mass Transfer*, 5th Ed., Wiley, New York, pp. 482–490.
[13] Hausen, H., 1943, ''Darstellung des Warmeubergages in Rohren durch verallgemeinerte Potenzbeziehungen,'' VDI Z, **4**, p. 91.
[14] Seider, E. N., and Tate, G. E., 1936, ''Heat Transfer and Pressure Drop of Liquids in Tubes,'' Ind. Eng. Chem., **28**, p. 1429.
[15] Shah, R. K., and London, A. L., 1978, ''Laminar Flow Forced Convection in Ducts (Supp. 1),'' in *Advances in Heat Transfer*, T. F. Irvine and J. P. Hartnett, eds., Academic, New York, pp. 96–98.
[16] Moffat, R. J., 1988, ''Describing the Uncertainties in Experimental Results,'' Exp. Therm. Fluid Sci., **1**, pp. 3–17.
[17] Issa, J. S., and Ortega, A., 2002, ''Experimental Measurements of the Flow and Heat Transfer of a Square Jet Impinging on an Array of Square Pin Fins,'' Paper 34244, Proceedings., IMECE2002, ASME International Engineering Congress & Exposition, New Orleans.

Microelectromechanical System-Based Evaporative Thermal Management of High Heat Flux Electronics

Cristina H. Amon
e-mail: camon@cmu.edu

S.-C. Yao

C.-F. Wu

C.-C. Hsieh

Mechanical Engineering Department,
Institute for Complex Engineered Systems,
Carnegie Mellon University,
5000 Forbes Avenue,
Pittsburgh, PA 15213

This paper describes the development of embedded droplet impingement for integrated cooling of electronics (EDIFICE), which seeks to develop an integrated droplet impingement cooling device for removing chip heat fluxes over 100 W/cm^2, employing latent heat of vaporization of dielectric fluids. Micromanufacturing and microelectromechanical systems are used as enabling technologies for developing innovative cooling schemes. Microspray nozzles are fabricated to produce 50–100 μm droplets coupled with surface texturing on the backside of the chip to promote droplet spreading and effective evaporation. This paper examines jet impingement cooling of EDIFICE with a dielectric coolant and the influence of fluid properties, microspray characteristics, and surface evaporation. The development of micronozzles and microstructured surface texturing is discussed. Results of a prototype testing of swiss-roll swirl nozzles with dielectric fluid HFE-7200 on a notebook PC are presented. This paper also outlines the challenges to practical implementation and future research needs. [DOI: 10.1115/1.1839586]

Introduction

In recent years, there have been significant increases in chip-level heat fluxes, along with increasing demands for miniaturization. Thus, thermal management is becoming a critical bottleneck to system performance. The increase in processor speeds has been made possible by greater chip level integration of electronic components and by trends such as single chip segmented processors with integrated cache memory.

Due to these enhancements, chip level heat fluxes have also gone up considerably; they are already reaching 50 W/cm^2 for many high-end commercial applications and are expected to exceed 100 W/cm^2 before the decade ends. Conventional air cooled designs are no longer adequate to remove these heat fluxes and, for a number of applications, direct air cooling will have to be replaced or supplemented by other high-performance cooling techniques. On the other hand, although the state-of-the-art cooling techniques currently available are able to meet the cooling requirement of the order of 100 W/cm^2, a simple, compact, scalable and reliable thermal management scheme is strongly desired for most electronic devices, especially for portable applications.

In the following sections, a review of high-heat-flux electronics thermal management is provided. In addition, since many of today's miniature electronics cooling devices utilize microelectromechanical systems (MEMS) technology, the background of relevant MEMS and microfabrication techniques is also briefly reviewed.

Heat Removal of High-Heat Fluxes: Literature Review

Liquid-vapor phase change, direct and indirect liquid cooling, impinging jets, droplets and sprays are attractive cooling options for removing high-heat fluxes because of their associated heat transfer coefficients. Two-phase heat transfer, involving the evaporation of liquid in a hot region and condensation of vapor in a cold region, can provide the removal of much higher heat fluxes than can be achieved through conventional forced air cooling, which is why considerable research has been redirected towards these approaches for thermal management of electronics.

In direct liquid cooling, the electronics are either immersed in a pool or in contact with droplets, jets or sprays of a dielectric liquid. Even though liquid cooling can be employed with or without boiling, boiling can greatly reduce electronic chip temperatures compared with single-phase liquid cooling. This approach of liquid cooling with boiling has been extensively studied in the past, starting with the pioneering work of Bergles and his group [1–9] and continuing with Incropera [10], Bar-Cohen [11] and other researchers. The main issues investigated are the critical heat flux (CHF) levels that can be attained, temperature overshoot and incipient excursion, bubble growth and departure, and the effect of surface enhancement. Critical heat flux (CHF) is the peak heat flux in the boiling curve of the coolant. Any further increase in the heat flux would cause a drastic increase in electronics temperatures; thus CHF is the upper thermal design limit for any phase-change cooling system.

Heat pipes [12] and thermosyphons [12,13] are examples of indirect liquid cooling with two-phase heat transfer which can transport large heat rates with small temperature differences and exploit the benefits of two-phase heat transfer. Palm and Tengblad [14] have presented a review of recent literature. Another example of indirect liquid cooling is microchannel cooling. The microstructures give rise to a considerable increase in coolant-solid contact area. At single-phase cooling, a heat flux of 790 W/cm^2 was achieved with a large temperature rise of 71°C of the silicon heat sink and a significant pressure drop of 220 kPa at a water flow rate of about 500 cm^3/min [15]. Two-phase microchannel cooling greatly reduces the coolant flow rate and streamwise temperature increase, making it more favorable to high-heat-flux electronics cooling [16]. A great deal of research on single- and two-phase microchannel cooling for high-heat-flux electronics can be found in the open literature [17–20].

Single-phase jet impingement cooling has been investigated experimentally and numerically. Stevens and Webb [21] have reported experimental results with single-phase, single-jet impingement cooling of a simulated chip with water as the cooling fluid. The important results of their investigation demonstrate that the heat transfer coefficient is highest in the stagnation zone of the

Manuscript received May 14, 2004; revised manuscript received August 13, 2004. Review conducted by: V. Dhir.

impinging jet, and that the velocity of the jet is most influential in determining the heat transfer coefficient. A series of papers by Womac et al. [22–24] have examined jet impingement cooling of a simulated chip with single and multiple jets using FC-77 and water as single-phase coolants.

Maddox and Bar-Cohen [25] conducted a study on the design of a submerged jet impingement cooling system. They concluded that the Martin correlation [26] for submerged jet impingement is the most appropriate for electronics cooling design calculations. Other important results indicate that Nu increases with increasing Re and Pr. Also, with an increase in the number of jets per chip, the pumping power reduces and the heat transfer improves. There are other papers also in the literature [27,28] dealing with single-phase jet impingement cooling yielding results similar to those discussed above. Analytical and numerical work has been performed with single-phase jets for electronics cooling. Lienhard et al. [29,30] considered a single free surface jet impinging on a constant heat flux surface. The energy equation is solved by integral analysis, and various zones in the wall jet region are identified based on the growth of the thermal and hydrodynamic boundary layers and point of transition to turbulence. Nusselt number correlation as a function of the radial coordinate is presented. Liu et al. [31] examined the influence of the Weber number on the stagnation point heat transfer. When the Weber number is very small, the stagnation point velocity gradient increases, resulting in enhanced heat transfer.

Nonn et al. [32] have reported investigations on jet impingement flow boiling with FC-72 and FC-87. They concluded that higher jet velocities give rise to higher CHF. Studies by Nakayama and Copeland [33] and Copeland [34] indicate that when the flow rate is kept constant and the number of nozzles is increased, the CHF increases. CHF values as high as 200 W/cm^2 were attained with FC-72 multiple jet impingement boiling on a chip. Ma et al. [35] present an extensive literature survey of jet impingement cooling both with and without boiling. Their studies, as well as other studies in the literature, indicate that cooling uniformity improves by using an array of jets. They point out that research is required in order to understand the interaction of jets in multiple jet impingement systems.

Numerical work, which incorporates two-phase effects in jet impingement, has been reported in the literature. With relevance to electronics cooling, Wang et al. [36] performed a computational study of two-phase jet impingement cooling of a simulated chip by solving the averaged transport equations for the two phases. Some of their important conclusions are that the boiling of an impinging jet produces the best cooling and that an optimized flow rate exists for the impinging jet.

Enhanced surfaces have proven successful in inducing higher heat transfer rates and lower temperature overshoots in pool and jet impingement boiling. Enhanced surfaces have been investigated at length by Bergles et al. [8,37,38] and several other researchers, and surveys have been published in the literature [39,40]. In the context of electronics cooling, Nakayama et al. [41,42] investigated the effect of nucleation sites and designed enhanced surfaces that achieved critical heat fluxes above 100 W/cm^2 with fluorinert dielectric liquids. Pool-boiling research with FC-72, using specially designed surface cavities on silicon substrates, achieved heat flux removal rates of about 10 W/cm^2 with a superheat of 10°C [43] and up to 55 W/cm^2 with a superheat of 42°C [44].

Work has also been reported on the surface enhancement of chips to improve heat transfer on jet impingement cooling. Sullivan et al. [45] used smooth and roughened spreader plates to increase heat transfer from the chip surface, on which a single jet impinged without any phase change. Smooth spreader plates reduced thermal resistance by 50% and roughened spreader plates reduced thermal resistance by 80%. Saw-cut and dimpled surfaces were used as roughened spreader plates. The authors emphasize the need to select roughness dimensions carefully in order to gain any advantage over smooth surfaces. Teuscher et al. [46] have reported similar work with surface enhancement. The effect of smooth surfaces and microstructured surfaces on the boiling of FC-72 jets was investigated by Wadsworth and Mudawar [47]. Surfaces with microgrooves and surfaces with microstuds were used. Their results indicate that enhanced surfaces augment heat transfer coefficients as well as CHF. The surface with microgrooves gave the best performance, yielding CHF values in excess of 160 W/cm^2 with a jet velocity of 2 m/s.

Boiling spray cooling of chips has been investigated experimentally by Yao et al. [48], using FC-72 as the coolant. They found that heat transfer from the chip surface is more uniform with sprays than with impinging jets. They also studied the influence of liquid subcooling and mass flux. Their experiments show that there is no boiling incipience temperature overshoot associated with spray cooling. This can be attributed to the fact that the deposited liquid film is so thin that the bubble nucleation from the surface is significantly suppressed, allowing the spray-entrained gas embryos to serve as preferred nucleate sites such that surface nucleation is impeded.

Chow and co-workers [49,50] used the air-atomizing spray system to study the effect of surface characteristics on evaporative water spray cooling. Their high spray-mass-flux results show that, for an ultrathin liquid film of the order of 0.1 μm, heat is evaporated from the free surface through direct conduction, yielding very high heat fluxes of the order of 1200 W/cm^2 at very low superheats. They concluded that the smoother the surface is, the thinner the deposited liquid film is. Estes and Mudawar [51] compared the performance of free jet and spray on two-phase electronics cooling. It was found that spray cooling produced much greater CHF at low subcooling because the spray droplets were more effective at securing liquid film contact with the surface.

Amon et al. [52] determined the optimal configuration of microstructured silicon surfaces etched with deep reactive ion etching (DRIE) into islands and studs. They found that the studs enabled the spreading of liquid by surface tension, whereas the islands created thin films for effective evaporation. Kim et al. [53] suggested that the microporous coated surface significantly increased the heat transfer coefficient of evaporative spray cooling due to the capillary pumping action. The microporous structure can also delay the occurrence of surface dryout.

In summary, compared to other cooling schemes for the thermal management of high-heat-flux electronics, such as direct liquid immersion, microchannel cooling and jet impingement, spray cooling appears more attractive. The nature of dispersed droplet impingement in a spray cooling system gives rise to a more uniform spatial surface temperature distribution over the entire spray impact area [54]. Boiling incipient superheat, which may cause severe thermal shock to electronic components and make heat transfer performance highly unpredictable, is much less pronounced in spray cooling systems than in pool or flow boiling systems [48]. Spray cooling can also provide significantly higher CHF than jet impingement cooling for given flow rates [51]. In addition, while CHF values in spray cooling are mainly controlled by the liquid supply [55], they are insensitive to heat flux fluctuations, making spray cooling a safer approach than jet cooling [51].

MEMS Fabrication

Micromanufacturing fabrication and the development of related processes are leveraged by the large investment in very large scale Integrated circuit manufacturing. Advantages of this approach include much lower manufacturing costs and greater integration and miniaturization. In addition, it enables the integration of sensors and actuators with better performance than those of conventional manufacturing approaches. The research performed at the Carnegie Mellon MEMS laboratory on fabrication and design of integrated MEMS is driven by the long-term objective of low-cost customized integrated microsystems for manufacturing, sensing and actuation applications.

Different integrated-MEMS process technologies have been proposed and demonstrated. The proper choice for a particular application is based on cost, manufacturability and design flexibility. Over the past six years, a unique process has been developed at Carnegie Mellon that integrates MEMS with conventional complementary metal-oxide-semiconductor (CMOS) electronics, which addresses the need for diverse, robust and low-volume integrated MEMS production [56]. CMOS is the most common integrated circuit technology used for the manufacturing of almost all of the digital electronics in computers and consumer appliances. The availability of foundry CMOS ensures both access and affordability, since the electronics market place dictates reliable and low-cost production resulting in high-yield manufacturing.

Within the embedded droplet impingement for integrated cooling of electronics (EDIFICE) project described next, we are investigating DRIE silicon structures for microfluidic systems, where microvalves and micronozzles are manufactured on a common silicon wafer. DRIE allows anisotropic etches and can create deep cavities with nearly vertical walls. DRIE is preferable to conventional machining methods, such as electric discharge machining and laser cutting, because it allows for greater precision and geometric complexity. The fabricated microfluidic systems can be combined with single-crystal-silicon (SCS) microstructures, building upon the CMOS CMU-MEMS process. The sequence employs a post-CMOS deep silicon backside etching, which enables fabrication of high aspect ratio and flat MEMS devices with integrated circuitry. This new CMOS-DRIE MEMS process incorporates the benefits of CMOS composite structures with the superior mechanical properties of SCS.

Overall Design of EDIFICE: Embedded Droplet Impingement for Integrated Cooling of Electronics

The objective of this paper is to describe ongoing work at Carnegie Mellon University to develop a droplet impingement-cooling device called EDIFICE for removing heat fluxes over 50 W/cm^2 for both portable and desktop electronics [57–59]. The goal is to integrate the chip cooling solutions with the chip level packaging using MEMS technology, which offers the possibility of miniaturization and inexpensive batch fabrication. The EDIFICE project utilizes the latent heat produced by the vaporization of dielectric coolants to obtain high chip heat transfer rates. Cooling is achieved through the impingement of micron-sized droplets (50–100 μm) generated through multiple nozzles manufactured with DRIE. EDIFICE employs MEMS-enabled technologies for manufacturing: (i) micronozzles, swirl nozzles and microinjectors for jet breakup [60], (ii) microstructured silicon surfaces for the enhancement of thin film evaporation [57], and (iii) electrostatic microvalves for on-demand control of dielectric coolant flow rates [61].

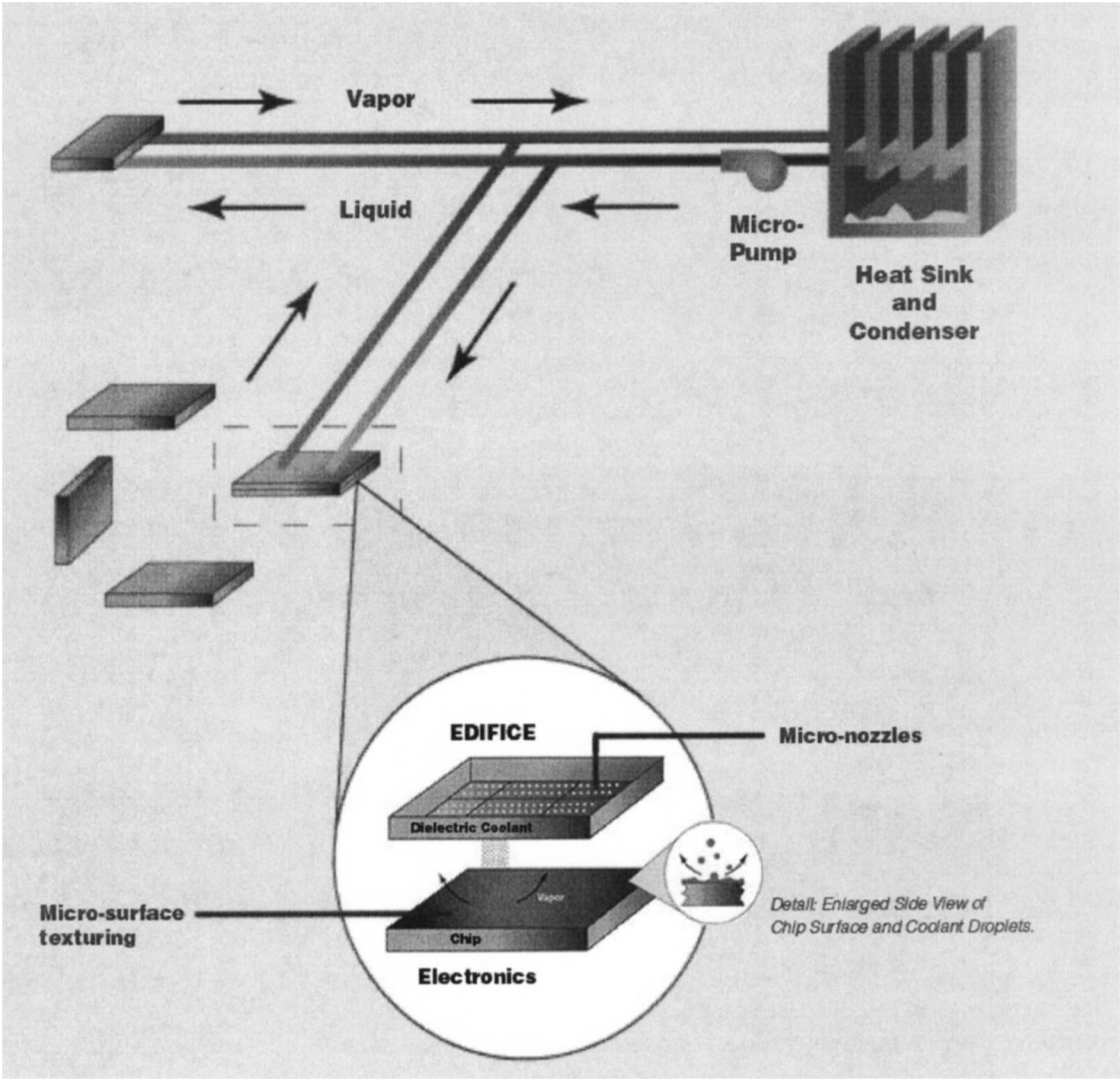

Fig. 1 Schematic of EDIFICE and overall system

A schematic of the EDIFICE design is shown in Fig. 1, along with the overall system. The droplet impingement mechanism, shown in Fig. 1, avoids temperature overshoot at boiling incipience and almost eliminates fluctuations in chip temperature and thermal cycling. The system level arrangement transports the removed heat to the periphery of the system, where it is either dissipated by a condenser or stored in a detachable heat storage unit [62]. In this way, the volume near the chip is made available for electronics. In the case of the detachable energy storage unit, it contains an organic phase change material (e.g., eicosene) with a melting temperature of about 50°C, along with thermal conductivity enhancers such as aluminum foams [63] or fins [64]. We first developed and implemented this energy storage device for embedded wearable computer applications [65]. In the case of the condenser arrangement, the vapor generated at the component level is transported through the system to the combined condenser, thereby minimizing thermal resistance offered by multi-material interfaces.

The work presented next describes the development of different components of the EDIFICE project. It reports the experimental test bed and the flow visualization to investigate the role of several parameters in jet/droplet impingement cooling. Experimental results include flow visualization of jet breakup, induced by irregular-shaped micronozzles and flow swirling, as well as microstructured silicon impingement surfaces fabricated for enhancing fluid spreading and evaporation.

The working fluid for most tests is HFE-7200, a dielectric fluid manufactured by 3M. Compared with water, the lower viscosity and surface tension of HFE are expected to result in better atomization performance. The smaller amount of latent heat of HFE compared to water requires a higher flow rate to remove the same amount of heat. While this is a disadvantage, higher HFE flow rates allow the use of turbulence to break up jets. Indeed, the corresponding flow rate for water would be so small as to cause difficulties for nozzle design. In addition, HFE is more environmentally friendly than FC-72 in terms of zero ozone depletion potential, low global warming potential and short atmospheric lifetime (0.8 years).

On the other hand, for ultrahigh-heat-flux removal applications, water could be more promising than HFE. To explore this possibility, the evaporative spray cooling on a microtextured silicon surface using water as the coolant is also addressed in this study. The characterization of microjet impingement with water has been previously reported in Wu and Yao [60,61].

Experimental Details

The test bed for the EDIFICE physical experimentation is depicted in Fig. 2. Three cartridge heaters were installed in an insulated aluminum block to provide power up to 600 W. The power level was controlled by varying the input voltage. Three sheathed J-type (Iron-Constantant) thermocouples with diameters of 0.8 mm were buried between the heater and the cooling surface to estimate the surface heat flux and the surface temperature uniformity. The cooling surface has an area of 25.4 by 25.4 mm^2. The cooling chamber is 10 mm high and has a transparent glass window for visualization. A silicon nozzle plate sealed on the top of the cooling chamber with 49 (7 by 7) microfabricated orifices on an area of 25.4 by 25.4 mm^2 was used to generate droplet streams. A pressure gauge located at the vapor exit was used to measure the system pressure in the cooling chamber. The liquid coolant was supplied with a pressurized tank or a mini pump. The characterizations of the atomization process and two-phase flow phenomena were observed with a two-dimensional laser sheet and a charge coupled device imaging system.

For experiments on micronozzle characterization, silicon nozzle strips with different orifices were sealed on a nozzle holder. The nozzle holder was connected to an air-pressurized liquid reservoir and placed on the top of the test chamber without a bottom piece. Images were taken and processed for liquid breakup length analysis.

During the tests, a specified power was constantly supplied to the heaters, and the droplet streams at a given flow rate impacted on the cooling surface simultaneously. The system eventually reached a steady state, and the related experimental parameters were recorded. The surface heat flux was evaluated by assuming one-dimensional heat conduction between the heaters and the cooling surface. The droplet flow rate was controlled by a needle valve and measured using a rotormeter.

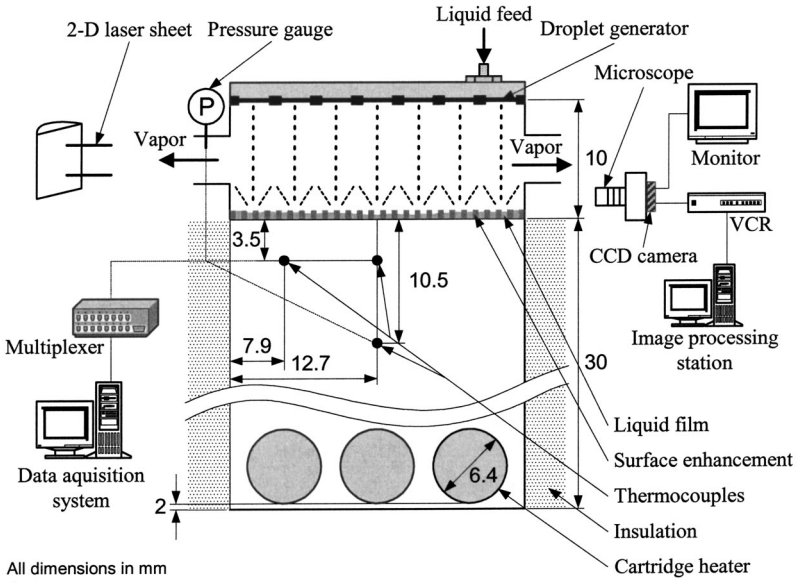

Fig. 2 Schematics of the test bed

The uncertainty of the calibrated thermocouples was less than 0.75%. The temperature discrepancy between any two thermocouples is within 0.3°C in the temperature range of current study. The uncertainty in the surface heat flux was estimated to be less than 8%. In addition, the droplet flow rate measurement has an uncertainty of less than 3%.

Development and Characterization of Micronozzles

The focus of micronozzle development is to gain an understanding of the breakup of jets emerging from irregularly shaped orifices at pressures of less than 15 psig. The micronozzle orifice geometries are designed to activate three primary destabilization mechanisms: (i) surface tension-related breakup, (ii) breakup due to generation of turbulent disturbances, or (iii) swirl-induced breakup. A detailed description can be found in Wu and Yao [60] and Yao et al. [59]

The orifice shapes investigated here are designed to excite these destabilization mechanisms and are shown in Fig. 3. The circular jet is considered the reference. The square, triangle, medal, cross and star may be considered axisymmetric distortions of a circle. The rectangle, dumbbell, V, I and H may be considered asymmetrical distortions. Sharp edges and cantilever intrusions are designed to promote disturbances.

Axisymmetric geometries are expected to show more cylindrical-jet behavior during disintegration, whereas asymmetric geometries tend to exhibit sheet-like behaviors. Swirl is also used as a breakup mechanism, as shown in Fig. 3. Here the swirl is created by combining an inlet chip [Fig. 4(*a*)] with a swirl chip [Fig. 4(*b*)] to create tangential slots through which fluid flows. Inlet chips, swirl chips and nozzle chips are aligned and fuse bonded at 500°C for 72 h. Performance comparisons between differently shaped nozzles are done either on an area-equivalent basis or on the basis of equal hydraulic diameter. All of the nozzles of a 100 μm area-equivalent diameter have the same opening area as a circle of 100 μm diameter. In this study, only two nozzle sizes are tested: the 100 μm area-equivalent diameter and the 150 μm hydraulic diameter.

The nozzle is made of silicon and is micromachined using DRIE. The silicon chips used here have a thickness of 500 μm and are processed in a single-turn helical inductively coupled plasma etching system developed by Surface Technology Systems Ltd. (STS). At 500 μm thickness, this system allows the smallest dimension machinable to be 16.6 μm. All nozzles microfabricated in this project have minimum dimensions greater than this limit.

Effect of Nozzle Shape. Figure 5 shows the nondimensional breakup length L/d (jet breakup length/area-equivalent diameter of orifice) for axisymmetric orifices for HFE. The inset in Fig. 5 shows the typical atomization curve. The Rayleigh breakup region (laminar region), the first wind-induced breakup region (transition region) and the second wind-induced breakup region (turbulent region) are identifiable in the experimental data. The laminar portions of all of the curves overlap. The laminar zone is extended and the transition to turbulence is delayed when the orifice geometry changes from circle to square, triangle, medal and cross. This is because the laminar disturbances introduced by the irregular shape of the nozzles, while compared to the surface tension of the liquid, are not strong enough to disintegrate the liquid stream. This suppression by surface tension causes the delay of Rayleigh jet breakup and delays the transition to turbulence. After shape-induced disturbances are damped, the irregularly shaped liquid jet returns to a circular cross section due to surface tension, and the process of Rayleigh jet breakup commences. The curve for the star-shaped orifice is very close to that for the circular jet. The curve for the cantilever-long nozzle deviates from the standard stability curve.

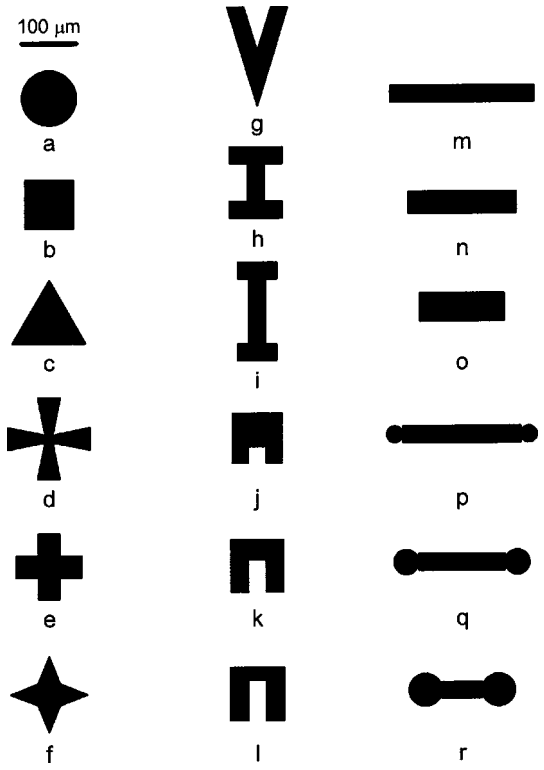

Fig. 3 Nozzle orifice shapes. (*a*) Circle, (*b*) square, (*c*) triangle, (*d*) medal, (*e*) cross, (*f*) star, (*g*) V-shaped, (*h*) H-shaped, (*i*) I-shaped, (*j*) cantilever-short, (*k*) cantilever-median, (*l*) cantilever-long, (*m*) rectangle-long, (*n*) rectangle-median, (*o*) rectangle-short, (*p*) dumbbell-long, (*q*) dumbbell-median and (*r*) dumbbell-short

Effect of Nozzle Size. Nozzles with 150 μm hydraulic diameters were fabricated for the same shapes discussed previously. A nozzle with a 150 μm hydraulic diameter gives an area-equivalent diameter that can range from 150 (circle) to 350 μm (H-shaped) due to the irregular geometry. Figure 6 shows the jet breakup behavior of various nozzles at 13.1 psig for HFE. The shape-induced disturbances are surprisingly significant for these large nozzles. Surface tension does not significantly damp the surface disturbances. The jets preserve the shape of the initial disturbance. For example, the central ''beam'' of the dumbbell nozzle, the rectangles, and each ''leg'' of the star, cross and medal all develop liquid sheets rather like fan sprays.

On the other hand, the jets from nozzles with 100 μm area-equivalent diameters are shown in Fig. 6. For these smaller jets, the odd-shaped nozzles create jets of various shapes. However, these jets do not further disperse very quickly. Instead, many of them restore back to almost circular jets afterwards due to the strong effects of surface tension. As expected, the effect of surface tension goes inversely with the jet diameter. For HFE at a 100 μm jet diameter, the surface tension suppresses the surface disturbance of the odd shapes in many cases.

Effect of Swirling. With swirl chips, jet breakup lengths are greatly reduced for all nozzle geometries, as shown in Fig. 7. For HFE, hollow cone sprays are known to develop. Swirl is more favorable for axisymmetric geometries of nozzles. Swirl-induced instabilities cause the formation of droplets with sizes much smaller than the jet diameter. Due to the radial component of the movement, jets disperse significantly and result in a wider distribution of liquids over the target.

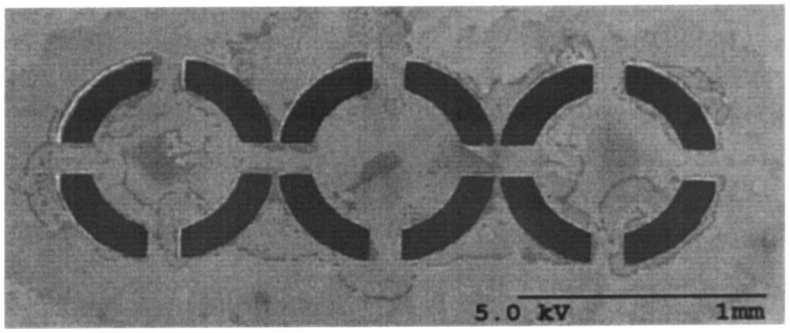

(a)

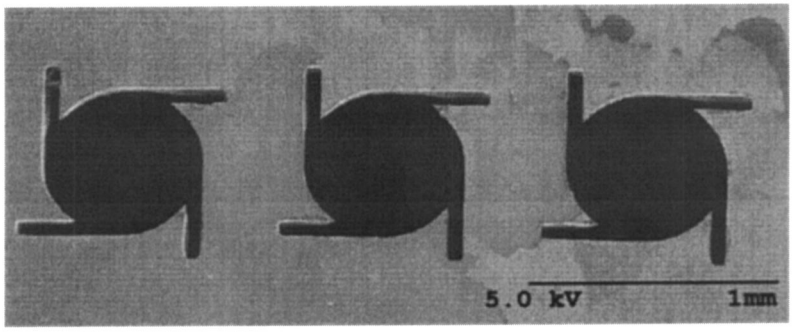

(b)

Fig. 4 (*a*) Inlet chip, and (*b*) swirl chip

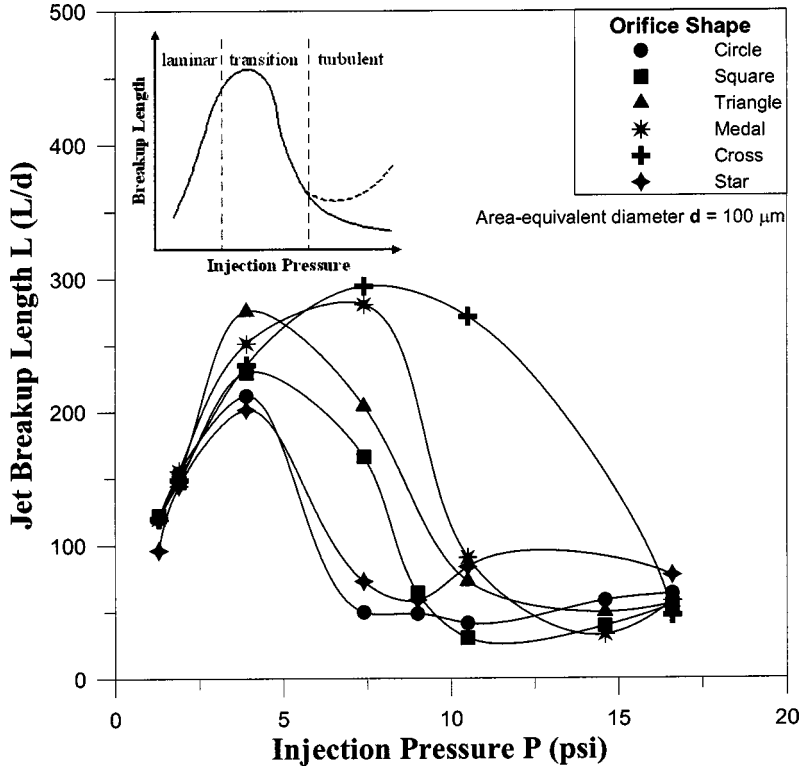

Fig. 5 HFE jet breakup length (L/d) of area-equivalent diameter of 100 μm nozzles of axisymmetric shapes. The inset shows a typical liquid jet atomization curve

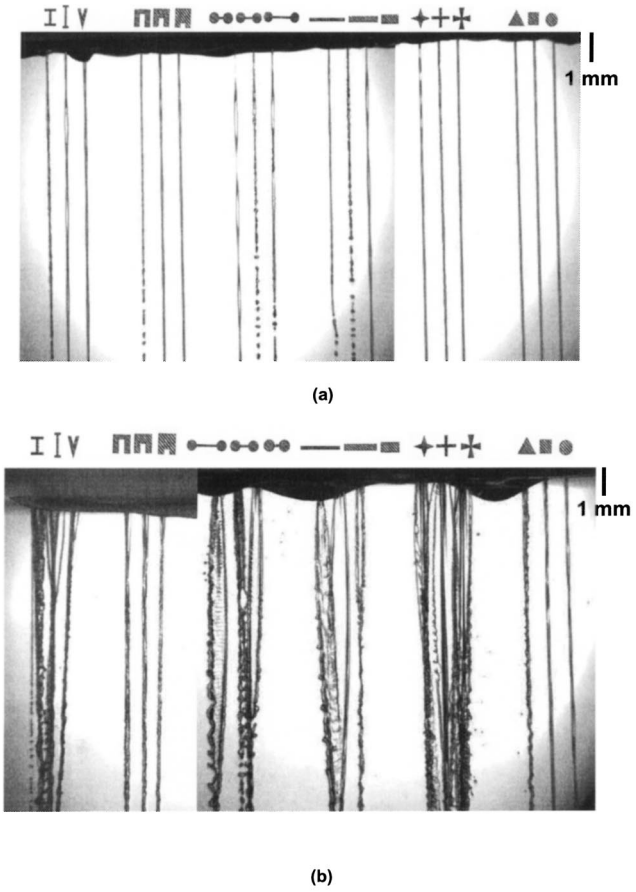

Fig. 6 Effect of nozzle shapes (*a*) same hydraulic diameter of 100 μm, 16.0 psig injection pressure, and (*b*) same hydraulic diameter of 150 μm, 13.1 psig injection pressure

Effect of Vapor Flow. All jet breakup results shown previously were tested in open space. When multiple nozzles are applied in a confined chamber for the purpose of cooling a target surface, a significant amount of vapor is generated on the heated surface due to the evaporation of the impinging liquid. A typical situation taken from the glass window of the test chamber is shown in Fig. 8, where multiple arrays of circular jets are coming from the ceiling of the chamber and a vapor layer is rising at the bottom. The droplets of the disintegrated jets encounter the opposing vapor flow and decelerate. Some of the droplets even form clusters. These droplets eventually arrive at the surface, but droplet dynamics are affected by the back flow and the fast side-sweeping flow of the escaping vapor in the vicinity of the surface. As a result, the escaping vapor flow may reduce the cooling performance.

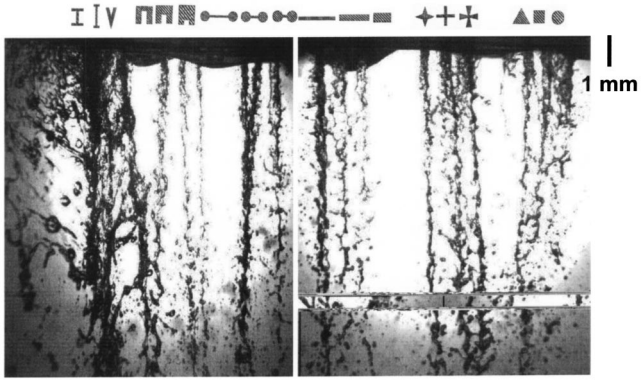

Fig. 7 Effect of swirling for same hydraulic diameter of 150 μm. Injection pressure is 15.3 psig

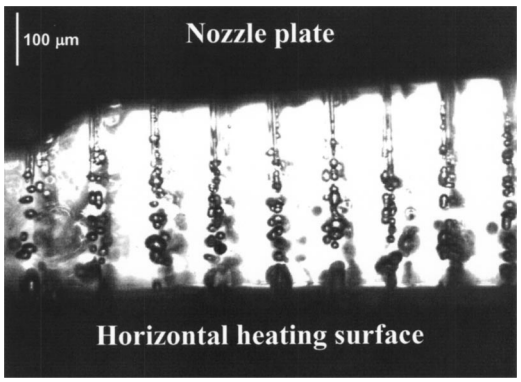

Fig. 8 Effect of vapor flow on multiple jets and droplets in the vapor chamber

Prototype Testing

A prototype of a notebook PC system has been developed, as shown in Fig. 9. The integrated droplet impingement cooling system consists of a cooling test bed, as shown in Fig. 2, a microdiaphragm liquid pump (NF1.30KT, KNF Neuberger Inc.), a coolant reservoir, and a fin-integrated condenser. The condenser, which is mounted on the back of the display panel, is made of a 13.7=mm-thick aluminum plate with an area of 316 by 254 mm^2 bonded with 58 aluminum fins. The fluidic interconnections are made of plastic tubes with 3.175 mm inner diameters.

The previous micronozzle characterization results suggest that neither the axisymmetric nor asymmetric orifices give satisfactory atomization results of a dispersed jet with a short breakup length. To provide uniform cooling within a confined chamber, a new orifice swiss-roll design is proposed, as shown in the inset of Fig. 9. The swiss-roll orifice has a diameter of 460 μm and slot width of 40 μm. A silicon nozzle plate with 7×7 swiss-roll orifices is fuse bonded with the inlet and swirl chip, as shown in Fig. 5, to provide atomized droplets in the prototype tests.

The coolant used in all prototype tests is the dielectric fluid HFE-7200. The inlet coolant subcooling is about 50°C. The pressure of the cooling chamber was maintained at about 1 atm; hence, the saturation temperature of the coolant was kept at 76°C.

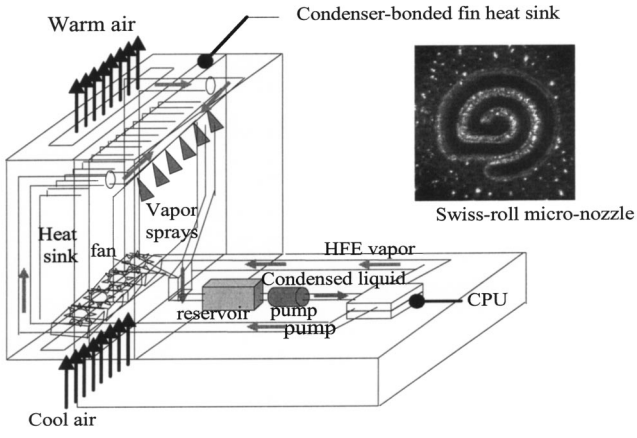

Fig. 9 Schematic of the prototype notebook PC evaporative spray cooling system. Inset shows a swirl silicon nozzle.

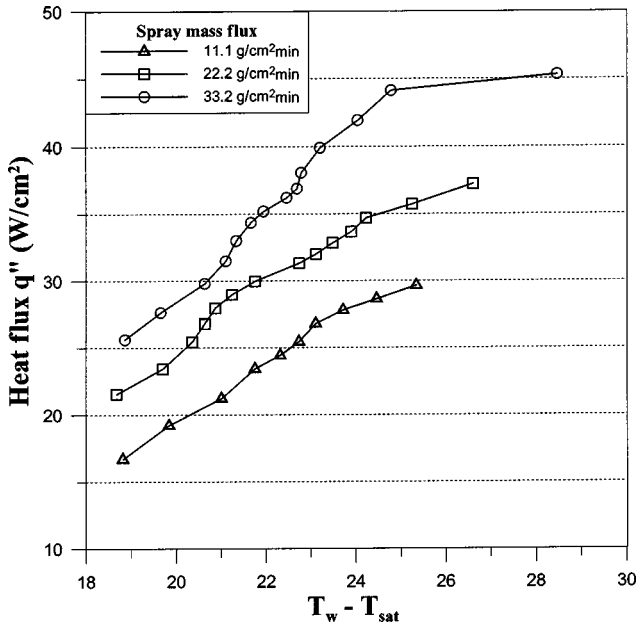

Fig. 10 Performance of the prototype notebook PC evaporative spray cooling system using silicon swiss-roll micronozzles

Typical test results are shown in Fig. 10. At 11.1 g/cm^{2}min, the silicon swiss-roll micronozzles have generated fully developed droplet streams at each micronozzle. At 33.2 g/cm^{2}min, a uniform heat flux removal of 45 W/cm^2 is achieved. The lateral heat flux is evaluated from the temperature difference between the TC2 and TC3, as shown in Fig. 2. It was found that the lateral heat fluxes are limited with ± 0.5 W/cm^2 for all tests.

The heat transfer results of the EDIFICE prototype using HFE-7200 as the coolant show satisfactory cooling capability to meet today's electronics thermal management requirements. However, due to the very low latent heat of vaporization of HFEs, this system may not be adequate for the next generation of portable electronics. Therefore, water-cooled electronic cooling could be a viable candidate due to the much higher latent heat of vaporization of water and the relatively lower coolant flow rate and pumping power. The major challenges behind incorporating water in electronic devices are its relatively high boiling temperature at atmospheric pressure and nondielectric property. However, the disadvantages can be overcome by circulating water in a hermetic enclosure at a reduced system pressure.

For this reason, the heat transfer results of evaporative spray cooling on a microtextured silicon surface using water as the coolant are presented in the following section.

Silicon Microsurface Texturing

The backside of the chip is textured using deep reactive ion etching (DRIE). This is done (i) to increase spreading in order to decrease the film thickness and (ii) to provide nucleation sites to promote boiling. Figure 11 shows three different surface textures that have been investigated. All microstructures were fabricated on a chip area of 25.2 by 25.2 mm^2. Figure 11(b) shows the standard geometric arrangement of studs, including stud width, height and spacing in μm. Arrangement (a), referred to as finer stud, is derived from arrangement (b) by decreasing the stud width to a third, thus increasing the overall heat transfer surface area by 1.5 times. Arrangement (c), referred to as wider spacing, is derived from (b) by increasing the groove width threefold, thus reducing the capillary force between the studs and giving poorer liquid spreading ability.

Figure 12 shows the heat transfer results of four different surface textures using a Delavan® WDB-2.0 full-cone spray nozzle with 60° spray angle. The nozzle pressure was maintained at 507 kPa (73.5 psi) $\pm$ 1.7 kPa (0.25 psi) in all experiments, and the nozzle-to-surface distance was fixed at 40.9 mm. The effective water spray mass flux over the heat transfer surface was measured to be 4.64 g/cm^{2}min. Two thermocouples were positioned at a distance of 6.5 mm (T_1) and 10.3 mm (T_2) from the center of the test surface to monitor the temperature uniformity. The surface temperatures (T^s) were then evaluated by extrapolation, assuming one-dimensional heat conduction. The heat flux presented here is based on base surface area, i.e., 25.2 by 25.2 mm^2.

Four distinct regions with different heat transfer mechanisms can be characterized in Fig. 9. In region I, the flooded regime, the main heat transfer contribution is due to forced convection induced by direct droplet impingement. Secondary effects are due to evaporation through the liquid film. Because the entire microstructured surface is covered by a thick liquid film, the heat transfer for all surfaces is about the same.

In the second region, the thin film regime, evaporation through the thin liquid film within the grooves becomes significant. No boiling is observed within the thin liquid film. When the surface temperature increases, the thin liquid film finally breaks up be-

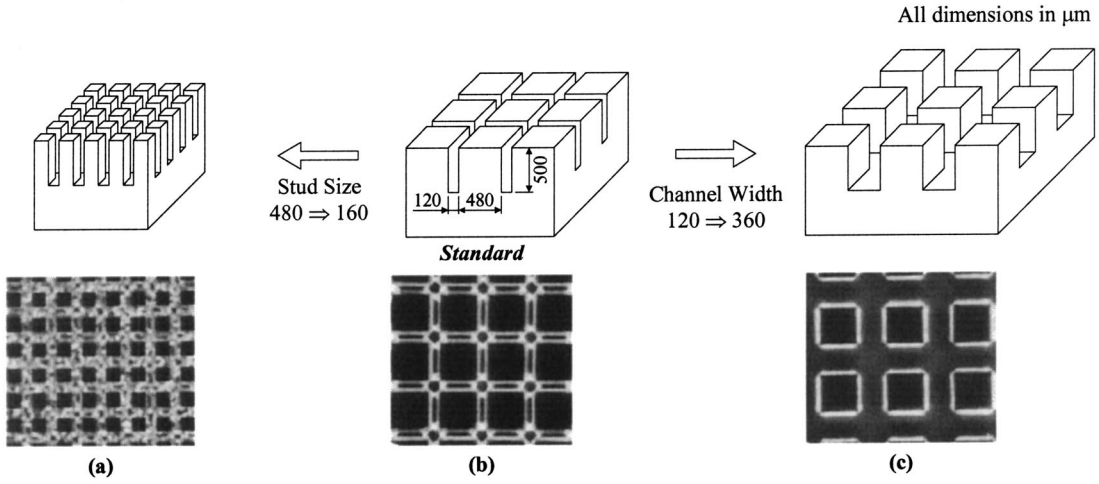

Fig. 11 Surface texture schematics and images of silicon microstructured surfaces

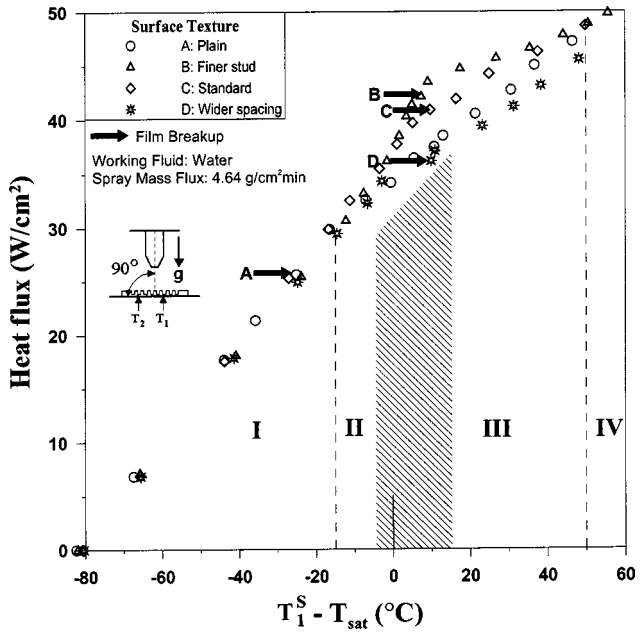

Fig. 12 Heat transfer results of different surface textures with up-facing surface

yond a certain temperature, and dry patches appear. This is the third region, the partial dryout regime, which is similar to the transition-boiling regime in pool boiling. The surface temperature fluctuation in this regime is the highest. The film breakup point is defined as a situation in which at least one spot on the base silicon surface is in direct contact with the impinging droplets.

As the surface temperature increases further, the entire surface eventually dries. This is region IV, the dryout regime. The heat transfer rate is hence determined by the amount of liquid droplets arriving to the surface. As shown in Fig. 9, the heat transfer curves for all surfaces converge in this region.

All microstructured surfaces are able to maintain the liquid film at a higher heat flux. Of all the textures, the surface with finer studs gives the highest liquid film breakup heat flux and the most uniform surface temperature distribution. Nevertheless, although the finer-stud texture has 50% more surface area than the standard texture, the increase in heat transfer rate is not as much as expected. Therefore, it is the capillary force of the grooves that helps liquid film stay on the surface, but the heat enhancement is only related to the exposed wet surface.

As shown in Fig. 12, the liquid film breakup heat flux for the finer-stud surface is 42.1 W/cm^2, which is comparable to the limiting heat flux in the previous prototype testing of HFE. However, the flow rate in water tests is only 4.64 g/cm^{2}min. In other words, similar heat transfer performance can be achieved with a much lower rate of coolant consumption in a water-cooled system. The maximum heat fluxes presented in Fig. 12 are still well below the CHF. However, even though the system was operated in the vicinity of the burnout point, no boiling incipient temperature overshoot was observed during the entire test period.

Concluding Remarks

Microprocessor power density has been steadily increasing over the past decade due to increases in microprocessor power dissipation and reduction in feature size of the processing core, where most of the power on a die is generated. This trend is expected to continue into the future, leading to the next generation of electronics with a power dense core covering a fraction of the total die surface area, bounded by regions of reduced power density cache, and with localized power densities exceeding 100 W/cm^2. Conventional cooling technologies in the electronics industry have limitations on removing these nonuniform, high-heat fluxes from the surface of microprocessors. This paper has presented an overview of state-of-the-art heat removal technologies that can meet the challenging cooling requirements of next generation electronics, including direct liquid cooling, liquid-vapor phase change techniques, nonrefrigeration phase change techniques, pool boiling, jet impingement cooling and evaporative spray cooling.

This paper has described the development of an integrated evaporative spray cooling device microfabricated in silicon for package-level cooling of high-heat-flux electronics. It combines efficient phase-change heat transfer and utilizes the latent heat of vaporization of dielectric coolants to provide effective cooling. Basic experiments to develop and characterize micronozzles are reported, as well as experiments with chip surface texturing to improve spreading and evaporative/boiling behavior. Testing of a notebook PC prototype using swirling-type nozzles gives a uniform heat flux removal of 45 W/cm^2 at a mass flux of only 33.2 g/cm^{2}min of HFE-7200 dielectric coolant.

Acknowledgments

The authors gratefully acknowledge the support of the DARPA HERETIC Program, Grant No. N00014-99-0481, as well as the Pennsylvania Infrastructure Technology Alliance (PITA). This paper is dedicated to R. C. Chu for his leadership and inspiration to all of us in the electronics cooling community and for his sustained contributions to the thermal management of electronics.

References

[1] Park, K. A., and Bergles, A. E., 1986, "Boiling Heat Transfer Characteristics of Simulated Microelectronic Chips with Detachable Heat Sinks," *Proc. 8th International Heat Transfer Conference*, Hemisphere Publishing Co., Washington, DC, **4**, pp. 2099–2104.

[2] Park, K. A., and Bergles, A. E., 1988, "Effects of Size of Simulated Microelectronic Chips on Boiling and Critical Heat Flux," J. Heat Transfer, **10**, pp. 728–734.

[3] Bergles, A. E., and Kim, C. J., 1988, "A Method to Reduce Temperature Overshoots in Immersion Cooling of Electronic Devices," *Proc. InterSociety Conference on Thermal Phenomena in the Fabrication and Operation of Electronic Components*, IEEE, New York, NY, pp. 100–105.

[4] Carvalho, R. D. M., and Bergles, A. E., 1990, "The Influence of Subcooling on the Pool Nucleate Boiling and Critical Heat Flux of Simulated Electronic Chips," *Proc. 9th International Heat Transfer Conference*, Hemisphere Publishing Co., New York, NY, pp. 289–294.

[5] Park, K. A., Bergles, A. E., and Danielson, R. D., 1990, "Boiling Heat Transfer Characteristics of Simulated Microelectronic Chips with Fluorinert Liquids," *Heat Transfer in Electronic and Microelectronic Equipment*, Bergles, A. E. ed., Hemisphere Publishing Co., New York, NY, pp. 573–588.

[6] Bergles, A. E., and Bar-Cohen, A., 1990, "Direct Liquid Cooling of Microelectronic Components," *Advances in Thermal Modeling of Electronic Components and Systems*, Kraus, A. D. ed., ASME Press, NY, pp. 233–250.

[7] Ma, C. F., and Bergles, A. E., 1983, "Boiling Jet Impingement Cooling of Simulated Microelectronic Chips Heat Transfer in Electronic Equipment," *Proc. Heat Transfer in Electronic Equipment*, ASME, **HTD-28**, pp. 5–12.

[8] Golobic, I., and Bergles, A. E., 1992, "Effects of Thermal Properties and Thickness of Horizontal Vertically Oriented Ribbon Heaters on the Pool Boiling Critical Heat Flux," *Proc. Engineering Foundation Conference on Pool and External Flow Boiling*, ASME, pp. 213–218.

[9] Zitz, J. A., and Bergles, A. E., 1993, "Immersion Cooling of a Multichip Module by Pool Boiling of FC-86," *Proc. ASME International Electronics Packaging Conference*, ASME, pp. 917–926.

[10] Incropera, F. P., 1990, "Liquid Immersion Cooling of Electronic Components," *Heat Transfer in Electronic and Microelectronic Equipment*, Bergles, A. E. ed., Hemisphere Publishing Co., New York, NY, pp. 407–444.

[11] Bar-Cohen, A., 1993, "Thermal Management of Electronic Components with Dielectric Liquids," Int. J. JSME, **36**(1), pp. 1–25.

[12] Peterson, G. P., 1994, *An Introduction to Heat Pipes*, Wiley, New York, NY.

[13] Haider, S. I., Joshi, Y. K., and Nakayama, W., 2002, "A Natural Circulation Model of the Closed Loop, Two-Phase Thermosyphon for Electronics Cooling," J. Heat Transfer, **124**(5), pp. 881–890.

[14] Palm, B., and Tengblad, N., 1996, "Cooling of Electronics by Heat Pipes and Thermosyphons-A Review of Methods and Possibilities," *Proc. 31st National Heat Transfer Conference*, ASME, **HTD-329**, pp. 97–108.

[15] Tuckerman, D. B., and Pease, R. F. W., 1981, "High-Performance Heat Sinking for VLSI," IEEE Electron Device Lett., **EDL-2**(5), pp. 126–129.

[16] Bower, M. B., and Mudawar, I., 1994, "High Flux Boiling in Low Flow Rate, Low Pressure Drop Mini-Channel and Micro-Channel Heat Sinks," Int. J. Heat Mass Transfer, **37**(2), pp. 321–332.

[17] Knight, R. W., Hall, D. J., Goodling, J. S., and Jaeger, R. C., 1992, ''Heat Sink Optimization with Application to Microchannels,'' IEEE Trans. Compon., Hybrids, Manuf. Technol., **15**, pp. 832–842.
[18] Qu, W., and Mudawar, I., 2002, ''Experimental and Numerical Study of Pressure Drop and Heat Transfer in Single-Phase Micro-channel Heat Sink,'' Int. J. Heat Mass Transfer, **45**(12), pp. 2549–2565.
[19] Bergles, A. E., Lienhard, V. J. H., Kendall, G. E., and Griffith, P., 2003, ''Boiling and Evaporation in Small Diameter Channels,'' Heat Transfer Eng., **24**(1), pp. 18–40.
[20] Peng, X. F., and Wang, B. X., 1993, ''Forced-Flow Convection and Flow Boiling Heat Transfer for Liquid Flowing Through Microchannels,'' Int. J. Heat Mass Transfer, **36**(14), pp. 3421–3427.
[21] Stevens, J., and Webb, B. W., 1989, ''Local Heat Transfer Coefficients Under an Axisymmetric, Single-phase Liquid Jet,'' J. Heat Transfer, **113**(1), pp. 71–78.
[22] Womac, D. J., Aharoni, G., Ramadhyani, S., and Incropera, F. P., 1990, ''Single-phase Liquid Jet Impingement Cooling of Small Heat Sources, Heat Transfer,'' *Proc. International Heat Transfer Conference*, pp. 149–154.
[23] Womac, D. J., Ramadhyani, S., and Incropera, F. P., 1993, ''Correlating Equations for Impingement Cooling of Small Heat Sources with Single Circular Liquid Jets,'' J. Heat Transfer, **115**(1), pp. 106–115.
[24] Womac, D. J., Incropera, F. P., and Ramadhyani, S., 1994, ''Correlating Equations for Impingement Cooling of Small Heat Sources with Multiple Circular Liquid Jets,'' J. Heat Transfer, **116**(2), pp. 482–486.
[25] Maddox, D. E., and Bar-Cohen, A., 1994, ''Thermofluid Design of Single-phase Submerged Jet Impingement Cooling for Electronic Components,'' J. Electron. Packag., **116**(3), pp. 237–240.
[26] Martin, H., 1977, ''Heat and Mass Transfer Between Impinging Gas Jets and Solid Surfaces,'' Adv. Heat Transfer, pp. 1–60.
[27] Wadsworth, D. C., and Mudawar, I., 1990, ''Cooling of a Multichip Electronic Module by Means of Confined Two-dimensional Jets of Dielectric Liquid,'' J. Heat Transfer, **112**(4), pp. 891–898.
[28] Zumbrunnen, D. A., and Aziz, M., 1993, ''Convective Heat Transfer Enhancement Due to Intermittency in an Impinging Jet,'' J. Heat Transfer, **115**(1), pp. 91–98.
[29] Liu, X., and Lienhard, J. H., 1989, ''Liquid Jet Impingement Heat Transfer on a Uniform Flux Surface, Heat Transfer Phenomena in Radiation,'' *Proc. Heat Transfer Phenomena in Radiation, Combustion, and Fires*, ASME, **HTD-106**, pp. 523–530.
[30] Liu, X., Lienhard, J. H., and Lombara, J. S., 1991, ''Convective Heat Transfer by Impingement of Circular Liquid Jets,'' J. Heat Transfer, **113**(3), pp. 571–581.
[31] Liu, X., Gabour, L. A., and Lienhard, J. H., 1993, ''Stagnation Point Heat Transfer During Liquid Jet Impingement: Analysis with Surface Tension,'' J. Heat Transfer, **115**(1), pp. 99–105.
[32] Nonn, T., Dagan, Z., and Jiji, L. M., 1989, ''Jet Impingement Flow Boiling of a Mixture of FC-72 and FC-87 Liquids on a Simulated Electronic Chip,'' *Proc. Heat Transfer in Electronics of National Heat Transfer Conference*, ASME, **HTD-111**, pp. 121–128.
[33] Nakayama, W., and Copeland, D., 1994, ''Heat Transfer from Chips to Dielectric Coolant: Enhanced Pool Boiling Versus Jet Impingement Cooling,'' J. Enhanced Heat Transfer, **1**(3), pp. 231–243.
[34] Copeland, D., 1998, ''Single-phase and Boiling Cooling of a Small Heat Source by Multiple Nozzle Jet Impingement,'' Int. J. Heat Mass Transfer, **39**(7), pp. 1395–1406.
[35] Ma, C. F., Gan, Y. P., Tian, Y. C., Lei, D. H., and Gomi, T., 1993, ''Liquid Jet Impingement Heat Transfer With or Without Boiling,'' J. Therm. Sci., **2**(1), pp. 32–49.
[36] Wang, D., Yu, E., and Przekwas, A., 1999, ''A Computational Study of Two-phase Jet Impingement Cooling of an Electronic Chip,'' *Proc. 15th Annual IEEE Semiconductor Thermal Measurement and Management Symposium*, IEEE, New York, pp. 10–15.
[37] Ravigururajan, T. S., and Bergles, A. E., 1994, ''Visualization of Flow Phenomena Near Enhanced Surfaces,'' J. Heat Transfer, **116**(1), pp. 54–57.
[38] Reid, R. S., Pate, M. B., and Bergles, A. E., 1991, ''A Comparison of Augmentation Techniques During In-tube Evaporation of R-113,'' J. Heat Transfer, **113**(2), pp. 451–458.
[39] Thome, J. R., 1990, *Enhanced Boiling Heat Transfer*, Hemisphere Publishing Co., New York, NY.
[40] Web, R. L., 1994, *Principles of Enhanced Heat Transfer*, Wiley, New York, NY.
[41] Nakayama, W., Daikoku, T., Kuwahara, H., and Nakajima, T., 1980, ''Dynamic Model of Enhancement Boiling Heat Transfer on Porous Surfaces, Part I: Experimental Investigation,'' J. Heat Transfer, **102**(3), pp. 445–450.
[42] Nakayama, W., Nakajima, T., and Hirasawa, S., 1984, ''Heat Sink Studs Having Enhanced Boiling Surfaces for Cooling Microelectronic Components,'' ASME, **84-WA/HT-89**.
[43] Miller, W. J., 1991, ''Boiling and Visualization from Microconfigured Surfaces,'' M.S. thesis, Univ. of Pennsylvania, Philadelphia, PA.
[44] Bhavnani, S. H., Tsai, C. P., Jaeger, R. C., and Eison, D. L., 1993, ''An Integral Heat Sink for Cooling Microelectronic Components,'' J. Electron. Packag., **115**(3), pp. 284–291.
[45] Sullivan, J., Ramadhyani, S., and Incropera, F. P., 1992, ''Use of Smooth and Roughened Spreader Plates to Enhance Impingement Cooling of Small Heat Sources with Single Circular Jets,'' *Proc. 28th National Heat Transfer Conference and Exhibition*, ASME, **HTD-206**(2), pp. 103–110.
[46] Teuscher, K. L., Ramadhyani, S., and Incropera, F. P., 1993, ''Jet Impingement Cooling of an Array of Discrete Heat Sources with Extended Surfaces,'' *Proc. Enhanced Cooling Techniques for Electronics Applications*, ASME, **HTD-263**, pp. 1–10.
[47] Wadsworth, D. C., and Mudawar, I., 1992, ''Enhancement of Single-phase Heat Transfer and Critical Heat Flux from an Ultra-high-flux Simulated Microelectronic Heat Source to a Rectangular Impinging Jet of Dielectric Liquid,'' J. Heat Transfer, **114**(3), pp. 764–768.
[48] Yao, S. C., Deb, S., and Hammouda, N., 1989, ''Impact Spray Boiling for Thermal Control of Electronic Systems,'' *Proc. Heat Transfer in Electronics of National Heat Transfer Conference*, ASME, **HTD-111**, pp. 129–133.
[49] Pais, M. R., Chow, L. C., and Mahefkey, E. T., 1992, ''Surface Roughness and its Effects on the Heat Transfer Mechanism in Spray Cooling,'' J. Heat Transfer, **114**(1), pp. 211–219.
[50] Sehmbey, M. S., Pais, M. R., and Chow, L. C., 1992, ''Effect of Surface Material Properties and Surface Characteristics in Evaporative Spray Cooling,'' J. Thermophys. Heat Transfer, **6**(3), pp. 505–512.
[51] Estes, K. A., and Mudawar, I., 1995, ''Comparison of Two-Phase Electronic Cooling Using Free Jets and Sprays,'' J. Electron. Packag., **117**, pp. 323–332.
[52] Amon, C. H., Murthy, J. Y., Yao, S. C., Narumanchi, S., Wu, C. F., and Hsieh, C. C., 2001, ''MEMS-Enabled Thermal Management of High-Heat-Flux Devices, Edifice: Embedded Droplet Impingement for Integrated Cooling of Electronics,'' J. Exp. Thermal Fluid Sci., **25**(5), pp. 231–242.
[53] Kim, J. H., You, S. M., Stephen, U. S., and Choi, U. S., 2004, ''Evaporative Spray Cooling of Plain and Microporous Coated Surface,'' Int. J. Heat Mass Transfer, **47**(14–16), pp. 3307–3315.
[54] Cho, C. S. K., and Wu, K., 1988, ''Comparison of Burnout Characteristics in Jet Impingement Cooling and Spray Cooling,'' *Proc. 1988 National Heat Transfer Conference*, ASME, **HTD-96**, pp. 561–567.
[55] Toda, S., 1974, ''A Study of Mist Cooling (2nd Report: Theory of Mist Cooling and its Fundamental Experiments),'' Heat Transfer-Jpn. Res., **3**(1), pp. 1–44.
[56] Fedder, G. K., Santhanam, S., Reed, M. L., Eagle, S. C., Guillou, D. F., Lu, M. S.-C., and Carley, L. R., 1996, ''Laminated High-Aspect-Ratio Microstructures in a Conventional CMOS Process,'' Sens. Actuators, A, **57**(2), pp. 103–110.
[57] Murthy, J. Y., Amon, C. H., Gabriel, K., Kumta, P., Yao, S. C., Boyalakuntla, D., Hsieh, C. C., Jain, A., Narumanchi, S. V. J., Rebello, K., and Wu, C. F., 2001, ''MEMS-based Thermal Management of Electronics Using Spray Impingement,'' *Proc. Pacific Rim/International, Intersociety Electronic Packaging Technical/Business Conference and Exhibition*, ASME, pp. 1–12.
[58] Narumanchi, S. V. J., Amon, C. H., and Murthy, J. Y., 2003, ''Influcence of Pulsating Submerged Liquid Jets on Chip-Level Thermal Phenomena,'' ASME J. Electron. Packag. **125**(3), pp. 354–361.
[59] Yao, S. C., Amon, C. H., Gabriel, K., Kumta, P., Murthy, J. Y., Wu, C. F., Hsieh, C. C., Boyalakuntla, D., Narumanchi, S. V. J., and Rebello, K., 2001, ''MEMS-Enabled Micro Spray Cooling System for Thermal Control of Electronic Chips,'' *Proc. ASME International Mechanical Engineering Congress and Exposition*, **HTD-369**(7), pp. 181–192.
[60] Wu, C. F., and Yao, S. C., 2001, ''Breakup of Liquid Jets from Irregular Shaped Silicon Micro Nozzles,'' *Proc. 4th Int. Conf. on Multiphase Flow*.
[61] Wu, C. F., Erdmann, L., Gabriel, K., and Yao, S. C., 2001, ''Fabrication of Silicon Sidewall Profiles for Fluidic Applications Using Modified Advanced Silicon Etching,'' *Proc. MEMS Design, Fabrication, Characterization, and Packaging*, Proc. SPIE, **4407**, pp. 100–108.
[62] Leoni, N., and Amon, C. H., 1997, ''Transient Thermal Design of Wearable Computers with Embedded Electronics Using Phase Change Materials,'' ASME, **HTD-343**(5), pp. 49–56.
[63] Vesligaj, M., and Amon, C. H., 1999, ''Transient Thermal Management of Temperature Fluctuations during Time Varying Workloads on Portable Electronics,'' IEEE Trans. Compon. Packag. Technol., **22**(4), pp. 541–550.
[64] Alawadhi, E. M., and Amon, C. H., 2000, ''Performance Analysis of an Enhanced PCM Thermal Control Unit,'' *Proc. 7th Intersociety Conference on Thermal and Thermomechanical Phenomena in Electronic Systems*, **1**, pp. 283–289.
[65] Leoni, N., and Amon, C. H., 2000, ''Bayesian Surrogates for Integrating Numerical, Analytical and Experimental Data: Application to Inverse Heat Transfer in Wearable Computers,'' IEEE Trans. Compo. Packag. Manuf. Technol., **23**(1), pp. 23–32.

An Assessment of Module Cooling Enhancement With Thermoelectric Coolers

R. E. Simons
M. J. Ellsworth
R. C. Chu

International Business Machines,
Poughkeepsie, NY 12601

The trend towards increasing heat flux at the chip and module level in computers is continuing. This trend coupled with the desire to increase performance by reducing chip operating temperatures presents a further challenge to thermal engineers. This paper will provide an assessment of the potential for module cooling enhancement with thermoelectric coolers. A brief background discussion of thermoelectric cooling is provided citing some of the early history of thermoelectrics as well as more recent developments from the literature. An example analyzing cooling enhancement of a multichip module package with a thermoelectric cooler is discussed. The analysis utilizes closed form equations incorporating both thermoelectric cooler parameters and package level thermal resistances to relate allowable module power to chip temperature. Comparisons are made of allowable module power with and without thermoelectric coolers based upon either air or water module level cooling. These results show that conventional thermoelectric coolers are inadequate to meet the requirements. Consideration is then given to improvements in allowable module power that might be obtained through increases in the thermoelectric figure of merit ZT or miniaturization of the thermoelectric elements.
[DOI: 10.1115/1.1852496]

Introduction

Many advances in computer technology have been made possible by a continuing series of increases in the packaging density of electronics. These advances began with the introduction of the transistor in 1947, and continue today with ultra-large scale integration at the chip level coupled with the utilization of multi-chip modules. The combination of increased circuit power dissipation coupled with increased packaging density led to substantial increases in chip and module heat flux over the past 40 years, particularly in high-end computers. Throughout this period the challenge was to limit chip temperature rise in order to ensure satisfactory electrical circuit operation and reliability.

Virtually all commercial computers were designed to operate at temperatures above ambient, generally in the range of 60 to 100°C. However, the potential for low temperature enhancement of CMOS electrical performance has been recognized for some time, even going back as far as the late 1960's and mid-1970's. Researchers [1–3] have identified the advantages of operating electronics at low temperatures. Among these advantages are faster switching times for semiconductor devices; increased speed due to lower electrical resistance of interconnecting materials; and a reduction in thermally induced failures of devices and components. Until recently the only computer to take advantage of the operation of CMOS chips at low temperature was the ETA-10 [4], which was a large scale scientific computer. This computer used direct immersion cooling of single chip modules immersed in liquid nitrogen. In 1997, IBM announced and shipped the RY5 S/390 client/server system. This computer system uses a conventional refrigeration system to maintain chip temperatures below that of comparable air-cooled systems, but well above cryogenic temperatures. In addition, there has been increased discussion in the semiconductor electronics community regarding scaling limits for CMOS devices and how to continue to achieve performance gains as scaling limits are approached. As discussed in a paper by Taur and Nowak [5], operation at lower temperature is seen as one of the ways to further extend CMOS performance. These developments not only foreshadow further applications of refrigeration cooling of electronics, but also potential opportunities to apply thermoelectric cooling to computer electronic packages.

Manuscript received April 19, 2004; revision received November 3, 2004. Review conducted by: C. Amon.

Thermoelectric Cooling

Although the principle of thermoelectricity dates back to the discovery of the Peltier effect in 1834, there was little practical application of the phenomenon until the middle 1950s. Prior to then the poor thermoelectric properties of known materials made them unsuitable for use in a practical refrigerating device. As discussed by Nolas et al. [6], from the mid-1950s to the present the major thermoelectric material design approach was that introduced by A.V. Ioffe. This approach was to select semiconducting compounds of heavy elements from the lower right of the periodic table and then to reduce the lattice thermal conductivity by forming mixed crystals. This technique led to compounds such as Bi_2Te_3 that is currently used in commercial thermoelectric modules. These materials made possible the development of practical thermoelectric devices for attaining temperatures below ambient without the use of vapor-compression refrigeration. The application of thermoelectric modules to cool electronics was discussed by Kraus [7] in the first book devoted to cooling electronic equipment. Thermoelectric modules offer the potential to augment the cooling of electronic module packages to (1) reduce chip operating temperatures at a given module heat load, or (2) allow higher module heat loads at a given chip temperature level. Thermoelectric cooling modules also offer the advantages of being compact, quiet, and having no moving parts. In addition, the degree of cooling may be readily controlled by varying the current supplied to the thermoelectric elements. Unfortunately, compared to vapor-compression refrigeration they are limited in the heat flux that they can accommodate and suffer from a lower coefficient of performance (C.O.P.). These two limitations have generally limited thermoelectrics to niche applications characterized by relatively low heat flux.

In recent years there has been increased interest in the application of thermoelectrics to electronic cooling, accompanied by efforts to improve the performance of thermoelectrics [8–14]. Efforts have been focused on the development of new bulk materials and thin film micro-coolers. The usefulness of thermoelectric ma-

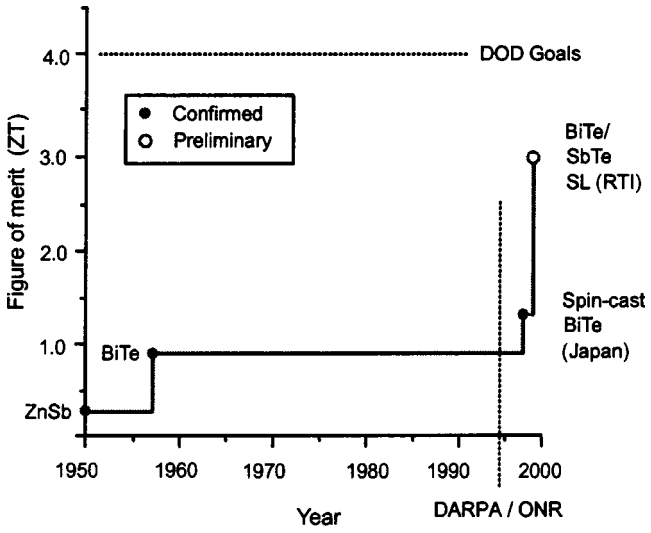

Fig. 1 History of room temperature thermoelectric figure of merit (ZT) adapted from [16]

terials for refrigeration is often characterized by the dimensionless thermoelectric figure of merit ZT. The value of Z is given by

$$Z = \frac{\alpha^2}{\rho \cdot \mathrm{K}} \tag{1}$$

As shown in Fig. 1, the room temperature value of ZT for BiTe that is used in commercial thermoelectric cooler modules remained unchanged for 40 years [8]. Fleurial et al. [12] reported that in 1991 JPL started a broad search to identify and develop advanced thermoelectric materials. Among the materials considered, skutterudite and Zn_4Sb_3-based materials appeared particularly promising and several of these materials are being developed. ZT values equal to or greater than 1 have been obtained for these materials over different ranges of temperature varying from 375 to 975 K. Unfortunately, to be particularly useful for electronic cooling applications improvements are needed in ZT over the temperature range of 300 to 325 K or below. Another strategy for enhancing ZT by focusing on reduced dimensionality as occurs in quantum wells (two-dimensional) or quantum wires (one-dimensional) is being pursued by researchers [13]. In 1995 the Defense Advanced Research Projects Agency (DARPA) initiated a program to stimulate the advancement of thermoelectric materials and devices. It was stated that the ultimate goal of the program ''is to quadruple the figure of merit of thermoelectric materials, thus making the resulting devices competitive with conventional phase change systems'' [8].

A number of recent papers have discussed the potential advantages of thin film thermoelectric coolers [10–14]. A paper by Vandersande and Fleurial [10] addressed thermal management of power electronics using thermoelectric coolers. They proposed to mount the highest power components on a diamond substrate which would be the top or cold side substrate of a thin film thermoelectric cooler. They noted that ''the main benefit of going to thin film coolers is the dramatic increase in cooling power density since it is inversely proportional to the length of the thermoelectric legs.'' As shown in Fig. 2, they reported the possibility of achieving cooling power densities above 100 W/cm^2, with the highest cooling power densities achieved with cooler leg lengths on the order of 20 to 50 microns. The structure of such a thin film thermoelectric element is shown in Fig. 3.

The heat pumping capacity, Q_p, of a thermoelectric cooling module is given by

$$Q_p = 2N\left(\alpha I T_c - \frac{\mathrm{I}^2\rho}{2G} - K\Delta T G\right) \tag{2}$$

where N is the number of couples, G is the ratio of cross-sectional area/length of each thermoelectric element, I is the electrical current, and T_c is the cold side temperature in K, and ΔT is the

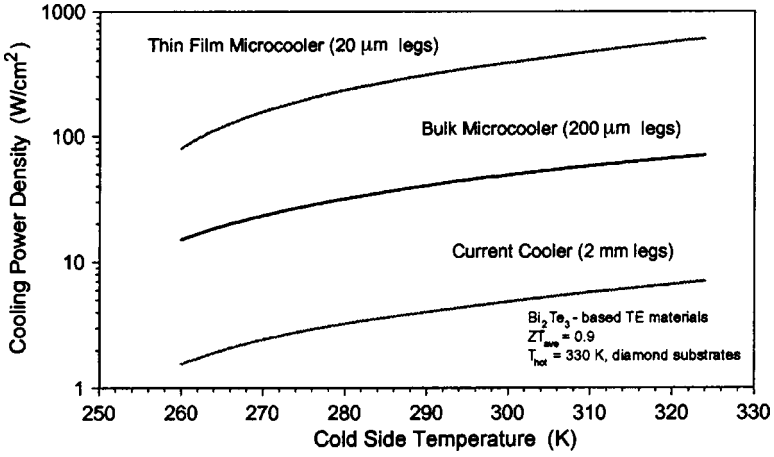

Fig. 2 Cooling power density for different T.E. cooler designs (adapted from Vandersande and Fleurial [10])

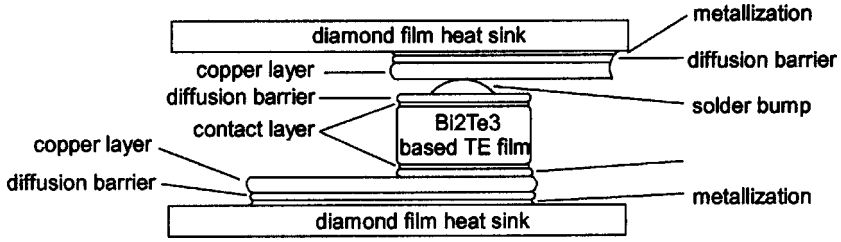

Fig. 3 Structure for a thin film thermoelectric device (adapted from Fleurial and Vandersande [10])

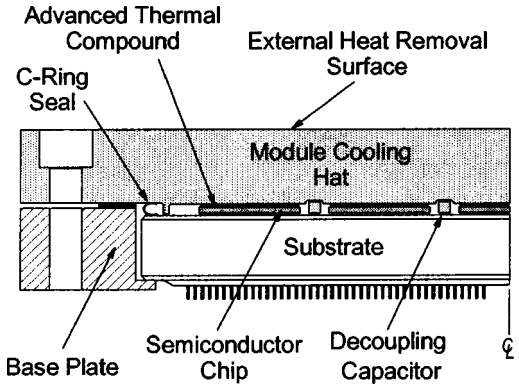

Fig. 4 Simplified cross-sectional view of a central processor module level package with thermal grease conduction paths

temperature difference ($T_h - T_c$) between the hot side and cold side of the thermoelectric elements. The amount of heat, Q_{te}, dissipated by a thermoelectric cooling module to perform the electronic pumping action is given by

$$Q_{te} = 2N\left(\frac{I^2\rho}{G} + \alpha I \Delta T\right) \tag{3}$$

The coefficient of performance, COP, which is the ratio of the heat pumped to the energy supplied to the thermoelectric cooling module to do the pumping, is given by

$$\text{COP} = Q_p / Q_{te} \tag{4}$$

Later in this paper these equations will be used to determine allowable module heat load or chip temperature with thermoelectric augmentation in an example multi-chip module cooling application.

MCM Thermoelectric Cooling Application

This section of this paper utilizes an example analysis of a multi-chip module (MCM) to provide a comparison of cooling capability with and without thermoelectric augmentation.

A 126 mm×126 mm multi-chip module containing thirty 15 mm×15 mm chips is assumed for the example calculations. A 0.18 mm layer of enhanced thermal grease with a thermal conductivity of 3.8 W/m-K is assumed between the chip and gap as shown in Fig. 4. The cap is assumed to be made of 10 mm thick copper. Figure 4 illustrates the cross-section of a chip site on the MCM with and without a thermoelectric module for enhancement. In both situations heat is assumed to flow via a serial path from the chip through the thermal resistances called out in Fig. 5 out to the cooling fluid.

The thermoelectric heat pumping Eq. (2) and thermoelectric heat dissipation Eq. (3) may be used to determine either allowable module power dissipation (Q_m) for a specified chip temperature (T_{chip}) or chip temperature for a specified module power. Before this can be accomplished; two additional equations relating chip temperature to cold-side temperature (T_c), and hot-side temperature (T_{hot}) to the cooling fluid temperature (T_o) are required. The chip temperature is related to the thermoelectric cold-side temperature by

$$T_{\text{chip}} = T_c + Q_m(R_0 + R_1) \tag{5}$$

where R_0 is the sum of thermal resistances across the chip, thermal grease layer, and thickness of the hat, and R_1 is the thermal resistance across the interface between the hat and heat sink base or between the cap and the cold-side of the thermoelectric module. The thermoelectric hot-side temperature is related to the cooling fluid temperature, T_o, by

$$T_{\text{hot}} = T_0 + (Q_m + Q_{te}) \times (R_2 + R_3) \tag{6}$$

where R_2 is the thermal resistance across the interface between the hot-side of the thermoelectric module and the base of the heat sink, and R_3 is the thermal resistance from the heat sink base to the cooling fluid. For steady-state operation the heat pumping capacity, Q_p, given in Eq. (2) will be equal to the module power dissipation term, Q_m in Eqs. (5) and (6). Using the symbolic algebra capability of Mathcad™ to perform the algebraic manipulations, Eqs. (2), (3), (5), and (6) were combined to obtain the expressions shown in Table 1. Given the material and thermoelectric module parameters, the electrical current supplied to the thermoelectric module, and the thermal resistances; the chip temperature may be determined for a given module power using Eq. (7). Similarly, the allowable module power may be determined for a given chip temperature using Eq. (8). These equations may also be applied to single chip modules by setting module power dissipation equal to chip power dissipation. For multi-chip modules, application of these equations is restricted to uniform power dissipation on all chips. It should be noted that all of the thermal resistances contained in Eqs. (5), (6), (7), and (8) should be computed on an overall module basis. Accordingly, thermal resistance, R_0, should be computed for an individual chip site and then divided by the number of chips on the MCM to convert it to an overall module basis before using it in any of the equations.

A commercially available 62 mm×62 mm thermoelectric module was chosen for use in the example presented here. The module chosen was picked because of its size which would allow four modules to virtually cover the surface of the entire MCM and also because the vendor catalog provided all the necessary thermoelectric material and geometry data required for the calculations. The specific values used in the calculations were

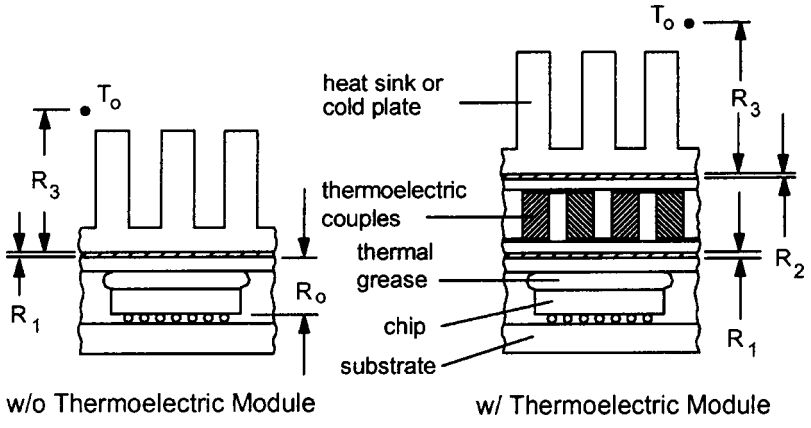

Fig. 5 Cross-section view of chip site on MCM showing thermal resistances w/ and w/o thermoelectric cooler augmentation

Table 1 Chip temperature and allowable power dissipation equations for thermoelectric cooling augmentation

$$T_{chip} = \frac{I}{\frac{\alpha I + KG}{KG} - \frac{2N(R_2+R_3)KG}{1-2N(R_2+R_3)(\alpha I - KG)}} \times \left[\frac{I^2\rho}{2KG^2} + \frac{Q_m}{2NKG} + \frac{T_o}{1-2N(R_2+R_3)(\alpha I-KG)} + \frac{N(R_2+R_3)I^2\rho}{(1-2N(R_2+R_3)(\alpha I-KG))G} \right] + Q_m(R_o+R_1) \quad (7)$$

$$Q_m = \frac{N(2\alpha I + 2KG - 4\alpha^2 I^2 N(R_2+R_3))}{1+2N(R_2+R_3)\cdot(KG-\alpha I)+2N(R_0+R_1)(\alpha I+KG)-4N^2\alpha^2 I^2(R_0+R_1)(R_2+R_3)} \cdot T_{chip} - \frac{2NKG}{1+2N(R_2+R_3)\cdot(KG-\alpha I)+2N(R_0+R_1)(\alpha I+KG)-4N^2\alpha^2 I^2(R_0+R_1)(R_2+R_3)} \cdot T_0 + \frac{N}{G} \frac{(2N\alpha\rho I^3 - 4N\rho K I^2 G)(R_2+R_3) - I^2\rho}{1+2N(R_2+R_3)\cdot(KG-\alpha I)+2N(R_0+R_1)(\alpha I+KG)-4N^2\alpha^2 I^2(R_0+R_1)(R_2+R_3)} \quad (8)$$

$\alpha = 0.0002$ volts/K $N = 127$

$\rho = 0.001$ ohm-cm $G = 0.28$ cm

$K = 0.015$ W/cm-K $I = 14$ amps

Since each thermoelectric module covered one-quarter of the MCM the thermal resistances and module power were scaled accordingly. The thermal resistance values and coolant reference temperatures used in the calculations were

$R_0 = 0.034$ K/W

$R_1 = 0.0054$ K/W

$R_2 = 0.0054$ K/W

$R_3 = 0.116$ K/W (air-cooled)

$R_3 = 0.0168$ K/W (H_2O-cooled)

$T_o = 30°C$ K/W (air-cooled)

$T_o = 25°C$ K/W (H_2O-cooled)

The values of interface thermal resistances (R_1 and R_2) used were based upon the interface thermal resistance achieved with the IBM ES/9000 TCM cooling technology [15]. Similarly the values used for heat sink (air) and cold plate (H_2O-cooled) thermal resistance (R_3) were based upon IBM high performance cooling technology scaled for one-quarter of the size of the example MCM.

The equations presented in Table 1 were incorporated in a Lotus 1-2-3 spreadsheet and executed with the above values. In addition, comparable equations for the case without thermoelectric augmentation were also included in the spreadsheet. The equation giving chip temperature for a specified module power is

$$T_{chip} = T_o + Q_m(R_o + R_1 + R_3) \quad (9)$$

and the equation giving allowable module power for a specified chip temperature is

$$Q_m = (T_{chip} - T_o)/(R_o + R_1 + R_3) \quad (10)$$

The results of these calculations are shown in Figs. 6 and 7. As noted earlier, thermoelectric cooling modules may be used to reduce chip operating temperatures given a module heat load. The degree of temperature reduction for a given module design is given by subtracting the results of Eq. (7) in Table 1 from the results of Eq. (9). The chip operating temperature reductions which could be achieved by applying thermoelectric cooling augmentation to the example MCM are shown in Fig. 6. Considering the cost of the thermoelectrics, the added manufacturing process steps, the additional power requirement, and the added reliability risk associated with the thermoelectrics it is doubtful that they would be considered for anything less than a 20°C reduction. It may be seen that for the example MCM a 20°C temperature reduction would occur at an MCM power of 275 watts for the air-cooled case and at 335 watts for the water-cooled case.

It was also noted earlier that thermoelectric cooling modules may be used to augment allowable module power dissipation at a given temperature. Comparisons of allowable module power dissipation with and without thermoelectric augmentation are shown in Fig. 7 for the example MCM for both air-cooling and water-cooling conditions. It can be seen that for the air-cooled case, at a chip temperature of 47°C, the allowable module power dissipation is the same with or without augmentation. At higher chip temperatures the allowable module power dissipation is higher without thermoelectric augmentation. A similar situation occurs for the water-cooled case at a chip temperature of 31°C. In both cases the power dissipation at which this occurs at is about 450 to 500 watts. Clearly, specific cases for which the application of thermoelectrics are being considered must be carefully assessed to determine if the use of thermoelectrics will be beneficial.

For purposes of comparison, it may be noted that if the example MCM were cooled using the IBM RY5 vapor compression refrig-

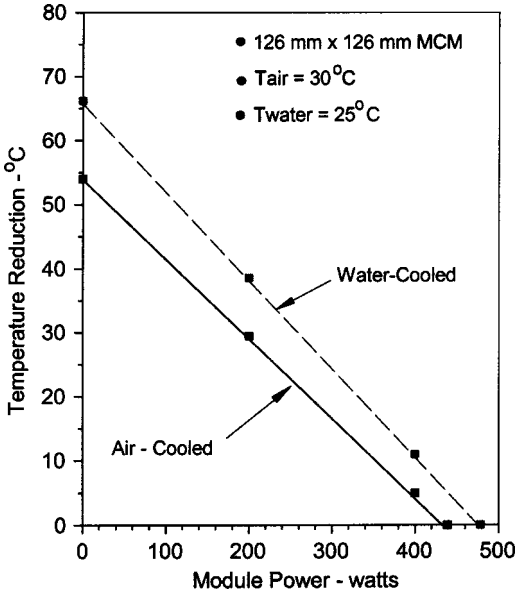

Fig. 6 Module temperature reduction versus module power for air or water-cooled 126 mm×126 mm multi-chip

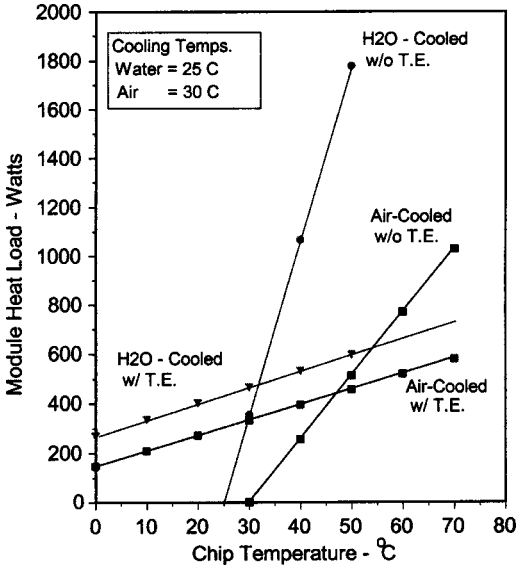

Fig. 7 Comparison of allowable module heat load with and without thermoelectric cooling enhancement

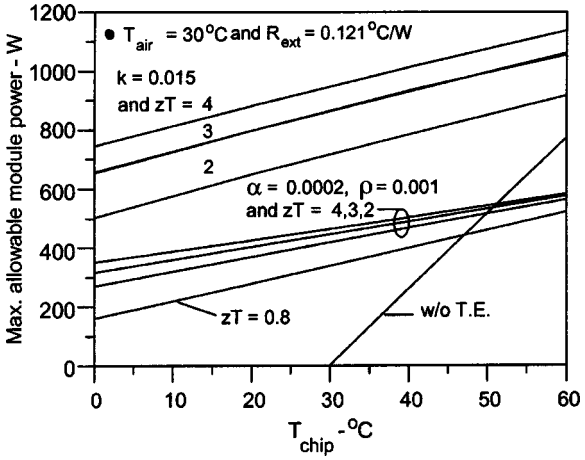

Fig. 8 Effect of increased thermoelectric ZT on maximum allowable module power

eration cooling system with a thermal load capacity of 1050 watts and a cold plate evaporator temperature of 21°C, the corresponding chip temperatures would be 30°C. It can be seen from Fig. 7, that the water-cooled thermoelectric augmented MCM would exhibit a thermal load capacity of only 467 watts, at the same chip temperature. In addition, the C.O.P. of the thermoelectric modules for this case would be 0.64 compared to a C.O.P. ranging from 1.9 to 3 for a vapor-compression refrigeration cooling system.

As shown in the example, the application of thermoelectric modules could provide cooling enhancement for a limited range of module power. Unfortunately, in most of the cases we are interested in at IBM, MCM powers are simply too high for current thermoelectric modules to handle effectively. The figure of merit, ZT, of the currently available thermoelectric materials, and the COP attainable with existing thermoelectric coolers, are just not good enough to be acceptable. Until and unless improvements can be made to enhance heat pumping capability and COP, thermoelectrics will not be a serious candidate for high performance electronic cooling application.

The next section of this paper will assess the effects that improvements in ZT might have for electronic cooling applications of the type considered in this paper.

Potential Effect of Improvement in ZT

As noted earlier, a number of efforts are underway to find or create materials with an increased thermoelectric figure of merit, ZT. From a cooling viewpoint the question to be answered is how significant might such improvements be for cooling high performance electronic modules? A theoretical expression can be derived directly relating the maximum temperature difference across a thermoelectric to Z and T_c. Likewise, an expression can be derived directly relating COP to Z, T_c, and ΔT. Unfortunately, inspection of Eqs. (7) and (8) reveals that it is not possible to obtain similar expressions for T_{chip} or Q_m in terms of Z. In fact as the subsequent discussion will reveal, it is possible to get different values of Q_m for the same value of Z. Since Z depends upon α, ρ, and k, for any given value of Z there are an infinite number of combinations of α, ρ, and k that will give the same value of Z.

Phelan et al. [16] estimated the effect of improved Z by assuming that the improvement is obtained by increasing the Seebeck coefficient while holding electrical resistivity and thermal conductivity constant. This approach is taken one step further here by evaluating 3 cases: (1) holding α and ρ constant to find the value of k needed to achieve a given Z; (2) holding ρ and k constant to find the value of α needed to achieve a given Z; and (3) holding α and k constant to find the value of ρ needed to achieve a given Z. For each case the combination of α, ρ, and k is then used in Eq. (8) in Table 1 to determine the maximum allowable module heat load for a given chip temperature. The maximum allowable module power for a given chip temperature is determined by increasing the current to the thermoelectric elements until the allowable module power peaks or a hot side temperature of 80°C is reached, whichever comes first. The 80°C hot side temperature constraint is based upon a recommendation in the Melcor thermoelectric catalog in order to avoid diffusion from the copper interconnections into the thermoelectric material, which would degrade its performance. The calculations were performed for the air cooling condition described earlier and for chip temperatures ranging from 0 to 60°C. The results of these calculations are shown in Fig. 8. In all the cases the value of T used in the figure of merit ZT is a room temperature value of 300 K. The line labeled $ZT=0.8$ is based upon the values of α, ρ, and k for present day BiTe thermoelectric elements, and is the same as that shown in Fig. 7 for the air-cooled case. The next group of lines for $ZT=2$, 3, and 4 is for case 1 and was obtained by holding α and ρ at present day values and using the k values needed to give the respective values of Z. The upper-most group of lines for $ZT=2$, 3, and 4 is for cases 2 and 3 which gave nearly identical results. These results show that thermoelectric materials with increased ZT would give increased module cooling capability that could be significant. They also clearly demonstrate that materials with the same value of ZT will not necessarily give the same thermoelectric cooling performance. They would also seem to suggest that it is preferable to increase ZT by increasing α or decreasing ρ rather than reducing k.

To further explore the effects of the thermoelectric material parameters on cooling performance, calculations were performed as already described, with α held constant at the present day value and ρ and k varied so that $ZT=0.8$. Figure 9 shows the results based upon a chip temperature of 40°C. These results show that for a given Seebeck coefficient there is an optimum combination of ρ and k that will maximize thermoelectric cooling performance. For purposes of comparison the horizontal lines represent the module cooling capability without any thermoelectric enhancement and with enhancement with present day materials for the conditions specified.

These results prompted further calculations to determine what would happen to the maximum module cooling capability at a constant value of ZT for different values of α as ρ and k are varied. The results shown in Fig. 10 demonstrate that for each value of α there is a unique combination of ρ and k that maximizes the allowable value of module power dissipation for a given

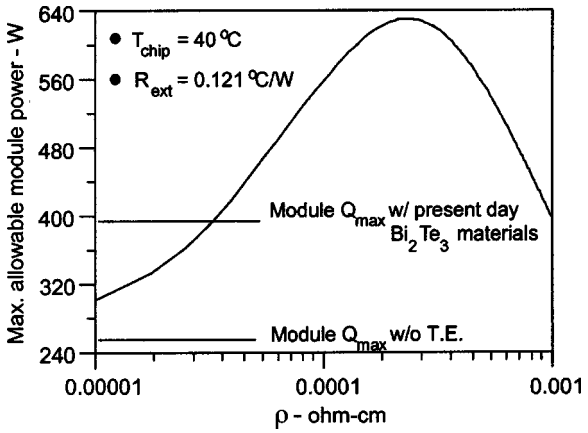

Fig. 9 Variation in module Q max with thermal conductivity of TE elements for a Seebeck coefficient=0.0002 and ZT=0.8

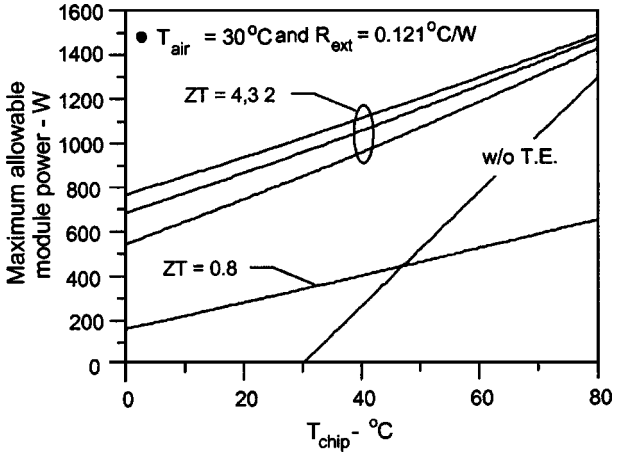

Fig. 11 Theoretical module power limit versus chip temperature for ZTs based upon optimal combination of thermoelectric element electrical resistivity and thermal conductivity

chip temperature and cooling condition. It may also be seen that the maximum allowable power is independent of the values of α. Based upon this observation, further calculations were performed varying ρ and k with α fixed at 0.0005 for $ZT=2$, 3, and 4 to determine the maximum allowable module power for chip temperatures ranging from 0 to 80°C. The results of these calculations are shown in Fig. 11. Based upon the previous results (i.e., Fig. 10) it is expected that the results shown in Fig. 11 are at least valid for $0.0003<\alpha<0.0007$ and probably beyond. Included for comparison are lines of cooling capability for thermoelectric elements with $ZT=0.8$ based upon the properties of present day BiTe and for cooling capability without thermoelectric augmentation.

Additional calculations were performed to illustrate the effect of external thermal resistance on the maximum thermal enhancement that might be achieved with materials offering an improved *Z*. These calculations were performed on the same basis as the previous ones by varying ρ and k with α fixed at 0.0005 for $ZT=0.8$, 2, 3, and 4 to determine the maximum allowable module power as a function of external thermal resistance. For these cases the chip and sink (i.e., air or water) temperatures were held constant at 40 and 30°C, respectively. The results are shown in Fig. 12. The line labeled "with present day BiTe materials" is for $ZT=0.8$ with α, ρ, and k at current values. For purposes of comparison the line labeled $ZT=0.8$ shows the module powers that could be supported with optimum values of ρ and k. It can be seen that as external thermal resistance is decreased, even thermoelectric elements with $ZT=0.8$ but with an optimum $\rho-k$ combination could provide a substantial improvement over the material used in present day thermoelectric coolers. Still further improvement could be obtained if it is possible to increase ZT with optimum combinations of $\rho-k$.

Effect of *TE* Geometry Scaling

It is well known that CMOS circuits run faster the smaller they are made. The semiconductor industry has taken full advantage of scaling CMOS geometry; proportionally reducing relevant CMOS device dimensions, from a characteristic length of several micrometers to below a tenth of a micrometer, to improve electrical performance. What happens to the thermal performance of a thermoelectric module, particularly when used in an electronic module cooling application, when its geometry is scaled accordingly?

Figure 13 illustrates a thermoelectric module's relevant geometry. Let the thermoelectric element length, L, represent the characteristic length (the length to be varied). The thermoelectric element edge length, X, may be scaled with L by holding G constant. The spacing between thermoelectric elements, S, may be scaled with X by holding the ratio, S/X, constant. The overall module size, W, as well as the distance from the outer most elements to the module (substrate) edge, E, is held constant. The geometric

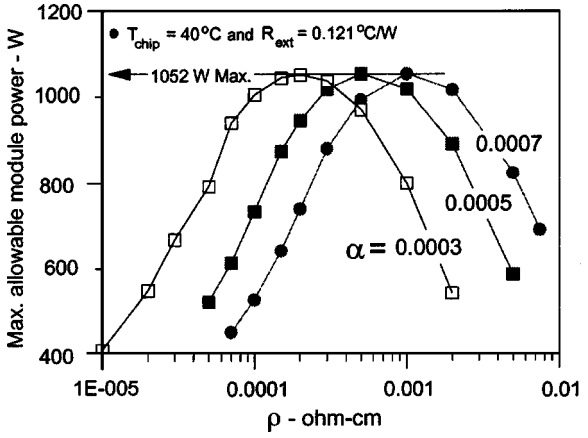

Fig. 10 Variation in maximum allowable module power with thermal conductivity of TE elements for different different values of Seebeck coefficient for ZT=3.0

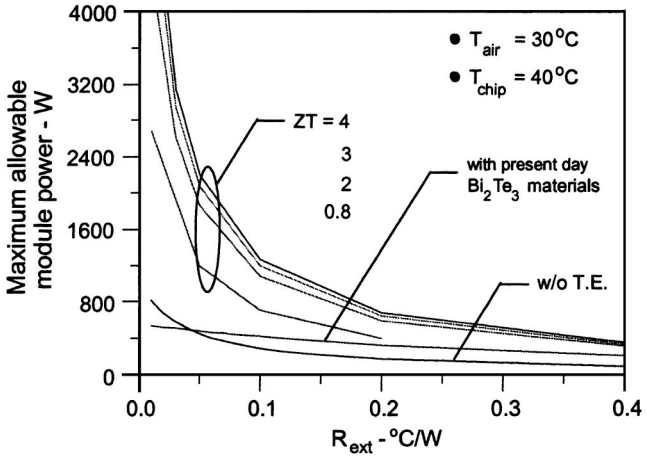

Fig. 12 Effect of external thermal resistance on theoretical module power limit for ZTs based on optimal combination of thermoelectric element electrical resistivity and thermal conductivity

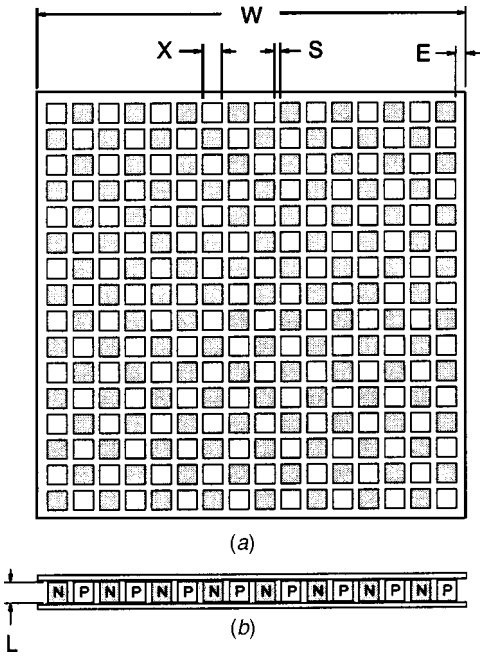

Fig. 13 Thermoelectric module (a) plan view with top substrate removed and (b) side view

reference or starting point is a commercially available thermoelectric module (Melcor CP-2-127-06L) with the following geometry definition:

$$W=62 \text{ mm} \quad L=3.073 \text{ mm} \quad X=2.933 \text{ mm}$$

$$G=0.28 \text{ cm} \quad S=0.938 \text{ mm} \quad E=0.5 \text{ mm}$$

$$N=127 \text{ couples}$$

As L is reduced, X will decrease exponentially and the number of thermoelectric couples, N, will increase exponentially as shown in Fig. 14.

To answer the scaling question properly in the context of an electronics cooling application, thermal performance will be determined for $T_{chip}=40°C$ and $T_o=30°C$. The thermoelectric material properties and module thermal resistances outlined in the earlier section on MCM Thermoelectric Cooling Application are used in the scaling analysis. For a given TE geometry, the thermoelectric current, I, is varied in order to determine the maximum module heat load that can be supported given the above temperature and thermal resistance constraints. The current that provides the maximum module heat load is designated I_{max}.

Figure 15 illustrates the effect of thermoelectric scaling on an electronic module's thermal performance. Notice that under the unrealistic condition where both T_h and T_c are held constant, the maximum module heat load continues to increase as the TE ge-

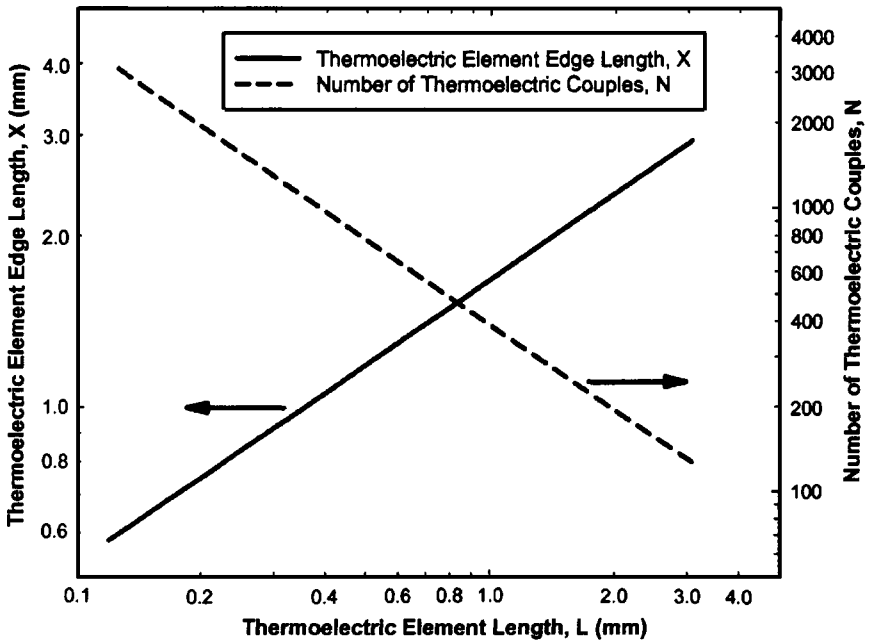

L (mm)	X (mm)	S (mm)	N
3.073	2.933	0.938	127
1.955	2.339	0.748	199
0.990	1.665	0.532	391
0.483	1.163	0.372	799
0.335	0.968	0.309	1151
0.214	0.773	0.247	1799
0.148	0.644	0.206	2591
0.120	0.580	0.185	3199

Fig. 14 Thermoelectric module geometry scaled from a thermoelectric element length of 3.07 mm to 0.12 mm

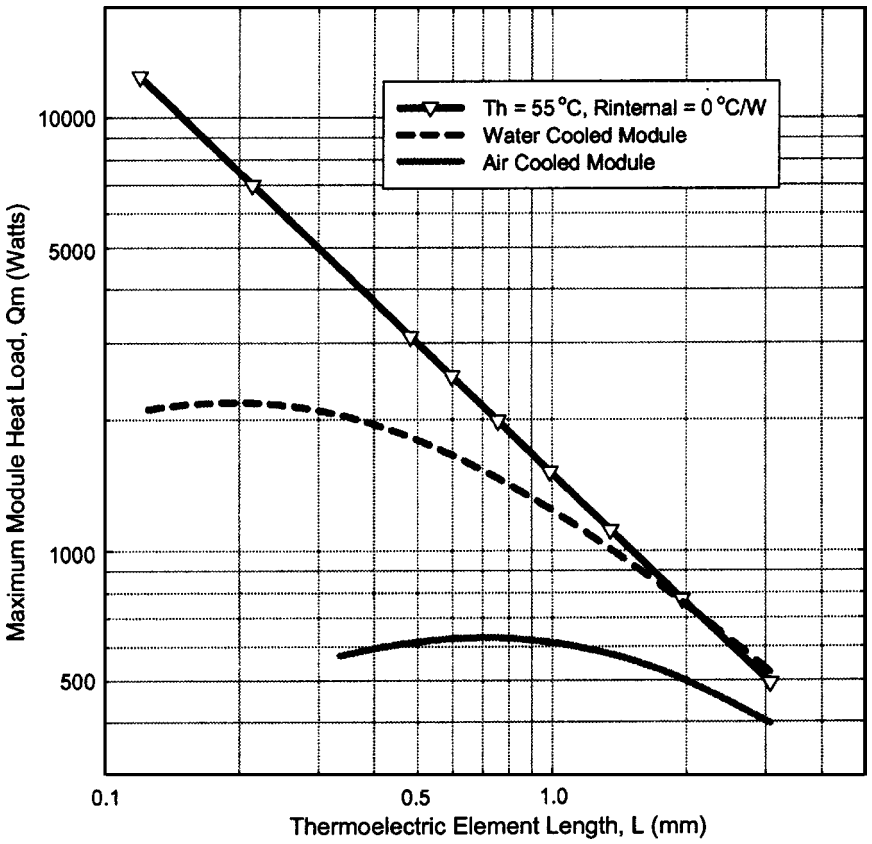

Fig. 15 Electronics module cooling capability when a thermoelectric module is included and its geometry is scaled

ometry is scaled downward. Under the realistic condition where T_h and T_c are governed by the module external and internal thermal resistance, respectively, there is an optimum geometry condition that produces a maximum thermal performance. Furthermore, the optimum geometry/thermal performance point is very sensitive to the module external thermal resistance. For example, for air cooling conditions, thermal performance can be improved by 1.6X where for water cooling conditions thermal performance can be improved by 4X. The primary reason for this behavior is that under the condition of a constant T_h and T_c, the current yielding maximum heat load, I max, is a constant with geometric scaling. It can be seen from examining Eq. (2) that the terms in parentheses will hold constant with scaling resulting in the maximum module heat load that can be supported as increasing solely with the number of couples. When T_h and T_c are governed by the module external and internal thermal resistance, respectively, I max will decrease with scaling and will decrease more rapidly the higher the external resistance (such as with air cooling).

Figure 16 shows that the increase in thermal performance achieved by scaling TE geometry does not come for free. The thermoelectric module coefficient of performance (COP) is just as important a consideration in an electronics cooling application as is thermal performance. COP is a measure of the amount of work (i.e., electrical power, Q_{te}) required to pump a given amount of heat, Q_p, as follows:

$$\mathrm{COP}=\frac{Q_p}{Q_{te}}=\frac{\left[\alpha I T_c-\frac{I^2\rho}{2G}-KG\Delta T\right]}{\left[\frac{I^2\rho}{G}+\alpha I\Delta T\right]} \tag{11}$$

For the constant temperature (T_h and T_c) condition, it is seen that COP remains constant with scaling. The result is that the amount of energy required to operate the thermoelectric module will increase linearly with the amount of module heat removed. COP is higher under the realistic module cooling cases, yet is still rather undesirable from a practical application viewpoint. To be practical COP should be greater or equal to 2. The fact that COP tends to increase with scaling for the air cooling case while it decreases for

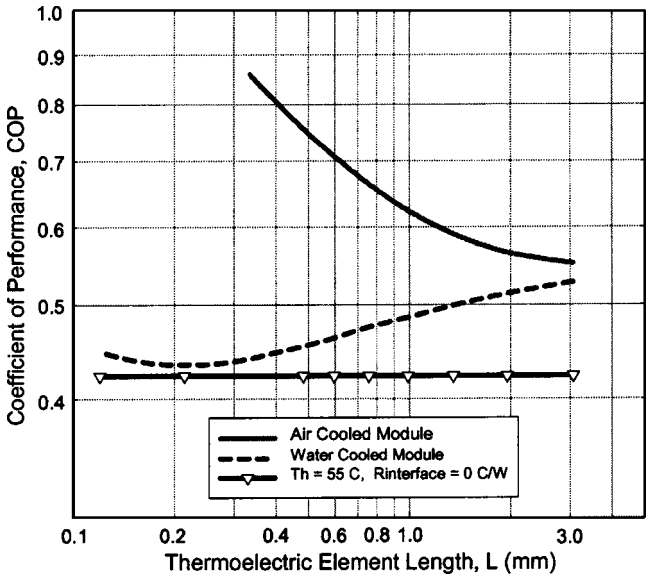

Fig. 16 Thermoelectric module coefficient of performance (COP) corresponding to module heat removal capability in Fig. 15

the water cooling case is intriguing and can be explained by examining Eq. (9) with scaling along with $I_{\max}$, T_h, and T_c.

Summary and Conclusions

In this paper we have sought to provide a brief review and discussion of the application of thermoelectrics to cooling electronics. Almost since the birth of electronic computer technology, heat flux has been increasing, and we may expect this trend to continue. In addition, the advantage offered in enhanced speed by a reduction in operating temperatures, adds a new dimension to the cooling challenge. With the continued demand for improved cooling technology to enhance the performance and reliability of CMOS applications, thermoelectric cooling may be considered a potential candidate for cooling enhancement. The chip temperature and allowable module power equations (Eqs. (7) and (8)) developed and described in this paper provide a useful means to perform trade-off analyses to assess whether or not thermoelectric augmentation will provide an effective enhancement over conventional cooling techniques.

As shown in the example, the application of thermoelectric modules using present day materials could provide cooling enhancement for a limited range of powers. Unfortunately, for most of the cases we at IBM (and presumably others) are interested in, chip and MCM powers are simply too high for current thermoelectric modules to handle effectively. The current figure of merit, Z, of the currently available candidate materials, and the coefficient of performance (COP) attainable with existing thermoelectric coolers, are just not good enough to be acceptable.

The latter portion of this paper considered the improvements in cooling that could be obtained by finding or developing materials with improved ZT. As has been shown by the calculations, materials with the same ZT will not necessarily provide equal degrees of enhancement. The calculations have further shown that for a given value of ZT there is a unique combination of ρ and k for each value of α that maximizes the allowable module power. The maximum allowable power so calculated represents the theoretical limit for a given ZT and set of specified cooling conditions. The degree to which materials with improved ZT approach this limit will depend on the actual values of α, ρ, and k that together make up the value of Z.

The latter portion of the paper also showed what improvement can be realized by scaling the thermoelectric module geometry downward. While improvements in heat dissipation capability can be had, COP must be considered carefully when leveraging scaling.

Other factors which will have to be taken into account to make the application of thermoelectrics viable include (1) long term thermoelectric couple and cooler assembly reliability; (2) thermoelectric power requirement; (3) mechanical integration of the thermoelectric cooler assembly with the electronic module package; and (4) design for cooling redundancy. Finally, considering the increasing need to drive down all computer hardware costs, the cost of thermoelectrics that can meet the cooling requirements will play a vital role in the decision to use them.

Nomenclature

A = cross-sectional area of thermoelectric element leg, m^2
COP = coefficient of performance
E = distance from outer thermoelectric element to substrate edge, m
G = thermoelectric element cross-sectional area/length
I = electrical current, amperes
K = thermal conductivity, W/m-K
L = length of thermoelectric element leg, m
N = number of thermoelectric couples
q = heat load, W
q'' = heat flux, W/m^2
R = thermal resistance, K/W
S = spacing between thermoelectric elements, m
T = temperature, Kelvin
ΔT = $T_h - T_c$, K
W = thermoelectric module width, m
x = distance from base of thermoelectric element leg, m
X = thermoelectric element edge length, m
Z = thermoelectric figure of merit, 1/K

Greek Symbols

α = Seebeck coefficient, V/K
ρ = electrical resistivity, ohm-cm

Subscripts

c = cold side
chip = chip condition
e = external
h = hot side
i = internal
m = module
p = Peltier pumping
o = cooling fluid condition
te = thermoelectric
max = maximum condition

References

[1] Gaensslen, F. H., 1980, "MOS Devices and Integrated Circuits at Liquid Nitrogen Temperature," *1980 IEEE ICCD Proceedings*, pp. 450–452.
[2] Jaeger, R. C., 1986, "Development of Low Temperature CMOS for High Performance Computer Systems," *IEEE International Conference on Computer Design: VLSI in Computers*, pp. 128–130.
[3] Kirschmann, R. K., 1986, "Development of Low Temperature CMOS for High Performance Computer Systems," *IEEE International Conference on Computer Design: VLSI in Computers*, pp. 128–130.
[4] Krane, R. J., Bar-Cohen, A., Jaeger, R. C., and Gaensslen, F. H., 1990, "MOS Electronics and Thermal Control for Cryogenically-Cooled Computer Systems," in *Advances in Thermal Modeling of Electronic Components and Systems*, **2**, ASME Press, New York, NY, pp. 185–232.
[5] Taur, Y., and Nowak, E. J., 1997, "CMOS Devices Below 0.1 μm: How High Will Performance Go?," *Electron Devices Meeting Technical Digest*, IEEE, Piscataway, NJ, pp. 215–218.
[6] Nolas, G. S., Slack, G. A., Cohn, J. L., and Schujman, S. B., 1998, "The Next Generation of Thermoelectric Materials," *Proceedings of the 17th International Conference on Thermoelectrics*, IEEE, Piscataway, NJ, pp. 294–297.
[7] Kraus, A. D., 1965, *Cooling Electronic Equipment*, Prentice-Hall, New York, NY.
[8] Dubois, L. H., 1999, "An Introduction to the DARPA Program in Advanced Thermoelectric Materials and Devices," *Proceedings of 18th International Conference on Thermoelectrics*, IEEE, Piscataway, NJ, pp. 1–4.
[9] Kolander, W. L., and Lyon, H. B., 1996, "Thermoelectric Cooler Utility for Electronic Applications," ASME HTD-Vol. 239, National Heat Transfer Conference, **7**, ASME, New York.
[10] Vandersande, J. W., and Fleurial, J.-P., "Thermal Management of Power Electronics Using Thermoelectric Coolers," *Proceedings of the 15th International Conference on Thermoelectrics*, IEEE, Piscataway, NJ, pp. 252–255.
[11] Stockholm, J. G., 1997, "Current State of Peltier Cooling," *Proceedings of the 16th International Conference on Thermoelectrics*, pp. 37–46.
[12] Fleurial, J.-P., Borshchevsky, A., Caillat, T., and Ewell, R., 1997, "New Materials and Devices for Thermoelectric Applications," IECEC, ACS Paper No. 97419, pp. 1080–1085.
[13] Dresselhaus, M. S., Koga, T., Sun, X., Cronin, S. B., Wang, Cronin, S. B., Wang, K. L., and Chen, G., 1997, "Low Dimensional Thermoelectrics," *Proceedings of the 16th International Conference on Thermoelectrics*, IEEE, Piscataway, NJ, pp. 12–20.
[14] Morelli, D. T., 1996, "Potential Applications of Advanced Thermoelectrics in the Automobile Industry," *Proceedings of the 13th International Conference on Thermoelectrics*, pp. 383–386.
[15] Chu, R. C., and Simons, R. E., 1994, "Cooling Technology for High Performance Computers: Design Applications," in *Cooling of Electronic Systems*, S. Kakac, H. Yuncu, and K. Hijikata, eds., Kluwer Academic Publishers, Dordrecht, Netherlands, pp. 71–95.
[16] Phelan, P. E., Chiriac, V., and Lee, T.-Y., 1996, "Current and Future Miniature Refrigeration Cooling Technologies for High Power Microelectronics," *Proceedings of the 17th Semiconductor Thermal Measurement and Management Symposium*, IEEE, Piscataway, NJ, pp. 158–167.

Effect of the Location and the Properties of Thermostatic Expansion Valve Sensor Bulb on the Stability of a Refrigeration System

Veerendra Mulay

Amit Kulkarni

Dereje Agonafer
ASME Fellow

Mechanical and Aerospace Engineering Department,
The University of Texas at Arlington,
Arlington TX 76010
e-mail: agonafer@uta.edu

Roger Schmidt
ASME Fellow
IBM Corporation, Poughkeepsie, NY
e-mail: c28rrs@us.ibm.com

The combination of increased power dissipation and increased packaging density has led to substantial increases in chip and module heat flux in high-end computers. The challenge has been to limit the rise in chip temperature. In the past, virtually all commercial computers were designed to operate at temperatures above the ambient. However, researchers have identified the advantages of operating electronics at low temperatures. The primary purpose of low-temperature cooling using a vapor compression system are faster switching times of semiconductor devices, increased circuit speed due to lower electrical resistance of interconnecting materials, and a reduction in thermally induced failures of devices and components. Achievable performance improvements range from 1% to 3% for every 10°C lower transistor temperature, depending on the doping characteristics of the chip. The current research focuses on IBM's mainframe, which uses a conventional refrigeration system to maintain chip temperatures below that of comparable air-cooled systems, but well above cryogenic temperatures. Although performance has been the key driver in the use of this technology, the second major reason for designing a system with low-temperature cooling is the improvement achieved in reliability to counteract detrimental effects, which rise as technology is pushed to the extremes. A mathematical model is developed to determine the time constant for an expansion valve sensor bulb. This time constant varies with variation in the thermophysical properties of the sensor element; that is, bulb size and bulb liquid. An experimental bench is built to study the effect of variation of evaporator outlet superheat on system performance. The heat load is varied from no load to full load (1 KW) to find out the system response at various loads. Experimental investigation is also done to see how the changes in thermophysical properties of the liquid in the sensor bulb of the expansion valve affect the overall system performance. Different types of thermostatic expansion valves are tested to investigate that bulb size, bulb constant, and bulb location have significant effects on the behavior of the system. Thermal resistance between the bulb and evaporator return line can considerably affect the system stability, and by increasing the thermal resistance, the stability can be further increased. [DOI: 10.1115/1.1839584]

Introduction

With the increased use of complementary metal-oxide-semiconductor (CMOS) chip technologies in today's computers, cooling has now become a strong influence on computer performance [1]. Electron and hole mobility is the primary electrical property that improves with the lowering of temperature. Transistor switching speed is proportional to the mean carrier velocity in the device and mobility is the ratio of electron or hole velocities to electric field. Mobility increases as temperature decreases due to a reduction of carrier scattering from thermal vibrations of the semiconductor crystal lattice. In addition to mobility the other major benefit in reducing temperature is an exponential reduction in leakage currents. Achievable performance improvements range from 1% to 3% for every 10°C lower transistor temperature, depending on the doping characteristics of the chip.

The primary purpose of low-temperature cooling using vapor compression system are faster switching times of semiconductor devices, increased circuit speed due to lower electrical resistance of interconnecting materials, and a reduction in thermally induced failures of devices and components. Over the past several years, computer systems have been shipped with refrigeration utilizing the vapor compression cycle to attain low temperatures. With the increase in CMOS performance achieved with lower temperatures, a number of companies have embarked on programs to investigate cooling electronics, some evolving to major product announcements and shippable products. Intel, DEC, AMD, Sun Microsystems, IBM, SYS Technologies, and Kryotech, Inc., have all shown computers utilizing the vapor compression refrigeration cycle. Typical evaporator refrigerant temperatures ranged from −40 to 20°C in these systems cooled with refrigeration. This paper describes the application of refrigeration to cooling of the multichip module (MCM) in the IBM S/390 G4 refrigeration system. Although performance has been the key driver in the use of this technology, the second major reason for designing a system with low temperature cooling is the potential improvement achieved in reliability to counteract detrimental effects, which rise as technology is pushed to the extremes. Many wear-out failure mechanisms follow the Arrhenius equation [2], showing that for die temperatures operating in the range of −20 to 140°C, every 10°C decrease in temperature reduces the failure rate by approximately a factor of 2. Some recent work by Needham et al. [3] clearly shows unique low-temperature-related failures during

Manuscript received May 6, 2004; revision received August 18, 2004. Review conducted by: C. Amon.

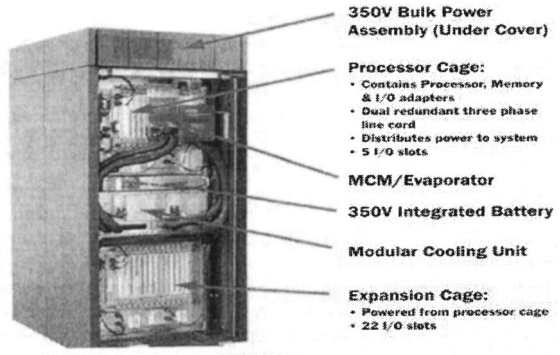

Fig. 1 IBM S/390 G4 CMOS system

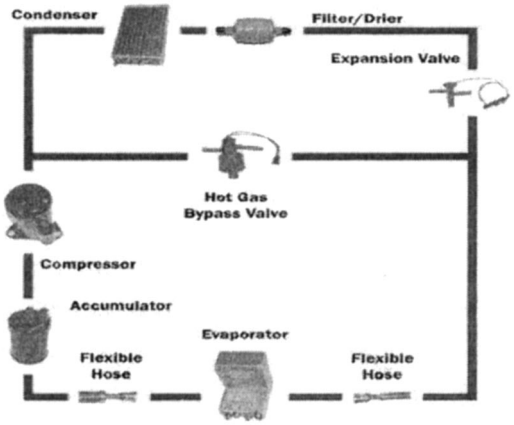

Fig. 2 Vapor compression refrigeration system

manufacturing. If these fails can be eliminated through a manufacturing test process then higher chip reliability can possibly be realized in the field.

The IBM S/390 G4 CMOS system [1], first shipped in 1997, can have 12 processing units, up to two levels of cache and the bus-switching logic packaged in a single MCM on one processor board. This delivers performance comparable to that of an IBM 9021-711 bipolar system in which the corresponding logic occupies 56 MCMs on 14 boards. This system was unique in that it was the first such IBM design to employ refrigeration cooling. The decision to employ refrigeration cooling versus other cooling options, such as high flow air-cooling or various water-cooling schemes, focused on the system performance improvement realized with the refrigeration system. Bulk power for the system, which is shown at the top of the frame, distributes 350 VDC throughout the frame. Below the bulk power is the central electronic complex (CEC) where the MCM, housing 12 processors, is located.

Various electronic ''book'' packages (memory, control modules, dc power supplies, etc.) are mounted on each side of the processor module. Below the CEC are blowers that provide air-cooling for all the components in the CEC except the processor module, which is cooled through refrigeration. Below the blowers are two modular refrigeration units (MRUs), which provide cooling via the evaporator mounted on the processor module. Only one MRU at a time runs during normal operation. Should one MRU fail, it can be replaced via quick connects located at the evaporator. Thus, a new MRU can be installed while the system continues to operate. The evaporator mounted on the processor module is redundant in that two independent loops utilizing copper tubes are interleaved through a thick copper plate, each loop attached to separate MRUs. Refrigerant passing through one loop is adequate to cool the MCM (which dissipates a maximum power of 1050 W for G4) under all environmental extremes allowed by the system.

In the bottom of the frame, the I/O electronic books are installed along with the associated blowers to provide the air-cooling. Air-cooling for the condenser located in the MRU's is provided by air exiting the I/O cage at the bottom of the frame. Airflow through the condenser as well as through the I/O cage is increased for room temperatures above 27°C. A general schematic of the various components of the vapor compression system used in the MRU are shown in Fig. 2.

Background

Evaporator and expansion valve dynamics and the instabilities associated with them have been the areas of research for many [4–31]. Numerous methods to model the evaporator have been summarized by Wang and Tauber [4] and very common methods, among others, are described in this chapter. These methods are

- distributed models
- control models
- two-zone models

Distributed models are much like finite volume computational fluid dynamics in which the evaporator is discretized into many small discrete control volumes. Control models use input–output relationships to describe components and transfer functions to predict the system response. In the two-zone models, the evaporator is divided into regions of two-phase flow and superheat. The conservation equations are then applied separately. This method generally uses the lumped parameter approach.

Distributed Models. Gruhle and Isermann [5] developed a theoretical model of a refrigerant evaporator based on the balance equations for enthalpy, mass, and momentum. They approximated distributed parameter process by using lumped parameter models to investigate the dynamic behavior of the evaporator. The transient responses were studied as the functions of manipulating signal and various disturbances. The position of expansion valve was the manipulating signal, whereas the disturbances consisted of air temperature, condenser pressure, and compressor speed. The superheating temperature was considered as the control variable to optimize the evaporator performance. They suggested the nonlinearity of the heat transfer coefficient to be a cause of random behavior. The simulations they carried out using their models indicate the oscillations of 5 Hz even for the constant input signals.

Wang and Tauber [4] developed a distributed model to optimize the evaporator performance using capacity control. Assuming that the lumped parameter models are not accurate in the case of direct expansion evaporators, they used a distributed model to gain accuracy. This distributed model was developed using a computer software program named PHOENICS. This model was not compared to any experimental data.

Jia et al. [6] tried to improve the model by Wang and Tauber by considering the effect of refrigerant pressure drop inside the evaporator. They stated that the heat stored in superheat section affects the time required by the flow to attain steady state following an increase in the flow. They focused on the transient response of the superheat to a step change in inlet flow rate and presented the distribution of refrigerant velocity, void friction, and temperature, both in space and time. They compared the responses of step increase to step decrease and showed that the response is faster for step decrease than for the step increase. Yasuda et al. [7] developed a system model to study the transient response of evaporator such as hunting. The mathematical model, which consists of compressor, condenser, thermostatic expansion valve, and the evaporator, is developed assuming linear relationship between mass flow through expansion valve and the superheat. While modeling the evaporator, the superheat region is modeled using distributed parameters and the two-phase region is simplified to the lumped parameter model. The values of evaporator pressure drop, mean

void friction, and local void friction were determined by experiment and the literature, while the maximum flow rate for the expansion valve was taken from the manufacturer's data.

Control Models. Stoecker [8] investigated the instable operations of evaporator and expansion valve. A disturbance propagates through the system and creates another disturbance when it reaches the exit. The output response lags input by 360 deg. The effect of a new disturbance will disappear if it has amplification less than one or the new disturbance is not greater than the original disturbance. However, if the amplification is grater than one or the new disturbance is greater than the original disturbance, then the feedback loop will make the operation of system unstable. According to Stoecker, the system will become more and more unstable with increase in transport lag.

Broersen and Van der Jagt [9] modeled the expansion valve by using an open loop transfer function. They used a single-input single-output feedback with refrigerant mass flow and superheat. The hunting at the evaporator, according to them, can be eliminated by decreasing the mass flow of the refrigerant and also by increasing the thermal resistance between the bulb and the evaporator. Although reduction in the mass flow of refrigerant increases the superheat and eliminates the oscillations at evaporator exit, it also reduces the efficiency of the system as cooling capacity is reduced with flow. Increasing the thermal resistance causes a problem during startup when the bulb response is expected to be fast. The slow response may cause flooding of the evaporator.

He, Liu, and Asada [10] say that the model they have developed to study vapor compression system is the first model to capture superheat signal with its dynamics. The model is a mixed lumped parameter and control model that analyzes the response of evaporating and condensing pressure and the superheat due to variation in compressor speed, fan speed and expansion valve opening. They expressed the need of multi-input multi-output methods as they found single-input single-output methods to be insufficient for the control purposes.

Two-Zone Models. Grald and MacArthur [11] believed the lumped parameter approach to be best simulation option in case of system interactions as it avoids the intensity of computations that is faced in distributed modeling. They modeled an evaporator using a lumped parameter approach. In their model, they transformed the governing equations into ordinary differential equations predicting the changing length of two-phase flow and vapor density. They observed that the superheat response is faster for step decrease in flow rate than for the step increase.

Wedekind and Kobus [12] developed a model for the system that predicts the transient response of the evaporator using a weighted average of individual passages. They used the mean void friction theory to study the thermal and flow maldistribution through multitube evaporator.

In their model, Dhar and Soedel [13] divided the evaporator into liquid and vapor regions. They combined the empirical parameters with conservation equations for analysis assuming the outlet conditions for both the control volumes to be the same as the bulk conditions within the control volumes. From their simulations they found that for large gain values the valve becomes unstable and with the lower values of gain, the valve takes longer time to reach operating condition. The gain here is the change in orifice area per change in superheat.

De Bruin, Van der Jagt, and Machielsen [14] developed a model to study hunting at the evaporator. They considered the thermal resistance of the expansion valve bulb and the offset temperature. They concluded that either increasing or decreasing the bulb resistance could reduce hunting. Considering the problems faced during startup in the case of increased resistance, they suggested decreasing the resistance.

Experimental Investigation. In his experimental investigations of refrigerant flows and the transients in fully evaporating refrigerant flows, Wedekind [15] used a heated glass tube to locate the vaporization point of refrigeration and tracked its variation with time. The two-phase region varied in the evaporator tube due to formation and propagation of a liquid slug, although the operating conditions at inlet were steady.

Barnhart [16], in his experimental study, analyzed the formation of a slug in the evaporator. He attributed the inlet flow variations at the evaporator to the slug formation and its effect on superheat and evaporator pressure. The slug causes a spike in pressure at the evaporator and a decrease in pressure drop across the valve. Barnhart recognized that this causes the inlet flow oscillations.

Mumma [17] designed a 26-foot-long evaporator to study the flow length oscillations. He observed that temperature fluctuations at the boundary of the two-phase region completely dissipate by the time the flows reach the exit. He also predicted that the expansion valve hunting is likely when the oscillations in the two-phase region exceed the evaporator tube length. He stated that the dry-out point fluctuates even during steady operating conditions. Mumma's observation is in agreement with that of Wedekind.

Tassou and Al-Nizari [18] compared the electronic expansion valves and the thermostatic expansion valves during both cold and hot starts to see how the gain of the valve affects stability and energy efficiency of the refrigeration system. Cold start refers to starting the system after it has been off for a considerably long time, whereas the hot start refers to on–off cycling of the compressor. They report the superheat oscillations for thermostatic expansion valve they used, during the cold start from 1 to 12°C, and during hot start from 6 to 10°C. The frequencies were 0.008 and 0.006 Hz, respectively.

Thermostatic Expansion Valve: Static Model

Ding, Agonafer, and Schmidt [19] presented a static model of the thermostatic expansion valve in which they developed a correlation to determine refrigerant mass flow rate through the thermostatic expansion valve based on the evaporating temperature, condensing temperature, the superheat, and liquid subcooling. This approach was preferred since these temperatures can be easily measured.

The refrigerant mass flow rate through the thermostatic expansion valve can be calculated by using the following expression, which is derived from the Bernoulli's equation:

$$G = \sqrt{\rho_1 \Delta p} A \tag{1}$$

In the above expression,

$$\Delta p = f_1(T_{cond}, T_{evap}) \tag{2}$$

$$\rho_1 = f_2(T_{cond} - T_{sub}) \tag{3}$$

$$A = f_3(T_{evap}, \Delta T_{sp}) \tag{4}$$

For constant evaporator and condensing temperature, the area of opening and hence the mass flow rate of the refrigerant through the thermostatic expansion valve depends on the superheat.

This superheat can further be divided into two parts: the static superheat (ΔT_{stsp}) and the opening superheat (ΔT_{opsp}). The static superheat is the superheat at no load that ensures sufficient spring force to keep the valve closed. The opening superheat is the increase in superheat required to open the valve to match the load, as shown in Fig. 3. It is shown that the open area of the valve depends upon the opening superheat.

Figure 4 shows an approximate linear relationship of refrigerant mass flow rate and opening superheat for constant pressure drop across the thermostatic expansion valve and subcooling at a certain evaporating temperature. When pressure drop and subcooling is constant, the refrigerant mass flow rate is proportional to the area (A). This relationship also applies to valves with different capacities. The orifice used determines the capacity curve of the valve.

In Fig. 4, one will notice a maximum flow rate exits, which corresponds to maximum kiloamperes. For a specific valve, when the pressure difference on the two sides of diaphragm is larger

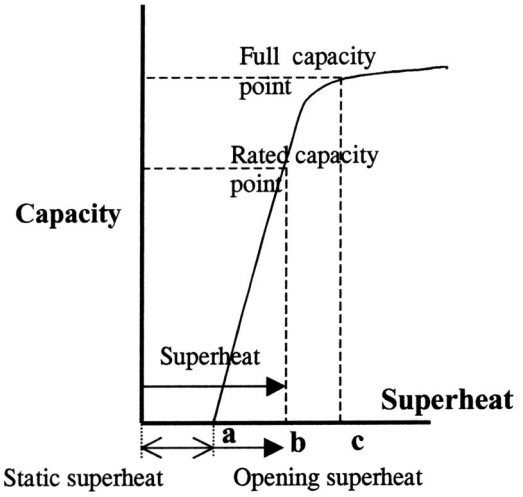

Fig. 3 Definition of static superheat and open superheat

than a certain value, A will no longer increase, stopping the increase of the refrigerant mass flow rate. The maximum pressure difference is determined by the valve configuration and characteristics of the spring. Corresponding to the maximum pressure difference, there is a maximum open superheat.

Minimum Stable Superheat

In 1988, Christensen and Robinson [20] studied the flow of refrigerant through the suction line of a typical vapor compression system. They observed the behavior of the refrigerant in the evaporator at a given capacity. During the experiment (Fig. 5), temperature probes T1 and T2 were placed at inlet and outlet of the evaporator to measure the superheat across the entire evaporator. It was found that by moving T2 closer to T2A, the temperature difference dropped as the liquid front was approached. Further, moving T2 even closer to T2B, some temperature fluctuations were seen. These temperature fluctuations were caused by T2B sensing both liquid droplets and vapor. The point just before the fluctuations were seen was defined as the minimum stable superheat point (MSS). It was observed that at MSS the highest efficiency was achieved for a given load condition. It was

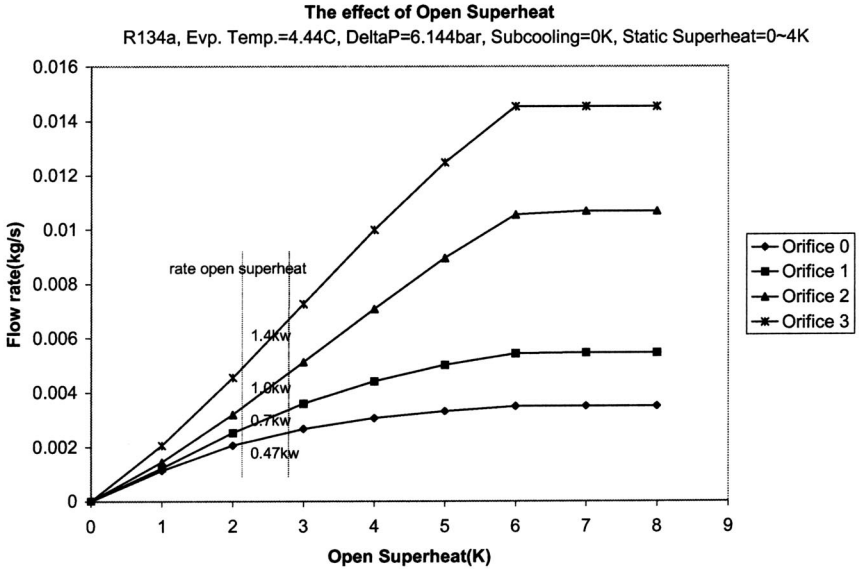

Fig. 4 Relationship of mass flow rate versus opening superheat for a constant pressure drop

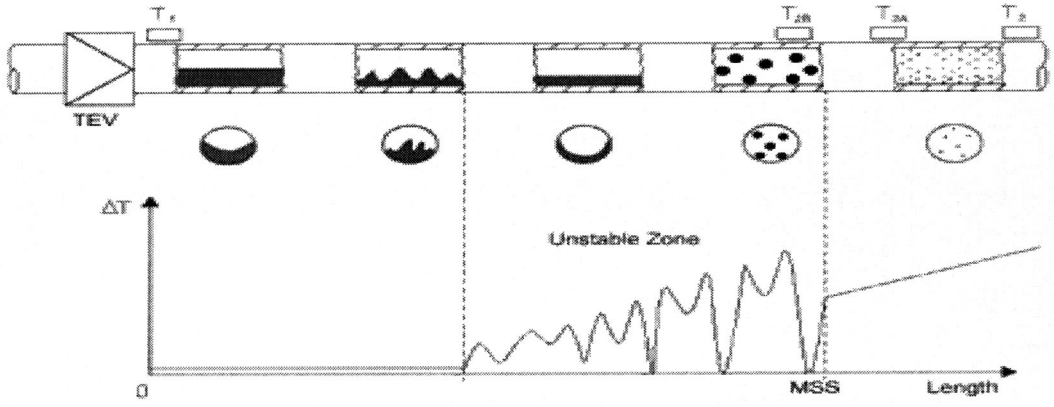

Fig. 5 Behavior of refrigerant inside the evaporator

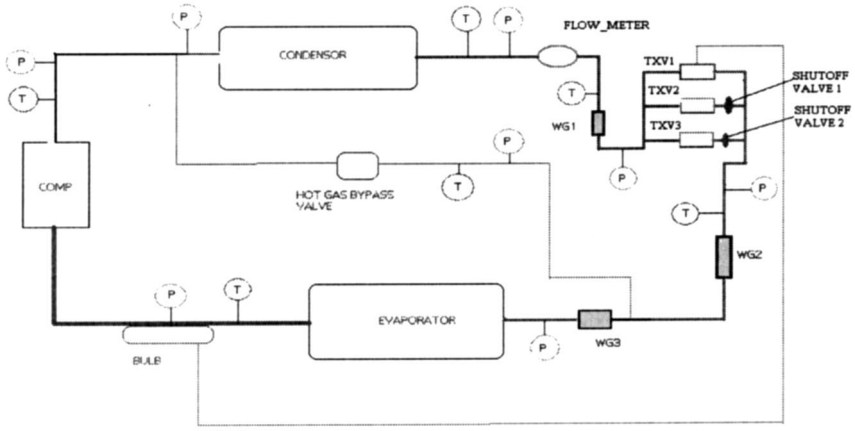

Fig. 6 Schematic of experimental bench

concluded that the evaporator is most efficient at the MSS point because this is the point at which all of the refrigerant has finished evaporating.

Evaporator Time Constant

Considerable amount of work has been done to investigate the hunting phenomena. Wedekind and Stoecker [21] formulated a theoretical model to predict the mean transient response of the mixture vapor transition point under sudden change in refrigerant mass flow rate. Two equations have been derived, one describing the mixture vapor behavior under step decrease in refrigerant inlet mass flow rate and the other describing the step increase [22]. The time constant associated with step decrease is the time required to evaporate all the excess refrigerant under the assumption that the rate of heat transfer to the excess refrigerant remains constant. The time constant associated with a step increase is defined as the time required to overcome the refrigerant shortage provided the rate of inlet mass remains constant. The time constant was reported to be in the order of 6 s. Danning [23] reported an evaporator time constant of 3.9 min.

A mathematical model to determine the time constant is presented. The evaporator and thermostatic expansion valve are assumed to be dynamic and the condenser and the compressor are neglected. It is assumed that the time lag is caused by the thermal resistance of the refrigerant vapor, tube wall, bulb wall, and bulb contents, as well as the thermal capacities of tube wall, bulb wall, and bulb contents.

Applying energy balance across evaporator and the bulb, energy stored in the bulb equals energy coming in the bulb from the evaporator:

$$(m_l c_{p_l} + m_c c_{p_c}) \frac{dT_b}{dt} = \left(\frac{T_b - T_R}{\frac{1}{h_l A_l} + R_{cb} + R_m + R_{cc} + R_{rad} + \frac{1}{h_R A_R}} \right) \tag{5}$$

Assuming that the temperature of the fluid inside the bulb is same as the temperature of the bulb wall and that the temperature of the refrigerant in the evaporator is same as that of evaporator wall, then

$$T_b = T_{bw} \qquad T_R = T_w \tag{6}$$

Hence Eq. (1) reduces to

$$(m_l c_{p_l} + m_c c_{p_c}) \frac{dT_b}{dt} = \left(\frac{T_b - T_R}{R_T} \right) \tag{7}$$

where

$$R_T = R_{rad} + R_m \tag{8}$$

$$R_T M_T \frac{dT_b}{dt} + T_b = T_R \tag{9}$$

where

$$M_T = \rho_l V_l C_{p_l} + \rho_c V_c C_{p_c} \tag{10}$$

$$T_b = C(t) e^{-t/R_T M_T} \tag{11}$$

$$R_T M_T \frac{d}{dt} (C(t) e^{-t/R_T M_T}) + C(t) e^{-t/R_T M_T} = T_R \tag{12}$$

$$R_T M_T C' e^{-t/R_T M_T} = T_R \tag{13}$$

$$C = \int_0^t \frac{T_R(\tau)}{R_T M_T} e^{\tau/R_T M_T} d\tau + C_1 \tag{14}$$

$$T_b = T_{bi} e^{-t/R_T M_T} + \int_0^t \frac{T_R(\tau)}{R_T M_T} e^{-(t-\tau)/R_T M_T} d\tau \tag{15}$$

which yields

$$\frac{T_b - T_R}{T_{bi} - T_R} = e^{-t/R_T M_T} \tag{16}$$

and the time constant τ is given by

$$\tau = R_T M_T \tag{17}$$

The Experimental Bench

Figure 6 shows a schematic of the experimental bench and Fig. 7 shows a picture of the actual experimental setup.

The schematic shows the four main components of the refrigeration system: the compressor, the condenser, the thermostatic expansion valve, and the evaporator. The evaporator has to be maintained at 15°C irrespective of changes in the load conditions. In order to avoid undershooting of evaporator temperature at 15°C with a sudden decrease in load, a hot gas bypass valve is installed in the system. As soon as the evaporator temperatures drops below 15°C due to sudden decrease in the load, the hot gas bypass valve opens and allows the hot refrigerant at the condenser inlet to directly enter the evaporator thereby bypassing the condenser and expansion valve. When the temperature of the evaporator is raised

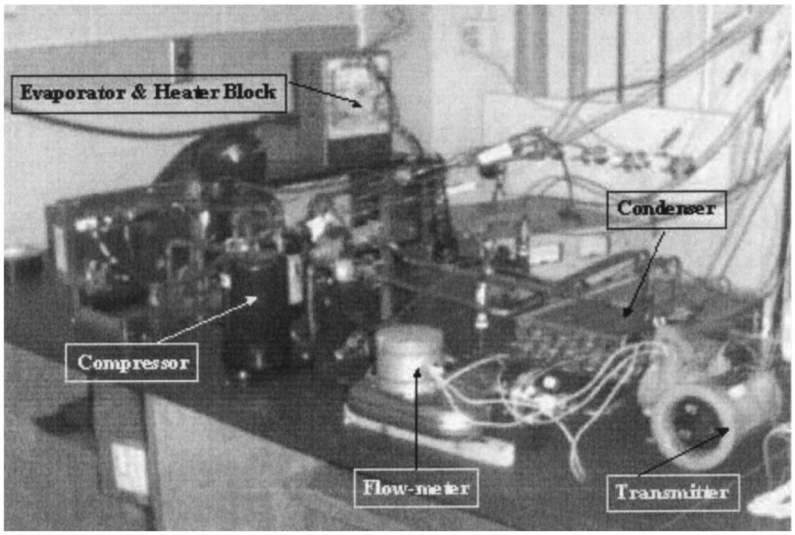

Fig. 7 Actual experimental setup

to 15°C, the hot gas bypass valve closes and the cycle continues its normal working conditions. The hot refrigerant vapor enters the air-cooled condenser. Air is blown over the single-circuit condenser with the help of a blower. The refrigerant then passes through a flow-meter that can quantify the flow rate of the refrigerant flowing through the system during normal working conditions. A bypass valve is installed just before the flow-meter just in case it is required to bypass the flow-meter when the flow readings are not being taken. The condensed refrigerant from the condenser enters the thermostatic expansion valve. The experiments were initially planned for three different types of expansion valves EQ2-JC, EQ2-JCP60, and EQ2-JZPM. These expansion valves are of the same sizes but differ in bulb properties, bulb fluids and response times. In order to facilitate experiments on all three expansion valves, the three valves were placed in parallel in the circuit, thus allowing any one valve to be operated at a time, while the other two are shut off using shutoff valves.

Effect of Bulb Location. In order to validate the Christensen and Robinson theory [20], five different bulb locations, namely, C, B, A, A1, and A2 distributed uniformly on the suction line were chosen. The test was conducted only on valve EQ2-JC. The other two valves were shut off during the entire operation of the experiments. The effect of change in the bulb location on the system stability was conducted for five different load conditions: no load (0 W), 250 W, 500 W, 750 W, and full load (1000 W). Figure 8 shows the bulb locations on the suction line. System instability is a direct function of superheat variation. The larger the superheat variation, more unstable is the system. Thus, in order to determine the system stability at different load conditions, superheat variation was studied. Previous studies have noted that as the load increases the system tends to become more stable. Similar results were found during the experiments. The first set of experiments were conducted at location C, the system load was varied from 0 W (no-load condition) to 1000 W (full-load condition) all other

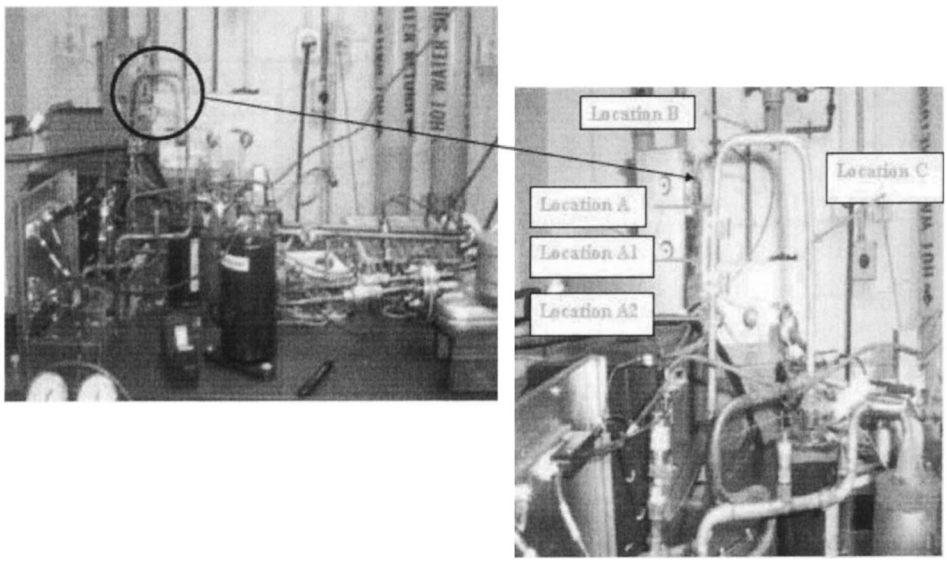

Fig. 8 Bulb locations C, B, A, A1, and A2 on the suction line

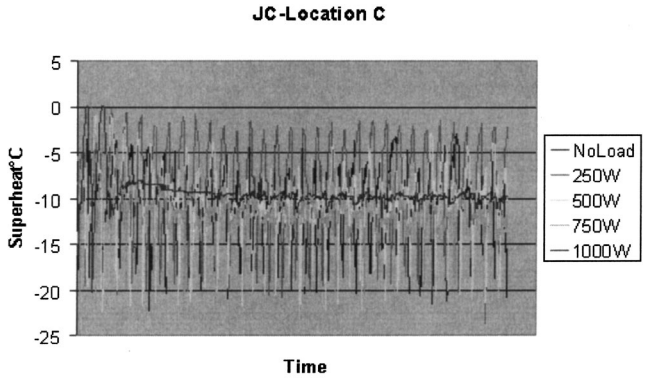

Fig. 9 Variation of evaporator outlet superheat; bulb location C

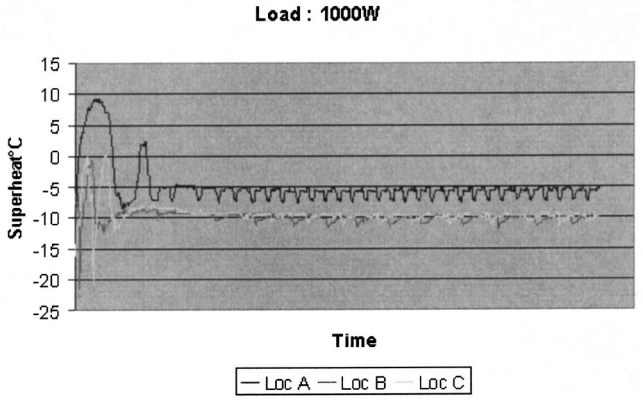

Fig. 12 Effect of change in bulb location at 1000 W load for locations A, B, and C

parameters were kept the same. Figure 9 shows the results for TXV EQ2-JC with bulb located at position C and load varied from no load to full load. Superheat variation was plotted against time.

Figure 9 shows the superheat variation at location C. It can be observed that as the load is increased from 0 to 1000 W, the system stability gradually increases. At the full-load condition, the system is most stable. At 1000 W it can be observed that superheat variation is within 2°C. Similar observations were made at locations B and A, which are presented in Fig. 10 and Fig. 11, respectively. Again it is seen that the system is most stable at full-load condition and the system becomes more and more unstable as we decrease the load.

Another important observation made was that as the bulb was moved from location C to A, each time the system became increasingly stable indicating that we were approaching the MSS point, the point of maximum system stability. This can be observed by looking at Figs. 12–15. These figures show that variation of superheat for all three bulb locations at full-load conditions. Similar results were observed at 250 W and 0 W load, but are not shown here.

Although the fact that the change in bulb location from C to A increases the system stability is not very clear from Fig. 12, the subsequent figures make it more convincing. Moreover, it was

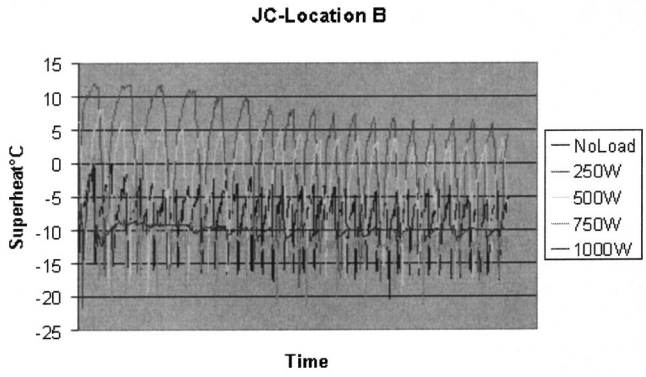

Fig. 10 Variation of evaporator outlet superheat; bulb location B

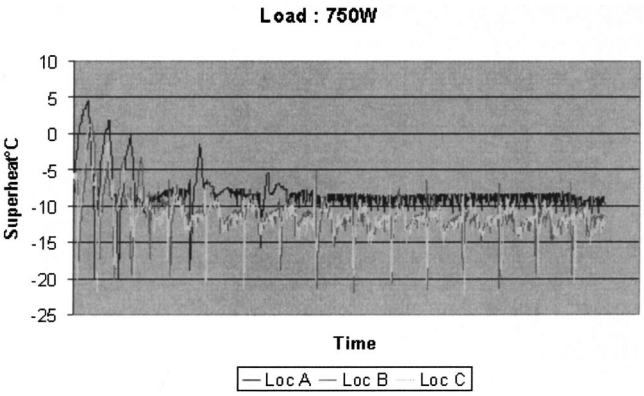

Fig. 13 Effect of change in bulb location at 750 W loads for locations A, B, and C

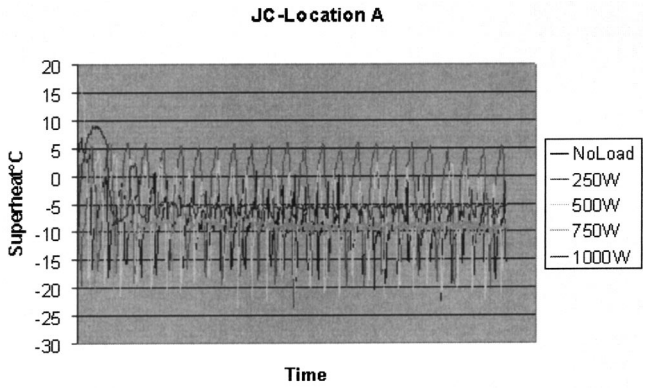

Fig. 11 Variation of evaporator outlet superheat; bulb location A

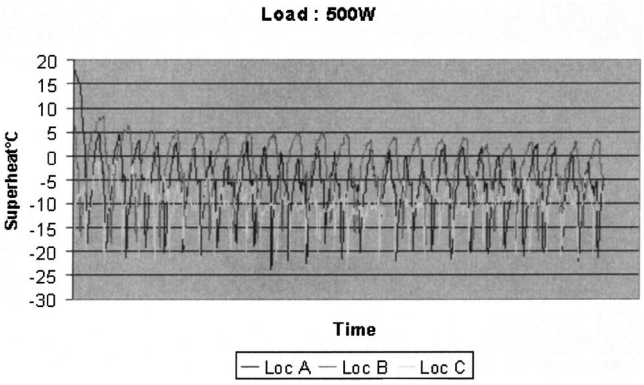

Fig. 14 Effect of change in bulb location at 500 W load for locations A, B, and C

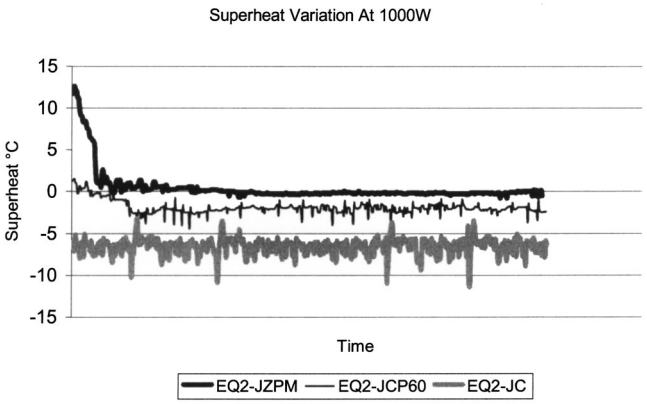

Fig. 15 Superheat variation at 1000 W

observed that below 500 W the system was highly instable, but behaved in the way similar to that mentioned above. In order to get a better idea of the location of MSS, two more trials were conducted at locations A1 and A2 similar to those mentioned above. It was observed that the system instability increased as we move away from A in the direction of A2. This showed that the MSS point should be somewhere close to location A. Although it is very difficult to find the exact position of MSS point, some more trial runs can be conducted by placing the bulb in the vicinity of location A to get a better idea of location of MSS point.

Although not of much relevance here, the interface temperature between the heater block and evaporator was also recorded to check if the system is cooling enough to keep the module temperature within acceptable limits. Figure 16 shows the variation of interface temperature for location A at 1000 W. It was seen that the interface temperature in all the cases was close to 40°C. This means that the system operates stably by maintaining the module temperature at 40°C.

Effect of Thermophysical Properties of Sensor Bulb. Three different thermostatic expansion valves are used to study the effect of thermophysical properties of sensor bulb on the stability of the modular refrigeration unit. Manufactured by Sporlan Valve Company, all the three valves are of $\frac{1}{2}$-ton capacity. The bulb size and time constant for each bulb, calculated using Eq. (17) are listed in following table.

Effect of Superheat. The control ability of the thermostatic expansion valve is greatly influenced by the variation in superheat. The working superheat of 5–8°C is common in commercial vapor compression system. The data represented by Figs. 12–14 indicate that the variation in superheat is more for lower heat

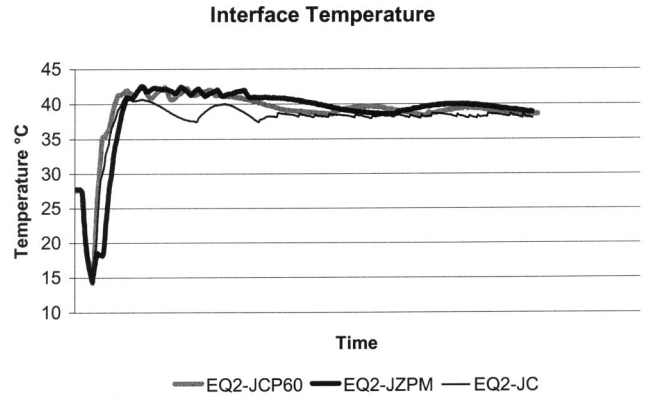

Fig. 16 Variation in interface temperature

Table 1 Bulb dimensions and time constants

Valve	Bulb dimensions (Outer diameter×L) [mm]	Time constant [sec]
JC	9.5×75	6.98
JCP60	12.75×76	13.54
JZPM	19×50	19.20

loads, and this is true for all the three thermostatic expansion valves. The evaporating process is a constant flux heat transfer-like process and the wall temperature responds very quickly to the disturbance caused by the heat load changes. The response of thermostatic expansion valve to these changes is, however, slower and hence the disturbances cannot be fully suppressed.

The superheat variation is least at the full-scale heat load (1000 W) and the oscillations increase as the load is reduced in steps (750 W, 500 W, 250 W). The valve EQ2-JZPM, however, yielded most stable results.

Effect of Bulb Time Constant. The sensor bulb of the thermostatic expansion valve located at evaporator outlet senses the superheat and sends the signal to expansion valve, controlling the opening of expansion valve and hence the flow of refrigerant through it. Increase in bulb temperature will cause the valve to open further accommodating more flow, whereas with a decrease in the bulb temperature, valve will close and the flow will be restricted. The rate at which the bulb responds to the outlet conditions is a function of thermal resistance of the bulb, contact area, and bulb mass.

Figures 17–19 show the bulb temperatures and evaporator outlet temperature. The bulb response lags to the evaporator outlet temperature. The bulb temperature starts to rise in response to the rising outlet temperature. It, however, continues to rise even when the outlet temperature has ceased to rise and started to decline. After some time, the bulb temperature starts falling and continues to fall even if the outlet temperature has begun to rise again after reaching the minimum.

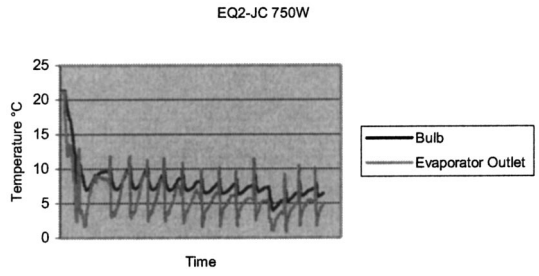

Fig. 17 Bulb and evaporator exit temperature for Valve EQ2-JC

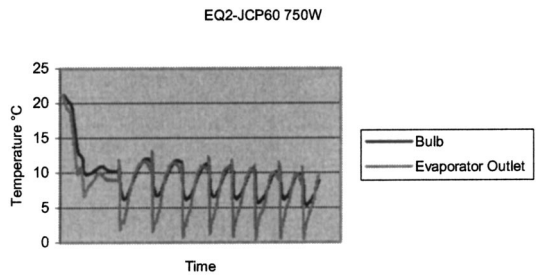

Fig. 18 Bulb and evaporator exit temperature for Valve EQ2-JCP60

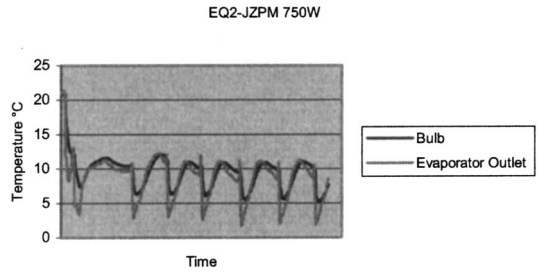

Fig. 19 Bulb and evaporator exit temperature for Valve EQ2-JZPM

This lag in the response is more for the bulb with higher thermal resistance. The bulb size affects the thermal resistance of the bulb. With higher thermal resistance, the expansion valve constants increase and improve the stability of the system. The data is in accordance with these statements as the expansion valve EQ2-JZPM has the highest thermal resistance and hence the time constant while the valve EQ2-JC has the lowest time constant. The response lag for EQ2-JZPM is longer than EQ2-JCP60 and EQ2-JC. Also it shows better stability.

Comments

The S/390 G4 CMOS system was dissembled and an experimental bench was built to study the effects of change in thermostatic bulb location on the stability of the S/390 G4 CMOS system. Although the valve studied is not used in current systems, the testing and analysis with this valve are valuable in understanding the operation and control aspects of the refrigeration system [32]. The system stability is sensitive to thermostatic bulb location. There exists a point in the suction line at which the superheat variation is the least. This point is defined as the MSS point (minimum stable superheat). If the bulb is placed exactly at this point then the superheat variation is the least and the system operation is most stable. A mathematical model for determining the bulb time constant was obtained. We can conclude that there has to be a critical time constant. at which the system stability remains unchanged. The thermal resistance between the bulb and evaporator can considerably affect system stability and by increasing this thermal resistance, the stability can be further improved. Similarly, the size of the bulb and the two-phase heat transfer coefficient have an effect on the system stability.

Nomenclature

A = effective passage
A_l = area for convective heat for refrigerant in the tube
A_R = area for convective heat for refrigerant in the tube
C_{p_c} = specific heat of copper
C_{p_l} = specific heat of liquid in bulb
G = mass flow rate
R_{cb}, R_{cc} = contact resistance for bulb and copper tube
R_m = resistance of insulation
R_{rad} = radiative thermal resistance
T_b = temperature of the bulb
T_{cond} = condensation temperature
T_{evp} = evaporation temperature
ΔT_{opsp} = opening superheat
T_R = temperature of refrigerant in the tube
ΔT_{sp} = superheat
ΔT_{stsp} = static superheat
ΔT_{sub} = subcooling
V_c = volume of copper tube
V_l = volume of liquid in bulb
h_l = coefficient of convective heat transfer for liquid in bulb
h_R = coefficient of convective heat for refrigeration in the tube
k = constant related to thermostatic expansion valve design
m_c = mass of copper tube
m_l = mass of liquid
Δp = pressure drop across valve
ρ_l = entrance liquid density
τ = time constant

References

[1] Schmidt, R., 2000, "Low Temperature Electronic Cooling," Electronics Cooling Magazine, **6**, No. 3.
[2] Laxminarayan, V., 2000, "What Causes Semiconductor Devices to Fail," Test and Measurement Europe.
[3] Needham, Prunty, and Yeoh, 1998, "High Volume Microprocessor Test Escapes, An Analysis of Defects Our Tests are Missing," *International Test Conference*, pp. 25–34, IEEE, Los Alamitas, CA.
[4] Wang, H., and Tauber, S., 1991, "Distributed and Non-Steady State Modeling of an Air Cooler," Int. J. Refrig., **14**, pp. 98–111.
[5] Gruhle, W. D., and Isermann, R., 1985, "Modeling and Control of a Refrigerant Evaporator," J. Dyn. Syst., Meas., Control, **107**, pp. 235–240.
[6] Jia, X., Tso, C. P., Chia, P. K., and Jolly, P., 1995, "A Distributed Model for Prediction of the Transient Response of an Evaporator," Int. J. Refrig., **18**, pp. 336–342.
[7] Yasuda, H., Touber, S., and Machielsen, C. H. M., 1983, "Simulation Model of a Vapor Compression Refrigeration Systems," ASHRAE Trans., **89**, No. 2, pp. 408–425.
[8] Stoecker, W. F., 1966, "Stability of an Evaporator-Expansion Valve Control Loop," ASHRAE Trans., **72**, No. 2, pp. IV.3.1–IV.3.8.
[9] Broersen, P. M. T., and Van der Jagt, M. F. G., 1980, "Hunting of Evaporators Controlled by a Thermostatic Expansion Valve," J. Dyn. Syst., Meas., Control, **102**, pp. 130–135.
[10] He, X., Liu, S., and Asada, H., 1997, "Modeling of Vapor Compression Cycles for Multivariable Feedback Control of HVAC Systems," J. Dyn. Syst., Meas., Control, **119**, pp. 183–191.
[11] Grald, E., and MacArthur, J., 1992, "A Moving-Boundary Formulation for Modeling Time-Dependent Two-Phase Flows," Int. J. Heat Fluid Flow, **13**, pp. 266–272.
[12] Wedekind, G. L., and Kobus, C. J., 1994, "Modeling Thermally Governed Transient Flows in Multitube Evaporating Flow Systems With Thermal and Flow Distribution Asymmetry," J. Heat Transfer, **116**, pp. 503–505.
[13] Dhar, M., and Soedel, W., 1979, "Transient Analysis of a Vapor Compression Refrigeration Systems: Part I—The Mathematical Model," *Proc. XVth International Congress of Refrigeration*, pp. 1035–1048.
[14] De Bruijn, M., van der Jagt, M., and Machielsen, C., 1979, "Simulation Experiments of a Compression Refrigeration System," *Proceedings IMACS Congress Simulation of Systems*, pp. 645–653.
[15] Wedekind, G. L., 1965, "Transient Response of the Mixture-Vapor Transition Point in Two-Phase Horizontal Evaporating Flow," Ph.D. thesis, University of Illinois at Urbana-Champaign.
[16] Barnhart, J. S., "An Experimental Investigation of Flow Patters and Liquid Entertainment in a Horizontal-Tube Evaporator," Ph.D. thesis, University of Illinois at Urbana-Champaign.
[17] Mumma, S., 1971, "Predicting the Dynamic Response Characteristics of a Refrigerant Evaporator," M.S. thesis, University of Illinois at Urbana-Champaign.
[18] Tassou, S. A., and Al-Nizari, H. O., 1993, "Effect of Refrigerant Flow Control on the Thermodynamic Performances of Reciprocating Chillers," Appl. Energy, **45**, pp. 101–116.
[19] Ding, Y., Agonafer, D., and Schmidt, R., 2000, "Mathematical Model for Thermostatic Expansion Valve," IMECE, Orlando.
[20] Christensen, J., and Robinson, M., "TXV Hysterisis and Evaporator Characteristics," www.arcnews.com/CDA/ArticleInformation/BNP_Features_Item/0,1338,19555,00.html
[21] Wedekind, G. L., and Stoecker, W. F., 1966, "Transient Response of the Vapor Transition Point in Horizontal Evaporator Flow," Fourth Technical Session of the ASRAE 73rd Annual Meeting, Toronto, Canada.
[22] Ibrahim, G. A., 1998, "Theoretical Investigation Into Instability of a Refrigeration System With an Evaporator Controlled by a Thermostatic Expansion Valve," Can. J. Chem. Eng., **76**.
[23] Danning, P., 1992, "Liquid-Feed Regulation by Thermostatic Expansion Valve," Journal of Refrigeration, **52**, No. 5.
[24] Jolly, P. G., Tso, C. P., Chia, P. K., and Wong, Y. W., 2000, "Intelligent Control to Reduce Superheat Hunting and Optimize Evaporator Performance in Container Refrigeration," HVAC&R Res., **6**, No. 3, pp. 243–255.

[25] Kulkarni, A., Mulay, V., Agonafer, D., and Schmidt, R., 2002, ''Effect of Thermostatic Expansion Valve Characteristics on the Stability of Refrigeration System Part-I,'' *Transactions of ITHERM 2002*, San Diego.
[26] Kulkarni, A., Agonafer, D., and Schmidt, R., 2003, ''Effect of Thermostatic Expansion Valve Characteristics on the Stability of Refrigeration System Part-II,'' *Transactions of INTERPACK 2003*, Maui.
[27] Huelle, R., 1967, ''Heat Load Influences Upon Evaporator Parameters,'' International Congress of Refrigeration, Madrid, (3.32), pp. 985–999.
[28] Huelle, Z. R., 1967, ''Thermal Balance of Evaporator Fed Through Thermostatic Expansion Valve,'' XII International Congress of Refrigeration, Madrid, (3.33), pp. 1001–1010.
[29] Huelle, Z. R., 1972, ''The Mass-Line—A New Approach to the Hunting Problem,'' ASHRAE, pp. 43–46.
[30] Lenger, M. J., 1998, ''Superheat Stability of an Evaporator and Thermostatic Expansion Valve,'' Master's thesis, University of Illinois, Urbana-Champaign.
[31] Heat/Piping/Air Cond., 1990, **62**, No. 7.
[32] Dr. Roger Schmidt, IBM (private communication).

Impact of Area Contact Between Sensor Bulb and Evaporator Return Line on Modular Refrigeration Unit: Computational and Experimental

Saket Karajgikar

Nikhil Lakhkar

Dereje Agonafer
Fellow ASME
e-mail: agonafer@uta.edu

Mechanical and Aerospace Department,
The University of Texas at Arlington, Arlington,
TX 76010

Roger Schmidt
Fellow ASME
IBM Corporation, Poughkeepsie, NY

In the past, virtually all commercial computers were designed to operate at temperatures above the ambient and were primarily air-cooled. However, researchers have always known the advantages of operating electronics at low temperatures. This facilitates faster switching time of semiconductor devices, increased circuit speeds due to lower electrical resistance of interconnecting materials, and reduction in thermally induced failures of devices and components. Depending on the doping characteristics of the chip, performance improvement ranges from 1% to 3% for every 10°C lower transistor temperature can be realized. The IBM S/390 high-end server system is the first IBM design which uses a conventional refrigeration system to maintain the chip temperatures below that of comparable air-cooled systems, but well above cryogenic temperature. In previous work, the focus was to study the effect of variation of evaporator outlet superheat on the flow through thermostatic expansion valve at varying evaporator temperature. The effect of change in bulb location and effect of bulb time constant on the hunting at the evaporator has been reported. The effect of area contact on the stability of the system is been predicted theoretically. Mechanical analysis is performed in order to check the stresses induced. The evaporator return line and the sensor bulb are simply attached. The effect of area contact is further studied experimentally on an experimental bench.
[DOI: 10.1115/1.1839585]

Introduction

With the strong move towards complementary metal-oxide-semiconductor (CMOS) chip technologies, cooling has now become a strong influence on computer performance [1]. It is known that mobility, which is a ratio of electron or hole velocities to electric field, is a function of temperature. Mobility increases as temperature decreases due to a reduction of carrier scattering from thermal vibrations of the semiconductor crystal lattice. In addition, there is an exponential reduction in leakage currents [1].

Reliability of a microelectronic system is the probability that the system will be operational within acceptable limits for a given period of time [2]. Reliability of an electronic component is inversely proportional to its temperature. The reliability of a silicon chip decreases by about 10% for every 2°C of temperature rise [3]. In addition, many wear-out failure mechanisms follow the Arrhenius [4] equation showing that for die temperatures operating in the range of −20 to 140°C, a decrease in temperature significantly reduces the failure rate. Therefore, a significant improvement could be achieved in chip failure rates with lower temperatures achievable through electronic cooling [1].

For increased reliability, improved performance, and to maintain the chip temperatures below functional limits, a number of computer companies have shown interest in low temperature cooling technology during the last few years [1]. This paper focuses on IBM's S/390 mainframe, which uses conventional refrigeration system to maintain low temperature, but well above cryogenic temperature.

Manuscript received May 6, 2004; revision received September 19, 2004. Review conducted by: C. Amon.

Background

The IBM S/390 G4 CMOS system [1], first shipped in 1997, can have 12 processing units, up to two levels of cache, and the bus-switching logic packaged in a single multichip module (MCM) on one processor board. This delivers performance comparable to that of an IBM 9021-711 bipolar system, in which the corresponding logic occupies 56 MCMs on 14 boards. This system was unique in that it was the first such IBM design to employ refrigeration cooling. The decision to employ refrigeration cooling versus other cooling options, such as high flow air-cooling or various water-cooling schemes, focused on the system performance improvement realized with the refrigeration system.

Bulk power for the system, which is shown at the top of the frame in Fig. 1, distributes 350 VDC throughout the frame. Below the bulk power is the central electronic complex (CEC) where the MCM, housing 12 processors, is located. Various electronic ''book'' packages (memory, control modules, dc power supplies, etc.) are mounted on each side of the processor module. Below the CEC are blowers that provide air-cooling for all the components in the CEC except the processor module, which is cooled through refrigeration. Below the blowers are two modular refrigeration units (MRU's), which provide cooling via the evaporator mounted on the processor module. Only one MRU at a time runs during normal operation. Should one MRU fail, it can be replaced via quick connects located at the evaporator. Thus, a new MRU can be installed while the system continues to operate. The evaporator mounted on the processor module is redundant in that two independent loops utilizing copper tubes are interleaved through a thick copper plate, each loop attached to separate MRU's. Refrigerant passing through one loop is adequate to cool the MCM (which dissipates a maximum power of 1050 W for G4) under all environmental extremes allowed by the system.

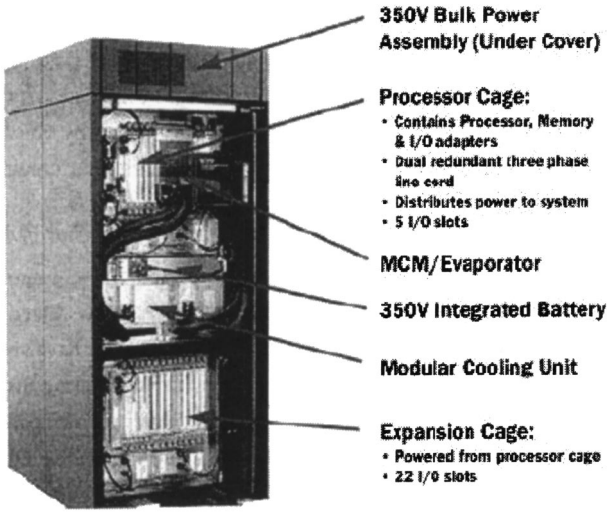

Fig. 1 IBM S/390 G4 CMOS system [9]

In the bottom of the frame, the I/O electronic books are installed along with the associated blowers to provide the air-cooling. Air-cooling for the condenser located in the MRU's is provided by air exiting the I/O cage at the bottom of the frame. Air flow through the condenser as well as through the I/O cage is increased for room temperatures above 27°C. A general schematic of the various components of the vapor compression system used in the MRU are shown in Fig. 2.

The Vapor Compression System

Refrigeration is the withdrawal of heat from a substance or space so that the temperature is lower than that of the natural surroundings. The vapor compression cycle is employed in most refrigeration systems. Refer to Figs. 3 and 4. It consists of four processes:

1→2 Isentropic compression in a compressor
2→3 Constant-pressure heat rejection in a condenser
3→4 Throttling in an expansion device
4→1 Constant-pressure heat absorption in an evaporator

In an ideal vapor compression refrigeration cycle, the refrigerant enters the compressor at state 1 as saturated vapor and is compressed isentropically to the condenser pressure. The temperature of the refrigerant increases during the isentropic compression process to well above the temperature of the surrounding medium. The refrigerant then enters the condenser as superheated vapor at state 2 and leaves as saturated liquid at state 3, as a result of heat rejections to the surroundings. The saturated liquid refrigerant at state 3 is throttled to the evaporator pressure by passing it through an expansion valve. The temperature of the refrigerant drops below the temperature of the refrigerated space during this process. The refrigerant enters the evaporator at state 4 as a saturated mixture, and it completely evaporates by absorbing heat from the refrigerated space. The refrigerant leaves the evaporator as saturated vapor and reenters the compressor, completing the cycle [5].

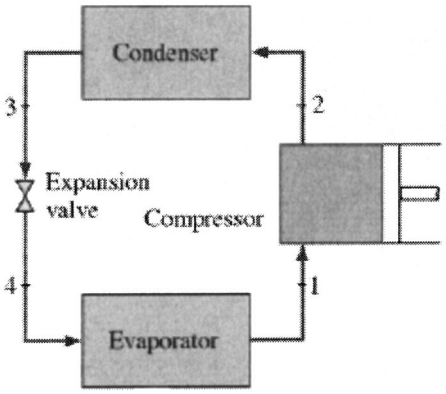

Fig. 3 Typical vapor-compression refrigeration cycle [5]

Evaporator Time Constant

Considerable amount of work has been done to investigate the hunting phenomena. Wedekind and Stoecker [6] formulated a theoretical model to predict the mean transient response of the mixture vapor transition point under sudden change in refrigerant mass flow rate. An equation was derived, describing the mixture vapor behavior under step decrease in refrigerant inlet mass flow rate and the step increase [7]. The time constant associated with step decrease is the time required to evaporate the entire excess refrigerant under the assumption that the rate of heat transfer to the excess refrigerant remains constant. The time constant associated with a step increase is defined as the time required to overcome the refrigerant shortage provided the rate of inlet mass remains constant. The time constant was reported to be on the order of 6 s. Danning [8] reported an evaporator time constant of 3.9 min [7].

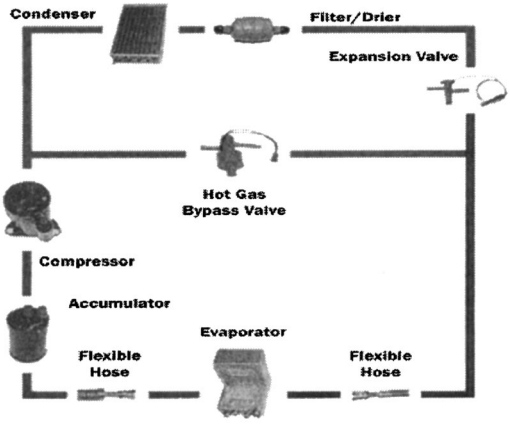

Fig. 2 Vapor compression refrigeration system [9]

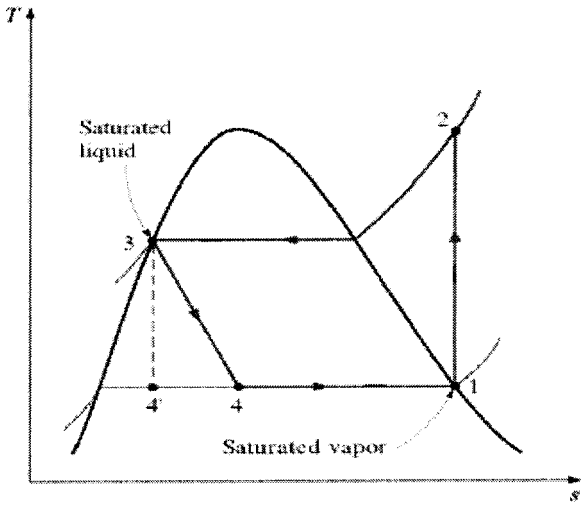

Fig. 4 *T–s* diagram for vapor-compression refrigeration cycle [5]

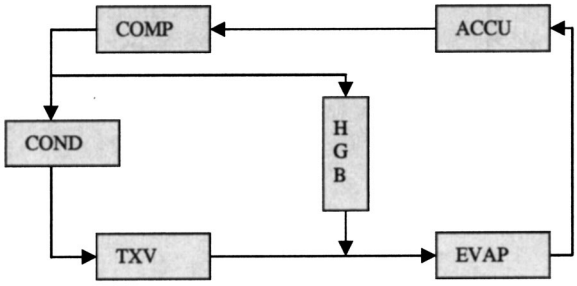

Fig. 5 Schematic diagram of experimental setup

Kulkarni [9] presented a mathematical model in which he derived an equation for evaporator time constant. Equation was derived on the assumptions that evaporator and thermostatic expansion valve are dynamic, neglecting condenser and compressor. He assumed that the time lag is caused by the thermal resistance of the refrigerant vapor, tube wall, bulb wall, and bulb contents, as well as the thermal capacities of tube wall, bulb wall, and bulb contents [9].

All the work mentioned above was based on line contact between evaporator return line and sensor bulb. This paper studies the effect of area contact between evaporator return line and sensor bulb on the stability of the system.

Operation of Modular Refrigeration Unit

Figures 5 and 6 shows the circuit diagram and experimental test bench of modular refrigeration unit. It can be seen that the compressor, condenser, thermostatic expansion valve and evaporator, accumulator, and the hot gas bypass valve are connected in the circuit. The evaporator return line and the sensor bulb surface are finely polished. The sensor bulb is placed on the evaporator return line such that polished surfaces of both are in thorough contact. The sensor bulb is attached to evaporator return line with the help of clips. Insulation tape is used to cover the bulb in order to avoid convection effects. The evaporator is controlled to a set-point of 15°C irrespective of load changes. Once the sensor bulb detects a drop in the evaporator temperature below 15°C a signal is immediately sent to the data acquisition system, which in turn activates the hot gas bypass valve. As a result, the hot gas from the compressor mixes with the low-temperature refrigerant before passing to the evaporator. As soon as the temperature rises above the set-point, the hot gas bypass valve is closed. The single-plate evaporator has a cold plate fitted on the top of it. The heater block is mounted on the evaporator with help of seven bolts. In order to improve thermal contact between the two mated areas, an interfacial thermal paste is applied between the two surfaces. The cold plate has six resistive heaters connected in parallel embedded into it which dissipate a nominal power of 1000 W. The power dissipated by the heaters can be varied from 0 W (no load) to 1000 W (full load) with the help of a rheostat. This heater block is a simulation of the MCM, which has to be cooled by the evaporator in the field. Figure 5 shows the actual experimental bench.

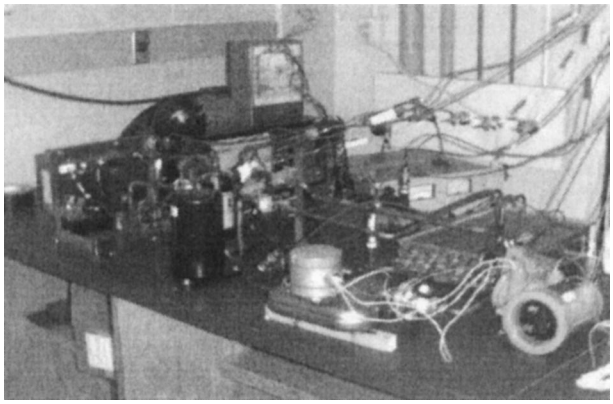

Fig. 6 Actual experimental bench [9]

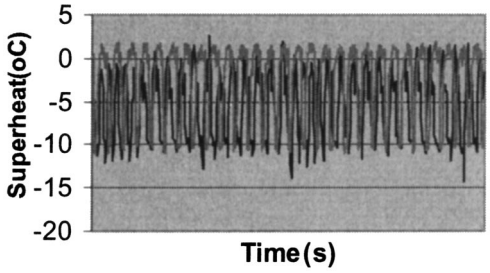

Fig. 7 750 W load superheat comparison

Measuring Instruments

The test unit was powered and controlled with the help of the standard control unit that comes along with the S/390 G4 CMOS system. The system could be remotely started and shut off using control software. Temperatures and pressures were measured at inlet/outlet of all major system components. Temperatures were measured using T-type thermocouples and pressures measured using pressure transducers. The pressure and temperatures were electronically recorded using a HP data acquisition system (DAQ). Data from the DAQ was received on a personal computer using commercial software LABVIEW 6.0 from National Instruments.

Effect of Superheat

The variation in temperature of refrigerant after its state has changed to vapor, with the addition of heat to an evaporator that has refrigerant exiting in a superheated state, leads to temperature variations resulting in what is referred to as superheat hunting. The common reasons for the superheat hunting are an oversized valve, an undercharged system, and poor bulb contact. It can be seen from the data shown in Figs. 7 through 11 that the superheat variation increases with reducing loads, i.e., it is more for lower loads and goes on decreasing as the load increases, as will be shown in Experimental Analysis section of the paper. In this paper, the effect of area contact on superheat variation is studied.

Why Area Contact

The sensor bulb of the thermostatic expansion valve located at evaporator outlet senses the superheat and signals to the expansion valve, controls the opening of expansion valve, and hence the flow of refrigerant through it. Increase in bulb temperature will cause an increase in the flow, whereas, if there is a decrease in the

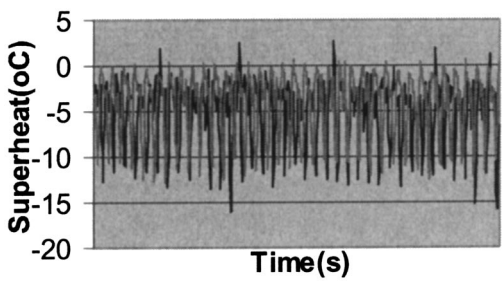

Fig. 8 1000 W load superheat comparison

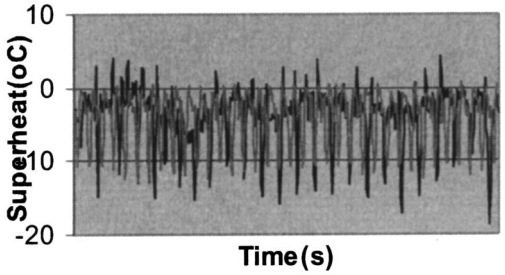

Fig. 9 Cylinders in area contact

bulb temperature, the valve will decrease the flow through the expansion valve. The rate at which bulb responds to the outlet conditions is determined by the term ''Bulb Time Constant.''

Kulkarni [9] suggested a mathematical model to determine the bulb time constant. In his work, he applied the energy balanced equation (1) across evaporator return line and bulb.

$$(m_l c_{p_l} + m_c c_{p_c}) \frac{dT_b}{dt} = \left(\frac{T_b - T_R}{\frac{1}{h_l A_l} + R_{cb} + R_m + R_{cc} + R_{rad} + \frac{1}{h_R A_R}} \right) \tag{1}$$

The solution to this equation is given by

$$\frac{T_b - T_R}{T_{bi} - T_R} = e^{-t/R_T M_T} \tag{2}$$

$$R_T = R_{rad} + R_m \tag{3}$$

$$M_T = \rho_l V_l C_{p_l} + \rho_c V_c C_{p_c} \tag{4}$$

In the above equation, the term $R_T M_T$ is nothing but the time constant; i.e., the rate at which the bulb responds and it is a function of thermal resistance of the bulb, contact area, and bulb mass. Taking this into consideration, this paper focuses on the area contact.

Effect of Area Contact

The effect of area contact on the stability of the system is first predicted computationally and then experimentally verified. In the computational analysis, ANSYS is used to predict the change in heat transfer rate with respect to change in the contact area. Further, experiments were performed to verify the results. Here, the contact area for all the trials was kept constant. In addition, a comparison is made between line contact and area contact.

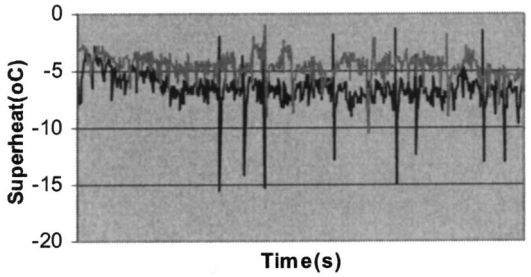

Fig. 10 Graph of heat flux versus distance between centers

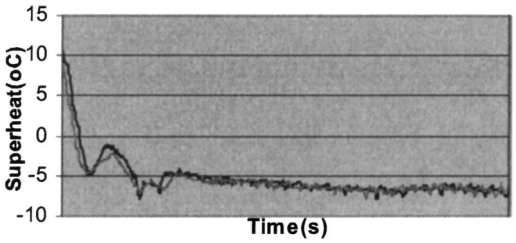

Fig. 11 Sensor bulb attached to evaporator return line

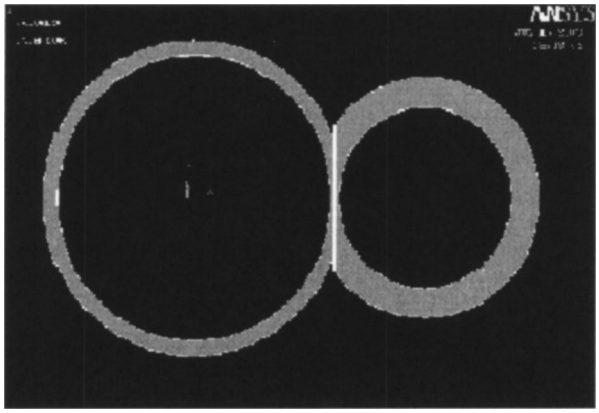

Fig. 12 No load superheat comparison

Computational Analysis. The sensor bulb of the thermostatic expansion valve located at the evaporator return line senses the superheat of the refrigerant and sends a signal to the expansion valve regulating the opening of the expansion valve and hence the amount of refrigerant entering the evaporator. Increase in the bulb temperature will cause the valve to open further accommodating more and more refrigerant in the evaporator, and vice versa. The time taken by the bulb to respond to the increase or decrease in superheat depends on the thermal resistance of the bulb, contact area, and the thermophysical properties of the fluid inside the bulb. With the bulb remaining the same, the thermophysical properties of the bulb fluid remain constant. Hence, we can say that the rate at which bulb responds to the increase or decrease in superheat depends largely on the thermal resistance, which again depends on the contact area of the bulb. Taking this as the main objective of research, a series of simulations were conducted in ANSYS. Figure 12 shows model of two cylinders in tangential contact with each other. Solid 92 was the element selected for analysis. A pressure analysis was performed considering the tube as a pressure vessel with the same shape and dimensions are they are in real. Pure copper was the material taken into consideration for the analysis. Both the ends were fixed and a pressure that was equal to the pressure, which we were getting at the evaporator return line for the line contact, was applied to it from inside.

Figure 13 shows a graph that indicates how heat transferred from the bulb to the tube varies with the change in distance between the centers. The initial temperature of bulb was taken as the atmospheric temperature, whereas for the tube, the temperature of evaporator return line was taken. It was observed that, with re-

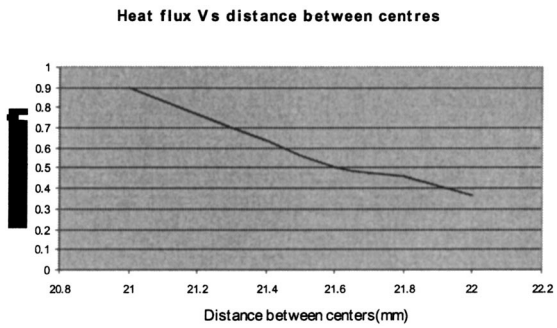

Fig. 13 250 W load superheat comparison

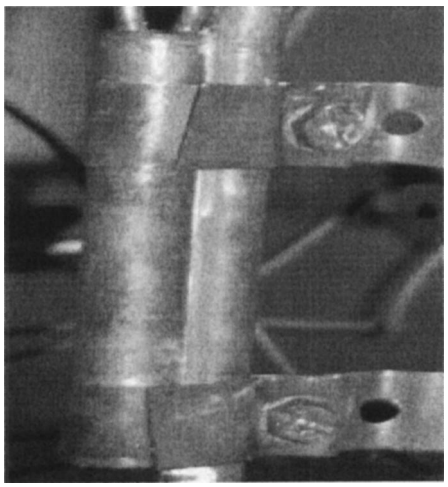

Fig. 14 500 W load superheat comparison

spect to the area contact, the heat transferred from the bulb to the tube increases significantly, which in turn means that as the distance between centers reduces, the heat transfer between them increases.

Experimental Analysis. Experiments were conducted for both line contact and area contact. The evaporator return line is polished to obtain a flat area with a surface roughness of 0.3 μm. The bulb was also polished to obtain the same surface roughness as that of evaporator return line. The bulb is attached to evaporator at the point determined by Kulkarni [9] with the help of metal clips, as shown in Fig. 14.

The heat load is varied from no load to full load (1 KW) in steps of 250 W. All other parameters were kept constant. In each case, the variation of superheat is observed. Figures 7 through 11 show the superheat variation achieved for different loads. The blue line in the graph shows superheat variation for line contact and the pink line shows superheat variation for area contact.

In Fig. 7, it is seen that superheat is within the range of 15°C for the line contact. For the area contact it can be said that for the same load, the superheat variation is less and is within the range of 13°C. Thus, the system is more stable when there is area contact between the sensor bulb and evaporator return line. Figure 8 shows the graph of the system at 250 W loads. Superheat variation is 15°C for the line contact and 12°C for the area contact. Figures 9 and 10 show the system performance at 500 W and 750 W heat load, respectively, for line and area contacts. Superheat variation is 14°C and 17°C for the line contact compared to 12°C for the area contact. Figure 11 shows that for 1000 W heat load, the system performance is almost identical. Superheat variation is within the range of 2°C after the system becomes stabilized. For both type of contacts, the system takes some initial time to stabilize.

In general, it can be seen that the system becomes more stable as the load increases and is independent of type of area contact. At no load, maximum instability is observed, while at 1000 W, maximum stability is observed.

Conclusion

An attempt was made to simulate the area contact between the bulb and the tube using ANSYS. After varying the distance between the centers, it can be concluded that as the distance between the centers decreases, the heat transferred from the bulb to the tube increases; i.e., the resistance between the bulb and the tube is reduced. This is because of a decrease in the lag between evaporator return line temperature and the sensor bulb temperature, which means that the bulb senses the superheat more quickly and hence the hunting is reduced.

From the experimental graphs, it is observed that superheat variation for the area contact is less than that for the line contact for all loads. Superheat variation for the area contact and the line contact at no load is within 13 and 15°C, respectively. In addition, from the nature of the graphs it is evident that for the area contact, the system functions more smoothly as compared to the line contact; i.e., hunting is comparatively less. The superheat variation for the line contact is within the range of 15, 20, and 17°C for 250, 500, and 750 W heat loads, respectively, while the superheat variation for area contact is within the range of 12, 14, and 12°C, respectively. At full load, system behavior is almost identical. From Figs. 7 to 11, it can be said that effect of area contact is more prominent at lower loads. Thus, it can be said that the stability of a system depends on the bulb time constant, which is a function of contact area [as per Eqs. (1)–(4)]. It can be seen that by changing the contact area, i.e., from line contact to area contact, system performance improves, and is comparatively stable. Therefore, by changing the contact area we are basically changing the bulb time constant. To control the stability of the system by changing the contact area is important, since this the only parameter that can be controlled externally. However, there is a limit to which we can polish the surfaces, the evaporator return line, and the sensor bulb. This is because (1) the bulb contains pressurized liquid and (2) the pressure is created in the evaporator return line due to flow of refrigerant.

The effect of area contact can be justified by the fact that there is lag between the evaporator return line temperature and the sensor bulb temperature. In the line contact, this lag is comparatively more than that during the area contact. The system will be fully stable when the lag between the two is zero. At that time there will be no hunting in the system. However, in practice, it is impossible to achieve this point. Whatever may be the contact area, there will be some contact resistance offered by the system. In addition, there is always a small amount of leakage to the atmosphere.

Nomenclature

A_l = area for convective heat for refrigerant in the tube
A_R = area for convective heat for refrigerant in the tube
C_{p_c} = specific heat of copper
C_{p_l} = specific heat of liquid in bulb
R_{cb}, R_{cc} = contact resistance for bulb and copper tube
R_m = resistance of insulation
R_{rad} = radiative thermal resistance
T_R = temperature of refrigerant in the tube
V_c = volume of copper tube
V_l = volume of liquid in bulb
h_l = coefficient of convective heat transfer for liquid in bulb
h_R = coefficient of convective heat for refrigeration in the tube
m_c = mass of copper tube
m_l = mass of liquid
ρ_l = entrance liquid density

References

[1] Schmidt, R., 2000, "Low Temperature Electronic Cooling," Electronics Cooling Magazine, **6**, No. 3.
[2] Tummala, R. R., ed., 2001, *Fundamentals of Micro Systems Packaging*, McGraw-Hill, New York.
[3] Bar-Cohen, A., Kraus, A. D., and Davidson, S. F., 1983, *Thermal Frontiers in the Designing and Packaging of Microelectronic Equipment*, ASME, New York.
[4] McQuiston, F. C., Parker, J. D., and Spitler, J. D., 2004, *Heating, Ventilating and Air Conditioning*, Wiley, New York.
[5] Cengel, Y. A., and Boles, M. A., 2002, *Thermodynamics An Engineering Approach-4th ed.*, McGraw-Hill, New York.
[6] Wedekind, G. L., and Stoecker, W. F., 1966, "Transient Response of the Vapor

Transition Point in Horizontal Evaporator Flow,'' *Fourth Technical Session of the ASHRAE 73rd Annual Meeting*, Toronto, Canada.
[7] Ibrahim, G. A., 1998, ''Theoretical Investigation Into Instability of a Refrigeration System With an Evaporator Controlled by a Thermostatic Expansion Valve,'' Can. J. Chem. Eng., p. 722–727.
[8] Danning, P., 1992, ''Liquid-Feed Regulation by Thermostatic Expansion Valve,'' J. Refrig.
[9] Kulkarni, A., Mulay, V., Agonafer, D., and Schmidt, R., 2002 ''Effect of Thermostatic Expansion Valve Characteristics on the Stability of Refrigeration System Part-I,'' *ITHERM 2002*, San Diego.

On the Nature of Critical Heat Flux in Microchannels

A. E. Bergles
Honorary Member, ASME, Mechanical Engineering Department, Massachusetts Institute of Technology, Cambridge, MA 02139
e-mail: abergles@aol.com

S. G. Kandlikar
Fellow, ASME, Mechanical Engineering Department, Rochester Institute of Technology, Rochester, NY 14623
e-mail: sgkeme@rit.edu

The critical heat flux (CHF) limit is an important consideration in the design of most flow boiling systems. Before the use of microchannels under saturated flow boiling conditions becomes widely accepted in cooling of high-heat-flux devices, such as electronics and laser diodes, it is essential to have a clear understanding of the CHF mechanism. This must be coupled with an extensive database covering a wide range of fluids, channel configurations, and operating conditions. The experiments required to obtain this information pose unique challenges. Among other issues, flow distribution among parallel channels, conjugate effects, and instrumentation need to be considered. An examination of the limited CHF data indicates that CHF in parallel microchannels seems to be the result of either an upstream compressible volume instability or an excursive instability rather than the conventional dryout mechanism. It is expected that the CHF in parallel microchannels would be higher if the flow is stabilized by an orifice at the entrance of each channel. The nature of CHF in microchannels is thus different than anticipated, but recent advances in microelectronic fabrication may make it possible to realize the higher power levels. [DOI: 10.1115/1.1839587]

Introduction: General Description of Microchannel Heat Exchangers

This paper will be directed toward microchannels, which invariably involve cooling channels in blocks, as opposed to mini and larger diameter channels that have individual confining walls and are usually thermally well controlled. Using commonly accepted definitions of microchannels [1,2], the hydraulic diameter D_h will be in the range 10–200 μm. The length of the flow passages, L, will be on the order of 10 000 μm. (The length will be less in the case of interrupted or ''cross-linked'' channels [3]). The channels will usually be cut in a block; for silicon, microelectronic fabrication techniques will be used [2], whereas for copper or other metals, an end mill, or a lamination-and-bonding process will be used. Typically, there will be of the order of 100 parallel channels. Heat is usually supplied to one side of the block. Assuming that the channels are cut from one side [4], a cover plate is provided on that side (Fig. 1), and inlet and exit headers couple the microchannel heat exchanger to the flow system.

The result of this arrangement is that two problems experienced in conventional heat exchangers are aggravated. The first of these is flow distribution among many parallel channels—a particularly serious concern with boiling and evaporating flows. The second is conjugate effects, circumferential and axial heat conduction in the material forming the channel. These complications make it extremely difficult to ascertain the flow in each channel, and it is virtually impossible to measure the heat flux and temperature distributions around the periphery of each channel.

It should be noted that boiling is desirable with heat sinks for cooling of electronic components, because the wall temperature is more likely to be uniform. This is due to the fact that the wall temperature is constrained to the fluid saturation temperature. In single-phase flow, the wall temperature tracks the fluid temperature, which may rise greatly at high heat input. The pressure drop is to be kept at a reasonable level, for structural reasons and to avoid wall temperature variation as the saturation temperature falls along the channel length. To minimize the pressure drop, the flow rate is so low that large heat inputs result in large enthalpy changes; thus, it is saturated boiling that is of interest. The occurrence of CHF must be regarded as an undesirable condition, as it will cause overheating of an individual channel or even the entire substrate containing the microchannels.

The main purpose of this paper is to highlight the existing CHF studies, deduce the cause of CHF, and give guidelines for new studies.

CHF in Small Diameter Tubes

Several hundred thousand CHF points have been reported in the boiling literature of the past 50 years. These data were overwhelmingly obtained with stable flow (see below) in single, thin-walled, circular tubes. The tubes were usually of uniform wall thickness, and direct electrical heating was utilized to simulate the constant heat flux boundary condition. The electric power (heat flux) was increased slowly until a vapor blanketing occurred, as evidenced by physical burnout of the tube or activation of a burnout protection device by the increased temperature. In the latter case, the power to the tube was rapidly disconnected before burnout occurred. Numerous correlations have been proposed for subcooled exit conditions (e.g., [5]) and for boiling with net vapor generation (e.g., [6]). Some studies of CHF have considered axial and/or circumferential flux tilts, usually by machining the tube. The critical heat flux condition is as well defined there as with uniform heating. Fluid heating of uniform-wall tubes has also been used (essentially simulating the uniform wall temperature boundary condition), and the CHF values are similar to those for uniform heat flux.

Single-tube CHF data are not available for microchannels, because of fabrication and instrumentation considerations. At the present time, the only alternative seems to be to derive guidance from the available CHF data in mini channels. Extensive experiments were conducted with subcooled boiling in tubes as small as $D=0.3$ mm (300 μm) [7]; however, the mass fluxes—and pressure drop—were very high. As mentioned above, the interest for microchannel heat exchangers is in even smaller channels, with bulk boiling at low mass flux and low pressure.

The modeling of saturated flow boiling CHF in microchannels under stable conditions has not received much attention in the literature. The pool boiling model by Kandlikar [8] employs an additional momentum force caused by the evaporating interface near the heater wall. The resulting nondimensional groups utilizing the evaporating momentum, inertia, and surface tension forces show promise [9]. However, accurate experimental data under stable operating conditions are essential for validating any model.

Flow Distribution in Microchannels

Two-phase heat sinks for cooling of microelectronic components will typically operate with single-phase inlet conditions. The inlet header pressure drop will, therefore, be small compared to the pressure drop in the channels (vaporization and large L/D). In spite of the fact that the outlet header has two-phase flow, the pressure drop of that header is also relatively small. The result of all this is a uniform flow distribution, provided the heat input is uniform. Even for nonuniform placement of electronic devices, the heat input at the top of the channels will tend to be uniform,

Manuscript received May 20, 2004; revision received September 22, 2004. Review conducted by: C. Amon.

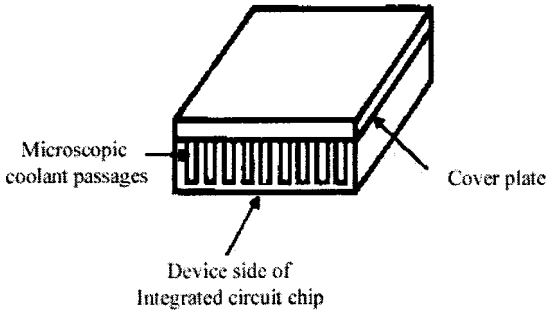

Fig. 1 Chip with integral cooling channels (see Ref. [4])

because of the use of heat spreaders or the high thermal conductivity of the channel block. The effects of persistent heat flux nonuniformities on device temperatures are considered in [3]. In general, flow distribution is not considered to be a problem with boiling microchannel heat sinks. Of course, flow distribution would be an issue if there were two-phase flow in the inlet header.

Incipient Boiling

It is important to determine whether there are any barriers to vapor formation in microchannels. There seems to be no reason why conventional theory cannot be used to predict incipient boiling in microchannels. There should be numerous imperfections on the heated surface and sidewalls that act as nucleation sites. These cavities are likely to contain a preexisting gas phase (vapor or foreign gas) with water (low wettability), but the requisite gas may be flooded out with refrigerants or fluorochemicals (high wettability). Nucleation cannot take place from a cavity unless the liquid surrounding an emerging bubble is sufficiently high in temperature.

For the low velocities encountered in microchannels, the analysis given in [10] predicts very large cavities at the point of incipient boiling. In practice, however, the large cavities called for may not be available as nucleation sites. That is, they may not exist at all or may not contain the necessary gas. As the largest, initially active nucleation site decreases in size, the superheat required to initiate boiling increases. This is not seen as a problem, though, and, with water, vapor should be formed at approximately the point where the bulk liquid temperature reaches the saturation temperature. With highly wetting liquids, the largest active cavity (one containing gas or vapor) may be quite small. Activation of that cavity will trigger a vapor bubble, which will activate larger cavities; this results in the familiar temperature overshoot and boiling curve hysteresis. There is a reduction in wall superheat at incipient boiling.

The available evidence seems to corroborate the preceding description of nucleation behavior. Bowers and Mudawar [11] reported some hysteresis in their microchannel with R-113. Jiang et al. [12] observed temperature profiles that indicated smooth vaporization of water in silicon channels of 40 or 80 μm hydraulic diameter. In a more recent study, however, Zhang et al. [13] reported unusual, reverse-temperature-overshoot behavior with water; that is, the wall temperature increased at incipient boiling. The magnitude of the temperature overshoot was reduced by etching artificial cavities into the surface. It is noted that there is precedent for such reverse-temperature overshoots with boiling of water [14].

Qu and Mudawar [15] reported a sophisticated analysis of incipient boiling in a microchannel. Their model examines the hydrodynamic and thermal conditions for bubble departure rather than simply the nucleation condition at a cavity. This is because the first bubbles in a low flow condition in a microchannel were observed to depart into the liquid flow, rather than sliding along the wall as they would in larger diameter channels employed in conventional evaporator applications. The shape of the bubbles varied depending whether the bubbles formed at the flat or corner regions of a rectangular channel. Since the bubble has already grown to a rather large size, the heat flux and wall superheat are larger than those for conventional incipient boiling. In any case, microscopic observations of bubble formation in subcooled water are in good agreement with the predictions, confirming the various assumptions in the numerical calculations. The conjugate nature of the heat flow in the copper block was acknowledged in defining the conditions for a large, stable bubble.

Conjugate Effects

There will usually be nonuniform heat flow around the circumference of a rectangular channel. This leads to preferential nucleate boiling from the channel base (heat input side), variations in heat transfer coefficient within the channel, and ultimately initiation of critical heat flux at the hottest surface. Numerous numerical studies of conjugate single-phase flow in microchannels have been carried out, but none have been reported for two-phase heat transfer. A numerical approach seems to be the only option to handle conjugate effects, as it is impossible to place temperature sensors around the circumference of a microchannel, so as to get the local wall temperature and heat flux.

As an example of the experimental difficulty, consider what it takes to get thermal information in simulated cooling channels for the plasma-facing components (PFCs) for the International Thermonuclear Experimental Reactor. Rather than use varying tube wall thickness to create the flux tilts, circular tubes are surrounded by a large block, heated over part of the outside perimeter. Boyd et al. [16,17] described a massive cylindrical test section heated over 180°C by five resistance heaters. Thermocouples placed at 48 stations give the three-dimensional distribution of the wall temperatures and heat fluxes. See Fig. 2. For reference, the tube inside diameter is 10.0 mm. The system is very complex, but it is considered capable of obtaining boiling curves around the channel circumference, including the local CHF. Earlier in the program, it was postulated that three different flow regimes could coexist within the channel: single-phase turbulent flow, subcooled flow boiling, and subcooled film boiling. Recently, Boyd et al. [17] demonstrated this coexistence.

The same phenomenon is expected in blocks with microchannels, the difference being that the small size makes it impossible to install a large number of temperature sensors around the flow channel. Implanted temperature sensors can get representative block temperatures along a channel length, but they are insufficient to calculate local heat transfer coefficients.

Character of Bulk Boiling

In conventional heated channels with bulk boiling, incipient boiling is normally followed by a progression of well-known flow patterns: bubbly flow (first at the wall, then in the core), slug flow, and annular flow (usually annular/dispersed flow). Mist flow follows CHF—that is dryout of the annular film. In microchannels, on the other hand, the bubbles depart—and the departure size is comparable to the channel width, according to the visual observations of Qu and Mudawar [15]. They then observed that there was an abrupt transition to annular flow at zero quality [18]. From a variety of published observations, Koo et al. [19] earlier concluded that bubbly flow and slug flow do not exist in microchannels; the flow goes suddenly to annular/dispersed flow. The same group concludes that a mist flow forms immediately after incipient boiling (Jiang et al., [20]; Zhang et al., [13]). It would be more reasonable, however, to envision that the wall remains wetted, perhaps with rivulets or heavy droplet deposition—until some form of dryout (CHF). Predictions of the heat transfer coefficient in annular flow are presented by Koo et al. [19] and Qu and Mudawar [18]. It should be noted that the recommendations of Tabatabai and Faghri [21] appear to be contrary to the above observations; they suggest that only flow patterns dominated by

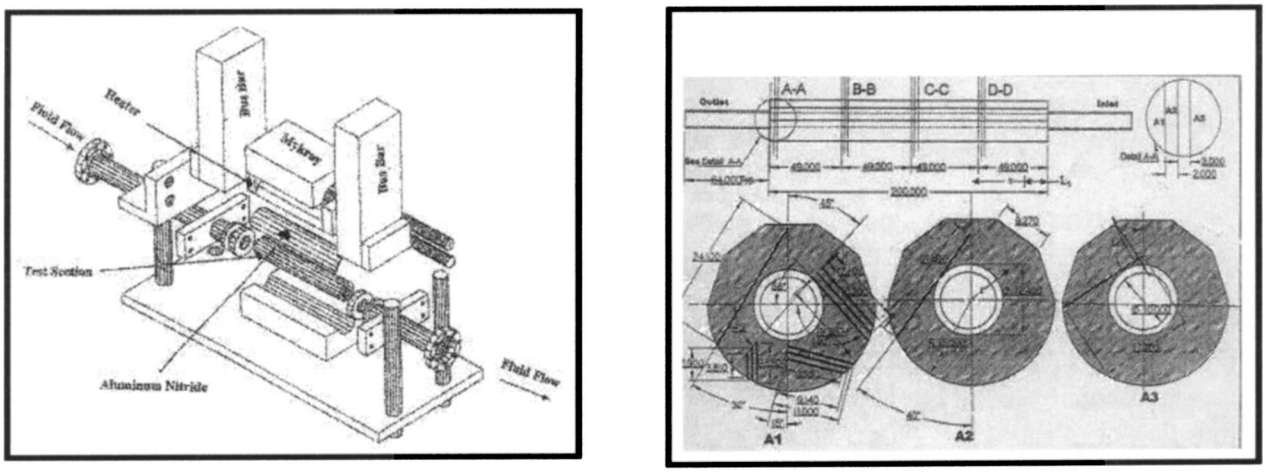

(A) (B)

Fig. 2 (*A*) Test-section cross section, (*B*) Assembly used for local temperature and heat flux measurements in a PFC simulation (see Ref. [16])

surface tension (bubble and slug) occur in tubes of 100 μm diameter. On the other hand, they do acknowledge that when the bubble size approaches the channel size (which is the case in microchannels), the result is annular flow.

The general conclusion from these studies is that annular flow is the dominant flow regime in a two-phase microchannel. It is then reasonable to suggest that the critical heat flux condition is caused by dryout of the annular liquid film. However, this may not cause failure of the cooling system, because of conduction in the microchannel block. Vapor blanketing of the portions of the channels near the heat input will lead to a major redistribution of the heat flow toward the opposite portions of the channels. If those portions are not vapor blanketed, they can efficiently accommodate the heat transfer, and no CHF will be recorded in the channel block.

An important aspect of bulk boiling is the fluctuations in flow and pressure, because these fluctuations can initiate instabilities. Two-phase-flow noise is always present in flow bulk boiling, due to bubble formation or the passage of liquid and vapor. A comprehensive discussion of fluctuations in minichannels is given by Kandlikar [22]. Pressure fluctuations, and associated temperature oscillations, seem to be associated with boiling in microchannels to a greater extent than in conventional channels. This is because the flow velocities are very low, and bubble formation can cause a significant disruption of low-quality flow. Observations of boiling in microchannels are reported by Hetsroni et al. [23]. They reported pressure drop fluctuations of about 1 kPa max and outlet temperature fluctuations of about 1°C max with the dielectric fluid Vertrel XF. Similar small-scale fluctuations were reported for water by Wu and Cheng [24].

CHF Experiments for Microchannels

The pioneering work on CHF in small channel arrays was carried out by Bowers and Mudawar [11]. They had an array of 17 circular channels, 510 μm diameter, 28.6 mm long, in a 1.59-mm-thick nickel block, heated over the central 10 mm. Although these were actually minichannels, the tests were carried out with R-113 at low mass fluxes typical of microchannels (7.0–28.2 kg/m^2 s.). Inlet pressure was 1.38 bar, and inlet subcooling ranged from 10 to 32°C. A single thermocouple monitored the average temperature of a 10 mm$\times$10 mm copper block coupling the electric heater to the block with the channels. Good conduction around the circumference of each channel was assumed, so that the heat flux was taken as the heat input divided by the channel wall area underneath the heater. Boiling curves (q'' versus $T_w - T_{in}$) were generated that terminated in well-defined critical heat fluxes. Unusually, the CHF was found to be independent of inlet subcooling, and almost directly proportional to mass flux. Although a dimensionless correlation was proposed, most of the quantities in the correlation were not varied. The bulk fluid condition at the end of the heated section was high quality or even superheated.

Jiang et al. [12] developed a microchannel heat sink integrated with a heater and an array of implanted temperature sensors. There were up to 58 or 34 channels of rhombic shape, having a hydraulic diameter of 40 or 80 μm, respectively, in the 10-mm-wide$\times$20-mm-long test section. Due to the fabrication method, there was no transparent cover plate to view the two-phase flow. CHF data were taken for once-through water entering at 20°C. It appears that the CHF condition was characterized by a rapid rise in the average of all the temperature sensors. The critical power was found to be a linear function of the total volume flow rate, which ranged from 0.25 to 5.5 ml/min, as shown in Fig. 3. Good conduction in the silicon wafers can be assumed, but it is not possible to determine the critical heat flux or the mass flux for the eight data points, because the channel cross-sectional areas are not reported by the authors.

Mukherjee and Mudawar [25] reported CHF data for ultralow

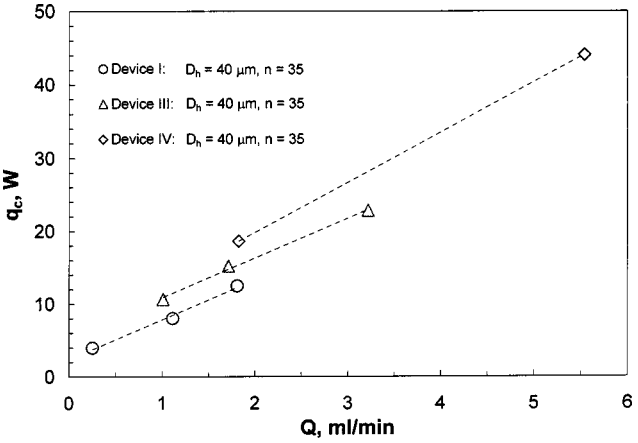

Fig. 3 Critical power dependence on total volumetric flow rate (see Ref. [12])

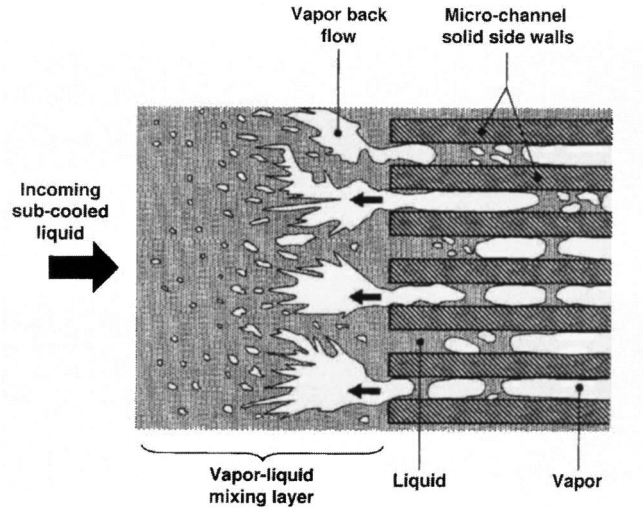

Fig. 4 Sketch of vapor backflow near CHF (see Ref. [26]); considered here to be onset of excursive instability

flow rates of water and FC-72, driven by a natural circulation thermosyphon. Both flat boiling surfaces and finned surfaces (vertical, 0.2 mm width, 0.2 mm spacing, and 0.66 mm height) were used in the 21.3×21.3 mm vertical heated surface, i.e., 53 fins. The gap width was varied from 0.13 to 21.5 mm. Thermocouples were installed to measure the fluid inlet, fluid outlet, and heater midpoint temperatures. The CHF data for the smallest gap are indicative of flow in a microchannel array; however, the data are of limited usefulness because there was no direct measurement of either the flow rate or the pressure. It is emphasized that the tests were designed primarily to demonstrate the advantages of the thermosyphon, pumpless system.

In a recent paper, Qu and Mudawar [26] report the first comprehensive study of CHF in rectangular microchannels. The heater block contained $21-215\times821$ μm channels. The heat flux was based on the heated three sides of the channel; in other words, no conjugate effects were considered. De-ionized, deaerated water was supplied over the mass flux range of $86-368$ kg/m^2 s, with an inlet temperature of 30 or 60°C and an outlet pressure of 1.13 bar. In order to eliminate upstream compressible volume instabilities, it was necessary to install a throttle valve upstream of the test section. For these typical microchannel conditions, an unusual phenomenon was observed as CHF was approached; there was vapor backflow from all of the channels into the inlet plenum. This is shown in the author's sketch, reproduced here as Fig. 4. The following correlation was developed for the 18 points of this study, as well as R-113 data from the previous study [11]

$$\frac{q''}{Gh_{\mathrm{fg}}}=33.43\left(\frac{\rho_g}{\rho_f}\right)^{1.11}\left(\frac{G^2L}{\sigma\rho_f}\right)^{-0.21}\left(\frac{L}{D_h}\right)^{-0.36} \tag{1}$$

It is noted that conventional correlations for water grossly overpredict the data, yet it is commonly observed that CHF increases with decreasing diameter. This trend is opposite to that expressed by the correlation. This fact, as well as the vapor backflow from the channel inlets (which contributed to the lack of a subcooling effect), suggests that the data do not actually characterize the real CHF of the channels.

We suggest that *all* of the CHF tests discussed above were affected by instabilities. The two major instabilities that affect microchannel heat exchangers are upstream compressible volume instability and excursive instability.

Upstream Compressible Volume Instability

When there is a significant compressible volume upstream of the heated section, an oscillating flow may lead to CHF. The compressibility could be caused by an entrained air bubble or a flexible hose, but for small channels, a large volume of degassed liquid is sufficient to cause the instability. The only investigators of microchannel heat exchangers reporting problems with upstream compressible volumes were Qu and Mudawar [26,27]. Note, though, that other studies of forced CHF used enclosed channels so that the flow behavior near CHF could not be observed. So, in those studies without an upstream throttle valve, a compressible volume instability was likely responsible for CHF. The cause of instability with a large upstream compressible volume is a minimum in the pressure drop versus flow rate curve, as demonstrated analytically [28] and experimentally [29]. In other words, the criterion for the constant volume instability (CVI) is

$$\left.\frac{\partial\Delta P}{\partial w}\right|_{\mathrm{CVI}}=0 \tag{2}$$

Operation at the minimum is unstable, because boiling fluctuations, discussed above, cause a transition to a condition where the heat flux can no longer be accommodated, and CHF is the result. As classified in [30], this is a *pressure drop oscillation* initiated by a flow excursion (see below), causing a dynamic interaction between the boiling channel and the compressible volume. This instability can be eliminated by isolating the boiling channel from the compressible volume by a throttle valve. Of course, this means an increased system pressure drop.

Excursive Instability

Microchannel heat exchangers invariably consist of an array of parallel channels conveying the coolant. The temptation is to design these channels using heat transfer and pressure drop data for single channels that have flow imposed. When boiling is involved, however, this procedure is not valid, because it fails to capture the excursive or Ledinegg instability that results from the unique pressure drop characteristics of a boiling channel.

The pressure drop characteristics of a single channel (including entrance and exit losses) are necessary to predict this "hydrodynamic" instability. Typical data for these "demand" curves are shown in Fig. 5; the pressure drop is given as a function of mass flow rate for a fixed geometry, but varying inlet temperature, heat flux, and exit pressure. Although this figure is for subcooled boiling, the general concept holds equally well for bulk boiling. The pressure drop starts out lower than the isothermal value for pure liquid, because of the reduced viscosity at the wall with heating. As the flow rate is reduced, boiling is initiated, whereupon the curve starts to turn around. A well-defined minimum is observed, and the curve rises sharply until CHF is observed at "*d*." If the experiment were not terminated by CHF, the curve would rise further, eventually reaching a maximum and joining the all-vapor curve.

The key to the parallel-channel behavior is the minimum, that is for the excursive instability (EI)

$$\left.\frac{\partial\Delta P}{\partial w}\right|_{\mathrm{EI}}=0 \tag{3}$$

If the "supply" curve is that of a centrifugal pump, "*A*," there will be two intersections on the "demand" curve: "*b*" and "*c*." Actually, the intersection *b* is not possible, since operation beyond the minimum cannot occur; at the minimum, a first-order instability occurs, since a perturbation in flow rate (assumed negative) causes an excursion to point "*a*." The classification of [30] considers this a *fundamental static instability*.

As demonstrated analytically and experimentally by Maulbetsch and Griffith [28], the heat flux for this hydrodynamic instability is considerably lower than the heat flux that would be

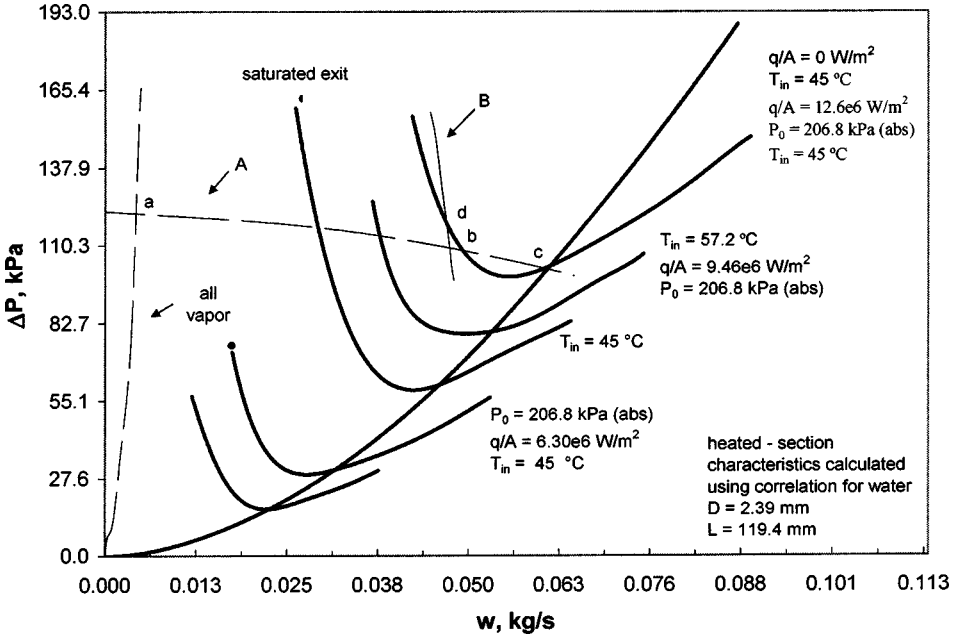

Fig. 5 Flow-rate dependence of subcooled boiling pressure drop for water, used to illustrate excursive instability (see Ref. [29])

obtained with a stabilizing pressure drop at the tube inlet such that the supply curve (pump inlet throttle) has a steeper negative slope than the demand curve chosen, ''B.'' Prediction of the minimum in the channel pressure drop versus flow rate curve is essential, but sufficient data to do this have been obtained only for minichannels, not microchannels. Once again, the stabilizing pressure drop will require a higher head pump.

Improved microfabrication techniques may make it possible to build flow restrictions at the inlet of each channel to accomplish the inlet pressure drop. Each orifice must be identical. Since the orifice will necessarily be smaller than the channels, it will require a tighter manufacturing tolerance than the channel itself. The papers by Thorsen et al. [31] and Kandlikar and Grande [32] discuss advanced fabrication methods that might be used to realize this.

It is noted that the criteria for instability for both the upstream compressible volume instability and the excursive instability are identical, Eqs. (2) and (3). Furthermore, the cures for the instability are identical: upstream throttling. This means that it would only be necessary to install the inlet orifices to cure both types of instability. On the other hand, it is insufficient to install a valve in the inlet line before the header; that will cure one type of instability but not the other. We suggest this is what happened in the experiments of Qu and Mudawar [26]. They installed the throttle valve to avoid the compressible volume instability, but were still subject to the excursive instability.

The first step in confirming that this phenomenon is prevalent in microchannel CHF, especially the observations of [26] as shown in Fig. 4, is to show that there is a minimum in the pressure drop curve. The model and earlier data of Koo and co-workers [19] shown in Fig. 6 demonstrate a well-defined minimum. It is emphasized that they obtained these results for a single channel; this must be the case, as parallel channels would exhibit CHF at the minimum. Although these results are for pressure drop versus power input, they can be transformed to pressure drop versus flow rate [33], also with a conspicuous minimum. *It is concluded that microchannels with vaporization are prone to excursive instability. The excursive instability results in a lower CHF than would be obtained with stable flow in the individual channels.*

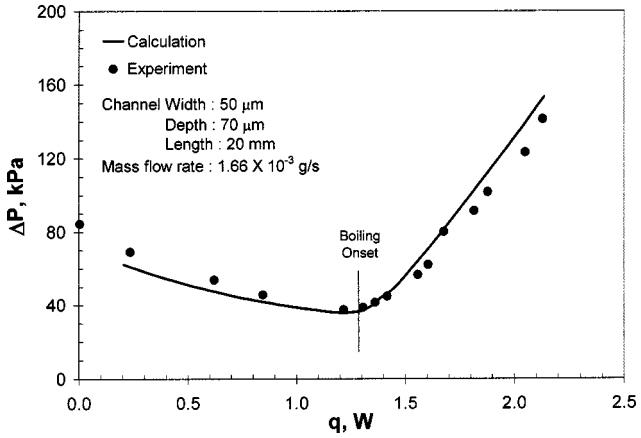

Fig. 6 Predictions and data for the pressure drop in a single microchannel (see Ref. [19])

Postdryout Behavior

The heat transfer coefficient beyond the CHF condition, whatever the cause, is needed to assess the consequences of exceeding the critical heat flux. Jiang et al. [12] report the CHF temperature excursions for the test section described earlier, and for data at flow rates of water less than 2 ml/min, as shown in Fig. 3. The postdryout wall temperatures were 185–250°C. While these temperatures are rather high, they may not result in destruction of the heat sink, unless gaskets, bonds, and the electronic device itself fail. Note that this is the situation for compressible volume or excursive instability; postdryout temperatures would be higher for true CHF.

Instrumentation

The experience of previous investigators provides meaningful guidance for the CHF instrumentation of microchannel heat exchangers. Visual observations of the boiling in rectangular channels through a transparent cover plate are useful to infer flow patterns, flow stagnation, and flow reversal. However, given the small dimensions of the channels and two-phase phenomena, such

as bubbles, microscopic observation must be used. Even with this, it is difficult to distinguish important features, such as the evaporating film in annular flow [23].

In terms of quantitative measurements, the heat input to the channel should be accurate. This usually means correcting for the heat losses to the ambient from actual electronic devices or electrical heaters. There are several ways to express the heat flux. The overall performance can be expressed as a heat flux based on the area of the heat input to the microchannel array. However, the channel behavior requires the effective channel surface area. Because of good conduction in the microchannel block, this will usually be the channel area exposed to the fluid (excluding the cover plate).

A knowledge of the channel surface temperature and heat flux would be desirable; however, thermocouples or other sensors cannot be readily installed around a channel to get the local behavior. The smallest practical thermocouple (36 gauge) has a bead size exceeding the upper limit of channel size (100 μm gap for a rectangular channel or hydraulic diameter equal to 200 μm). Multiple thermocouples [12] are preferable to a single thermocouple recording the entire block temperature [11]. They can be placed in the side near the heater, along the flow direction. Due to expected uniform flow distribution, it is necessary to do this only for a single channel.

Experimental uncertainties are another area where particular attention needs to be given. The small passage dimensions, and associated errors in measuring temperature differences, heat fluxes, and pressure gradients make it extremely difficult to achieve a high degree of accuracy with conventional measurement techniques.

Conclusions

This paper has considered major issues associated with the use of microchannels. The emphasis is on bulk boiling heat transfer, which occurs when high heat loads are to be accommodated in microelectronic heat sinks. The upper limit of heat flux is the critical heat flux (CHF).

Existing small-tube CHF data are inapplicable to microchannels, mainly because of being taken at high mass fluxes.

Flow distribution in parallel microchannels is not considered to be a problem with the usual subcooled inlet conditions.

There appear to be no barriers to incipient boiling in microchannels, so vapor will appear without difficulty. Water is clearly not a problem, but highly wetting fluids may experience temperature overshoots.

Conjugate effects may become important in microchannels such that CHF occurs in the region near the heater, whereas the opposite side of the channel may have conventional boiling. Many microchannel blocks have a high thermal conductivity and the heat transfer coefficient is rather uniform circumferentially; thus, the heat flux is uniform around the circumference (except for the adiabatic cover plate in the case of rectangular channels).

The few available CHF experiments for parallel microchannels are discussed. The database is only of order 10, as opposed to conventional channels having a database of order 100 000. Clearly, more data are needed. But, it is important to recognize the character of CHF in microchannels that have been studied to date.

The case is made that all of the available CHF data were taken under unstable conditions. *The critical condition is the result of an upstream compressible volume instability or the parallel channel, Ledinegg instability*. As a result, the CHF values are lower than they would be if the channel flow were kept stable by an inlet restriction at the inlet of each channel. A proper inlet restriction can eliminate both kinds of instability. It is suggested that the next step in microchannel research be the fabrication and study of the effects of such orifices.

Acknowledgment

It is indeed a pleasure to acknowledge the contribution of Richard C. Chu to this paper. Nearly 40 years ago, he caused the career of A.E.B. to include cooling of computers, particularly ''high end'' thermal management. Microchannels with vaporization are a natural outgrowth of the many studies promoted by Dick Chu. The second author, Satish Kandlikar, would like to gratefully acknowledge the continued IBM faculty award for conducting research in this area.

Nomenclature

D = tube diameter, m
D_h = hydraulic diameter, m
G = mass flux, kg/m^2 s
h_{fg} = latent heat of vaporization, J/kg
L = length of channel, m
P_o = pressure, bar
ΔP = heated section pressure drop, kPa
Q = volumetric flow rate, ml/min
q = power, W
q_c = power at CHF, W
$q'', q/A$ = heat flux, W cm^{-2}
T_{in} = inlet temperature, °C
T_w = wall temperature, °C
w = mass flow rate, kg/s

Greek Symbols

ρ_f = density of liquid, kg/m^3
ρ_g = density of vapor, kg/m^3
σ = surface tension, N/m

References

[1] Mehendale, S. S., Jacobi, A. M., and Shah, R. K., 2000, ''Fluid Flow and Heat Transfer at Micro- and Meso-Scales with Application to Heat Exchanger Design,'' Appl. Mech. Rev., **53(7)**, pp. 175–193.

[2] Kandlikar, S. G., and Grande, W. J., 2003, ''Evolution of Microchannel Flow Passages—Thermohydraulic Performance and Fabrication Technology,'' Heat Transfer Eng., **24(1)**, pp. 3–17.

[3] Cho, E. S., Koo, J.-M., Jiang, L., Prashar, R. S., Kim, M. S., Santiago, J. G., Kenny, T. W., and Goodson, K. E., 2003, ''Experimental Study on Two-Phase Heat Transfer in Microchannel Heat Sinks with Hotspots,'' *Proceedings of 19th Semi-Therm Symposium*, IEEE, Piscataway, NJ, pp. 242–246.

[4] Tuckerman, D. B., and Pease, R. F. W., 1981, ''High-Performance Heat Sinking for VLSI,'' IEEE Electron Device Lett., **EDL-2**, pp. 126–129.

[5] Hall, D. D., and Mudawar, I., 2000, ''Critical Heat Flux (CHF) for Water in Tubes-II, Subcooled CHF Correlations,'' Int. J. Heat Mass Transfer, **43**, pp. 2605–2640.

[6] Bowring, R. W. 1972, ''A Simple but Accurate Round Tube Uniform Heat Flux Dryout Correlation Over the Pressure Range 0.7–17 MN/m^2 (100–2500 psia),'' Report No. AEEW-R789, Winfreth, UK.

[7] Vandervort, C. L., Bergles, A. E., and Jensen, M. K., 1994, ''An Experimental Study of Critical Heat Flux in Very High Heat Flux Subcooled Boiling,'' Int. J. Heat Mass Transfer, **37**, Suppl. 1, pp. 161–173.

[8] Kandlikar, S. G., 2001, ''A Theoretical Model to Predict Pool Boiling CHF Incorporating Effects of Contact Angle and Orientation,'' ASME J. Heat Transfer, **123**, pp. 1071–1079.

[9] Kandlikar, S. G., 2004, ''Heat Transfer Mechanisms During Flow Boiling in Microchannels,'' ASME J. Heat Transfer, **126**, pp. 8–16.

[10] Bergles. A. E., 1992, ''Elements of Boiling Heat Transfer,'' in *Boiling Heat Transfer—Modern Developments and Advances*, pp. 389–445, Elsevier Science Publishers, Amsterdam, The Netherlands.

[11] Bowers, M. B., and Mudawar, I., 1994, ''High Flux Boiling in Low Flow Rate, Low Pressure Drop Mini-Channel and Micro-Channel Heat Sinks,'' Int. J. Heat Mass Transfer, **37**, pp. 321–332.

[12] Jiang, L., Wong, M., and Zohar, Y., 1999, ''Phase Change in MicroChannel Heat Sinks with Integrated Temperature Sensors,'' J. Microelectromech. Syst., **8**, pp. 358–365.

[13] Zhang, L., Wang, E. N., and Koo, J.-M., 2002, ''Enhanced Nucleate Boiling in Microchannels,'' *Proceedings of the 5th IEEE Conference on MEMS*, IEEE, Piscataway, NJ, pp. 89–92.

[14] Ayub, Z. H., and Bergles, A. E., 1987, ''Pool Boiling from GEWA Surfaces in Water and R-113,'' Waerme- Stoffuebertrag., **21**, pp. 209–219.

[15] Qu, W., and Mudawar, I., 2003, ''Prediction and Measurement of Incipient Boiling Heat Flux in Micro-Channel Heat Sinks,'' Int. J. Heat Mass Transfer, **45**, pp. 3933–3945.

[16] Boyd, R. D. Sr., Cofie, P., Li, Q.-Y., and Ekhlassi, A. A., 2002, ''A New Facility for Measurement of Three-Dimensional, Local Subcooled Flow Boil-

ing Heat Flux and Related Critical Heat Flux for PFCs,'' Fusion Sci. Technol., **41**, pp. 1–12.
[17] Boyd, R. D. Sr., Cofie, P., and Ekhlassi, A., 2002, ''Conjugate Heat Transfer Measurements in a Non-Uniformly Heated Circular Flow Channel Under Flow Boiling Conditions,'' Int. J. Heat Mass Transfer, **45**, pp. 1605–1613.
[18] Qu, W., and Mudawar, I., 2003, ''Flow Boiling Heat Transfer in Two-Phase Micro-Channel Heat Sinks-II. Annular Two-Phase Flow Model,'' Int. J. Heat Mass Transfer, **46**, pp. 2773–2784.
[19] Koo, J.-M., Jiang, L., Zhang, L., Zhou, P., Banerjee, S. S., Kenny, T. W., Santiago, J. G., and Goodson, K. E., 2001, ''Modeling of Two-Phase Microchannel Heat Sinks for VLSI Chips,'' *Proc. 4th IEEE Conference on MEMS*, IEEE, Piscataway, NJ, pp. 422–426.
[20] Jiang. L., Koo, J.-M., Zeng, S., Mikkelsen, J. C., Zhang, L., Zhou, P., Sabtiago, J. G., Kenny, T. W., and Goodson, K. E., 2001. ''Two-Phase Microchannel Heat Sinks for an Electrokinetic VLSI Chip Cooling System,'' in *Proc. 17th IEEE Semi-Therm Symposium*, IEEE, Piscataway, NJ, pp. 153–157.
[21] Tabatabai, A., and Faghri, A., 2001, ''A New Two-Phase Flow Map and Transition Boundary Accounting for Surface Tension Effects in Horizontal Miniature and Micro Tubes,'' ASME J. Heat Transfer, **123**, pp. 958–968.
[22] Kandlikar, S. G., 2002, ''Two-Phase Flow Patterns, Pressure Drop, and Heat Transfer during Boiling in Minichannel Flow Passages of Compact Evaporators,'' Heat Transfer Eng., **23**(**1**), pp. 5–23.
[23] Hetsroni, G., Moysak, A., Segal, Z., and Ziskind, G., 2001, ''A Uniform Temperature Heat Sink for Cooling of Electronic Devices,'' Int. J. Heat Mass Transfer, **45**, pp. 3275–3286.
[24] Wu, H. Y., and Cheng, P., 2003, ''Visualization and Measurements of Periodic Boiling in Silicon Microchannels,'' Int. J. Heat Mass Transfer, **46**, pp. 2603–2614.
[25] Mukherjee, S., and Mudawar, I., 2002, ''Smart, Low-Cost, Pumpless Loop for Micro-Channel Electronic Cooling Using Flat and Enhanced Surfaces,'' *Proc. ITherm*, 2002, IEEE, Piscataway, NJ, pp. 360–370.
[26] Qu, W., and Mudawar, I., 2004, ''Measurement and Correlation of Critical Heat Flux in Two-Phase Micro-Channel Hat Sinks,'' Int. J. Heat Mass Transfer, **47**, pp. 2045–2059.
[27] Qu, W., and Mudawar, I., 2003, ''Measurement and Prediction of Pressure Drop in Two-Phase Micro-Channel Heat Sinks,'' Int. J. Heat Mass Transfer, **46**, pp. 2737–275.
[28] Maulbetsch, J. S., and Griffith, P., 1966, ''A Study of System Induced Instabilities in Forced Convection Flows with Subcooled Boiling,'' *Proc. 3rd Int. Heat Transfer Conf.*, **III**, AIChE, New York, pp. 247–257.
[29] Daleas, R. S., and Bergles, A. E., 1965, ''Effects of Upstream Compressibility on Subcooled Critical Heat Flux,'' ASME Paper No. 65-HT 67, ASME, New York.
[30] Boure, J. A., Bergles, A. E., and Tong, L. S., 1973, ''Review of Two-Phase Flow Instability,'' Nucl. Eng. Des., **25**, pp. 165–192.
[31] Thorsen, T., Maerkl, S. J., and Quake, S. R., 2002, ''Microfluidic Large-Scale Integration,'' Science, **298**, pp. 580–584.
[32] Kandlikar, S. G., and Grande, W. J., 2004, ''Evaluation of Single Phase Flow in Microchannels for High Flux Chip Cooling—Thermohydraulic Performance Enhancement and Fabrication Technology.'' *Proc. 2nd Int. Conf. Microchannels and Minichannels*, June 17–19, 2004, Rochester, NY, ASME, New York.
[33] Pabisz, R. A., and Bergles, A. E., 1997, ''Using Pressure Drop to Predict the Critical Heat Flux in Multiple Tube, Subcooled Boiling Systems,'' Exp. Heat Transfer, **2**, pp. 851–858, Edizioni ETS, Pisa, Italy.

Thermal Transport in Nanostructured Solid-State Cooling Devices

Deyu Li
Department of Mechanical Engineering, Vanderbilt University, Nashville, TN 37235
e-mail: deyu.li@vanderbilt.edu

Scott T. Huxtable
Department of Mechanical Engineering, Virginia Tech, Blacksburg, VA 24061

Alexis R. Abramson
Department of Mechanical and Aerospace Engineering, Case Western Reserve University, Cleveland, OH 44106

Arun Majumdar
Department of Mechanical Engineering, University of California, Berkeley, CA 94720; Materials Science Division, Lawrence Berkeley National Lab, Berkeley, CA 94720

Low-dimensional nanostructured materials are promising candidates for high efficiency solid-state cooling devices based on the Peltier effect. Thermal transport in these low-dimensional materials is a key factor for device performance since the thermoelectric figure of merit is inversely proportional to thermal conductivity. Therefore, understanding thermal transport in nanostructured materials is crucial for engineering high performance devices. Thermal transport in semiconductors is dominated by lattice vibrations called phonons, and phonon transport is often markedly different in nanostructures than it is in bulk materials for a number of reasons. First, as the size of a structure decreases, its surface area to volume ratio increases, thereby increasing the importance of boundaries and interfaces. Additionally, at the nanoscale the characteristic length of the structure approaches the phonon wavelength, and other interesting phenomena such as dispersion relation modification and quantum confinement may arise and further alter the thermal transport. In this paper we discuss phonon transport in semiconductor superlattices and nanowires with regards to applications in solid-state cooling devices. Systematic studies on periodic multilayers called superlattices disclose the relative importance of acoustic impedance mismatch, alloy scattering, and crystalline imperfections at the interfaces. Thermal conductivity measurements of monocrystalline silicon nanowires of different diameters reveal the strong effects of phonon-boundary scattering. Experimental results for Si/SiGe superlattice nanowires indicate that different phonon scattering mechanisms may disrupt phonon transport at different frequencies. These experimental studies provide insight regarding the dominant mechanisms for phonon transport in nanostructures. Finally, we also briefly discuss Peltier coolers made from nanostructured materials that have shown promising cooling performance. [DOI: 10.1115/1.1839588]

Introduction

The Peltier effect describes the release or absorption of heat when an electric current passes across a junction of two dissimilar materials. Ever since the discovery of the Peltier effect in 1835, there have been efforts towards developing solid-state refrigeration devices based on this phenomenon. The development of the fundamental physics and materials science of thermoelectrics occurred mainly during two periods over the last 200 years. The basic effects were discovered and macroscopic understanding was achieved between the 1820s and the 1850s. Interest in thermoelectric coolers was renewed in the middle of the 20th century when it was discovered that doped semiconductors made for better thermoelectric materials than metals. In fact, the initial interest in semiconductors and semiconductor physics was not for applications in microelectronics, but for thermoelectrics [1]. Following several decades of research, the efficiency of thermoelectric cooling devices reached about 10% Carnot efficiency, which pales in comparison to the 30% efficiency typical of vapor compression refrigerators [2]. Thermoelectric research again waned until the early 1990s, when theoretical predictions indicated that low-dimensional materials such as two-dimensional (2D) superlattices, one-dimensional (1D) nanowires, or zero-dimensional (0D) quantum dots made for excellent candidates as high-performance thermoelectric materials [3–5].

The efficiency of a Peltier cooling device is given by its coefficient of performance (COP). Based on the definitions of thermoelectric effects and fundamental transport equations, it can be shown [6,7] that the COP of a Peltier cooling device is related to its basic material properties, through the dimensionless thermoelectric figure of merit, ZT. The figure of merit is defined as $ZT = S^2\sigma T/k$, where S is the thermopower or Seebeck coefficient, σ is the electrical conductivity, k is the thermal conductivity, and T is the absolute temperature. The ZT value for the best bulk semiconductor materials is approximately unity, corresponding to about 10% Carnot efficiency, and has improved only incrementally in the past several decades. In order for thermoelectric coolers to become competitive with conventional refrigerators, materials with $ZT>3$ must be developed. Increasing ZT is difficult because the three basic material parameters, S, σ, and k, are all related to the free carrier concentration and are not independent. In general, doping increases the semiconductor's electrical conductivity but decreases its Seebeck coefficient. Heat transport in semiconductors is controlled predominantly by lattice vibrations (phonons), while electrons generally play a minor role. Nonetheless, the excess mobile charge carriers added as dopants can lead to an increase in the thermal conductivity of the material. Efforts to reduce the lattice thermal conductivity through alloying or the introduction of interfaces can have the undesirable effect of also scattering the mobile charge carriers and reducing the electrical conductivity.

Although it is theoretically possible [2], it is unlikely that a naturally occurring bulk material with $ZT>3$ will ever be found. However, with advances in micro/nanofabrication and metrology over the last decade, novel low-dimensional nanostructured materials such as superlattices, nanowires, and quantum dots have shown promise as potential thermoelectric materials. Observations of $ZT>1$ have recently been reported for superlattices and quantum dots [8,9]. Figure 1 shows representative data of historical improvements of ZT at room temperature [10].

Why are low-dimensional nanostructured materials promising candidates for high efficiency thermoelectric devices? In semiconductors, electrons and holes carry charge, while lattice vibrations, called phonons, dominate heat transport. When the characteristic length of a structure becomes comparable to the electron wavelength, λ, its electronic density of states changes and sharp edges and peaks are produced. The locations of these edges and peaks depend on the characteristic size of the structure and can be manipulated with respect to the Fermi energy to tailor the thermopower, S. In addition, such quantum confinement may also increase the electron mobility, which leads to a higher value of σ. The overall effect is an enhanced power factor, $S^2\sigma$, due to the quantum confinement of nanostructures [10]. Furthermore, when the characteristic size of a nanostructure becomes comparable to

Manuscript received May 21, 2004; revision received July 31, 2004. Review conducted by: C. Amon.

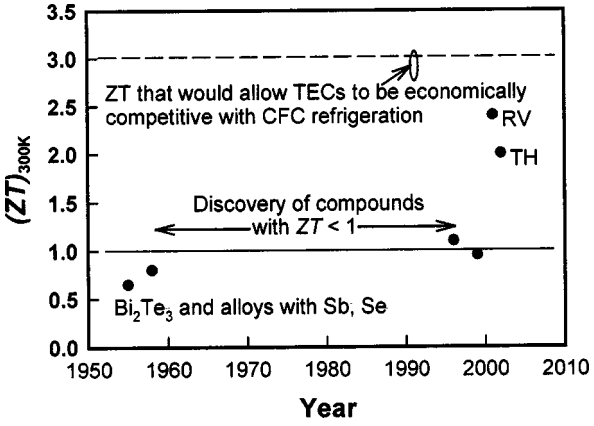

Fig. 1 Thermoelectric improvements (see Ref. [10]). History of thermoelectric figure of merit, ZT, at 300 K. Since the discovery of the thermoelectric properties of Bi_2Te_3 and similar alloys with Sb and Se in the 1950s, no bulk materials with $(ZT)_{300\ K} > 1$ have been discovered. Recent studies in nanostructured thermoelectric materials have led to a dramatic increase in $(ZT)_{300\ K}$. In the figure, RV denotes Venkatasubramanian et al.'s data in Ref. [8] and TH denotes Harman et al.'s data in Ref. [9]

the phonon mean free path, ℓ, the increased importance of boundary and interface scattering of phonons may cause the thermal conductivity of the nanostructure to fall well below that of a comparable bulk material. In addition, the phonon spectra and phonon density of states may also be altered when the characteristic size becomes comparable to the phonon wavelength, causing a further reduction in thermal conductivity.

In general, nanostructures provide the possibility of using confinement effects to increase S and σ, while reducing k. Even though significant progress has been made in this area over the past decade, a deeper understanding of charge and phonon transport in semiconductor nanostructures must be achieved in order to design materials with ZT greater than 3. In this paper, we focus on thermal transport in nanostructures and discuss recent experimental work on semiconductor superlattices and nanowires. Our focus is on phonon transport since the contributions of mobile charge carriers to the thermal conductivity are generally small and can often be accurately estimated using the Wiedemann–Franz law.

Thermal Transport in Low-Dimensional Nanostructures

Size Effects on Phonon Transport. Thermal transport in low-dimensional semiconductor nanostructures has been studied extensively over the last decade [11–17]. Despite these efforts there is still much to be learned about heat transport in these nanoscale materials due to the complexity that arises from the interplay between: (i) the broadband nature of phonons, i.e., thermal transport involves phonons of a wide range of frequencies; (ii) the temperature dependence of the phonon spectral energy distribution, which is similar to the photon spectral energy distribution from blackbody radiation; and (iii) the size of a nanostructure, which is often comparable to the phonon mean free path and/or wavelength and requires that the effects of interfaces and boundaries be considered. Because of this complexity, it is often difficult to predict the nature of thermal transport in nanostructured materials without a fundamental understanding of the relationships between the aforementioned characteristics. Systematic studies over the last decade have provided some clues as to how to control thermal transport using nanostructures, and, more interestingly, how to reduce the thermal conductivity for thermoelectric applications.

The influence of the nanostructure size on thermal conductivity arises primarily from two types of interactions. The first interaction occurs when the size is comparable to the phonon mean free path (mfp). The phonon mean free path can range from about 1 nm to hundreds of nanometers, depending on the material and its temperature. For example, when phonon dispersion is considered, the calculated phonon mean free path in mono-crystalline silicon at room temperature is close to 300 nm [18]. When the characteristic size of a nanostructure becomes comparable to the phonon mean free path, boundary, or interface, scattering becomes significant, and the structure size becomes the limiting factor in the mfp. The second type of interaction relates to wave interactions in a medium, i.e., when the wavelength of a phonon corresponds to the nanostructure size, the phonon dispersion relation can be altered. This modifies the phonon group velocity and density of states. Furthermore, because phonon-phonon scattering (normal and Umklapp) depends on certain selection rules of momentum and energy conservation, changes in the phonon dispersion relation could also alter the mean free path due to the changes in phonon scattering. Despite substantial theoretical investigations regarding these interactions and some experimental observations providing preliminary data, considerable work needs to be done in order to achieve a more complete understanding of phonon transport in nanostructures. In the sections that follow, we first discuss heat transport in 2D confined materials or superlattices, and then 1D confined materials or nanowires.

Thermal Transport in Superlattices. Experimental studies on thermal transport in epitaxial superlattices, or periodic multilayers, span more than two decades. Most experimental studies have used superlattices of Si, Ge, and/or their alloys or superlattices composed of various III–V compounds. In superlattices, both wave and particle-like phonon effects have been observed, offering not only richness in physics but also difficulties in predictions.

The pioneering work on phonon transport in superlattices was done by Narayanamurti et al. [19] in the late 1970s. They studied monochromatic phonon transport across lattice matched GaAs/AlGaAs superlattices at extremely low temperatures ($\sim$1 K). Their results showed the existence of a phonon band gap, which resulted from the interference of waves reflected from multiple interfaces, i.e., Bragg reflection. For wave-like interference to occur, the mean free path of phonons must span multiple interfaces in order for coherence to be preserved. In this regime, the phonon dispersion relation is modified and zone folding occurs, resulting in multiple phonon band gaps [20]. Effects from this miniband formation could lead to altered thermal transport behavior in superlattices. First, the group velocity of phonons is reduced significantly, especially for higher energy acoustic phonons. Second, because the dispersion relations are modified, there are many more possibilities for conservation of momentum (with reciprocal lattice vector $\mathbf{G}$) and energy involved in normal and Umklapp scattering [21]. Hence, the scattering rate is increased. However, miniband formation requires coherent phonons. At room temperature, a broadband of phonons is thermally excited and various scattering mechanisms limit the coherence length to a few nanometers at most, which prevents wave interference [22]. Therefore, it is unlikely that these wave effects play a significant role in heat transport at room temperature.

Phonon scattering at individual interfaces may arise from: (i) an acoustic impedance mismatch: acoustic impedance is defined as the product of the mass density and the phonon speed of sound and is analogous to the index of refraction in optics, i.e., a phonon may scatter when it encounters an interface between materials of different acoustic impendence just as a photon scatters when it encounters a change in the optical index of refraction; (ii) phonon spectra mismatch: if the two adjacent materials exhibit different phonon spectra characteristics, phonons of specific frequencies cannot propagate to the neighboring layer without undergoing mode conversion; (iii) interfacial dislocations and defects: interfaces between materials with different lattice constants often contain dislocations and defects, which can also scatter phonons and

alter thermal conductivity; (iv) interface roughness: depending on the processes used to grow the materials, there could be both physical roughness as well as alloying at the interface, which can further hinder phonon transport; (v) interfacial strain: even in a perfectly aligned, dislocation/defect free interface, strain experienced by one or both materials may affect the thermal characteristics.

Thermal transport in GaAs and AlAs superlattices has been studied widely [23–26]. The results indicate that the thermal conductivity decreases as the interface density increases, clearly showing the importance of the interfacial thermal resistance. As pointed out by Mahan [1], as much as a fivefold reduction in the thermal conductivity in comparison with the bulk constituents has been found.

Systematic measurements on Si and Ge superlattices [27–31] disclosed some phonon transport mechanisms, but also presented some further puzzles. Lee et al. [27] measured the cross plane thermal conductivity of a series of Si/Ge superlattices with periods ranging from 30 to 275 Å over a temperature range of 80–400 K. These data suggest that for small periods (<70 Å), when the layer thickness is less than the critical thickness for misfit dislocations to be nucleated at the interface, the thermal conductivity decreases with decreasing layer thickness (or increasing density of interfaces). However, as the layer thickness increases beyond 140 Å, the thermal conductivity also decreases and falls below the value of the short-period samples. The authors argued that for these longer-period superlattices, a high density of defects was likely present due to the strain in the thicker lattice-mismatched layers and that these defects caused the reduction in thermal conductivity. Chen and Neagu [28] and Borca-Tascuic et al. [29] observed similar phenomena but they speculated that the lower thermal conductivity of thicker period superlattices could be the result of residual stress in the layers. Their argument was based on the fact that the measured dislocation densities in their samples were orders of magnitude lower than the densities required to account for the strong reduction in thermal conductivity. Recent molecular dynamics studies [32,33] showed that an imposed strain can result in a significant decrease in the thermal conductivity. Moreover, for short-period superlattices, the atoms adjust their positions and minimize the interfacial strain between adjacent layers, while for longer period superlattices, some atoms can keep their natural lattice constants and the interfacial strain is larger. The calculated interfacial thermal resistance of each interface gets larger as the period length increases. This result favors the argument made by Borca-Tascuic et al. [29].

The effects of interface dislocations and defects are extremely hard to address accurately. Interface disorder introduces diffuse scattering but disorder in a superlattice is typically modest. It is mainly limited to interface roughness (a finite density of interface steps) and substitutional alloying at the interfaces caused by surface segregation during growth. Unfortunately, this interface roughness in an epitaxial superlattice is sensitive to the material, growth method, growth conditions, and deposition rate—and thus it is extremely difficult to control and characterize. Furthermore, asymmetry of the interface is often pronounced, i.e., the growth of material A on the surface of material B creates a different interface than the growth of B on A. Strained-layer superlattices such as Si–Ge can harbor high densities of crystalline defects when the layer thickness exceeds the critical thickness for the extension of misfit dislocations; growth on relaxed buffer layers reduces the density of threading dislocations but the misfit density will still be large when the critical thickness is exceeded.

To further explore the interfacial thermal resistance, Huxtable et al. [30] more recently have shown that for superlattices of Si and $Si_{0.7}Ge_{0.3}$, where the critical thickness is much larger than that for Si and Ge superlattices, the thermal conductivity scaled almost linearly with interface density supporting the data of Lee et al. [27] and Borca-Tascuic et al. [29]. The measurement results in Fig. 2 show that as the interface density increases, the thermal

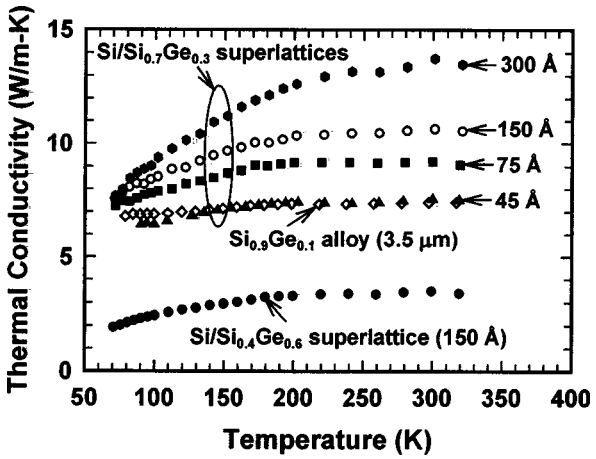

Fig. 2 Cross-plane thermal conductivity of Si/Si_xGe_{1-x} superlattices and a 3.5-μm-thick $Si_{0.9}Ge_{0.1}$ alloy. The labels on the plot refer to the period thickness (see Refs. [30,31]). Since thermal conductivity data as a function of temperature for Si_xGe_{1-x} alloys of arbitrary x is not readily available, all comparisons are made with a $Si_{0.9}Ge_{0.1}$ alloy. Since the thermal conductivity Si_xGe_{1-x} alloy changes only marginally for $0.1<x<0.9$ this makes for a reasonable comparison

conductivity approaches, but never falls below, that of a $Si_{0.9}Ge_{0.1}$ alloy. To explain this, Huxtable et al. [31] then systematically studied thermal transport in Si and $Si_{0.4}Ge_{0.6}$ and $Si_xGe_{1-x}/Si_yGe_{1-y}$ superlattices (see Fig. 3). It is worth noting that for Si_xGe_{1-x} alloys both the lattice parameter and the acoustic impedance can be estimated as a linear combination of the respective Si and Ge properties. Hence, by varying x and y one could methodically span the range of acoustic impedance and lattice mismatch that was previously unavailable in Si/Ge superlattice studies. These investigations led to the following understanding. When $|x-y|\leq 0.1$, acoustic impedance and lattice mismatches in the two materials are sufficiently small that interfacial phonon scattering is marginal, whereas alloy scattering is dominant, rendering the superlattice structure unimportant. When $|x-y|\approx 0.3$, the lattice mismatch is still sufficiently low that, depending on the growth conditions, the generation of interfacial defects and dislocations can be reduced or eliminated. However, the acoustic impedance mismatch is large enough for phonon reflection at the interfaces to be the dominant scattering mechanism.

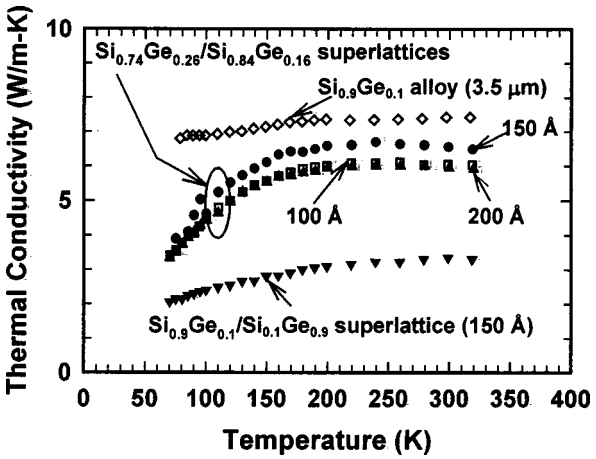

Fig. 3 Cross-plane thermal conductivity of $Si_xGe_{1-x}/Si_yGe_{1-y}$ superlattices and a 3.5-μm-thick $Si_{0.9}Ge_{0.1}$ alloy. The labels on the plot refer to the period thickness (see Ref. [31])

In such cases, although the superlattice thermal conductivity is inversely proportional to the interfacial density, it is difficult to decrease the thermal conductivity below the alloy scattering limit, i.e., if the $Si_xGe_{1-x}/Si_yGe_{1-y}$ superlattice is mixed homogenously into an alloy. For $|x-y| \geq 0.6$, however, the acoustic impedance mismatch is large and the lattice mismatch is sufficient such that defects and dislocations are generated at the interfaces. In such cases, the superlattice thermal conductivity is generally lower than the alloy scattering limit. However, since acoustic impedance mismatch increases along with lattice mismatch, it is difficult to determine whether the strong reduction in thermal conductivity observed in these samples is due to the additional defects, or if it is due to the fact that the acoustic impedance mismatch is much greater. Further measurements [34] on similar superlattices grown at lower temperatures to minimize the defect density indicate that the acoustic impedance mismatch is the dominant mechanism for the reduction in thermal conductivity in these structures.

There have been two reports of thermal conductivity of Bi_2Te_3 and Sb_2Te_3 superlattices. These materials are of significant interest in thermoelectric applications since they possess large ZT values. Venkatasubramanian [8] showed that as the superlattice period thickness increases, the room temperature thermal conductivity reaches a minimum for a period thickness of 5 nm, and that this value is lower than the thermal conductivity of the corresponding alloy. It was suggested that this was due to phonon band gap effects. However, Touzelbaev et al. [35] examined similar superlattices yet did not find any significant change in thermal conductivity when the superlattice period was varied. Hence, it remains inconclusive as to whether phonon band gap effects are indeed present.

Thermal Transport in Semiconductor Nanowires. Nanowires are quasi-1D or 1D materials with diameters below 100 nm. Due to the large surface area to volume ratio and small diameter, phonon boundary scattering in nanowires is much stronger than in bulk materials, which leads to a reduced phonon mean free path and reduced thermal conductivity for nanowires. Additionally, when nanowire diameters are reduced to tens of nanometers, the phonon dispersion relation could be altered due to confinement. If the phonon spectrum is altered, the phonon group velocity and density of states will be affected. Furthermore, the scattering rate of phonon-phonon interactions will be modified, which will also alter the thermal transport. Finally, if the wire diameter reduces to several nanometers, quantum confinement will limit the available phonon energy states, which reduces the lattice heat capacity and, hence, thermal conductivity.

For low to moderate frequency phonons, the phonon dispersion can be calculated by acoustic wave theory if the medium may be regarded as continuous. It is well known that in continuum materials, classical acoustic wave theory gives a linear dispersion relation. However, this dispersion relation for acoustic phonons is altered for low-dimensional materials because of the boundary conditions imposed. Auld [36] gives a detailed discussion on this topic with regards to waveguides for both 2D thin plates and 1D cylindrical rods. In the 1990s, when electron transport in nanowires was considered, several studies on the phonon dispersion modification in nanowires based on acoustic wave theory were published [37,38]. It was claimed that confined phonons produced larger scattering rates for electrons than the bulk-like phonons. Based on acoustic wave theory, in nanowires phonon confinement will result in nonlinear dispersion and a series of acoustic subbands at wave vectors close to the Brillouin zone center. However, direct experimental evidence of the acoustic phonon modes in nanowires is very limited. In 1992, Seyler and Wybourne [39] presented an experiment showing that the steady state resistance of metal wires with cross sections between 600 and 1800 nm^2 subject to an electric field exhibited periodic resonances that scaled with the width of the wire. They found that the resonances corresponded to the phonons in higher acoustic subbands of the nanowires. In a more recent study [40], the phonon density of states of nanocrystalline iron (with an average particle size of 9 nm) was measured using nuclear resonant inelastic x-ray scattering under various pressures. Results showed that the nanocrystalline material exhibited an enhancement in its density of states by a factor of 1.7–2.2. Even though this work was not directly on wire-like samples, similar phenomena could be expected when wire diameters are in the same regime.

Experimental measurements of thermal transport in nanowires is an extremely challenging task since: (i) handling and manipulating individual nanowires is not trivial; and (ii) isolating, and quantifying, heat flow through a single nanowire is difficult at best. At the present time, only two techniques have been developed to quantitatively measure thermal transport in nanowires. Shi et al. [41] developed a general technique to measure the thermal conductivity of individual nanowires and nanotubes. In this technique, a microfabricated test structure consisting of two adjacent symmetric silicon nitride (SiN_x) membranes (islands) suspended by long silicon nitride beams was batch fabricated. A platinum resistor was deposited on each membrane such that it could serve as a heater to increase the temperature of the suspended island, as well as a resistance thermometer to measure the temperature of the island. Each resistor was electrically connected to four contact pads by metal lines on the suspended SiN_x beams, thus enabling a four-point measurement of the voltage drop and resistance associated with each resistor. Individual nanowire, nanotube, and nanobelt samples may be placed across the two suspended membranes enabling the sample to thermally bridge the two islands. One membrane can be Joule heated to cause heat conduction through the sample to the other membrane. With this known heat flux through the sample, the thermal conductance, and hence thermal conductivity can be determined once the temperatures of each island are measured.

One major source of error in this technique comes from the thermal contact resistance. The measured thermal conductance is a series conductance of the two junctions between the nanowire and the suspended membranes in addition to the intrinsic thermal conductance of the nanowire itself. Li et al. [42] addressed this problem by locally depositing amorphous carbon films at the nanowire-heater pad junctions with a scanning electron microscope to reduce the thermal resistance at the nanowire-island junctions. It was estimated that with the carbon deposition, the error from the thermal contact resistance could be reduced to a few percent of total thermal resistance for most nanowire samples. This technique can be regarded as a general technique for nanowire and nanotube thermal conductivity measurements since nanowires and nanotubes made of any material can be measured as long as they can be placed in between the two suspended membranes.

With this technique, the thermal conductivities of individual single crystalline Si nanowires with diameters ranging from 22 to 115 nm have been measured [42] [see Fig. 4*a*]. Compared to the thermal conductivity of bulk Si, the thermal conductivity of Si nanowires is reduced significantly, indicating that phonon-boundary scattering dominates the thermal transport in these nanostructures. For the 37-, 56-, and 115-nm-diam wires, thermal conductivities reached maximum values around 210, 160, and 130 K, respectively. This shows a sharp contrast to that of bulk Si, which has a peak value of about 6000 W/m K near 25 K. The shift of the peak suggests that as the wire diameter is reduced, phonon-boundary scattering dominates over phonon-phonon Umklapp scattering, which decreases thermal conductivity with increasing temperature. At low temperature, the thermal conductivity of a 22-nm-diam wire deviated significantly from the Debye T^3 law [see Fig. 4*b*], suggesting that at this scale effects other than phonon-boundary scattering—possibly changes in phonon dispersion due to confinement—may have appreciable effects. The thermal conductivity of the 22 nm wire also fell below a theoretical prediction [43] that only considers boundary scattering enhance-

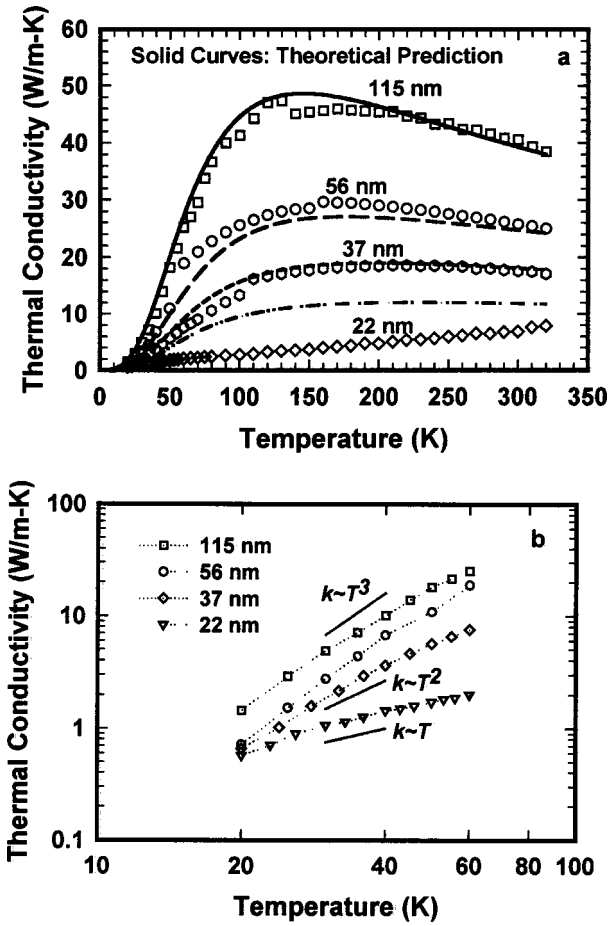

Fig. 4 Thermal conductivity of single crystalline Si nanowires (see Ref. [42]). The solid line in (*a*) is the best fit from Ref. [43]. The low temperature behavior is shown in (*b*)

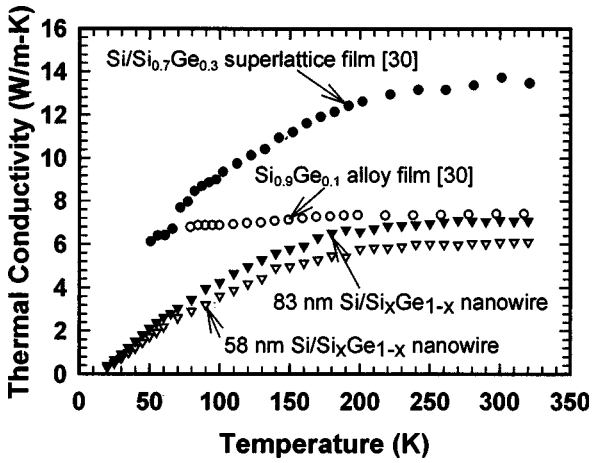

Fig. 5 Thermal conductivity of Si/Si_xGe_{1-x} superlattice nanowires (see Ref. [46]). The thermal conductivities of a $Si/Si_{0.3}Ge_{0.7}$ superlattice film and $Si_{0.9}Ge_{0.1}$ alloy film are also shown for comparison

ment, indicating that some other effect must be responsible for the reduction in thermal transport observed for this nanowire. It is interesting to note that thermal conductivity measurements on nanocrystalline $ZrO_2:Y_2O_3$ [44,45] thin films showed similar size dependence. The thermal conductivity reduction with grain size was marginal until the grain size approached 30 nm, where the thermal conductivity decreased rapidly with further reduction in grain size. It is not clear if there is any direct correlation between these two phenomena.

The thermal conductivities of 58- and 83-nm-diam Si/SiGe single crystalline superlattice nanowires have also been reported [46] (see Fig. 5). The results for these nanowires indicated that alloy scattering was the dominant phonon scattering mechanism, although boundary scattering also played a role in reducing the thermal conductivity. It was argued that while short-wavelength acoustic phonons were effectively scattered by atomic scale point imperfections in the SiGe alloy segments, long-wavelength acoustic phonons were scattered by the nanowire boundary. This result is consistent with the pioneering theoretical work of Goldsmid and Penn [47], which states that in solid solutions or alloys, the high frequency phonons are strongly scattered by point imperfections. Thus, even at high temperatures, boundary scattering, which affects the low frequency phonons, can be important to phonon transport. These results provide some insight into methods to control thermal transport in nanostructures for thermoelectric applications. By distinguishing the contributions to the thermal conductivity from low, moderate, and high frequency phonons, and using different scattering mechanisms to block transport of phonons of different frequencies, carefully designed nanostructures can tailor the thermal conductivity for thermoelectric applications.

Another experimental technique to measure phonon transport in 1D nanostructures was developed by Tighe et al. [48]. Their efforts started with the design and fabrication of a microdevice in which a thin, rectangular intrinsic GaAs thermal reservoir ($\sim 3\ \mu m^2$) was suspended above the substrate by four intrinsic GaAs beams (200 nm$\times$300 nm). The latter constituted the thermal conductors of interest. The isolated reservoir was Joule heated by a source transducer patterned above it. The reservoir cooled through the long, narrow, monocrystalline GaAs bridges that suspended it. Measurements of an elevated reservoir temperature, arising in response to the heat input, were achieved using a second, and separate, local sensor transducer. These transducers were made by $n+$ doped GaAs ($N_D=2\times10^{18}\ cm^{-3}$, $\sim$100 nm linewidth, 150 nm thick). With this device, they successfully measured the total thermal conductance of the four GaAs bridges and deduced the phonon mean free path in the GaAs beams from 1.5 to 6 K. Later, similar measurements were performed on 100 nm $\times$250 nm doped and undoped GaAs beams from 4 to 40 K [49]. All of these measurements showed a strong thermal conductance reduction in comparison with corresponding bulk values. An interesting observation here is that between 20 and 40 K, the thermal conductance deviated from the Debye T^3 law and the phonon-phonon scattering rate deduced from the curve fitting of a Callaway analysis is approximately ten times higher than corresponding bulk values. This phenomena is not yet fully understood.

A significant result obtained with this technique was the demonstration of quantum phonon transport in nanostructures at very low temperature ($<$6 K) [50,51]. The device was modified from GaAs to silicon nitride films with Cr/Au resistors serving as the heater and thermometer on the phonon cavity. Theoretical arguments from Rego and Kirczenow [52] were used to design the shape of the beam to ensure ideal coupling between beams and the thermal reservoir. Experimental results showed that at extremely low temperature, the thermal conductance by ballistic phonon transport through a one-dimensional channel approaches a maximum value of $g_0=\pi^2k_B^2T/3h$ (where k_B is Boltzmann's constant and h is Planck's constant), the universal quantum of thermal conductance.

Nanostructured Cooling Devices

While intense research is being performed on the thermoelectric, electric, and thermal properties of nanostructured materials, the overall performance of nanostructured cooling devices has

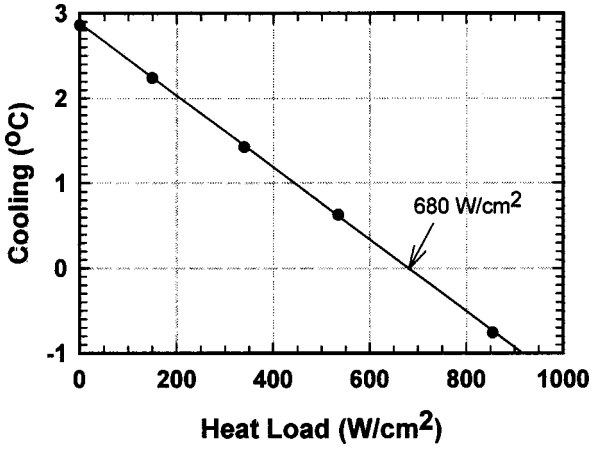

Fig. 6 Device performance of a Si/SiGeC thermoelectric cooler (see Ref. [54])

also been explored. Venkatasubramanian et al. [8] reported a value of $ZT=2.4$ and cooling power densities as high as 700 W/cm^2 for thermoelectric devices made from Bi_2Te_3 and Sb_2Te_3 superlattices. Harman et al. [9] measured the overall thermoelectric figure of merit of PbSeTe/PbTe quantum dot superlattice structures and found ZT values between 1.3 and 1.6. A maximum cooling of 43.7 K was obtained compared with 30.8 K for the best conventional bulk $(Bi,Sb)_2(Se,Te)_3$ thermoelectric materials. A prototype cold point-contact thermoelectric cooler based on p-type $Bi_{0.5}Sb_{1.5}Te_3$ and n-type $Bi_2Te_{2.9}Se_{0.1}$ material system has also been fabricated [53] and an enhanced thermoelectric figure merit of 1.4–1.7 was achieved at room temperature. Nanostructured cooling devices based on Si/SiGeC superlattices have also been examined [54] with reports of cooling power densities up to 680 W/cm^2 (see Fig. 6). While the efficiency of devices made from these materials is less than devices made from BiTe based devices, these results are interesting since coolers made from Si and SiGe materials can be readily integrated with microelectronic components. Additionally, Abramson et al. proposed using a composite of semiconductor nanowires and a polymer matrix to achieve a high thermoelectric performance and fabricated a prototype device [55].

One important technical issue in the fabrication of nanostructured thermoelectric devices is contact resistance between thermoelectric elements and the metal connectors. The electrical and thermal contact resistance may be even larger than the resistances of the nanostructured materials and may ultimately limit the device performance. More details on this issue can be found in a recent discussion by da Silva and Kaviany [56].

Summary

Nanostructured solid-state cooling devices may achieve significantly improved performance in comparison with their bulk counterparts. Understanding, and controlling, the thermal transport in nanostructures is crucial for designing nanostructured materials for thermoelectric applications. In the last two decades, significant progress has been made with regards to understanding thermal transport in these nanostructures. Phonon transport across interfaces in superlattices may involve scattering due to acoustic impedance mismatch, phonon spectra mismatch, interface defects and dislocations, interface roughness, interfacial strain and miniband gap formation. Thermal conductivities of nanowires are often much less than the values for corresponding bulk materials due to enhanced boundary scattering. Preliminary experimental results indicate that modifications of the phonon dispersion relation in nanowires may also be significant. Quantized phonon transport in nanostructures at very low temperature has also been demonstrated experimentally.

Due to the complex physics involved with phonon transport in low-dimensional nanostructures, the available experimental data are still not sufficient to enable accurate description of the phenomena. The effects of interfacial phenomena and phonon dispersion modification are still not well understood. For 1D nanostructures, only limited experimental data on GaAs, Si, Si/SiGe superlattice nanostructures exist. Nanowires with promise for thermoelectric devices, such as SiGe, Bi, Bi_2Te_3, and BiSb, have not been thoroughly studied to date. To fully understand the transport phenomena, heat capacity measurements on individual nanowires should also be carried out. While it is imperative to understand the fundamental transport phenomena in nanostructures in order to design a device with $ZT>3$, it is equally important to fabricate actual nanostructured cooling devices so that the overall device performance can be measured. For example, theory predicts extremely desirable thermoelectric properties of Bi and Bi_2Te_3 nanowires [57], yet no nanowire based thermoelectric device has been made from these materials.

Nomenclature

h = Planck's constant [J s]
k_B = Boltzmann's constant [J/K]
k = thermal conductivity [W/m K]
S = thermopower or Seebeck coefficient [V/K]
T = temperature [K]
ZT = dimensionless thermoelectric figure of merit
ℓ = mean free path (mfp) [m]
λ = wavelength [m]
σ = electrical conductivity [S/m]

References

[1] Mahan, G., Sales, B., and Sharp, J., 1997, "Thermoelectric Materials: New Approaches to an Old Problem," Phys. Today, **50**, pp. 42–47.
[2] DiSalvo, F. J., 1999, "Thermoelectric Cooling and Power Generation," Science, **285**, pp. 703–706.
[3] Hicks, L. D., and Dresselhaus, M. S., 1993, "Effect of Quantum-Well Structures on the Thermoelectric Figure of Merit," Phys. Rev. B, **47**, pp. 12727–12731.
[4] Hicks, L. D., Harman, T. C., and Dresselhaus, M. S., 1993, "Use of Quantum-Well Superlattices to Obtain a High Figure of Merit from Nonconventional Thermoelectric Materials," Appl. Phys. Lett., **63**, pp. 3230–3232.
[5] Hicks, L. D., and Dresselhaus, M. S., 1993, "Thermoelectric Figure of Merit of a One-Dimensional Conductor," Phys. Rev. B, **47**, pp. 16631–16634.
[6] Nolas, G. S., Sharp, J., and Goldsmith, H. J., 2001, *Thermoelectric: Basic Principles and New Materials Developments*, Springer, Heidelberg.
[7] Rowe, D. M., 1995, *CRC Handbook of Thermoelectrics*, CRC, Boca Raton, FL.
[8] Venkatasubramanian, R., Siivola, E., Colpitts, T., and O'Quinn, B., 2001, "Thin-Film Thermoelectric Devices with High Room-Temperature Figures of Merit," Nature (London), **413**, pp. 597–602.
[9] Harman, T. C., Taylor, P. J., Walsh, M. P., and LaForge, B. E., 2002, "Quantum Dot Superlattice Thermoelectric Materials and Devices," Science, **297**, pp. 2229–2232.
[10] Majumdar, A., 2004, "Thermoelectricity in Semiconductor Nanostructures," Science, **303**, pp. 777–778.
[11] Chen, G., 2000, "Phonon Heat Conduction in Nanostructures," Int. J. Therm. Sci., **39**, pp. 471–480.
[12] Cahill, D. G., Goodson, K., and Majumdar, A., 2002, "Thermometry and Thermal Transport in Micro/Nanoscale Solid-State Devices and Structures," J. Heat Transfer, **124**, pp. 223–241.
[13] Cahill, D. G., Ford, W. K., Goodson, K. E., Mahan, G. D., Majumdar, A., Maris, H. J., Merlin, R., and Phillpot, S. R., 2003, "Nanoscale Thermal Transport," J. Appl. Phys., **93**, pp. 793–818.
[14] Chen, G., and Shakouri, A., 2002, "Heat Transfer in Nanostructures for Solid-State Energy Conversion," J. Heat Transfer, **124**, pp. 242–252.
[15] Chen, G., 2001, "Phonon Transport in Low-Dimensional Structures," Semicond. Semimetals, **71**, pp. 203–258.
[16] Faghri, M., and Sundén, B., 2004, *Heat and Fluid Flow in Microscale and Nanoscale Structures*, WIT, Boston, MA.
[17] Chen, G., Zeng, T., Borca-Tasciuc, T., and Song, D., 2000, "Phonon Engineering in Nanostructures for Solid-State Energy Conversion," Mater. Sci. Eng., A, **292**, pp. 155–161.
[18] Ju, Y. S., and Goodson, K. E., 1999, "Phonon Scattering in Silicon Films with Thickness of Order 100 nm," Appl. Phys. Lett., **74**, pp. 3005–3007.

[19] Narayanamurti, V., Störmer, H. L., Chin, M. A., Gossard, A. C., and Wiegmann, W., 1979, ''Selective Transmission of High-Frequency Phonons by a Superlattice: The ''Dielectric'' Phonon Filter,'' Phys. Rev. Lett., **43**, pp. 2012–2016.
[20] Simkin, M. V., and Mahan, G. D., 2000, ''Minimum Thermal Conductivity of Superlattices,'' Phys. Rev. Lett., **84**, pp. 927–930.
[21] Ren, S. Y., and Dow, J. D., 1982, ''Thermal Conductivity of Superlattices,'' Phys. Rev. B, **25**, pp. 3750–3755.
[22] Chen, G., 1999, ''Phonon Wave Heat Conduction in Thin Films and Superlattices,'' J. Heat Transfer, **121**, pp. 945–953.
[23] Yao, T., 1987, ''Thermal-Properties of AlAs/GaAs Superlattices,'' Appl. Phys. Lett., **51**, pp. 1798–1800.
[24] Yu, X. Y., Chen, G., Verma, A., and Smith, J. S., 1995, ''Temperature Dependence of Thermophysical Properties of GaAs/AlAs Periodic Structure,'' Appl. Phys. Lett., **67**, pp. 3554–3556.
[25] Capinski, W. S., and Maris, H. J., 1996, ''Thermal Conductivity of GaAs/AlAs Superlattices,'' Physica B, **219 and 220**, pp. 699–701.
[26] Capinski, W. S., Maris, H. J., Cardona, T. M., Ploog, K., and Katzer, D. S., 1999, ''Thermal Conductivity Measurements of GaAs/AlAs Superlattices using a Picosecond Optical Pump-and-Probe Technique,'' Phys. Rev. B, **59**, pp. 8105–8113.
[27] Lee, S.-M., Cahill, D. G., and Venkatasubramanian, R., 1997, ''Thermal Conductivity of Si-Ge Superlattices,'' Appl. Phys. Lett., **70**, pp. 2957–2959.
[28] Chen, G., and Neagu, M., 1997, ''Thermal Conductivity and Heat Transfer in Superlattices,'' Appl. Phys. Lett., **71**, pp. 2761–2763.
[29] Borca-Tasciuc, T., Liu, W., Liu, J., Zeng, T., Song, D. W., Moore, C. D., Chen, G., Wang, K. L., Goorsky, M., Redetic, T., Gronsky, R., Koga, T., and Dresselhaus, M. S., 2000, ''Thermal Conductivity of Symmetrically Strained Si/Ge Superlattices,'' Superlattices Microstruct., **28**, pp. 199–206.
[30] Huxtable, S., Abramson, A., Tien, C.-L., Majumdar, A., LaBounty, C., Fan, X., Zheng, G., Bowers, J. E., Shakouri, A., and Croke, E. T., 2002, ''Thermal Conductivity of Si/SiGe and SiGe/SiGe Superlattices,'' Appl. Phys. Lett., **80**, pp. 1737–1739.
[31] Huxtable, S. T., Abramson, A. R., Majumdar, A., Shakouri, A., Croke, E. T., and Ahn, C. C., 2002, ''The Role of Defects and Acoustic Impedance Mismatch on Heat Conduction in SiGe Based Superlattices,'' *Proc. ASME IMECE, (MEMS Division)*, New Orleans, LA, pp. 19–23.
[32] Abramson, A. R., Tien, C. L., and Majumdar, A., 2002, ''Interface and Strain Effects on the Thermal Conductivity of Heterostructures: A Molecular Dynamics Study,'' J. Heat Transfer, **124**, pp. 963–970.
[33] Chen, Y. F., Li, D., Yang, J., Wu, Y., Lukes, J. R., and Majumdar, A., 2004, ''Molecular Dynamics Study of the Lattice Thermal Conductivity of Kr/Ar Superlattice Nanowires,'' Physica B, **349**, pp. 270–280.
[34] Huxtable, S. T., Abramson, A. R., Majumdar, A., Shakouri, A., Croke, E. T., and Ahn, C. C., 2004 (unpublished).
[35] Touzelbaev, M. N., Zhou, P., Venkatasubramanian, R., and Goodson, K. E., 2001, ''Thermal Characterization of Bi_2Te_3/Sb_2Te_3 Superlattices,'' J. Appl. Phys., **90**, pp. 763–767.
[36] Auld, B. A., 1973, *Acoustic Fields and Waves in Solids*, Wiley, New York.
[37] Nishiguchi, N., Ando, Y., and Wybourne, M. N., 1997, ''Acoustic Phonon Modes of Rectangular Quantum Wires,'' J. Phys.: Condens. Matter, **9**, pp. 5751–5764.
[38] Yu, S. G., Kim, K. W., Stroscio, M. A., and Iafrate, G. J., 1995, ''Electron-Acoustic-Phonon Scattering Rates in Cylindrical Quantum Wires,'' Phys. Rev. B, **51**, pp. 4695–4698.
[39] Seyler, J., and Wybourne, M. N., 1992, ''Acoustic Waveguide Modes Observed in Electrically Heated Metal Wires,'' Phys. Rev. Lett., **69**, pp. 1427–1430.
[40] Papandrew, A. B., Yue, A. F., Fultz, B., Halevy, I., Sturhahn, W., Toellner, T. S., Alp, E. E., and Mao, H.-K., 2004, ''Vibrational Modes in Nanocrystalline Iron under High Pressure,'' Phys. Rev. B, **69**, p. 144301.
[41] Shi, L., Li, D., Yu, C., Jang, W., Yao, Z., and Majumdar, A., 2003, ''Measuring Thermal and Thermoelectric Properties of One-Dimensional Nanostructures Using a Microfabricated Device,'' J. Heat Transfer, **125**, pp. 881–888.
[42] Li, D., Wu, Y., Kim, P., Shi, L., Yang, P., and Majumdar, A., 2003, ''Thermal Conductivity of Individual Silicon Nanowires,'' Appl. Phys. Lett., **83**, pp. 2934–2936.
[43] Mingo, N., Yang, L., Li, D., and Majumdar, A., 2003, ''Predicting the Thermal Conductivity of Si and Ge Nanowires,'' Nano Lett., **3**, pp. 1713–1716.
[44] Soyez, G., Eastman, J. A., Thompson, L. J., Bai, G. R., Baldo, P. M., McCormick, A. W., DiMelfi, R. J., Elmustafa, A. A., Tambwe, M. F., and Stone, D. S., 2000, ''Grain-Size-Dependent Thermal Conductivity of Nanocrystalline Yttria-Stabilized Zirconia Film Grown by Metal-Organic Chemical Vapor Deposition,'' Appl. Phys. Lett., **77**, pp. 1155–1157.
[45] Yang, H.-S., Bai, G.-R., Thompson, L. J., and Eastman, J. A., 2002, ''Interfacial Thermal Resistance in Nanocrystalline Yttria-Stabilized Zirconia,'' Acta Mater., **50**, pp. 2309–2317.
[46] Li, D., Wu, Y., Fan, R., Yang, P., and Majumdar, A., 2003, ''Thermal Conductivity of Si/SiGe Superlattice Nanowires,'' Appl. Phys. Lett., **83**, pp. 3186–3188.
[47] Goldsmid, H. J., and Penn, A. W., 1968, ''Boundary Scattering of Phonons in Solid Solutions,'' Phys. Lett., **27A**, pp. 523–524.
[48] Tighe, T. S., Worlock, J. M., and Roukes, M. L., 1997, ''Direct Thermal Conductance Measurements on Suspended Monocrystalline Nanostructures,'' Appl. Phys. Lett., **70**, pp. 2687–2689.
[49] Fon, W., Schwab, K. C., Worlock, J. M., and Roukes, M. L., 2002, ''Phonon Scattering Mechanisms in Suspended Nanostructures from 4 to 40 K,'' Phys. Rev. B, **66**, p. 045302.
[50] Schwab, K., Fon, W., Henriksen, E. A., Worlock, J. M., and Roukes, M. L., 2000, ''Quantized Thermal Conductance: Measurements in Nanostructures,'' Physica B, **280**, pp. 458–459.
[51] Schwab, K., Henriksen, E. A., Worlock, J. M., and Roukes, M. L., 2000, ''Measurement of the Quantum of Thermal Conductance,'' Nature (London), **404**, pp. 974–977.
[52] Rego, L. G. C., and Kirczenow, G., 1998, ''Quantized Thermal Conductance of Dielectric Quantum Wires,'' Phys. Rev. Lett., **81**, pp. 232–235.
[53] Ghoshal, U., Ghoshal, S., McDowell, C., and Shi, L., 2002, ''Enhanced Thermoelectric Cooling at Cold Junction Interfaces,'' Appl. Phys. Lett., **80**, pp. 3006–3008.
[54] Fan, X., Zeng, G., LaBounty, C., Bowers, J. E., Croke, E., Ahn, C., Huxtable, S., Majumdar, A., and Shakouri, A., 2001, ''SiGeC/Si Superlattice Microcoolers,'' Appl. Phys. Lett., **78**, pp. 1580–1582.
[55] Abramson, A. R., Huxtable, S. T., Kim, W. C., Yan, H., Wu, Y., Majumdar, A., Tien, C. L., and Yang, P., 2004, ''Fabrication and Characterization of A Nanowire/Polymer-Based Nanocomposite for a Prototype Thermoelectric Device,'' J. Microelectromech. Syst., **13**, pp. 505–513.
[56] da Silva, L. W., and Kaviany, M., 2004, ''Micro-Thermoelectric Cooler: Interfacial Effects on Thermal and Electrical Transport,'' Int. J. Heat Mass Transfer, **47**, pp. 2417–2435.
[57] Dresselhaus, M. S., Lin, Y.-M., Cronin, S. B., Rabin, O., Black, M. R., Dresselhaus, G., and Koga, T., 2001, ''Quantum Wells and Quantum Wires for Potential Thermoelectric Applications,'' Semicond. Semimetals, **71**, pp. 1–121.